Study of Electrical Conduction Mechanism, Optical and Mechanical Properties of Quaternary Vanadate-Phosphate Glasses

Thesis submitted by

Souvik Brahma Hota

Doctor of Philosophy (Engineering)

Department of Mechanical Engineering,
Faculty Council of Engineering & Technology
Jadavpur University
Kolkata, India
2025

Title of the thesis**: Study of Electrical Conduction Mechanism, Optical and Mechanical P roperties of Quaternary Vanadate-Phosphate Glasses**

Name, Designation & Institution of the Supervisor /s:

1. **Dr. Debasish Roy**
   Professor

   Department of Mechanical Engineering

   Jadavpur University, Kolkata, West Bengal

   And

2. **Dr. Dipankar Biswas**
   Assistant Professor (Research)

   Department of Electronics and Communication Engineering

   GLA University, Mathura, UP

List of Publications:

Journal article

[1] **Souvik Brahma Hota**, D. Roy, B. K. Ghosh, A.S. Das, R. Mondal, S. Kabi, C. Chakrabarti, D. Biswas, "Effect of transition metal and alkali oxides on structural, optical and dielectric properties in Zinc-Phosphate amorphous glassy systems," Journal of Non-Crystalline Solids, Volume 609,2023. (SCI, Scopus) (Q2)

[2] **Souvik Brahma Hota**, D. Biswas, S. K. Hazra, A.S. Das, R. Mondal, S. Kabi, D. Roy, Mixed ionic and electronic conductivity in the quaternary V_2O_5–Na_2O–ZnO–P_2O_5 glass system, Materialia, Volume 28,2023,101777, ISSN 2589-1529, doi: 10.1016/j.mtla.2023.101777(Scopus)(Q1)

[3] D. Biswas, **Souvik Brahma Hota**, R. Mondal, S. Mukherjee, P. C. Chandra, A. S. Das, S. Kabi, D. Roy, "Effect of heavy metal and alkaline earth oxides on the optical and electrical mechanism of vanadium-phosphate amorphous glassy systems", Journal of Non-Crystalline Solids, Volume 620,2023,122593, ISSN 00223093, doi: 10.1016/j.jnoncrysol.2023.122593. (SCI, Scopus) (Q2)

[4] D. Biswas, **Souvik Brahma Hota,** R. Mondal, A. Das, S. Kabi, D. Roy, Effect of Bi incorporation in adjusting structural, optical, and electrical conduction mechanism of xBi_2O_3-(0.40-x) Fe_2O_3-0.35V_2O_5-0.25P_2O_5 glass nanocomposites, Journal of Non-Crystalline Solids, Volume,641,2024,123145, ISSN 0022-3093, https://doi.org/10.1016/j.jnoncrysol.2024.123145.(https://www.sciencedirect.com/science/article/pii/S0022309324003223)(SCI, Scopus) (Q2)

[5] **Souvik Brahma Hota**, S. Nandy, K. Das, D. Biswas, R. Mondal, D. Roy, "Effect of Bi_2O_3 Addition on the Mechanical and Dielectric Properties of Bi_2O_3-BaO-P_2O_5-V_2O_5 Glasses with Improved Thermal Stability", Journal of Materials Science: Materials in Electronics, **36**, 1248 (2025). https://doi.org/10.1007/s10854-025-15323-8

Book chapter

[1] **Souvik Brahma Hota,** D. Biswas, R Mondal, D. Roy, (2025). Effect of Na_2O on Ionic-Electronic Conduction and Dielectric Relaxation of P_2O_5–ZnO–V_2O_5 Glass System. In: Sahoo, P., Barman, T.K. (eds) Advances in Materials, Manufacturing and Design. Lecture Notes in Mechanical Engineering. Springer, Singapore. https://doi.org/10.1007/978-981-97-6667-3_1

[2] **Souvik Brahma Hota**, D. Patra, D. Roy, A. Rakshit, D. Biswas "Effect of Transition Metal Oxides on Optical and DC Conduction Mechanism of Zinc-Phosphate Amorphous Semiconducting Glass"), River Publishers Series in Proceedings,2023,39-46, doi:10.13052/rp-9788770040099, (Scopus).

List of Presentations in National/International/Conferences/ Workshops:

[1] **Souvik Brahma Hota**, A. Rakshit, D. Roy, D. Patra, Dipankar Biswas, Effect of Transition Metal Oxides on Optical and DC Conduction Mechanism of Zinc-Phosphate Amorphous Semiconducting Glass,2022 6th International Conference on Electronics, Materials Engineering & Nano-Technology (IEMENTech), December 2-4, 2022,

[2] **Souvik Brahma Hota,** D. Biswas, D. Roy, Mixed ionic-electronic conductivity and dielectric relaxation of Na_2O doped ZnO-P_2O_5-V_2O_5 quaternary glass system, INCOM24: Proceedings of the 2nd International Conference on Mechanical Engineering Jadavpur University Kolkata India January 5 & 6, 2024, Paper No. INCOM24

[3] **Souvik Brahma Hota,** R. Mondal, D. Roy, D. Biswas, "Effect of Bi_2O_3 addition on the mechanical and dielectric properties of Bi_2O_3-BaO-V_2O_5-P_2O_5 Glasses with improved Thermal Stability", International Conference on Frontiers in Materials Science and Technology (ICFMST 2024), held on 5th December 2024.

[4] **Souvik Brahma Hota**, Rittwick Mondal, Dipankar Biswas, Debasish Roy, Mechanical Characterization of BBVP Glass Nanocomposites: Nanoindentation and Fracture Analysis, INCOM 2026: Proceedings of the 3rd International Conference on Mechanical Engineering, Jadavpur University, Kolkata, India (Submitted)

"Statement of Originality"

I Souvik Brahma Hota registered on 18th April 2022, do hereby declare that this thesis entitled **"Study of Electrical Conduction Mechanism, Optical and Mechanical Properties of Quaternary Vanadate-Phosphate Glasses"** contains literature survey and original research work done by the undersigned candidate as part of Doctoral studies.

All information in this thesis have been obtained and presented in accordance with existing academic rules and ethical conduct. I declare that, as required by these rules and conduct, I have fully cited and referred all materials and results that are not original to this work.

I also declare that I have checked this thesis as per the "Policy on Anti Plagiarism, Jadavpur University, 2019", and the level of similarity as checked by iThenticate software is 3 %.

Signature of Candidate: Souvik Brahma Hota

Date : 21/08/2025

Certified by Supervisor(s): (Signature

with date, seal)

1. Debasish Roy 21/08/2025

PROFESSOR
MECHANICAL ENGINEERING DEPTT.
JADAVPUR UNIVERSITY
KOLKATA-700 032

2. Dipankar Bhim 21/08/2025

Assistant Professor (Research)
Department of Electronics and
Communication Engineering
GLA University, Mathura, UP-281406

CERTIFICATE FROM THE SUPERVISOR/S

This is to certify that the thesis entitled **"Study of Electrical Conduction Mechanism, Optical and Mechanical Properties of Quaternary Vanadate-Phosphate Glasses"** submitted by Shri **Souvik Brahma Hota**, who got his/her name registered on 18th April 2022 for the award of Ph. D. (Engineering) degree of Jadavpur University is absolutely based upon his own work under the supervision of Dr. Debasish Roy, Professor, Department of Mechanical Engineering, Jadavpur University and Dr. Dipankar Biswas, Assistant Professor(Research), Department of Electronics and Communication Engineering, GLA University and that neither his/her thesis nor any part of the thesis has been submitted for any degree/diploma or any other academic award anywhere before.

1. Debasish Roy 21/03/2025
Dr. Debasish Roy, Professor, Department of Mechanical Engineering, Jadavpur University

PROFESSOR
MECHANICAL ENGINEERING DEPTT.
JADAVPUR UNIVERSITY
KOLKATA-700 032

2. Dipankar Biswas 21/03/2025
Dr. Dipankar Biswas, Assistant Professor (Research), Department of Electronics and Communication Engineering, GLA University, Mathura

Assistant Professor (Research)
Department of Electronics and
Communication Engineering
GLA University, Mathura, UP-281406

Acknowledgement

I take this opportunity, with profound respect and deep appreciation, to extend my sincere gratitude to my supervisors, Dr. Debasish Roy, Professor, Department of Mechanical Engineering, Jadavpur University, and Dr. Dipankar Biswas, Assistant Professor (Research), Department of Electronics and Communication Engineering, GLA University, Mathura. Their immense knowledge, patience, and remarkable ability to guide with both precision and empathy have been a constant source of inspiration throughout my research journey. I remain truly indebted to them for the confidence they placed in me, their invaluable guidance during moments of uncertainty, and their unfailing generosity in imparting wisdom—qualities that I regard as rare blessings. Their mentorship extended beyond academics, shaping my outlook on perseverance, ethics, and the pursuit of excellence, for which I will always remain grateful.

I would also like to take this opportunity to thank with immense gratitude my esteemed members of the Research Advisory Committee: Dr. Arunabha Chanda and Dr. Sandip Sarkar at the Department of Mechanical Engineering, Jadavpur University. They provided meaningful comments and criticisms, positive remarks and frequent suggestions, which were crucial to shaping my work and making it rich in content.

I owe a special note to Mr. Rittwik Mandal, who has been a firm pillar to me in my research process, ready to help at all times and a firm supporter. I am also happy to express my gratitude to Dr. Soumyajyoti Kabi, Head, Department of Physics, Hijli College, who, through his immense help, suggestions, advice, and encouragement, gave me just the amount of impetus when needed.

I want to warmly thank the fellow researchers, Arpan Mandal and Bidyut Kumar Ghosh, as the presence of the companions who have provoked my thinking and deepened my ways of thinking, has allowed me to create an atmosphere of mutual learning and development of the research situation. I gratefully acknowledge my colleagues in the Department of Mechanical Engineering, Techno India University, West Bengal.

Such a journey would not have been possible without the lifelong guidance provided by my parents, Mr. Sujit Kumar Hota and Mrs. Sarbani Nanda Hota, retired eminent Headmasters of Government High Schools and real worshippers of education. Their devotion to the cause of learning, their sense of right and wrong and their invariable blessings have been the pillars my ambitions have rested on. I also bow in reverence to my grandfather, Pandit Jnanranjan Hota, whose scholarly mastery of Sanskrit and deep-rooted wisdom have been a guiding light in my life.

Finally, my deepest and most personal gratitude goes to my beloved life partner, Prof. Niti Dey, whose constant encouragement, unwavering belief in my potential, and inspiring companionship have been my greatest source of strength. Her presence has been an anchor during turbulent times and a source of joy in moments of triumph.

To the Almighty, above all, I bend my knees in grateful submission to the inexpressible grace of God, the divine wisdom and blessings that have been my only source of strength and endurance and direction throughout this experience.

To everyone who has contributed even a little to this journey, big and small, I am eternally grateful.

Sourik Brahma Hota
21/08/2025

TABLE OF CONTENTS

LIST OF FIGURES

LIST OF TABLES

List of Abbreviations and Symbols

CRN	Continuous Random Network
NBOs	Non-bridging oxygens
MRN	Modified Random Network
BMGs	Bulk metallic glasses
TEC	Thermal expansion coefficient
MME	Mixed modifier effect
XRD	X-ray diffraction
FWHM	Full width at half maxima
FTIR	Fourier Transform Infrared spectroscopy
HN	Havriliak–Negami
VRH	Variable Range Hopping
CBH	Correlated Barrier Hopping
CSM	Continuous Stiffness Measurement
DSC	Differential Scanning Calorimetry
$\mathbf{V_M}$	Molar volume
$\mathbf{d_c}$	Nanocrystallite size
$\boldsymbol{\beta}_{\mathbf{correct}}$	Corrected full-width at half maximum
$\boldsymbol{I_{Raman}}$	Raman scattering intensity
$\boldsymbol{\alpha}$	Absorption coefficient
$\mathbf{E_U}$	Urbach energy
$\boldsymbol{E}_{\mathbf{opt}}$	Optical bandgap energy
$\boldsymbol{\varepsilon'}$	Dielectric constant
$\boldsymbol{\varepsilon''}$	Dielectric loss
$\mathbf{tan}\boldsymbol{\delta}$	Dielectric loss tangent
$\boldsymbol{M^*}$	Complex electric modulus
$\boldsymbol{\phi(t)}$	Kohlrausch–Williams–Watts (KWW) function
$\boldsymbol{\beta}$	Kohlrausch-Williams-Watts (KWW) stretched exponential parameter
$\mathbf{H_v}$	Vickers hardness number
$\boldsymbol{s}$	Contact stiffness
$\boldsymbol{h_c}$	Contact depth
$\boldsymbol{A_p}$	Projected contact area
$\boldsymbol{E}$	Elastic modulus
$\boldsymbol{K_{IC}}$	Fracture toughness
$\boldsymbol{U_r}$	Strain energy released
L	Longitudinal Modulus
S	Shear modulus
K	Bulk modulus
Y	Young's modulus
$\boldsymbol{\sigma}$	Poisson's ratio
$\mathbf{T_g}$	Glass transition temperature
$\mathbf{T_c}$	Crystallisation temperature
$\mathbf{T_p}$	Peak crystallization temperature
$\mathbf{\Delta T}$	Thermal stability factor
$\mathbf{T_m}$	Fusion temperature

ABSTRACT

This study synthesized three unique quaternary glass systems: V_2O_5-Na_2O-ZnO-P_2O_5(VNZP), Bi_2O_3-BaO-V_2O_5-P_2O_5(BBVP) and Bi_2O_3-Fe_2O_3-V_2O_5-P_2O_5 (BFVP) via the standard melt-quenching method, and systematically modified each by variable doping to observe the material structure and optical, dielectric, electrical, mechanical, and thermal properties. The focus was to have some precise structure-property correlations to determine the effects of compositional tuning to functional performance to application in optoelectronics, high-temperature dielectrics and energy-related devices. X-ray diffraction (XRD) structural analysis established that all compositions are predominantly amorphous, as evident in the broad diffuse halo, with nanocrystalline phases in dopant-rich samples detected and quantified through Rietveld refinement. Systematic phosphate- and vanadate-based structural unit modifications were systematically characterized optically using Raman and Fourier-transform infrared (FTIR) spectroscopy, where additions of V_2O_5 favoured network depolymerization. UV-visible absorption spectroscopy revealed that the optical band gap (E_{opt}) reduced systematically in a consistent way, and Urbach energy (E_u) increased, suggesting increased structural disorder and increased density of defect states. Composition-dependent changes in the refractive index, molar polarizability and extinction coefficient demonstrated that the optical performance could be tuned to deliver photonic applications. Different behaviours were shown in the dielectric analysis in all three systems. In VNZP, the dielectric constant ($\varepsilon^{/}$) and dielectric loss ($\varepsilon^{//}$) were both frequency dependent and temperature dependent, where the former declined with frequency and rose with temperature. In electric modulus scaling, non-exponential behaviour was interpreted as temperature-independent and (relatively) composition-dependent relaxation, with the exponent ($n < 1$) in the Bergman representation of relaxation proving to be non-Debye behaviour. BBVP glasses had the same trends, with scaling behaviour that was independent of temperature and composition and relaxation that depends on the re-organization of structure. In BFVP, $\varepsilon^{/}$ increased up to 15 per cent at 413 K at low frequencies and was thermally stable; $\varepsilon^{//}$ revealed optimal dipolar relaxation at $x = 0.3$. The activation energy of dielectric relaxation decreased by 0.67 eV (x 0.1) to 0.49 eV (x 0.4), and the electric modulus spectra were consistent with the lack of Debye relaxation in all systems. Electric conductivity measurements showed that the AC conductivity was correlated with a modified correlated barrier hopping (CBH) model, and DC conductivity showed a flux in ionic conduction to small-polaron hopping with the

increased temperature and the doping density. The addition of Bi_2O_3 led to increased DC conductivity because of reduced hopping distances and the high density of defect pairs. The assessment of mechanical properties was done both at the micro- and nanoscale. Vickers microhardness (Hv) declined systematically with increasing concentration of V_2O_5 in the VNZP series, consistent with a progressively softer, less rigid network that is formable but less ideal in higher-durability applications. In this series, too, there was a sharp indentation size effect (ISE); the value of Hv was nearly linearly dependent upon the load applied. Conversely, both the micro- and nano hardness of BBVP and BFVP glasses monotonically enhanced with higher Bi_2O_3 content because of the packing density of the network, a decrease in the number of non-bridging oxygens and the creation of robust Bi–O–P/Bi–O–V linkages. Nano-mechanical properties, determined via the Oliver and Pharr method with a Continuous Stiffness Measurement (CSM) nano-indenter, confirmed increases in instrumented hardness (HIT) and elastic modulus (EIT). In the case of BBVP, fracture toughness (K_{IC}) and stored elastic strain energy (U_r) increased with Bi_2O_3 loading and increased elastic constants were confirmed by ultrasonic pulse 2D echo measurements.

Thermal stability, determined by Differential Scanning Calorimetry (DSC), increased consistently with Bi_2O_3 incorporation across the BBVP and BFVP series, with systematic rises in glass transition temperature (T_g), crystallisation onset temperature (T_c), and peak crystallisation temperature (T_p). The T_g increased by 34% at 35 mol% Bi_2O_3, showing that cross-linking occurred in the network through strong Bi–O bonding, enhancement of the network cross-link density and decreased tendency to devitrify. The overall findings show that careful compositional engineering, especially via Bi_2O_3 enrichment, is capable of optimising mechanical strength, dielectric stability, electrical transport, optical tunability, and thermal resistance all at once. The VNZP glasses have increased formability, BBVP glasses are superior in mechanical and thermal resilience, and BFVP glasses are stiff with the added property of improved dielectric. These results form a strong foundation to build the next generation of optoelectronic devices, thermally stable dielectrics, mechanically robust optical windows and energy-storage interfaces to future electronic, photonic and sustainable energy technologies.

Chapter 1

Overview of Electrical, Optical, and Mechanical Properties in Glassy Materials

1.1. Overview of Inorganic Glasses

Since ancient times, scientists and technologists have studied glass because it continues to develop and fascinate with its unique properties. From its ancient origins as a structural and protective material renowned for its optical transparency and dielectric properties, glass has evolved into an active functional material with numerous applications. Glass has found essential applications beyond windows and containers, serving critical functions in advanced sectors such as electronics and biomedical sciences. Due to its exceptional physicochemical properties, which incorporate high thermal stability together with tunable refractive index and controlled ionic conductivity, glass has become integrated into advanced technological applications like resistive switching memory devices, optical sensors, photovoltaic cells and heterogeneous catalysts. Modern scientific developments and industrial applications demonstrate a paradigm shift that confirms glass's crucial importance in contemporary materials science and engineering [1].

Scientists have long debated the definition of glass, which has been examined through numerous renowned researchers' structural and thermodynamic perspectives.

Zachariasen (1932): "Glass is a rigid material formed by continuous cooling of a melt without crystallization, where the atomic arrangement lacks long-range periodicity but retains short-range order"[2].

Shelby (2005): "Glass is an amorphous solid that exhibits a glass transition, transforming from a brittle state to a more rubber-like state upon heating"[3].

Mauro (2011): "Glass is a non-equilibrium, non-crystalline state of matter that continuously transforms into a supercooled liquid upon heating through the glass transition temperature"[1].

Doremus (1994): "Glass is a material that has no long-range order and undergoes a continuous change in viscosity upon cooling, rather than exhibiting a sharp melting point "[4].

These definitions emphasize the amorphous, non-crystalline nature of glass and its characteristic glass transition behavior. Glass differs from crystalline solids because it lacks a sharp melting point yet transitions into a supercooled liquid which makes it a unique and versatile material across scientific and industrial domains.

1.2. The History and Evolution of Glass

Glass is among the oldest materials humans use, with its origins tracing back thousands of years.

Long before the advent of synthetic glass, early civilizations encountered naturally occurring glasses such as obsidian, fulgurites, impactites, and tektites, which were utilized for crafting tools, weapons, and ornamental artefacts due to their sharp edges and durability [6]. The exact origins of man-made glass are shrouded in history, but archaeological findings indicate that its production began in ancient Egypt and Mesopotamia around 3500 BCE [7].

A pivotal advancement in glass manufacturing occurred in the 1st century BC with the invention of glassblowing in the region corresponding to modern-day Syria. This revolutionary technique significantly expanded the applications of glass, making it more accessible for both functional and decorative purposes. From 1500 BC onwards, the commercial trade of glass spread its production techniques to Europe and East Asia, leading to its gradual integration into various cultural and technological domains. Using glass for architectural value was common by the 15th century, particularly in building and cathedrals, with increasing use of glass windows [8].

The 16th and 17th centuries were considered the era of innovation in glass in Europe. Significant breakthroughs resulted from the industrialization of glass making, especially in England from the late 17th century, not only the introduction of lead glass by George Ravenscroft, but also the development of the glassblowing hammer and puffing tools. The lead oxide, potash and silica all made a slightly better grade of glass, which was used in the 18th century to make optical clear glassware and the development of long-range telescopes. Lead glass which still finds wide use today because of high refractive index and of its radiation shielding property, is used today [9].

In the 20th century glass manufacturing made great advancements including continuous glass casting first taken out by Pilkington Brothers in 1959. The invention of this glass sheet mass produced product with consistent thickness and ultra-flat surface enabled the architecture and automotive industries. Furthermore, this technique is also a pertinent aspect in the technological evolution of glass for screen glass used in modern displays [10].

Both from its ancient beginnings to its modern industrial applications, glass has advanced in ways incomparable in history and so has driven the material sciences and technology forward. For today, glass production is an essential piece of today's global industry and constitutes a million distinct

uses from optoelectronic to biomedical engineering, energy efficient building and aerospace technologies [11].

1.3. Definition of Glass

The American Society for Testing and Materials (ASTM) [5] formally characterizes glass as "an inorganic product of fusion which, without crystallization, cools from a rigid condition" [8,12]. This definition emphasizes the fundamental nature of glass being an amorphous material formed by the melt quenching process, as fast cooled below the crystallization temperature of the liquid to prevent long-range atomic organization. More broadly, glass is described as a disordered solid that completely lacks long-range structural periodicity and undergoes a distinct glass transition process [13,14]. The terms amorphous and disordered solid are frequently used interchangeably in materials science.

The glass transition is a fundamental characteristic of glassy materials, where an amorphous structure undergoes a rapid alteration in its derivative thermodynamic properties, shifting from a rigid, solid-like state to a more fluid-like condition as the temperature increases [15]. This transition is fundamentally different from the melting of crystalline solids, as it occurs over a temperature range rather than at a sharply defined melting point.

While historically, glass was primarily synthesized via melt-quenching, modern fabrication methods such as atomic layer deposition (ALD), plasma-enhanced chemical vapor deposition (PECVD), and hydrothermal synthesis now enable the production of non-crystalline materials that are structurally and functionally equivalent to thermally quenched glasses with identical chemical composition. As a result, contemporary glass science defines glass as encompassing all amorphous solids that exhibit glass transition behavior, irrespective of the synthesis route [16].

From a thermodynamic perspective, the glassy state is a metastable phase that fundamentally differs from its crystalline counterpart. Unlike crystals, which exist in a unique lowest-energy configuration, glasses occupy a local minimum in free energy, dependent on the thermal history of the melt. Over extended periods, glass undergoes structural relaxation toward a configuration with reduced free energy, contingent on overcoming the activation barrier for atomic

rearrangement [17]. Yet relaxation in conventional glasses experiences a process that is so long, so long that even geological epochs can be exceeded, and the metastable nature of glass has become a theoretical rather than a practical constraint [18].

1.4. Glass Transition: Fundamental Aspects and Theoretical Considerations

Glass transition temperature (T_g) is an important fundamental property of any glassy material, being different from that of a crystalline solid. Although this phenomenon is intrinsically intricate, and unique, attributed to its dependence on many of the thermodynamic and kinetic parameters. Many conceptual frameworks have been devised to explain the underlying mechanisms of this transition, with a focus on some physical attributes characterizing glasses. Nevertheless, despite their multi-factor nature, these models have not yet found much success due to the complexity of T_g, which depends on system-specific heat capacity, thermal diffusivity, fusion temperature (T_m), cooling kinetics, molecular relaxation dynamics, and viscosity [19].

The singularly most difficult aspect of identifying T_g is in the marked variation in T_g values measured; these values are extremely sensitive to the test method in use. This variability arises because, during the rapid quenching of a melt, various molecular degrees of freedom become kinetically arrested, preventing structural relaxation into a crystalline form. Upon subsequent heating, these degrees of freedom relax at different rates, leading to variations in the experimentally determined T_g depending on the physical property used for measurement [20].

When a liquid is cooled, two possible scenarios arise: it either undergoes crystallization at the solidification (or fusion) temperature (T_m) or circumvents crystallization, transitioning into a super-cooled metastable phase. In the latter case, as the temperature decreases, the supercooled liquid exhibits a progressive increase in viscosity until it reaches $\eta \approx 10^{14.6}$ dPa·s, at which point it behaves mechanically as a solid [21]. Although the atomic arrangement of glass resembles that of a liquid in terms of structural disorder, it exhibits macroscopic properties—such as rigidity and elastic modulus—consistent with those of a solid.

This transition from a supercooled liquid to an amorphous solid can be effectively described by tracking variations in thermodynamic parameters such as enthalpy (H) and volume (V) as functions of temperature. Crystallization is marked by an abrupt discontinuity in these extensive

thermodynamic variables at Tm, whereas vitrification manifests as a progressive change in the slope of these curves [22].

The thermal interval within which this structural relaxation occurs is termed the glass transformation range [19,20]. Due to the gradual nature of this transition, T_g lacks a singular, well-defined value. Instead, it is frequently represented by the fictive temperature (T_f), which is determined as the intersection point of extrapolated enthalpy or volume curves corresponding to the liquid and glassy states (**Fig. 1.1**).

The fictive temperature and, consequently, the glass transition temperature, are strongly dependent on the cooling rate (q) of the supercooled liquid. A slower cooling rate allows more time for structural relaxation, extending the supercooled region and resulting in a lower T_g. Conversely, rapid cooling limits molecular rearrangement, leading to a higher T_g. This dependency implies that T_g is not an intrinsic material property, but rather a function of the thermal history of the glass [20]. The quantitative relationship between Tg and cooling rate q is often expressed as:

$$q = q_0 \, e^{\frac{-1}{c}\left(\frac{1}{T_g} - \frac{1}{T_M}\right)} \qquad (1.1)$$

The parameters c and q are material-specific constants [20]. The experimentally determined value of Tg is not absolute, as it varies based on the temporal resolution of the measurement technique employed. The glass transition temperature is inherently dependent on the timescale of observation, reflecting the kinetics of structural relaxation in the material.

As the temperature decreases, the rate of configurational rearrangements diminishes significantly. At Tg, the material demonstrates solid-like characteristics when the experimental observation timescale (t_0) is shorter than the structural relaxation time (tr). Conversely, when $t_r < t_o$, the material retains its liquid-like properties. A transition is considered to occur when measurable physical parameters, such as specific heat capacity, thermal expansion coefficient (TEC), and enthalpy exhibit a pronounced deviation from their liquid-state values. Thus, Tg is operationally defined as the temperature at which t_0 and t_r become comparable [21].

The glass transition is fundamentally characterized by abrupt changes in the derivative thermodynamic properties of the material. This phenomenon corresponds to the Ehrenfest scheme for categorizing phase transitions, which determines the transition order based on the lowest-order

differential of Gibbs free energy (G) that demonstrates a sudden change [21]. During the transformation from liquid to solid at the freezing (or melting) point (T_m), thermodynamic properties such as volume (V) and enthalpy (H), which represent first-order differentials of Gibbs free energy (G), experience an abrupt shift, thereby identifying crystallization as a first-order phase transition. In contrast, during the liquid-to-glass transition, the first-order thermodynamic variables (V, H, and entropy S) remain continuous, whereas the second-order derivatives of G, such as thermal expansion coefficient (α_T), isothermal compressibility (K_T), and heat capacity (C_P), exhibit discontinuities. This discontinuity in second-order derivatives suggests that the glass transition shares key thermodynamic attributes with second-order phase transitions [21].

The conventional thermodynamic framework does not fully account for the experimentally observed influence of thermal history on T_g, including variations arising from cooling rate, annealing conditions, and prior thermal cycling. This discrepancy implies that the glass transition cannot be strictly a simple second order thermodynamic phase transition because second order phase transitions are independent of thermal history in general. To overcome this limitation, Prigogine and Defay [22] developed a more general way describing the glass transition by introducing a dimensionless parameter R, which takes into account the deviations from the second order transition behavior. It offers a more complete thermodynamic description to understand the complexity of the glass transition, in which both kinetic and thermodynamic factors are taken into account.

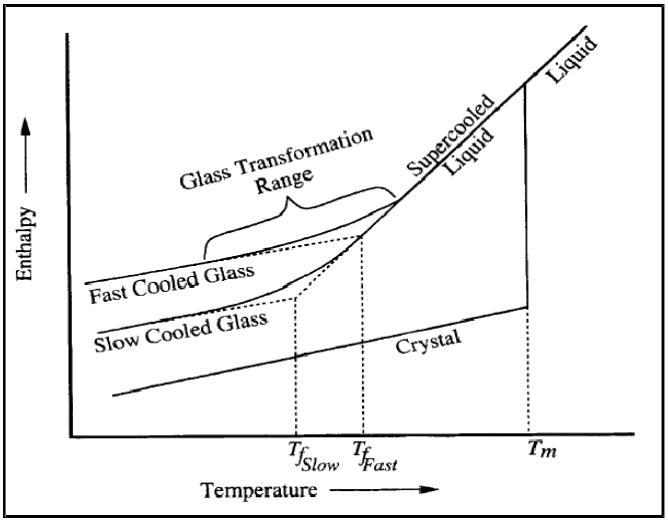

Fig. 1.1. Temperature-Dependent Changes in Enthalpy and Volume of a Glass-Forming Melt [22].

Intrinsically, a glass transition is an amorphous solid thermo-kinetic event associated with a distinct shift of differential thermodynamic properties such as specific heat capacity (Cp), coefficient of thermal expansion (α_T), and isothermal bulk modulus (K_T) at the transition temperature [22]. According to the Ehrenfest framework, phase transitions are classified concerning the lowest-order differential of Gibbs free energy (G) that undergoes an abrupt change at the critical transition point [22].

Crystallization is a first-order phase transition characterized by an abrupt discontinuity in thermodynamic properties of the system, such as volume (V) and enthalpy (H), derivatives ($\partial G/\partial P$) of Gibbs free energy, during a liquid to crystal, first-order, liquid to crystal transition at the fusion temperature (T_m).

Conversely, continuous thermodynamic variables, V, H and S, whereas continuous second-order derivatives of G, i.e., C_p, α_T, K_T, etc. display sharp discontinuity during the liquid-to-glass transition. This characteristic behavior therefore suggests that the glass transition also has thermodynamic features in common with higher-order phase transitions [22].

Nevertheless, the concepts of the glass transition are not fully encompassed by a conventional thermodynamic treatment, because they involve kinetic constraints and molecular heterogeneity. The glass transition temperature (T_g) is unlike equilibrium phase transitions, a thermodynamic constant, rather it is highly dependent upon factors such as cooling kinetics, thermal history and annealing conditions. In classical second-order phase transition, the transition temperature is invariant concerning the external factors. However, contrary to a purely second-order thermodynamic classification, the T_g observed in the experiment shows strong history dependence.

This limitation was recognized by Prigogine and Defay [12] who introduced a more general thermodynamic framework which is not based on strict second-order phase transition formalism. They suggest a dimensionless parameter R which allows to inclusion of both a thermodynamic and a kinetic content in the equation of the glass transition and enables a broader view of the glass transition than the classical thermodynamic framework.

$$R = \frac{\Delta K_T \Delta C_P}{TV(\Delta \alpha_T)^2} \qquad (1.2)$$

When, for a relaxing system, the equilibrium state is determined by a single ordering parameter, this ratio is unity (R = 1). Indeed, in most glass-forming materials, the structural relaxation process involves several ordering parameters, and the real part of the spectral is found to be R > 1, not displaying classical second-order phase transition behavior. The glass transition is therefore not well described in the framework of equilibrium thermodynamics but requires a kinetic point of view.

Despite the glass transition having a strong relaxation-driven nature, a thermodynamic component is present as suggested by the Kauzmanns paradox [13]. Its existence is a paradox (extrapolating the entropy of a supercooled liquid to lower temperatures and anticipating an entropy crisis where the liquid would achieve a configurational entropy lower than that of the corresponding crystalline phase). An outcome such as this would violate the third law of thermodynamics, therefore there must exist an additional thermodynamic constraint or kinetic arrest mechanism before reaching absolute zero. The glass transition displays an apparent contradiction because it possesses kinetic features but lacks true thermodynamic second-order phase transition attributes. The glass transition resembles a second-order phase change but changes heat capacity because it depends on the cooling rate so it follows non-equilibrium kinetic principles.

To determine if a material will vitrify rather than crystallize when cooling, Hruby [14] proposed the glass forming ability (GFA) parameter (K_g) a measure of important thermal characteristics including the glass transition temperature (T_g), melting temperature (T_m), and crystallization temperature (T_c).

The exact functional form captures the relative thermal stability of the glassy phase against crystallization, while this parameter gives an insight into the stability of the supercooled liquid phase.:

$$K_C = \frac{T_C - T_g}{T_M - T_C} \tag{1.3}$$

The relative thermal stability of the glassy phase against crystallization is captured for a particular functional form. The higher the Kg, the stronger the glass-forming tendency of the material, and it is a critical parameter in the development of materials for meeting applications that need an amorphous structure.

Characteristic temperatures, in general, have a significant impact on the glass-forming ability (GFA) of a material. If the thermal gap between T_c and T_g is larger and the interval between T_M and T_c is smaller, then the nucleation rate is lower and crystallization propensity is lower, and verification tendency is higher. This would indicate that systems with a wider temperature gap between crystallization and glass transition are less susceptible to crystallization and thus retaining in the amorphous state under condensed samples more likely. From a kinetic standpoint, the glass transition temperature (T_g) is also defined relative to the experimental observation timescale, representing the temperature at which a supercooled liquid attains a viscosity characteristic of a rigid solid, approximately $10^{14.6}$ dPa·s. Within this framework, glass can be interpreted as a kinetically arrested liquid, wherein molecular mobility is sufficiently constrained to prevent the system from reaching equilibrium. It is well established that the viscosity (η) and structural relaxation time (τ) of glass-forming systems increase dramatically as cooling approaches T_g.

The thermodynamic glass transition temperature is identified as the point where viscosity or relaxation time becomes so large that the system departs from thermodynamic equilibrium with its surroundings. In silica-based glasses, this thermodynamic T_g typically occurs at approximately two-thirds of the melting temperature (T_M). The temperature dependence of viscosity in glass-forming systems follows two distinct phenomenological trends, classified based on their relaxation dynamics:

1. **Strong Glass Formers**: These exhibit Arrhenius-type viscosity behavior, where viscosity (η) and relaxation time (τ) grow exponentially at lower temperatures, following the well-known Arrhenius law [15]:

$$\eta = \eta_0 \, e^{\left(\frac{A}{T}\right)} \tag{1.4}$$

Where η_o represents the pre-exponential factor, E_a denotes the activation energy for viscous flow, R is the universal gas constant, and T corresponds to the absolute temperature. Silica (SiO_2) serves as a quintessential example of a strong glass, exhibiting an Arrhenius-type viscosity behavior with a relatively high activation energy for molecular rearrangement.

2. **Fragile Glass Formers**: These deviate significantly from Arrhenius behavior, exhibiting a super-Arrhenius temperature dependence, where viscosity increases more sharply as temperature decreases. This non-Arrhenius behavior is often described by the Vogel-

Fulcher-Tammann (VFT) equation, which better captures the kinetic slowing-down near T_g.

$$\eta = \eta_0 \, e^{\left(\frac{B}{T-T_0}\right)} \tag{1.5}$$

where the empirical constants are η_0, B, and T_0. A divergence of the viscosity at a finite temperature (T_0), typically below T_g, is predicted by the VFT equation as opposed to the Arrhenius equation, in accord with the super-Arrhenius behaviour in fragile glass formers. Indeed, this model describes very well the rapid slowing down of the molecular dynamics at T_g, where viscosity increases much faster than the Arrhenius law predicts. Examples of such far-from-simple activated flow behaviour include borate and metallic glasses.

It is important to differentiate between strong and fragile glass formers to understand the relaxation dynamics of supercooled liquids and the kinetic principles controlling the glass transition behaviour.

1.4.1. Free Volume Model of the Glass Transition

The free volume theory provides an alternative view of the glass transition phenomenon [17]. Here, the total volume (V) is factored into two principal distributions:

- **Occupied volume** (V_{oc}) – The space physically occupied by the molecules.
- **Free volume** (V_f) – The unoccupied regions within the structure that allow for molecular motion.

The free volume of a glassy material remains nearly constant in cooling and gets kinetically solidified to particular locations when the glass is formed. However, in liquids, there is a redistribution of available space, and in both the free and occupied volumes contract as the temperature is decreased. As per the free volume hypothesis, the glass transition takes place when the fractional free volume (V_{ff}) drops below a critical limit, effectively restricting large-scale molecular motion and structural reorganization.

The fractional free volume is expressed as:

$$V_{ff} = \frac{V_{fg}}{V_g} = T_g \times \Delta\alpha_T \quad (1.6)$$

Here, V_{fg} represents the free volume within the glass, while V_g denotes the total volume of the glass. The term $\Delta\alpha_T = \alpha_{TL} - \alpha_{Tg}$ defines the difference between the volume thermal expansion coefficients of the liquid (α_{TL}) and the glass (α_{Tg}). Experimental findings indicate that, for many glass systems, nearly 10% of the total volume persists as free volume at the glass transition temperature (T_g) [15].

To enhance the applicability of free volume theory, percolation theory has been integrated [18,19], enabling the redistribution of free volume among liquid-like regions while maintaining structural stability in solid-like domains. This modification accounts for dynamic heterogeneity in supercooled liquids, providing a more generalized framework for glass transition modelling.

Despite substantial theoretical progress, no single framework fully accounts for the multifaceted nature of the glass transition. Each model—whether focused on relaxation dynamics, thermodynamic principles, or free volume constraints—addresses specific aspects of the phenomenon but remains inherently limited in scope. A comprehensive theoretical framework must encompass both kinetic mechanisms (structural relaxation) and thermodynamic principles (equilibrium considerations) to accurately characterize the transformation from a liquid to a glassy state.

Recent modifications of free volume theory using percolation arguments provide a promising direction toward achieving this goal, potentially bridging the gap between empirical observations and fundamental theory.

1.5. Melt-Quenching: A Fundamental Technique for Glass Formation

The melt-quenching technique is the oldest and most widely employed method for producing amorphous solids by rapidly cooling a molten material to suppress nucleation and crystal growth, thereby stabilizing the material in a disordered, glassy state [68]. Historically, amorphous materials produced via this method were referred to as glasses; however, the modern definition of glass encompasses any material that exhibits a glass transition, regardless of its formation process. Despite this broader classification, most melt-quenched amorphous solids undergo a glass transition, making this technique highly relevant for commercial glass production. The

fundamental characteristic of melt-quenching is that the transition from the liquid to the amorphous solid state occurs through a continuous increase in viscosity, distinguishing it from the discontinuous solidification of crystalline materials. The required cooling rates for glass formation vary significantly depending on the material, with easy glass formers such as SiO_2, P_2O_5, and B_2O_3 forming glasses even under slow cooling conditions (~1 K/s), while metallic glasses require extremely high cooling rates, typically in the range of 10^4–10^6 K/s, due to their strong tendency to crystallize. The melt-quenching process involves several critical steps, beginning with batch preparation and melting, where raw materials in pre-determined proportions are mixed and heated in a tank furnace or crucible at high temperatures (typically 1400–1500°C for commercial glasses) to achieve homogeneity and remove bubbles. This is followed by quenching and cooling, where the molten glass is rapidly cooled through methods such as direct quenching in water, pouring between metal plates, or casting into graphite molds to control heat dissipation. The next stage involves shaping and forming, wherein the glass is processed at viscosities of 10^3–10^4 dPa·s (900–1100°C for oxide glasses) using techniques like mold casting, blowing, pressing, rolling, and floating, allowing for the fabrication of diverse geometries. Annealing is then performed near the glass transition temperature (T_g) to eliminate residual thermal stresses induced by rapid cooling, given the inherently low thermal conductivity of glass. The melt-quenching method is extensively used for producing oxide glasses based on traditional network formers such as SiO_2, P_2O_5, and B_2O_3, but the fabrication of metallic glasses requires specialized techniques like melt spinning (rapid quenching on a rotating copper wheel) and melt extraction (solidifying a thin ribbon by extracting molten droplets). The primary advantage of melt-quenching lies in its broad compositional flexibility, enabling the production of glass compositions tailored for optical, electronic, and structural applications. However, a major limitation is its inability to achieve ultra-high-purity glasses, necessitating alternative methods such as chemical vapor deposition (CVD) or sol-gel processing. Despite this, melt-quenching remains the dominant industrial technique for glass production, offering high scalability, structural tunability, and efficient processing, with ongoing advancements in quenching technologies and compositional control expected to expand its applications, particularly in the development of high-strength metallic glasses and functional Nano glasses. The Schematic block diagram of the process depicted in **Fig.1.2**.

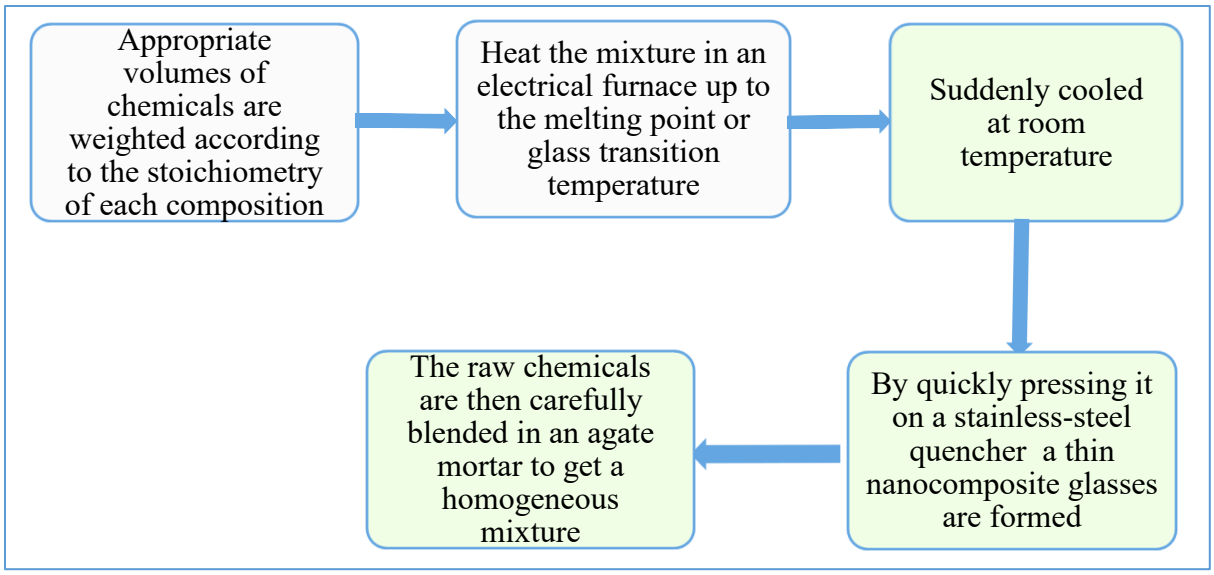

Fig.1.2. Schematic block diagram of the Melt quenching process

1.6. Structural Considerations in Amorphous Solids

A comprehensive understanding of the atomic arrangement in any material is essential for elucidating its physical, chemical, and functional properties. While the structural classification of crystalline materials is well-established through the concept of the unit cell, a similar approach does not apply to amorphous materials due to their lack of long-range periodicity and symmetry. However, despite the absence of long-range translational order, amorphous solids often exhibit significant structural organization over intermediate length scales, typically extending over several angstroms [20]. This distinction allows for the arbitrary definition of a length scale that separates the microscopic (short-range) structure from the macroscopic (long-range) structure in amorphous solids [21].

The progress of experimental methodologies has significantly improved our capability to analyze and comprehend the structural arrangement in glassy substances. Techniques such as Nuclear Magnetic Resonance (NMR), Extended X-ray Absorption Fine Structure (EXAFS) spectroscopy, and Small-Angle X-ray/Neutron Scattering (SAXS/SANS) have been essential for examining both local and intermediate-range ordering in non-crystalline solids [22].In particular, diffraction methods (X-ray, neutron, or electron) provide detailed information regarding the first and second coordination spheres around an atom, enabling the characterization of local atomic arrangements

and interconnections between short-range structural regions [23]. Additionally, Raman and Infrared (IR) vibrational spectroscopy offer powerful tools for probing the bonding environment in heteronuclear glass-forming systems, providing insights into the presence of structural units, network connectivity, and vibrational dynamics [23].

1.6.1. Structural Models of Glass

Unlike crystalline materials, where atomic arrangement is dictated by the unit cell, the formation of glass does not depend on a specific type of chemical bonding. Glasses can be broadly categorized into:

- Inorganic glasses (with mixed covalent-ionic bonding, such as silicate and phosphate glasses),
- Metallic glasses (formed via metallic bonding), and
- Organic glasses (stabilized primarily by van der Waals interactions).

Due to this diverse bonding nature, the determination of glass structure remains an active research area, necessitating the use of various theoretical models and experimental techniques for structural characterization.

One of the most influential models describing oxide glasses was suggested by Zachariasen [24] in 1932, known as the Continuous Random Network (CRN) model. This model posits that the glass structure is composed of interconnected polyhedral units, forming a random yet chemically coordinated network. According to Zachariasen, the local atomic arrangements in crystalline and glassy oxides should be similar, with both phases exhibiting comparable coordination polyhedra. However, in the glassy state, there exists a distribution of bond angles and bond lengths, resulting in structural disorder while preserving the fundamental connectivity of the network. Moreover, the network flexibility in the glassy state allows for the incorporation of disorder without significantly altering the internal energy, ensuring that the energetic difference between the crystalline and amorphous phases remains minimal.

The validity of the Continuous Random Network model was later supported by Warren [25], whose X-ray diffraction (XRD) studies provided strong experimental evidence for the absence of

long-range periodicity while confirming the existence of short-range order in oxide glasses. A diagrammatic depiction highlighting the structural distinctions between the crystalline and amorphous phases of an idealized two-dimensional oxide (A_2O_3) is presented in **Fig. 1.3(a)** and **1.3(b).**

This evolutionary understanding of glass structure, supported by both theoretical modelling and experimental validation, has laid the foundation for modern studies on the structural, mechanical, and electronic properties of amorphous materials, facilitating their widespread application in optical, electronic, and energy storage technologies.

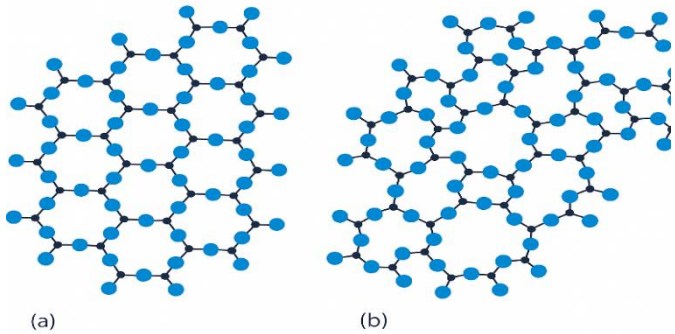

Fig. 1.3. Schematic atomic structure of an A_2O_3 crystalline phase (a) and an A_2O_3 glassy phase (b) (Filled circles represent A = cations, while open circles denote O = oxygen).

Both the crystalline and amorphous phases are composed of AO_3 triangular units linked through corner-sharing; however, the glassy state introduces structural irregularities due to fluctuations in A–O–A bond angles and A–O bond distances. Importantly, the O–A–O bond angles within individual polyhedral units remain largely constant, maintaining the fundamental coordination environment.

As outlined by Zachariasen's Continuous Random Network (CRN) model, the formation of glass in simple compounds such as SiO_2, B_2O_3, P_2O_5, GeO_2, As_2S_3, As_2Se_3, BeF_2, and $ZnCl_2$ adheres to specific structural principles:

1. Glass-forming compounds must readily form polyhedral structural units as their fundamental building blocks.
2. Cation polyhedra should connect exclusively through corner-sharing rather than edge- or

face-sharing to minimize internal strain and enhance structural stability.

3. Anions (O^{2-}, S^{2-}, Se^{2-}, F^{-}, Cl^{-}, etc.) should not coordinate with more than two central atoms, ensuring network connectivity through bridging anions.
4. The coordination number of the polyhedral units should be less than six to maintain an open and flexible network structure.
5. At least three corners of each polyhedral unit must be linked with neighboring polyhedra to form a well-connected three-dimensional (3D) glass network, ensuring structural cohesion and stability.

1.6.2. Classification of Cations in Glass Structure

Zachariasen further categorized cations in glass-forming systems based on their structural roles:

Network Formers (NWFs): Elements such as Si, B, and P, which primarily adopt threefold or fourfold coordination, forming the backbone of the glass network.

Network Modifiers (NWMs): Alkali and alkaline-earth elements such as Li, Na, Sr, and Ba, which typically exhibit coordination numbers ≥6 and disrupt the glass network.

Intermediates: Cations capable of adopting multiple coordination states, either strengthening the network via cross-linking (with a coordination number of 3 or 4) or diminishing connectivity through depolymerization (with a coordination number of 6–8). Notably, intermediate cations by themselves cannot generate a single-component glass.

1.6.3 Role of Network Modifiers in Glass Structure

Network-modifier oxides (e.g., Na_2O) depolymerize the continuous random network of glass formers (e.g., SiO_2) by breaking bridging oxygen bonds, generating non-bridging oxygens (NBOs). This disruption reduces the connectivity of the silica network, leading to changes in macroscopic properties such as viscosity, ionic conductivity, and mechanical strength. The formation of NBOs, illustrated in **Fig. 1.4**, is not exclusive to silica-based glasses but occurs in a wide range of inorganic glass systems, influencing their overall physical and chemical behaviour.

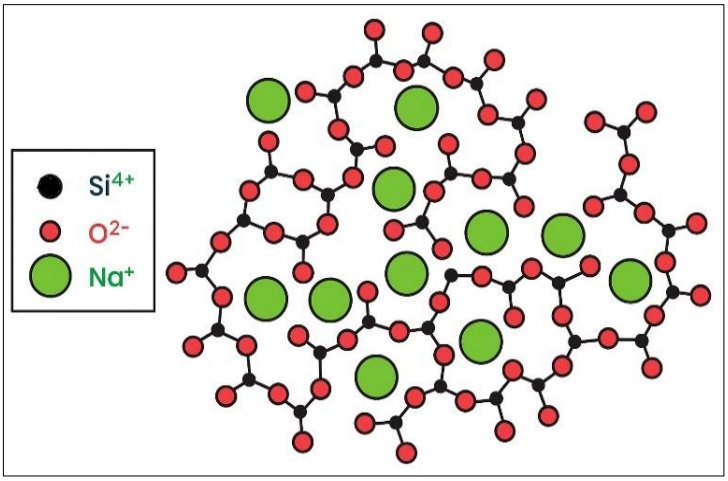

Fig. 1.4. Schematic two-dimensional representation of the silicate glass structure, illustrating the influence of modifier ions like Na^+ and the generation of non-bridging oxygens.

The Continuous Random Network (CRN) model, originally proposed by Zachariasen [24] has been instrumental in explaining the structural organization of oxide glasses. However, this model has since been extended to describe the structures of strongly ionic non-oxide glasses (e.g., halides) and covalent non-oxide glasses (e.g., chalcogenides). These materials exhibit structural characteristics distinct from traditional oxide glasses due to differences in bonding nature, atomic coordination, and network connectivity. To address structural modifications introduced by network-modifying cations, Greaves [26] proposed the Modified Random Network (MRN) model. This framework refines the CRN model by incorporating the effects of network modifiers, which disrupt the continuous glass network and introduce non-bridging oxygens (NBOs), resulting in altered mechanical, optical, and transport properties.

At the opposite end of the structural spectrum, organic glasses, where molecular units are predominantly held together by van der Waals forces, exhibit structural disorder distinct from that of oxide glasses. In contrast to the knowledge base acquired from amorphous solids as described by metallic glasses, glass science has a limited source for experimental structural information, especially to describe long range connectivity of polymerized structures. This limitation is overcome by Sprenger [22,29], who then used the Atom Specific Structural Elements (ASE) model to describe local glass structure utilizing characteristic structural motifs corresponding to specific atomic species. This method thus provides more detailed understanding of the short and

intermediate-range order in glasses, and bridges the gap between theoretical models and experimental work.

1.7. Classification of Glasses: Composition and Functional Applications

Glasses are broadly classified using two distinct approaches: composition-based classification and application-based classification.

Composition-Based Classification: This categorization is based on the primary network-forming elements present in the glass structure. Common types include:

- Halide glasses (fluoride, chloride, or bromide-based glasses)
- Chalcogenide glasses (containing S, Se, or Te instead of oxygen)
- Metallic glasses (amorphous metals with disordered atomic arrangements)
- Organic glasses (formed by molecular organic compounds rather than oxides)
- Oxide glasses (composed of oxygen-containing compounds of various elements, such as P,B,Si etc)

Application-Based Classification: This classification is based on the intended functional use of the glass in various industries and technologies. Examples include:

- Optical glasses (engineered for high refractive index and minimal dispersion)
- Sealing glasses (used in hermetic sealing applications, particularly in electronics)
- Laser glasses (doped with rare-earth ions for laser amplification)
- Bioactive glasses (designed for medical applications, such as bone regeneration)
- Radiation-shielding glasses (lead-based glasses for X-ray and gamma-ray shielding)
- Conductive glasses (used in touchscreens and electrochromic devices)

Each type of glass exhibits distinct structural and physicochemical properties that define its suitability for specific applications. The following sections analyze in detail the structural organization, bonding properties and key properties of selected glass systems and expound on their variety of functionalities and industrial importance.

1.7.1. Halide Glasses: Structural Characteristics, Stability, and Technological Applications

Halide glasses, composed of Group VII-A halogens (F^-, Cl^-), exhibit distinct structural and optical properties compared to oxide glasses. BeF_2 and $ZnCl_2$ glasses, synthesized via rapid quenching, form 3D Continuous Random Networks (CRN) with corner-sharing tetrahedral units (BeF_4 and $ZnCl_4$). Despite structural similarities to silica-based networks, halide glasses differ in ionic character, bond strength, and thermal stability, affecting their durability and applications.

Fluoride glasses, particularly BeF_2-based, are prized for their low refractive indices and broad optical transparency from near-UV to mid-IR, making them ideal for laser windows, waveguides, and infrared optical fibers. However, devitrification limits their use in long-length fibre applications. $ZnCl_2$ and BeF_2 glasses also suffer from hygroscopicity, restricting their industrial viability. Researchers have attempted to improve chemical stability by incorporating halides such as $PbCl_2$, $CdCl_2$, and $CdBr_2$, though chloride-based glasses remain highly susceptible to oxidative degradation and devitrification due to weak M–Cl bonds.

To overcome these challenges, multi-component heavy metal fluoride (HMF) glasses have been prepared, enhancing devitrification resistance, optical transmission, and mechanical stability for infrared photonics and fibre optics. Despite advancements, manufacturing constraints on fibre length and boule size persist. Ongoing research focuses on composition optimization and processing innovations to improve the long-term stability of fluoride-based optical materials, expanding their potential in next-generation optical technologies.

1.7.2. Chalcogenide Glasses: Structural Characteristics, Optical Properties, and Technological Applications

Chalcogenide glasses, composed of Group VI-B elements (S, Se, Te), exhibit unique optical, electronic, and nonlinear properties, distinguishing them from traditional oxide glasses. Their semiconducting behavior (band gaps of 1–3 eV) and exceptional infrared (IR) transparency make them essential for photonics, infrared optics, and electronic applications. These glasses are synthesized primarily through vapor-quenching for thin films and melt-quenching for bulk materials, though the latter has a more limited compositional range.

One of their most significant advantages is superior IR transmission, making them ideal for infrared lenses, windows, fibre optics, and thermal imaging systems used in night vision and remote sensing. The low-loss optical wave-guiding reduces Rayleigh scattering and improves optical communication performance. Furthermore, they have a high nonlinear refractive index (n_2) that supports all-optical switching, super continuum generation and photonic computing, necessary for high-speed optical networks and next-generation photonics.

Beyond optics, chalcogenide glasses play a key role in semiconductor and memory technologies**,** particularly in phase-change random-access memory (PCRAM) and threshold-switching devices used in data storage and microelectronics. These materials demonstrate essential properties as emerging memory and computing technologies because they can transform between amorphous and crystalline states. Ongoing research aims to enhance their thermal and environmental stability**,** further expanding their potential in telecommunications, sensing, and advanced computing**.**

1.7.3. Metallic Glasses: Formation, Structure, and Technological Significance

Amorphous metals, or metallic glasses, are atoms ordered in such a way that they are better for high-performance applications: they are more elastic, more mechanically strong and more corrosion resistant, and magnets make them better. Discovered unintentionally through rapid quenching (RQ) techniques**,** the first metallic glass, Au-Si, required extremely high cooling rates ($\sim 10^6$ K s^{-1}) to prevent crystallization. However, advancements in multi-component alloy systems have enabled the formation of bulk metallic glasses (BMGs) at significantly lower cooling rates (~ 1 K s^{-1}), allowing for the production of large, monolithic amorphous components.

BMGs exhibit high atomic packing density, minimal free volume, and elevated elastic limits, leading to superior corrosion resistance and mechanical stability compared to crystalline metals. Inoue classified them into metal-metal (e.g., Zr-, Ti-, Cu-based), metal-metalloid (e.g., Fe-B, Co-B, Ni-P), and Pd-metalloid (e.g., Pd-Si, Pd-Cu-Si) systems. Their high fictive temperatures result in metastable atomic structures, which undergo atomic rearrangements upon annealing**,** improving density, mechanical properties, and conductivity, though crystallization may occur.

Metallic glasses also exhibit exceptional soft magnetic properties, including low hysteresis losses and high saturation magnetization, making them widely used in high-efficiency transformers, power electronics, and electromagnetic shielding**.** The development of BMGs has revolutionized amorphous materials research, with ongoing studies aimed at enhancing their glass-forming ability, thermal stability, and processing techniques for broader applications in structural, biomedical, and electronic devices.

1.7.4. Organic Glasses: Structural Characteristics, Formation, and Functional Properties

Metallic glasses, or amorphous metals, exhibit a liquid-like atomic arrangement in the solid state, lacking long-range periodic order. This structure grants them exceptional mechanical strength**,** elasticity, corrosion resistance, and unique magnetic properties, making them valuable for high-performance applications. Initially discovered through rapid quenching (RQ) techniques, early metallic glasses like Au-Si required extremely high cooling rates (~10^6 K s^{-1}) to prevent crystallization. However, advancements in multi-component alloy systems have enabled the formation of bulk metallic glasses (BMGs) at much lower cooling rates (~1 K s^{-1}), facilitating large-scale production.

BMGs possess densely packed atomic configurations with minimal free volume, leading to high elastic limits, superior corrosion resistance, and enhanced mechanical stability. Inoue classified BMGs into metal-metal (e.g., Zr-, Ti-, Cu-based), metal-metalloid (e.g., Fe-B, Co-B, Ni-P), and Pd-metalloid (e.g., Pd-Si, Pd-Cu-Si) systems based on their composition. Their high fictive temperature results in a metastable atomic structure, which can undergo atomic rearrangement upon annealing, improving density, mechanical properties, and conductivity, though it may also trigger crystallization.

Metallic glasses also display remarkable soft magnetic properties, including low hysteresis losses and high saturation magnetization, making them ideal for high-efficiency transformers, power electronics, and electromagnetic shielding. The development of BMGs has revolutionized amorphous materials, and ongoing research aims to enhance their glass-forming ability, thermal stability, and processing techniques for broader applications in structural, biomedical, and electronic devices**.**

1.7.5. Oxide Glasses: Historical Significance, Industrial Relevance, and Technological Applications

For centuries, oxide glasses have contributed to human civilization, with the earliest uses of such glasses including as a container, window, and decorative object. Their applications have now spread far and wide over time; modern technology owes a lot to them, from optical communication, data storage, semiconductor devices and nuclear waste containment. Modern industrial glasses include silicate and alumino-borosilicate compositions, which receive different oxides for controlling their thermal features and mechanical and optical behavior. Multiple sectors utilize these essential materials for their operations, such as:

- **Construction and automotive industries** (offering durability and transparency)
- **Optoelectronics** (used in lasers, optical fibres, and display systems)
- **Semiconductor technology** (providing sealing and packaging solutions with high-temperature and chemical resistance)
- **Biomedical applications** (including bioactive glasses for tissue regeneration)
- **Nuclear waste management** (ensuring chemical stability and resistance to radiation)

While silicate-based glasses dominate the market, other oxide glass types, such as phosphate, germanate, and tellurite glasses, are used in specialized fields due to their distinct optical and electronic properties. They stand out for their excellent transmission in the infrared range, their High nonlinear optics, their high ionic conductivity and are indispensable to the most cutting-edge photonics, solid-state batteries and high-performance optical coatings.

1.8. Phosphate Glasses: Structural Characteristics, Functional Properties, and Applications

The phosphate glasses are a distinctive class of amorphous materials where phosphate glasses, P_2O_5, are the main network formers. However, distinct electronic, optical and thermal properties distinguish these glasses from conventional silicate-based glasses. Phosphate glasses also have superior ultraviolet (UV) transmission due to their larger band gaps and are therefore especially desirable for UV optics and photonics.

1.8.1. Thermal and Mechanical Properties

Higher ease of manufacturing exists for phosphate glasses because they show a lower glass transition temperature when compared to silicate glasses. Additionally, they have a relatively high thermal expansion coefficient (TEC) that is similar to that of the metals. Because of this characteristic, phosphate glasses are well-suited for hermetic sealing of low-melting, high-expansion metals such as aluminium (Al) and copper (Cu). In addition to the niche applications mentioned above, phosphate glasses find themselves in an even more valuable place in the aerospace sector: aluminium and its alloys are often employed for the design of aerospace applications because they are lightweight, have high mechanical strength, and are cost-effective, making them a valuable role in aerospace technologies.

1.8.2. Application of Phosphate glasses

Optical and Laser Applications

The combination of high rare earth-induced emission cross sections and low thermo-optical coefficients exists within specific $AlPO_4$-based glass compositions. These attributes make phosphate glasses superior to silicate glasses when applied in high-power laser technology. The optical dispersion of phosphate glasses remains low while their refractive indices are reasonable enough to produce achromatic optical elements essential for precise high-precision systems.

Ionic Conductivity and Electrochemical Applications

Phosphate glasses are highly soluble in heavy cations and anions, thus performing as fast as ion-conducing electrolytes in the solid state. These materials demonstrate great potential for use as solid-state ionic devices including batteries, fuel cells and electrochromic devices because they exhibit high ionic conductivity alongside thermal stability and electrochemical durability.

Biocompatibility and Biomedical Applications

Recently, phosphate glasses have been of interest for their biocompatibility making them attractive for biomedical applications including bioactive implants, bone scaffolds and controlled drug delivery systems. In addition, they are of great significance for biomedical engineering because they are capable of dissolving in physiological environments, supporting cell adhesion and tissue regeneration.

Application in Nuclear Waste Immobilization

The development of low-melting iron phosphate glasses with improved chemical durability is a major advancement in phosphate glass technology and is applicable for nuclear waste vitrification. The incorporation of Fe_2O_3 enhances resistance to radiation-induced damage and aqueous corrosion, ensuring the long-term containment of radioactive waste.

1.8.3. Structural Organization and Synthesis

In contrast to silicate glasses, phosphate glasses are assembled from PO_4 tetrahedra coordinated to the three edges. This structural difference leads to differences in their network connectivity and dissolution behaviour. The highly hygroscopic and reactive nature of P_2O_5 based glasses prohibits their practical applications. Thus, to make anhydrous P_2O_5 glasses, the P_2O_5 or P_4O_{10} is purified by high-purity P_2O_5 or P_4O_{10} by vacuum distillation under dry conditions, and the P_2O_5 is normally synthesized in sealed silica ampoules.

The Q notation, n for several bridging oxygens per phosphate tetrahedron, is commonly used to describe the evolution of phosphate glasses' structure. The understanding of this structural

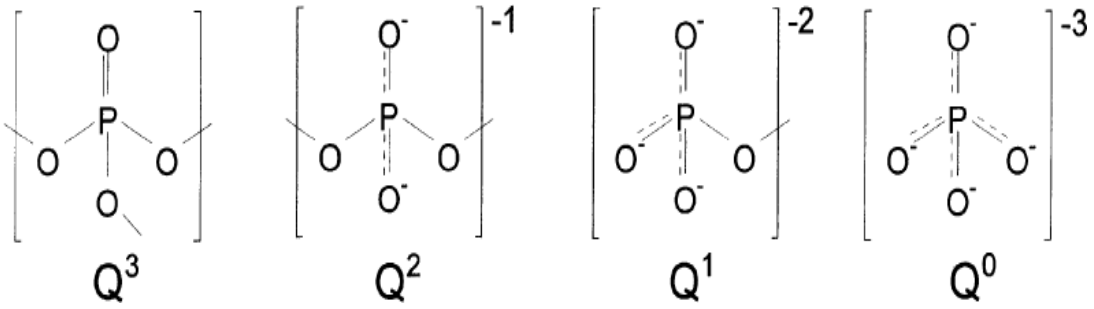

Fig. 1.5. The phosphate tetrahedral units which appear in phosphate glasses.

progression offers useful help with the physical and chemical behavior of these compounds and should be advantageous in application in several advanced technologies.

1.8.4. Chemical Durability of Phosphate Glasses

Recent neutron diffraction studies of Vitreous-P_2O_5-based glasses have found two different types of P–O bonds. Isolated phosphate tetrahedra or depolymerized units are assigned P–TO (Terminal Oxygen) or P–NBO (Non-Bridging Oxygen) bonds whose bond lengths are slightly shorter. On the other hand, the P–BO (Bridging Oxygen) bond contributes to the polymerized phosphate network and has a longer bond length. This distinction was further validated by complementary

infrared (IR) and Raman spectroscopic studies that provide more structural information on phosphate glasses.

1.8.5. Effect of Network Modifiers on Phosphate Glass Structure

The glassy P_2O_5 structure is changed by introducing the network-modifying oxides like alkali and alkaline earth oxides, as in binary silicate glasses. Because these oxides convert bridging oxygens (BOs) to non-bridging oxygens (NBOs), so much so that they have such a great impact on the thermal, mechanical, and chemical characteristics of phosphate glasses. Despite the high affinity of alkali phosphate glasses with atmospheric moisture, critical in analyzing the structural and physicochemical behavior of these glasses, the main factor does not allow one to predict whether they will be stable or not and whether they will be able to retain their performance over time.

The structure of glass changes when alkali metals and heavy metal oxides such as Na_2O, K_2O, Bi_2O_3 and BaO are added, as these compounds break network bonds and form non-bridge oxygens. As a result of depolymerization, density, refractive index and the ability to conduct ions are changed in the polymer.

Bi_2O_3, among other heavy metal oxides, makes glass denser, stronger and better able to resist heat by improving its packing and reducing any defects in the structure due to its large ionic radius and high polarizability [27]. Also, adding alkali modifiers increases ionic movement, a requirement for making solid electrolytes in batteries and fuel cells [28].

Therefore, choosing the correct modifier and amount is necessary to make glasses that suit particular technical functions, whether at high temperatures or for tough optoelectronics.

1.8.6. Importance of Mixed Modifiers

Mixed modifier effect (MME) is a situation where the addition of multiple glass modifiers causes their effects on glass properties to be both non-linear and often work together in unexpected ways. The results include better hardness, electrical conductivity and thermal properties than what can be achieved by using a single modifier [29].

Combining Bi_2O_3 with BaO is said to result in glasses with improved mechanical and dielectric properties because the network structure and ion distribution are more efficient, according to Patel

et al. [30,31]. Understanding MME is essential for designing glasses that can perform several functions in electronics, photonics and energy fields.

1.9. Vanadate-Phosphate Glass Systems

Phosphate glasses become more interesting structurally and functionally when vanadium oxide (V_2O_5) is included. Whether vanadium ions function as building blocks in minerals or modify those structures depends on their environment and number of charges (V^{4+} and V^{5+}). As a result of playing both roles, the network of polymers changes and electrons can be transferred using small local polaron hopping [16,17].

Increasing the proportion of V_2O_5 in the glass mix has led researchers to observe that the optical bandgap drops and the Urbach energy climbs, which points to a higher amount of disturbance in the glass structure [18,19]. During heat treatment, $Zn_2V_2O_7$ and $Na_3P_8VO_{23}$ are among the nanocrystalline phases that are formed, and this improves both the strength and thermal stability of the materials [20-22].

Vanadate-phosphate glasses fulfil well the roles needed for optoelectronic devices and energy storage systems, which require electricity, visibility and durability.

1.10. Importance of Adding Transition Metal Oxides (TMOs)

TMOs such as V_2O_5, Fe_2O_3 and ZnO play an important role in changing the properties of glass by having changeable valences and d-electron orbitals that are close together. Their inclusion in the glass brings new electronic states that alter how the glass conducts electricity, behaves magnetically and absorbs light.

Electron transport within the glass is achieved fast in V_2O_5 thanks to its ability to generate small polaron hopping which improves electrical conductivity [23,24] Magnetic and catalytic properties [25] are included in iron oxide (Fe_2O_3) and the addition of zinc oxide (ZnO) boosts transparency and luminescence useful for photonic purposes [26]. Therefore, these materials can display optical, electrical and magnetic features at the same time.

1.11. Review the work of some glassy systems

In 1977, P.W. Anderson, N.F. Mott and J.H. Van Vleck have completely changed the course of research in non-crystalline solids or glass semiconductors by winning the Nobel Prize for their pioneering work on hypothetical analysis of the structural, electronic, and magnetic characteristics of disordered materials. The motivation of the present work is derived from the research gap obtained by critically evaluating the following literature.

R.K. Brow [32] analysed the spectroscopic and diffraction studies of simple phosphate glasses such as those with the compositions v-P_2O_5 and binary phosphates. Particular care was paid to anhydrous ultraphosphate glasses, as the glass community has only started to pay close attention to them in recent years.

Rao, P.S. et al. [33] have discussed the effect of Mo ions on the structure and dielectric relaxation of ternary ZnF_2–Bi_2O_3–P_2O_5 glass-ceramics. The presence of various crystalline phases in ZnF_2–Bi_2O_3–P_2O_5:MoO_3 glass-ceramic samples has been revealed by XRD and SEM.

D. Souri [34] noted that, electrical conductivity of semiconducting oxide glasses in the $(60-x)V_2O_5$–$40TeO_2$–xSb_2O_3 system, synthesized using press quenching and studied at temperatures from 305 to 472 K, rises as more V_2O_5 is added.

Terny and Frechero [35] stated that as tellurite polyhedra change because of the three transition metal oxides, there are modifications in the cut-off wavelength, optical band gap, Urbach's energy, refractive index and permittivity values that can show the MAEE in different ways. Changing the type of transition metal oxide in the structure had the biggest impact, and optical and electrical properties were strongly influenced by mixing the TMO with modifiers.

Biswas et al. [36] investigated the microstructure, optical properties and method of electrical conduction in two ternary and four quaternary glasses of $0.65ZnO$–$0.1P_2O_5$–0.25 [$xTeO_2$– $(1-x)$ MoO_3] composition to identify a suitable system for different uses. XRD and TEM analysis showed that the material consisted of amorphous regions with a small number of layered nanocrystals.

Majhi, K. et al. [37] have explored the dielectric relaxation in CaO-Bi_2O_3-B_2O_3 Glasses. Authors have reported that the ion transport mechanism is the same over the temperature range, which has been indicated by the scaling of the modulus and impedance study. The stretched exponent

is invariant with temperature. The study of the conductivity suggests that the conductivity at high temperature is owing to the motion of oxygen ions, and it is ionic. Almond–West type of expression has been used for the fitting of the ac conductivity.

Kashif et al. [38] synthesised sodium borate glasses blended with iron and molybdenum ions while the concentration of transition ions remained constant and sodium oxide was replaced gradually by borate oxide. Different types of measurements are conducted: Densities, molar volume, DC conductivity, AC conductivity. Changes in how the glass network is built explain the trends in these materials. The conductivity of both DC and AC improved as the amount of NaOH increased in the solution.

Singh and Singh [39] prepared iron oxide-doped cerium lead borate glasses and studied the glass in terms of structure, physical features and optical characteristics by using XRD, FTIR, density measurements and UV–Visible spectroscopy. The structure of the glasses has been investigated using studies conducted with IR spectroscopy, focusing on iron oxide.

Mondal *et al.* [40] reported on an extensive study on structural, thermal, optical, and non-linear optical properties of zinc oxide modified phospho-tellurite glass as a function of doped samarium oxide content. By using the well-known Archimedes method, the densities of the samples have been estimated. The thermal properties of the glasses have been investigated by differential scanning calorimetry (DSC) measurements.

Al-Harbi *et al.* [41] used a UV–Vis spectrophotometer to study the absorption spectra of the fabricated glasses between 200 and 1100 nm. The refractive index fell, going from 2.438 to 2.328, and the direct energy gap increased, moving from 3.626 to 3.880 eV, when the concentration of P2O5 was raised.

Hussain *et al.* [36] synthesized (60–x) P_2O_5–10MgO–30ZnO–xSm_2O_3 zinc-magnesium-phosphate glasses doped with samarium, with x equal to 0.1, 0.3, 0.6 and 1.0 mol % using melt quenching. Their densities, which are between 2.65 and 2.91 g/cm^3, were measured using Archimedes' procedure. The trend of higher density at higher Sm_2O_3 % suggests that the non-bridging oxygen is replacing the bridging oxygen. Ghosh et al. [43] have reported that the DC-conductivity of V_2O_5–Bi_2O_3 glasses are greater than that of the V_2O_5–P_2O_5 and V_2O_5–TeO_2 glasses. With the rising concentration of V_2O_5, the increment of conductivity is found to be non-linear. The activation energy has been affected by the glass-forming oxides. This type of nature

has been described in polaronic conduction and Mott's model (Mott 1979).

Minakshi, M. *et al.* [44] have explained the methodology of a ternary molybdate glass composite both theoretically and experimentally, and the application of the glassy composites for hybrid energy storage capacitors

Das *et al*. [45] made semiconducting glassy nanocomposites with the structure V_2O_5-(1-x) (0.05CdO-0.95ZnO), where x is 0.3, 0.5, 0.7 and 0.9. The XRD, FT-IR, TEM and UV-vis spectroscopies methods were used to examine the structural, physical and optical qualities of the prepared samples. They have determined connections between how dense, how much space is within, the packing structure of oxygen and the average stretchiness of nanocomposite glasses containing CdO and similar additives. All our results were examined using small polaron hopping theory to study their semiconducting behaviour. When the V_2O_5 concentration is increased in a polymer, the polymer's density goes down because more NBOs are evolving as the polymer changes volume. As the V_2O_5 content increases, the optical band gap goes down, showing that these films are semiconductive. The strongly nonlinear DC conductivity seems to be related to the movement of polarons or the jumping of carriers through several comparable energies.

At first, Biswas *et al.* [46] were interested in producing high-quality bulk glass nanocomposites by slow-cooling the synthesis. In addition, they investigate and discuss both the physical and microstructural features of the nanocomposite samples and the effects of MoO_3 content. According to the data, a greater concentration of MoO_3 corresponds to lower values of optical bandgap energy, Urbach energy and average crystallite size. This shows that the decrease in the power-law exponent with an increase in temperature is consistent with correlated barrier-hopping (CBH) behaviour.

Biswas *et al.* [47] have focused on understanding how two ternary and four quaternary glassy systems of the composition $0.65ZnO–0.1P_2O_5–0.25$ [$xTeO_2$–(1-x) MoO_3] work by analyzing their structure, optical and electrical properties, to discover a convenient semiconductor nanocomposite system suitable for many applications. They found that both the DC and AC chargeability of the compound increase as temperature rises, a sign of its semiconducting character. For DC conductivity, there is a non-linear behaviour linked to easy hopping of small polarons, but for AC conductivity, the modified correlated barrier-hopping model is used.

Ningthemcha [48] prepared two kinds of ternary glass nanocomposites and three types of

quaternary ones with a chemical formula of $0.45Bi_2O_3$-$0.15P_2O_5$-$(0.4-x)V_2O_5$-$xMoO_3$ (x equals 0, 0.1, 0.2, 0.3 and 0.4) using the melt quenching process. The dc conductivity of each glass nanocomposite is reportedly explained using Mott and Greaves's variable range hopping model. The trend of d_c conductivity decreasing as MoO_3 content increases is explained by the calculated values of small polaron hopping energy (W_{hop}) and hopping distance (R_{hop}). They assumed that dynamic conductivity follows a non-Debye behaviour and the relaxation time shows Arrhenius properties.

Biswas *et al*. [49] reported the preparation of various quaternary nanocomposites containing zinc oxide and phosphorus pentoxide, along with a transition metal combination of vanadium pentoxide and molybdenum trioxide, using the melt quenching method. By comparing the structures and electronic conductivity of various unique composites made from six different systems, they have found the best semiconductor nanocomposite system for a range of applications. The research showed that all the ternary and quaternary nanocomposites had non-linear dc conductivity as a result of the dissimilar small polaron hopping activation energies at various temperature regions. Activation energies of ac conductivity and the small polaron migration process were reduced as conductivity increased. The relaxation of conductivity depended on the structure of the composites and not on temperature, as seen in scaled ac conductivity spectra. As materials, they can be used in gas sensors, surviving temperatures up to 1,000°C, thanks to their ability to become semiconductors and the wide range of valence electron states of the transition metal ions they contain.

Vijoy et. al. [50] tested microhardness on glasses consisting of $(1-x-y)$ (B_2O_3)–$x(Li_2O)$–$y(MCl_2)$ and where both M = Cd and M = Zn on a scale of 25–500 g. It was shown that microhardness initially dropped as the load increased up to 50 g., but then rose and settled down at heavier loads. According to the researchers, this type of response is related to the network reorganisation and increased flatness of the glass as pressure increased, allowing them to understand how robust these modified glass systems are.

Salman et. al. [51] conducted an in-depth investigation of the crystallization, phases, hardness and resistance to chemicals in glasses and glass-ceramics made from a $LiAlSi_2O_6$–$YAlSiO_5$ mixture. The focus of the investigation was on the results of using $LiFeSi_2O_6$ for some $LiAlSi_2O_6$ and completely changing $YAlSiO_5$ with $CaMgSi_2O_6$. In certain compositions, Cr_2O_3 was introduced to

aid nucleation and usually, Fe_2O_3 was substituted for parts by chromium or indium oxides. Controlling the heat of the samples produced β-spodumene solid solutions, some pyroxene-type crystals and lithium indium silicates. Microhardness, at 4610–6185 MPa, changed in the glasses depending on their composition, but glass-ceramics had higher values of up to 8175 MPa and also showed better resistance to chemical change due to their crystalline structure.

Singh et al. [52] studied how gallium (Ga) replaces aluminium (Al) in the $Zr_{69.5}Al_{7.5-x}Ga_xCu_{12}Ni_{11}$ metallic glasses and examined the effects on quasicrystal (QC) formation, their structure and mechanical performance. Investigations found that adding zirconium, gallium, copper and nickel to sodium borate yielded a glass called Zr-Ga-Cu-Ni, with a glass transition temperature (Tg) of 441 K and showed how modifying the cooling rate changed both the glass formation and the material's strength. Key parameters in indentation, like microhardness, yield strength and shear band formation, were properly analysed to connect the structure and properties of these Zr-based materials.

Kundu et. al. [53] examined ZnO-doped silver–molybdate glass–nanocomposites with a composition of 0.3 Ag_2O–0.7 [0.075 ZnO–0.925 MoO_3], which were made by the melt-quenching technique. The research investigated ionic conductivity over a wide range of temperatures and frequencies, together with microhardness measurements using the Vickers method. In addition, controlled heat treatments were studied to see how they affected both the electronic and mechanical properties of the glass–nanocomposite materials.

Yongchang Guo et al. [54] emphasized that extremely hard glasses with high Young moduli and fracture toughness are a must for protective covers of electronic displays. In this study, the researchers developed a conceptual design paradigm for crafting high-performance oxide glasses through high-entropy materials. The compositions of glasses were selected as $18.77R_2O_3$–$4.83Y_2O_3$–$28.22TiO_2$–$8.75ZrO_2$–$39.43Al_2O_3$, where R = La, Sm, Gd under a containerless solidification process. These glasses give very good mechanical and optical properties. High-entropy glass with R=Gd has a hardness of 12.58 GPa, Young's modulus of 177.9 GPa, and indentation fracture toughness of 1.52 $MPa \cdot m^{0.5}$, which are among the highest values reported for oxide glasses. Structural characterization attributed the excellent mechanical properties to the high dissociation energies and field strengths of constituent oxides (Al_2O_3, TiO_2, and ZrO_2), besides further complex atomic interactions caused by high-entropy effects.

Ibrahim et al. [55] investigated a series of phosphate-based glasses with the chemical formula $20Na_2O–15BaO–10ZnO–(9–x)\ Fe_2O_3–xIn_2O_3–46P_2O_5$, where x ranged from 0 to 9 mol%, to see how the substitution of Fe_2O_3 by In_2O_3 would influence the structural, thermal, and mechanical properties of the glass system. The glass samples were prepared by a common melt-quenching method at room temperature. Structural studies by means of XRD proved the amorphous nature of all samples prepared.

The thermal investigation provided by means of DSC indicated that the indium ions preferably occupied network-forming sites therein, increasing the rigidity of the structural glass matrix. This inference was drawn from the increase in values of Tg, Tp, and ΔGS with increasing In_2O_3 content, while the ΔCp showed the opposite trend.

The density values linearly increased from 3.57 to 3.83 g/cm³, accompanied by a linear decrease in molar volume from 34.48 to 34.11 cm³/mol, implying a fairly tight network structure for higher In_2O_3 concentrations. However, there was a marked decrease in mechanical strength, as reflected by a lowering in all evaluated elastic parameters, this was including Poisson's ratio.

Alsaif et al.[56] explored the effect of compositional change on the physical, mechanical, optical, and radiation shielding properties of a series of cadmium–bismuth–silicate-based glasses with a general composition of $25CdO–30Bi_2O_3–XSm_2O_3–(45–X)\ bSiO_2$, where X = 0, 0.5, 1, and 2 mol%. The primary intention of the study was to determine how replacing a small amount of SiO2 (smaller than 2 mol%) with Sm_2O_3 affects the overall behavior and performance of the glass system. X-ray diffraction (XRD) data confirmed the amorphous character of all glasses, and further insight into the internal glass structure was provided through Fourier-transform infrared (FTIR) analysis, which established that with the addition of Sm_2O_3, bridging oxygens (BO) were converted into non-bridging oxygens (NBO). With these changes, density increased (from 6.08 to 6.24 g/cm³) and molar volume slightly increased (from 32.72 cm³/mol to 32.80 cm³/mol). With the increasing addition of Sm_2O_3, the volume deviation (V_o) approached a minimum of 2.57 cm³/mol, indicating better expanded packing through the incorporation of Sm^{3+} and the presence of a relatively homogenous structure. For mechanical properties, all the elastic moduli evaluated (Young's modulus, bulk modulus, and shear modulus) increased with Sm^{3+} content. This improvement was attributed to reinforcing the glass network.

1.12. Research Gap

Despite significant advances in the development of phosphate and vanadate glasses, there remain notable gaps in understanding the comprehensive influence of mixed transition metal oxides (TMOs) and heavy/alkaline earth metal oxides as modifiers on the multifunctional properties of these glasses. While numerous studies have explored individual dopants like V_2O_5 or Bi_2O_3 and their impact on structural or optical characteristics, the synergistic effects of mixed modifiers on electrical conductivity, dielectric relaxation, mechanical hardness, and thermal stability are not fully elucidated.

Most prior research focuses on isolated properties or limited compositional ranges, often neglecting the interdependent nature of these physical attributes in real-world applications. For example, how the nanoscale crystallization behavior triggered by certain dopant combinations influences both mechanical and optical properties simultaneously remains underexplored. Similarly, the detailed conduction mechanisms—especially the transition from ionic to polaron hopping—and their dependence on mixed dopants need further quantitative assessment.

Mechanical properties, especially microhardness, have not been studied in a systematic way for mixed modifier effects on quaternary vanadate-phosphate glass systems. Though some studies have examined elastic moduli and directed bulk properties, a limited understanding exists to depict the effect of individual or combined modifiers on localized scaling of hardness models. Because glasses are inherently amorphous materials, performing nano-scale evaluations of hardness is especially important. Localized tests like microhardness tests can show the differences in structure on small scales and how certain modifiers alter the short-range order and network connectivity, which defines the glass matrix. Nanoindentation, therefore, provides great potential to characterize the mechanical response of these materials on small scales that are generally lumped into bulk measurements or ignored altogether when assessing modifying effects.

Furthermore, the majority of investigations lack systematic correlations between microscopic structural changes (such as the formation of nanocrystallites) and macroscopic property enhancements, which are critical for designing glass materials tailored for advanced optoelectronic and energy applications. There is also limited data on how the mixed modifier effect (MME) can

be harnessed to improve the sustainability and scalability of these glass systems in high-temperature and high-frequency environments.

Addressing these gaps requires an integrated study combining advanced synthesis methods with multi-technique characterization, including XRD, SEM, Raman, UV-Vis spectroscopy, dielectric measurements, and thermal analysis. Such a comprehensive approach will clarify the fundamental structure-property relationships and guide the engineering of novel glasses with optimized performance for future technologies.

1.13. Research Objectives

The main goal of this research is to systematically investigate and tailor the structural, optical, electrical, mechanical, and thermal properties of vanadium-phosphate-based glasses modified by transition metal oxides and mixed heavy/alkaline earth metal oxides. Specifically, this study aims to:

1. Synthesize three series of vanadium-phosphate glasses with carefully controlled concentrations of TMOs (V_2O_5, Fe_2O_3, ZnO) and modifiers (Bi_2O_3, BaO, Na_2O) using the melt-quenching technique, ensuring reproducibility and compositional precision: -**VNZP (V_2O_5–Na_2O–ZnO–P_2O_5)**, **BBVP (Bi_2O_3–BaO-V_2O_5–P_2O_5)**, and **BFVP (Bi_2O_3–Fe_2O_3–V_2O_5–P_2O_5)** using the conventional melt-quenching technique, while systematically varying dopant concentrations.
2. **Characterize the structural evolution** of these glasses, focusing on the transition from amorphous to nanocrystalline phases, and identify the formation of specific nanocrystallites like $Na_3P_8VO_{23}$ and $Zn_2V_2O_7$ using XRD and SEM.
3. **Analyze optical properties** through Raman and UV-Visible absorption spectroscopy to determine changes in bandgap, Urbach energy, refractive index, and related parameters as a function of dopant concentration.
4. **Evaluate dielectric behavior and electrical conductivity**, examining frequency- and temperature-dependent dielectric relaxation, AC/DC conductivity, and underlying conduction mechanisms, with particular attention to the influence of mixed modifiers.

5. **Assess mechanical properties** such as micro- and nano-hardness and elastic modulus, correlating these with structural densification effects introduced by modifiers like Bi_2O_3.
6. **Examine thermal behaviors** by using DSC to identify the glass transition temperature and changes in stability induced by the addition of heavy metal oxide doping.
7. **Establish clear correlations** between compositional modifications, structural features, and multifunctional properties, thereby elucidating the mixed modifier effect and its potential for property optimization.
8. **Demonstrate the applicability of these tailored glasses** for practical optoelectronic and energy-related devices, providing a foundation for future sustainable material design.

This research attempts to address important gaps in knowledge and to help develop multifunctional inorganic glasses that work better and have more uses in future technology.

1.14. References

1 Mauro, J. C., Yue, Y., Ellison, A. J., Gupta, P. K., & Allan, D. C. (2009). Viscosity of glass-forming liquids. *Proceedings of the National Academy of Sciences, 106*(47), 19780-19784.https://doi.org/10.1073/pnas.0911705106

2 Zachariasen, W. H. (1932). The Atomic Arrangement in Glass. *Journal of the American Chemical Society, 54*(10), 3841–3851.DOI: 10.1021/ja01349a006

3 Shelby, J. E. (2005). *Introduction to Glass Science and Technology* (2nd ed.). Royal Society of Chemistry.. 10.1039/9781847551160-FP005

4 Doremus, R. H. (1994). *Glass Science* (2nd ed.). Wiley-Interscience.ISBN13:**978-0471891741**

5 ASTM. (2020). *Standard Terminology Relating to Glass and Glass Products*. ASTM International.

6 Kingery, W. D., Bowen, H. K., & Uhlmann, D. R. (1976). *Introduction to Ceramics* (2nd ed.). Wiley,ISBN:0471478601, 9780471478607

7 Scholze, H. (1991). *Glass: Nature, Structure, and Properties*. Springer.https://doi.org/10.1007/978-1-4613-9069-5

8 Newton, R. G., & Davison, S. (1989). *Conservation of Glass*. Butterworth-Heinemann.,https://doi.org/10.4324/9780080569314

9 Pilkington, A. (1969). Review of the Float Glass Process. *Proceedings of the Royal Society of London. Series A, Mathematical and Physical Sciences, 314*(1516), 1–25.https://doi.org/10.1098/rspa.1969.0212

10 Varshneya, A. K. (1994). *Fundamentals of Inorganic Glasses*. Academic Press. ISBN: 9780128162255

11 Macfarlane, A., & Martin, G. (2002). *Glass: A World History*. University of Chicago Press.ISBN-13 : 978-0226500287

12 Ediger, M. D., Angell, C. A., & Nagel, S. R. (1996). Supercooled liquids and glasses. *Journal of Physical Chemistry, 100*(31), 13200-13212.,DOI: 10.1021/jp953538d

13 Angell, C. A. (1995). Formation of glasses from liquids and biopolymers. *Science, 267*(5206), 1924-1935.DOI: 10.1126/science.267.5206.1924

14 Debenedetti, P. G., & Stillinger, F. H. (2001). Supercooled liquids and the glass transition. *Nature, 410*(6825), 259-267. DOI: 10.1038/35065704

15 Greer, A. L. (1995). Metallic glasses. *Science, 267*(5206), 1947-1953.DOI: 10.1126/science.267.5206.1947

16 Tanaka, H. (2005). Two-order-parameter model of the liquid–glass transition. *Journal of Non-Crystalline Solids, 351*(43-45), 3371-3384.https://doi.org/10.1016/j.jnoncrysol.2005.09.008

17 Brawer, S. A. (1985). *Relaxation in Viscous Liquids and Glasses*. American Ceramic Society. doi:10.1063/1.447697.

18 Ehrenfest, P. (1933). Phase transitions in the usual and extended sense classified according to the singularities of the thermodynamic potential. *Communications from the Physical Laboratory of the University of Leiden, 75*, 1-6.,DOI:10.1007/s004070050021

19 Zhiliang Cao, Henry Gu Cao. Unified Field Theory and the Hierarchical Universe. *International Journal of Physics*. 2013; 1(6):162-170. doi: 10.12691/ijp-1-6-5.

20 Kauzmann, W. (1948). The Nature of the Glassy State and the Behavior of Liquids at Low Temperatures. *Chemical Reviews, 43*(2), 219–256. DOI: 10.1021/cr60135a002

21 Tischendorf, B. C., Alam, T. M., Cygan, R. T., & Otaigbe, J. U. (2003). The structure and properties of binary zinc phosphate glasses studied by molecular dynamics simulations. Journal of Non-Crystalline Solids, 316, 261–272. https://doi.org/10.1016/S0022-3093(02)01795-7

22 Pascuta, P., Boscaa, M., Borodi, G., & Culeaa, E. (2011). Thermal, structural and magnetic properties of some zinc phosphate glasses doped with manganese ions. Journal of Alloys and Compounds, 509, 4314–4319. https://doi.org/10.1016/j.jallcom.2011.01.056

23 Schindler, M., & Hawthorne, F. C. (1999). Structural characterization of the β-Cu2V2O7–α-Zn2V2O7 solid solution. Journal of Solid-State Chemistry, 146, 271–276. https://doi.org/10.1006/jssc.1999.8371

24 Meyer, J., Hamwi, S., Kröger, M., Kowalsky, W., Riedl, T., & Kahn, A. (2012). Transition metal oxides for organic electronics: energetics, device physics and applications. Advanced Materials, 24(40), 5408–5427. https://doi.org/10.1002/adma.201201630

25 Bih, L., El Omari, M., Réau, J.-M., Haddad, M., Boudlich, D., Yacoubi, A., & Nadiri, A. (2000). Electronic and ionic conductivity of glasses inside the Li_2O–MoO_3–P_2O_5 system. Solid State Ionics, 132(1–2), 71–85. https://doi.org/10.1016/S0167-2738(00)00697-4

26 Poirier, G., Ottoboni, F., Cassanjes, F., Remonte, A., Messaddeq, Y., & Ribeiro, S. (2008). Redox behavior of molybdenum and tungsten in phosphate glasses. The Journal of Physical Chemistry B, 112, 4481–4487. https://doi.org/10.1021/jp711709r

27 Rosenthal, A., & Garofalini, S. (1987). Structural role of zinc oxide in silica and soda-silica glasses. Journal of the American Ceramic Society, 70, 821–826. https://doi.org/10.1111/j.1151-2916.1987.tb05634.x

28 Mekki, A., Khattak, G., & Wenger, L. (2006). Structural and magnetic investigations of Fe2O3–TeO2 glasses. Journal of Non-Crystalline Solids, 352, 3326–3331. https://doi.org/10.1016/j.jnoncrysol.2006.05.007

29 Ouaha, A., Taoussi, S., Ouachouo, L., Hadouch, Y., Es-soufi, H., Hoummada, K., Mezzane, D., & Bih, L. (2025). Bi^{3+} doped $Na_2O–TiO_2–P_2O_5$ phosphate glasses: Insight into structural, physical, mechanical, thermal, chemical, crystallization, dielectric, and energy storage properties. Ceramics International, 51(10), 12600–12616. https://doi.org/10.1016/j.ceramint.2025.01.100

30 Griebenow, K., Bragatto, C., Kamitsos, E., & Wondraczek, L. (2017). Mixed-modifier effect in alkaline earth metaphosphate glasses. Journal of Non-Crystalline Solids, 481. https://doi.org/10.1016/j.jnoncrysol.2017.11.041

31 Rani, A., Parmar, R., & Kundu, R. S. (2025). Investigating the influence of barium oxide on bismuth borovanadate glasses: Physical, structural, optical, and dielectric properties. Applied Physics A, 131, 250. https://doi.org/10.1007/s00339-025-08373-6

32 Brow, R. K. (2000). Review: The structure of simple phosphate glasses. Journal of Non-Crystalline Solids, 263–264, 1–28. https://doi.org/10.1016/S0022-3093(99)00620-1

33 Rao, P. S., Teja, P. M. V., Babu, A. R., Rajyasree, C., & Rao, D. K. (2012). Influence of molybdenum ions on spectroscopic and dielectric properties of ZnF2–Bi2O3–P2O5 glass ceramics. Journal of Non-Crystalline Solids, 358(23), 3372–3381. https://doi.org/10.1016/j.jnoncrysol.2012.08.017

34 Souri, D. (2010). Small polaron hopping conduction in tellurium based glasses containing vanadium and antimony. Journal of Non-Crystalline Solids, 356, 2181–2184. https://doi.org/10.1016/j.jnoncrysol.2010.08.020

35 Terny, S., & Frechero, M. (2020). Understanding how the mixed alkaline-earth effect tunes transition metal oxides-tellurite glasses properties. Physica B: Condensed Matter, 583, 412054. https://doi.org/10.1016/j.physb.2020.412054

36 Biswas, D., Das, A. S., Mondal, R., Banerjee, A., Deb, D., Dutta, A., Bhattacharya, S., Kabi, S., & Singh, L. S. (2020). Study of microstructure and electrical conduction mechanisms of quaternary semiconducting glassy systems: Effect of mixed modifiers. Journal of Non-Crystalline Solids, 542, 120104. https://doi.org/10.1016/j.jnoncrysol.2020.120104

37 Majhi, K., & Varma, K. B. R. (2009). Dielectric relaxation in CaO-Bi2O3-B2O3 glasses. International Journal of Applied Ceramic Technology, 7, E89–E97. https://doi.org/10.1111/j.1744-7402.2009.02438.x

38 Kashif, I., Rahman, S. A., Soliman, A. A., Ibrahim, E. M., Abdel-Khalek, E. K., Mostafa, A. G., & Sanad, A. M. (2009). Effect of alkali content on AC conductivity of borate glasses containing two transition metals. Physica B: Condensed Matter, 404, 3842–3849. https://doi.org/10.1016/j.physb.2009.07.102

39 Singh, D. P., & Singh, G. P. (2013). Conversion of covalent to ionic behavior of Fe2O3–CeO2–PbO–B2O3 glasses for ionic and photonic application. Journal of Alloys and Compounds, 546, 224–228. https://doi.org/10.1016/j.jallcom.2012.08.105

40 Mondal, R., Biswas, D., Das, A. S., Ningthemcha, R. K. N., Deb, D., Bhattacharya, S., & Kabi, S. (2020). Influence of samarium content on structural, thermal, linear and non-linear optical properties of ZnO–TeO2–P2O5 glasses. Materials Chemistry and Physics, 255, 123561. https://doi.org/10.1016/j.matchemphys.2020.123561

41 Al-Harbi, N., Sayyed, M. I., Al-Hadeethi, Y., A. B. K., Elsafi, M., Mahmoud, K. A., Khandaker, M. U., & Bradley, D. A. (2021). A novel CaO–K2O–Na2O–P2O5 glass system for radiation shielding applications. Radiation Physics and Chemistry, 188, 109645. https://doi.org/10.1016/j.radphyschem.2021.109645

42 Hussain, S., Ahmed, R. J., Tanveer, M., Nadeem, M., Mahmood, H., Sattar, A., Iqbal, A., Hussain, I., Amjad, Z., Hussain, S. Z., Siddique, S. A., & Dousti, M. R. (2017). Viscosity of glass-forming liquids. Glass Physics and Chemistry, 43, 538–547. https://doi.org/10.1134/S1087659617060219

43 Ghosh, A., & Chaudhuri, B. K. (1986). DC conductivity of V_2O_5–Bi_2O_3 glasses. Journal of Non-Crystalline Solids, 83, 151–161. https://doi.org/10.1016/0022-3093(86)90065-7

44 Minakshi, M., Watcharatharapong, T., Chakraborty, S., & Ahuja, R. (2018). A combined theoretical and experimental approach of a new ternary metal oxide in molybdate composite for hybrid energy storage capacitors. APL Materials, 6, 047701. https://doi.org/10.1063/1.4994750

45 Das, A. S., Biswas, D., Roy, M., Roy, D., & Bhattacharya, S. (2019). Effect of V_2O_5 concentration on the structural and optical properties and DC electrical conductivity of ternary semiconducting glassy nanocomposites. Journal of Physics and Chemistry of Solids, 124, 44–53. https://doi.org/10.1016/j.jpcs.2018.08.026

46 Biswas, D., Ningthemcha, R. K. N., Das, A. S., & Singh, L. S. (2019). Structural characterization and electrical conductivity analysis of MoO_3–SeO_2–ZnO semiconducting glass nanocomposites. Journal of Non-Crystalline Solids, 515, 21–33. https://doi.org/10.1016/j.jnoncrysol.2019.04.002

47 Ningthemcha, R. K. N., Biswas, D., Singh, Y. B., Sarkar, D., Mondal, R., Mandal, D., & Singh, L. S. (2020). Temperature and frequency dependent electrical conductivity and dielectric relaxation of mixed transition metal doped bismuth-phosphate semiconducting glassy systems. Materials Chemistry and Physics, 249, 123207. https://doi.org/10.1016/j.matchemphys.2020.123207

48 Biswas, D., Das, A. S., Mondal, R., Banerjee, A., Dutta, A., Kabi, S., Dey, D., & Singh, L. S. (2020). Structural properties and electrical conductivity mechanisms of semiconducting quaternary nanocomposites: Effect of two transition metal oxides. Journal of Physics and Chemistry of Solids, 144, 109505. https://doi.org/10.1016/j.jpcs.2020.109505

49 Vijoy, P. S., Abdul Khadar, M., & Joseph, C. (1999). Microhardness study of (1-x-y)(B_2O_3)-x(Li_2O)-y(MCl_2), (M = Cd, Zn) glasses. Bulletin of Materials Science, 22(7), 1061–1065. https://doi.org/10.1007/BF02745621

50 Salman, S., Salama, S., & Mahdy, E. (2015). Contribution of di- and trivalent oxides to crystal phase formations and properties of yttrium aluminosilicate glass-ceramics. Processing and Application of Ceramics, 9, 139–149. https://doi.org/10.2298/PAC1503139S

51 Singh, D., Mandal, R. K., Tiwari, R. S., & Srivastava, O. N. (2016). Mechanical behavior of Zr-based metallic glasses and their nanocomposites. In InTech. https://doi.org/10.5772/64221

52 Kundu, R., Roy, D., & Bhattacharya, S. (2016). Electrical and mechanical properties of ZnO doped silver-molybdate glass-nanocomposite system. AIP Conference Proceedings, 1728(1), 020064. https://doi.org/10.1063/1.4946115

53 Guo, Y., Li, J., Zhang, Y., Feng, S., & Sun, H. (2021). High-entropy R_2O_3–Y_2O_3–TiO_2–ZrO_2–Al_2O_3 glasses with ultrahigh hardness, Young's modulus, and indentation fracture toughness. iScience, 24(7), 102735. https://doi.org/10.1016/j.isci.2021.102735

54 Ibrahim, S., Khattari, Z., & Mahdy, E. (2025). Impact of In_2O_3 content on the structural, thermal, and mechanical hallmarks of Na_2O–BaO–ZnO–Fe_2O_3–P_2O_5 glass systems. Journal of Materials Science: Materials in Electronics, 36. https://doi.org/10.1007/s10854-025-14680-8

56 Alsaif, N., Alfryyan, N., Al-Ghamdi, H., Rammah, Y., Mahdy, E., Abo-Mosallam, H. A., & Talaat, S. (2025). Impact of Sm ions on the structure, physical, FTIR spectroscopy and mechano-radiation shielding capabilities of high dense CdO–Bi_2O_3–SiO_2 glasses. Applied Physics A, 131. https://doi.org/10.1007/s00339-025-08385-2

Chapter 2

Synthesis and Characterization Approaches for Amorphous Vanadate-Phosphate Glasses

2.1. Introduction

The approaches of this research are essentially based on the experimental testing of the glass materials and their overall characterisation. By definition, Glass should be an inorganic solid that is created by the melting of raw materials, and is of rigid, non-crystalline (amorphous) texture. Various chemical precursors were chosen strategically to fabricate glassy substances bearing nano-crystalline phases in this inquiry.

In this chapter, there is a brief description of the analytical methods used in determining the structural, thermal, mechanical, electrical and dielectric characteristics of the synthesized glass nanocomposites. These characterization techniques play a significant role in comprehending the structure of the network (inside) and the level of amorphousness or semi-crystallinity of the laboratory-prepared samples.

It is necessary to accurately identify the compositional classification and structure-property relationship (especially what type of disorder the materials have) to determine the degree of disorder that directly impacts the mechanical strength and thermal stability of the materials. The assessment of mechanical parameters (viz. elastic modulus, hardness, etc) provides some information about the mechanical integrity of the glasses, whereas such methods as differential scanning calorimetry (DSC) may contribute to the explanation of the thermal transitions and decomposition reactions.

The basis of interpreting the electrical and dielectric properties observed in the glass systems is complete structural knowledge. Such an atomistic level structure understanding would be hard to get, without which it will not be easy to infer any significant relation between composition, structure, and consequent physical behavior of the glassy matrices.

2.2. Synthesis of Glass Nano-Composite Systems

In this research, the melt quenching method has been used in the manufacture of the BBVP glass samples because it is efficient in synthesizing homogeneous and amorphous glass materials. The individual chemicals (grade-purity of 99.9 percent) were initially accurately weighed as per their stoichiometric ratios on their respective standard measurement using digital Dona weighing machine, hence ensuring the accurate formulation of each batch. The blending of these raw materials was done carefully in a mortar and pestle to come up with a uniform blend of powder. The completed homogenized mixture was poured into a high-purity

alumina crucible that allowed melted materials to stabilize and preventing reaction with it. The crucible was then taken to an electric furnace through which the contents were melted at a temperature of 700-1000ºC depending on the composition, to facilitate thorough mixing of the melt. After the molten state had become homogenous; the molten metal was then poured rapidly into an already cooled quencher usually a stainless steel plate or mould to stop crystallization and create a rapid cooling effect producing a glass state. The final glass was produced in the form of pellets, and a part of the bulk glass was ground into fine powder in a mortar and a pestle to conduct additional structural and thermal evaluations. To guarantee reproducibility, structural integrity, and amorphous character of the synthesized BBVP glasses in this study, this was achieved by this approach. The schematic diagram of the above-mentioned main component of the melt quenching set-up and the synthesized glass samples are represented in **Fig.2.1**.

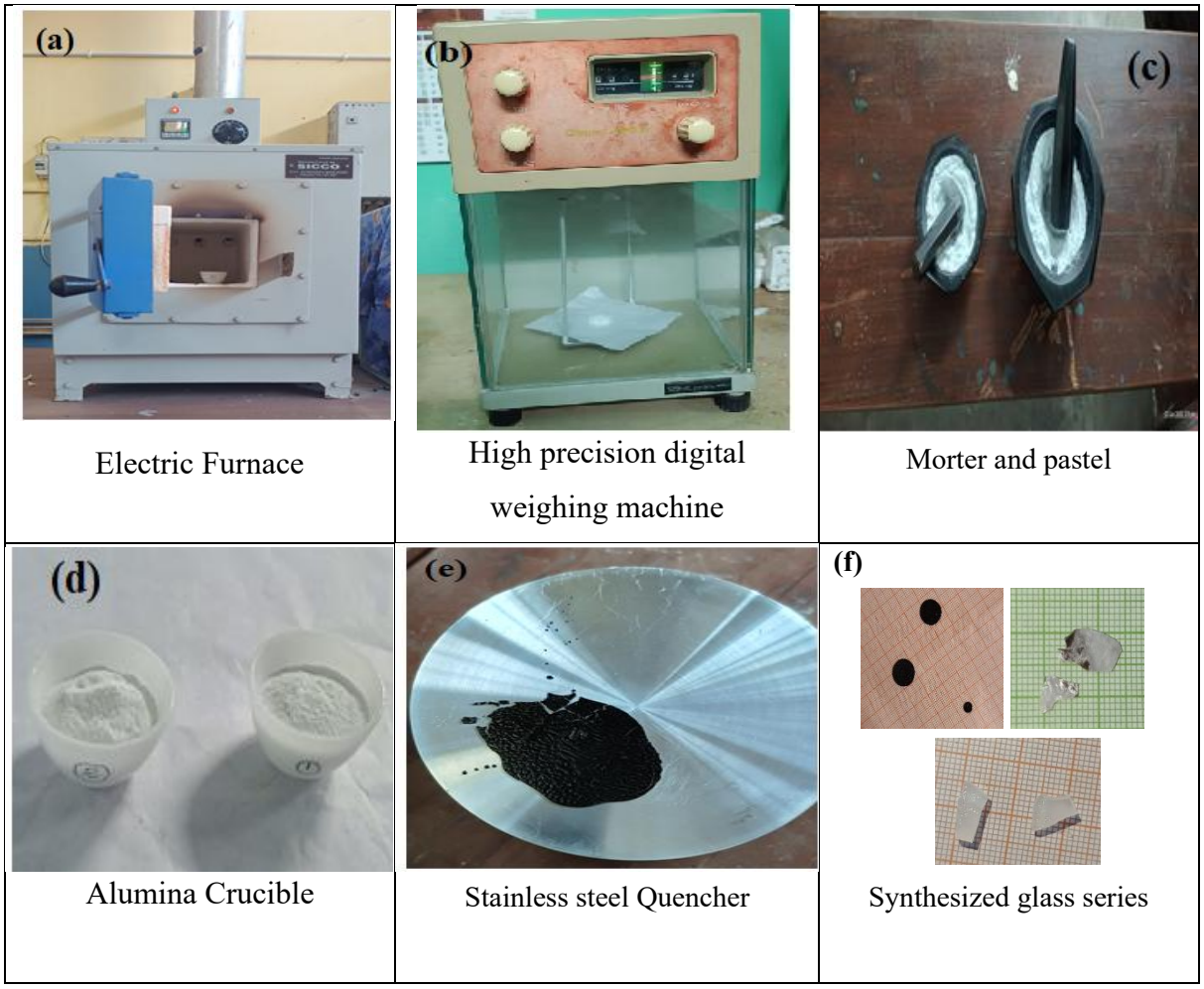

Fig. 2.1. (a-e) Main components of the melt quenching process and (f) Synthesized samples

2.2.1. Preparation of quaternary V_2O_5–Na_2O–ZnO–P_2O_5 glass system

In the study of glassy systems containing TMO and alkali oxide, the general melt-quench procedure has been employed, with a chemical compositional formula of xV_2O_5-(0.4-x) Na_2O-0.35ZnO-0.25P_2O_5 (x = 0.05, 0.1, 0.15, 0.2, and 0.25). The desired glass samples have been synthesised using analytical-grade chemicals: V_2O_5 (powder), Na_2CO_3 (powder), ZnO (powder), and P_2O_5 (powder), all of which have a grade purity of 99.9 per cent. According to their chemical composition, batches of 15 g of each glass sample were weighed on a digital balance with a precision of 0.0001 g. They were then cautiously sorted in an agate mortar by successive grinding to achieve homogeneity of the assortments. The assortments are then melted in atmospheric air and a high-temperature electrical muffle furnace. The melts fuse over 650°C to 700°C, depending on the chemical stoichiometry. Then the melting mass is maintained at the melting temperature (1hr) and periodically stirred to obtain more homogeneous liquid glass. The molten body is then at once quenched, at room temperature, by a highly polished metal melt-quencher to give plates of glass, 0.2- 0.3 mm thick. Subsequently, the glassy plates are powdered to carry out several measurements.

2.2.2. Preparation of quaternary Bi_2O_3-BaO-V_2O_5-P_2O_5 glass system

The Bi_2O_3 and BaO doped quaternary glasses xBi_2O_3-(0.4-x) BaO-0.3V_2O_3-0.3P_2O_3(x=0.05, 0.15, 0.15,025, and 0.35) were synthesised using the conventional melt-quenching technique. Raw materials Bi_2O_3, $BaCO_3$, V_2O_5, and $NH_4H_2PO_4$, each in powder form with over 99.8 per cent purity, were ground appropriately with an agate mortar and pestle for 15 minutes. The volatile products of all mixtures were removed by heating the batches to 600°C in an alumina crucible. They were subsequently heated to 1000°C and soaked in the electric furnace for 1 hour, before being poured and quenched on a brass plate to obtain semi-transparent glasses with a thickness of 1-2 mm. The glass samples were then polished thoroughly using sandpaper to produce opposite parallel faces measuring between 8 and 10 mm in diameter and about 1 mm in thickness to facilitate precise electrical measurements. The samples were subsequently rolled together to create a fine powder for the determination of their structure and optical properties.

2.2.3. Preparation of quaternary Bi_2O_3-Fe_2O_3-V_2O_5-P_2O_5 glass system

Quaternary glasses with the composition xBi_2O_3-(0.40-x) Fe_2O_3-0.25P_2O_5-0.35V_2O_5 (x = 0, 0.1, 0.2, 0.3, and 0.4) were synthesized using the standard melt-quenching method. The prepared mixtures, following careful weighing and accurate blending, were heated in alumina

crucibles up to 570 °C to minimize the formation of volatile products. The batches were then heat-treated at 990 °C for one hour in an electric furnace before pouring and quenching them on a stainless steel plate. This process produced glasses with varying thicknesses of exactly semi-opaque effect and varied from 1.3mm to 2.6mm. The glass samples were manually lapped using fine sandpaper (Abrasive: micro Al_2O_3 powder of average particle size ranging from 0.1-1μm) to create two opposite, plane-parallel faces. The resulting circular pieces had a diameter ranging from 9 to 12 mm, depending on the initial size and shape of the as-prepared glass pieces, and a thickness of approximately 1.2 mm. Manual lapping consists of continuous rubbing of glass samples against the fine micro alumina (Al_2O_3) abrasive grits, which are kept on a plane surface. These alumina (Al_2O_3) grits have been wetted with deionised water to form a slurry before the process. The circular shape was achieved manually by carefully grinding and shaping the edges during the lapping process. These particular temperatures and thicknesses were deliberately set to meet the optimal conditions for synthesising glasses to allow for further research into the glasses' mechanical and dielectric characteristics.

2.3. Physical Characterization

The actual physical definition of the prepared glass samples is mainly directed at the assessment of two of its key characteristics, namely the density (ρ) and the volume per molar (V_M). These parameters are used to give important results on the compactness, arrangement structure and the packing efficiency of the glass network [1-2]. Determination of density assists in the determination of mass per unit volume of the glass, and this is directly connected with the arrangement of atoms and the binding used between the constituent elements. Conversely, molar volume, which is calculated using molecular weight and density, will provide data regarding the amount of volume occupied by a single mole of the glass material. All these physical parameters in combination can be key measures of structural robustness and compositional influences on the glass framework. The above-mentioned properties are measured and analyzed through the methods following the details below.

2.3.1. Density measurement

One of the fundamental and frequently measured physical properties of any glass system is called density. It offers useful information about atomic packing, the compactness of the structure, and the connectivity of the glass matrix. Due to its straightforward measurement process and high accuracy, density can serve as a critical diagnostic parameter for assessing the effects of composition on the internal structure of both amorphous and polycrystalline

materials. The addition of modifying oxides to a glass system typically causes structural changes; in this case, replacing bridging oxygen (BO) with non-bridging oxygen (NBO), which alters the overall connectivity within the network. These structural changes directly influence the volumetric mass density (ρ) of the glass and are therefore a reliable indicator of variations in network structure, coordination environment, and atomic mass distribution. Consequently, density can increase or decrease depending on the molecular weight of the constituent oxides, as well as variations in ionic radii, coordination numbers, and the efficiency of packing within the glass lattice.

Regular density measurements are made by utilizing Archimedes' principle, and it has been standardized as a technique to utilize since it is non-destructive and the experimental setup is not as complicated. This is done by weighing the sample in air, then under a suitable immersion liquid, a liquid whose density is known (generally a non-reactive fluid like acetone) at room temperature (~25°C). The very common choice is based on the low viscosity, inertness to most glass compositions, and the availability of well-documented property measurements of acetone.

The equation for calculating the bulk density (ρ) of the sample is[3]:

$$\rho = \left(\frac{\mathrm{Wg_{air}}}{\mathrm{Wg_{air}} - \mathrm{Wg_{acetone}}}\right) \times \rho_{\,\mathrm{acetone}} \qquad (2.1)$$

In this equation, Wg_{air} and $Wg_{acetone}$ represent the estimated weights of the glass sample when suspended in air and immersed in acetone, respectively, and $\rho_{acetone}$ symbolizes the density of acetone. The density value of a sample has been determined through multiple measurements using different glassy plates, and the average density value is reported.

Uncertainty in the experiment is kept to a minimum as parameters are well controlled, including temperature, purity of liquid, removal of bubbles on the surface of a liquid, etc.

Patterns in density within the series of glasses can provide valuable data about the importance of each component in determining the structure of the glass. As an example, the concentration of heavy metal oxides or network modifiers tends to raise the values of density, and lighter or more loosely structured forms of the former can cause them to decrease. When coupled with the molar volume and other parameters related to structure information, density data can therefore give a complete picture of the internal alignment of the material and how it changes due to a change in composition.

2.3.2. Molar Volume measurement

The molar volume (V_M) of an individual sample can be calculated utilizing the estimated density (ρ) value and the subsequent equation [3]:

$$V_M = \sum \frac{x_i \times M_i}{\rho} \quad (2.2)$$

Here, x_i and M_i denote the molar fraction and molecular weight of the i^{th} oxide, respectively.

2.4. Structural Characterization methods

2.4.1. X-ray Diffraction Technique

X-ray diffraction (XRD) represents a non-destructive, universally accepted method to investigate the properties of structural characteristic of both amorphous and polycrystalline materials (**Fig. 2.2 and 2.3**). In the research, the use of XRD was applied to analyze the structural ordering to identify possible nanocrystalline phases that are embedded within transition metal or heavy metal-doped glass matrices. The diffraction in powder XRD patterns was determined by room temperature increment on a Rigaku TTRAX-III diffractometer. The measurements were done under CuK rays (λ = 1.5418 A), 35 kV and 25 mA, scanned invariant of 2θ (10° to 80°), a rate of 4°/min, and the step was 0.02°. The instrumental configuration enabled a high-resolution detection of either broad amorphous halos or sharp peaks in their presence.

Bragg law provides quantitative support of information on structural details that XRD reveals; it connects the diffraction angle and the interplanar spacing [4]:

$$n\lambda = 2d\sin\theta \quad (2.3)$$

In this case, n and d in the order of reflection and the spacing between its layers in the crystal.

They can be applied to amorphous materials that lack long-range atomic periodicity, producing no sharp diffraction peaks. Rather, a wide diffuse halo would be observed in the XRD profile, which is typical of a disordered glassy system. Any nanocrystalline domains that exist will be demonstrated by broad and weak diffraction peaks on top of an amorphous background. The XRD patterns were confirmed by the fact that the observed patterns could be described as mostly amorphous with a small nanocrystalline pattern at the heavier concentration of dopants. The individual nanocrystallite size (d_c) is determined by applying the well-known Scherrer expression (**Eq. (2.4)**) with the full width at half maxima (FWHM) of the relevant diffraction peak [3-4]:

$$d_C = \frac{0.89\ \lambda}{\beta_{correct}\ \cos\theta} \tag{2.4}$$

The X-ray radiation wavelength, corrected full width at half maximum, and Bragg diffraction angle are represented by the symbols λ, $\beta_{correct}$, and θ in **Eq. (2.4)**, respectively.

Deducting the observed broadening ($\beta_{observed}$) value and instrumental broadening ($\beta_{instrument}$) value line broadening profile of the peak observed is corrected, which is called $\beta_{correct}$ [3]. According to the Gaussian distributions, the corrected full width at half maxima of the investigated sample is represented as [3-4]:

$$\beta_{correct} = \sqrt{\beta_{observed}^{\ 2} - \beta_{instrument}^{\ 2}} \tag{2.5}$$

To determine the proportion of the amorphous phase in the glass, the following relationship can be employed, which is derived from an equation estimating the percentage of crystallinity (**Eq. (2.6)**) [4]:

$$\text{Crystallinity (\%)} = 100 \times \frac{\text{The area under the crystalline peak}}{\text{Total area under the diffraction curve}} \tag{2.6}$$

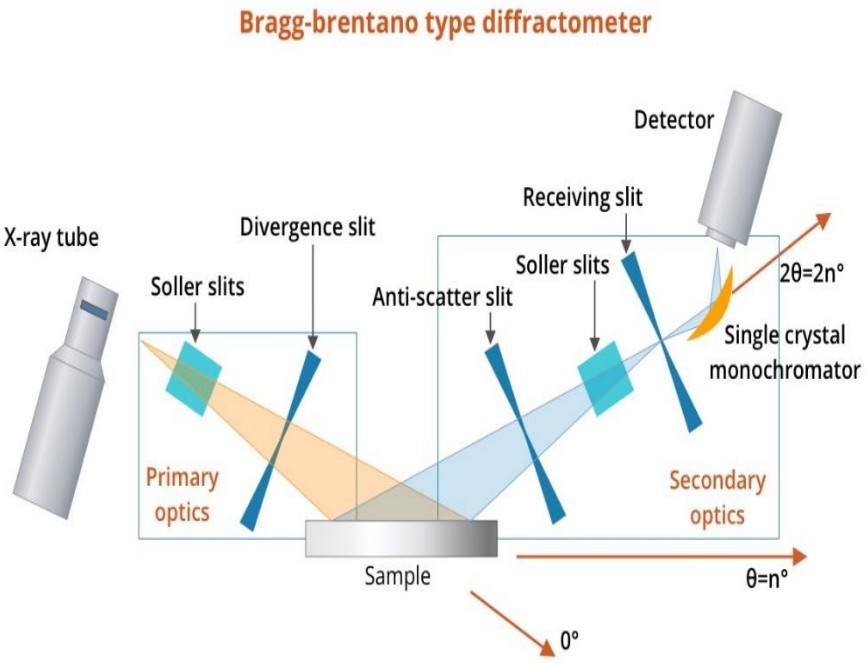

Fig. 2.2. Schematic representation of an X-ray diffractometer**.**

Fig. 2.3. Image of Rigaku TTRAX-III diffractometer.

2.4.2. Fourier Transform Infrared (FTIR) spectroscopy

Fourier Transform Infrared spectroscopy (FTIR) is a broadly utilized type of vibrational spectroscopic methodology, which is also considered conventional and is widely regarded as a successful method to determine the functional group(s) in a mixture of material systems. The working principle of FTIR is based on the reaction of infrared radiation with the material under analysis. As the IR beam passes through the sample, some part of the incident radiation is taken up by molecular bonds and the rest is passed through. This interaction produces a range of peaks representing absorption and transmission properties of the material that, in effect, forms a unique molecular fingerprint of the sample.Coupled to its great interest in bond vibrations and structural motifs, FTIR spectroscopy can be regarded as one of the most general and useful instruments of the qualitative analysis of organic, inorganic, hybrid and glassy substances [5,6]. A typical schematic illustration of an FTIR spectrometer is depicted in **Fig. 2.4**. In the current research, FTIR spectra have been carried out in a transmission mode, with a pellet technique, in which we have used a mixed chunk of powdered glass sample well blended with spectroscopically pure KBr in equal proportion (1:100 sample: KBr). The obtained pellet was examined under a Shimadzu 8400S FTIR Spectrometer. FTIR absorption

spectra are recorded in the wave number range of 400-1800 cm^{-1} at ambient temperature (25 °C, ~50-60 per cent relative humidity).The main objective of FTIR analysis used in this work is to look into the manner of bonding and the mechanical structure of the synthesized glass systems. When the IR beam meets with the vibration of the molecules, absorption happens at resonances along certain vibrational frequencies. These absorption peaks are typical of numerous straightening and bending vibrations and indicate details of the structural units that can be found in the glass matrix.

It is important to note that overlapping vibrational bands are common in light of the fact that the glass network is usually complex. To fix this, spectral deconvolution was done with OriginPro 17 software. The Gaussian or Lorentzian line-shape functions were used to fit each of the composites, so that the area under single bands could be calculated accurately. Such a deconvolution procedure contributes to the better interpretation of the different structural units and bonding environments to be found in the sample.

FTIR spectroscopy, with its aid of deconvolution and curve fitting, is therefore a very important method in the current study that is used in explaining the vibration patterns and composition chemistry of the glass species prepared.

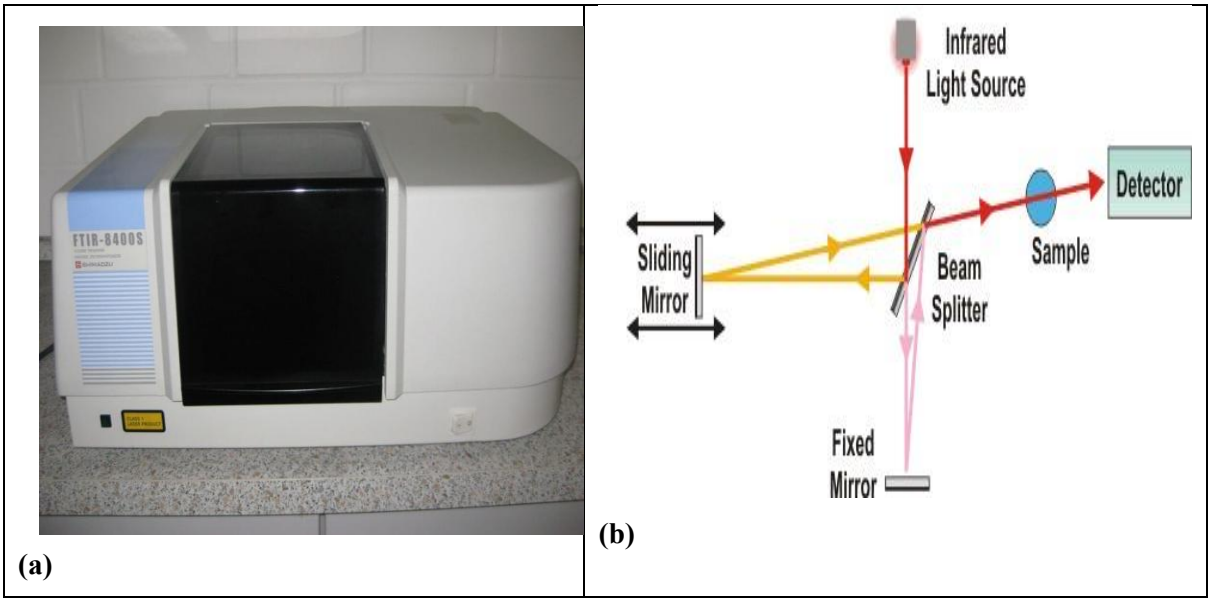

Fig. 2.4. (a) Image and **(b)**Schematic layout of FTIR Spectrometer

2.4.3. Raman spectroscopy

Raman spectroscopy is an analytical method that is based on the non-destructive investigation of the vibrational characteristics of the material based on the analysis of inelastic light scattering. During this process, monochromatic light, usually provided by a laser operating at a visible wavelength, is incident upon a sample. Most of the photons are elastically scattered (Rayleigh scattering); an extremely small number experience inelastic scattering, so that their energy is shifted, corresponding to vibrations of the molecules. This migration which is also called Raman shift gives a lot of information on the structural properties of the material being investigated.

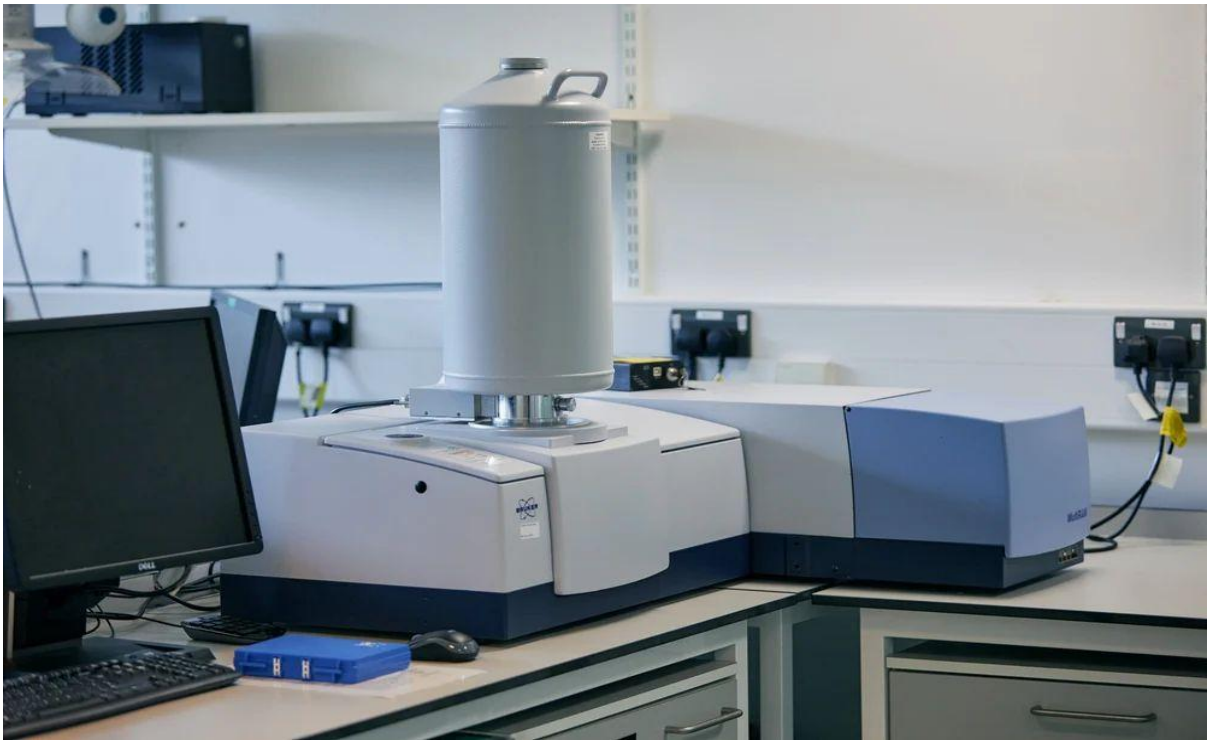

Fig. 2.5. Image of Raman Spectrometer (Bruker Optics Multi-RAM)

The Raman process is conducted when incident radiation at a specific frequency (ν_0) interacts with the sample under study and is scattered at a slightly altered frequency ($\nu_0 + \Delta\nu$) because it exchanges energy with molecular vibrations. The result of such interaction is a spectrum which serves as a molecular fingerprint, which is made by the composition of the material and bonding environment.

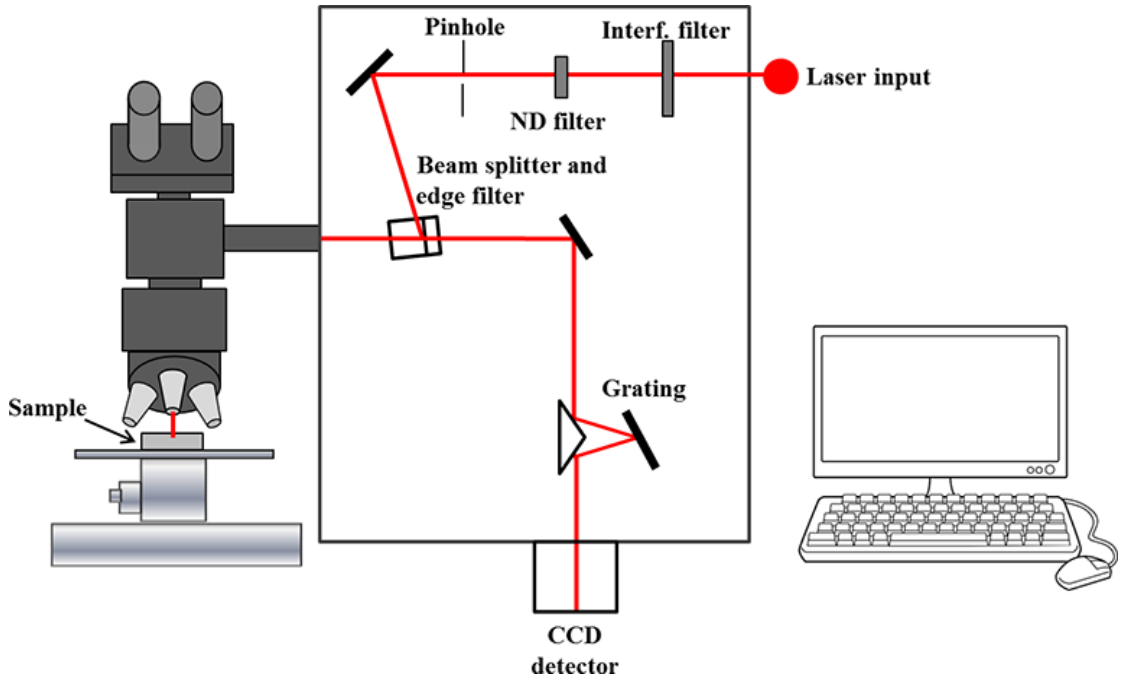

Fig. 2.6. Schematic layout of a Raman Spectrometer

Among sources, Lasers are preferred because they have a narrow wavelength and are strong sources and also have excellent coherence. The light is dispersed; the dispersed light contains Raman plus Rayleigh components and is directed to a spectrometer. The very strong Rayleigh scattering can be much stronger than the Raman signal (10^3-10^5 times more intense than the Raman signal), so to suppress this a notch filter is positioned in front of the entrance slit. This filter cuts light all around the laser wavelength preferentially. But because of the limited bandwidth of the filter, Raman shifts below a few 100 to 150 cm^{-1} may not be visible.

Since Raman scattering, by its nature, has a very low intensity, a very sensitive detector with minimum noise is required. The CCD detectors, which have two-dimensional arrays of pixels, are common in modern instruments because they allow to collection of a vast amount of scattered light simultaneously with high sensitivity. In my research, Raman spectrometer (Bruker Optics MultiRAM) is used to examine the structural alteration in BBVP glass samples, with a spectral range of 3600-50 cm^{-1} [**Fig.2.5**].

Among the major merits of Raman spectroscopy, one should mention its simplicity; the sample may be investigated under ambient conditions with no special preparation. Raman bands are most sensitive to the variation in molecular polarizability (α) in the course of vibration.

The Raman scattering intensity, I_{Raman} of a particular vibrational mode, can be written as [7]:

$$I_{Raman} = K \times I_L \times (v_0 - v_i)^4 \times (\frac{d\alpha}{dQ_i})^2 \quad (2.7)$$

Where:

- I_L is the power of the laser on the sample,
- ν_0 and ν_i are the frequencies of incident and scattered light,
- $\frac{d\alpha}{dQ_i}$ denotes the rate of change in polarizability for the vibrational coordinate Q_i,
- K is a constant dependent on system geometry, collection efficiency, detector sensitivity, and signal amplification.

Raman spectra are commonly affected by frequency and temperature, especially at low wavenumbers, in situations where the glass systems are examined. At such frequencies, the spectra might become distorted because of the existence of some spurious scattering components. To be able to correct this, a frequency-dependent correction factor, R, was added to the raw spectral data [7]:

$$R = \frac{(1-e^{\frac{-h\nu}{kT}})}{(\nu_0+\nu)^4} \quad (2.8)$$

Here, ν_0 and ν represent the excitation and Raman shift frequencies (in cm^{-1}), h is Planck's constant, k is Boltzmann's constant, and T is the absolute temperature. This correction compensates for thermal population effects and detector response variations. Baseline correction was also performed to remove background contributions. Due to the inherently broad and overlapping bands observed in glassy materials, instrumental linewidth effects were not explicitly included in the spectral deconvolution process.

2.5. Optical Characterization Method

The optical properties of the glass samples under ambient conditions (300 K) in a wide spectral range of 190 to 750 nm were examined using ultraviolet-visible (UV-Vis) absorption spectroscopy. The quantifications were performed with a PerkinElmer Lambda 750 spectrophotometer(**Fig.2.8**) working in absorbance mode. The method is a critical analytical construct to study the electronic transitions and learn the structural development in amorphous forms [8,9].

The samples to be measured in terms of absorption were prepared by dispersing the finely powdered glass in ethyl alcohol. The resulting suspension was then treated with ultrasound through a probe-type sonicator, ensuring good homogenization was achieved, which involved the breakdown of agglomerates of particles and even dispersion of the mostly dispersed material. It is an important step to reproducible and substantive spectral measurements [9,10].

The UV-$_{Vis}$ spectroscopic system is shown in a simplified drawing in **Fig. 2.7**, showing the main components used in the process of measuring the absorption.

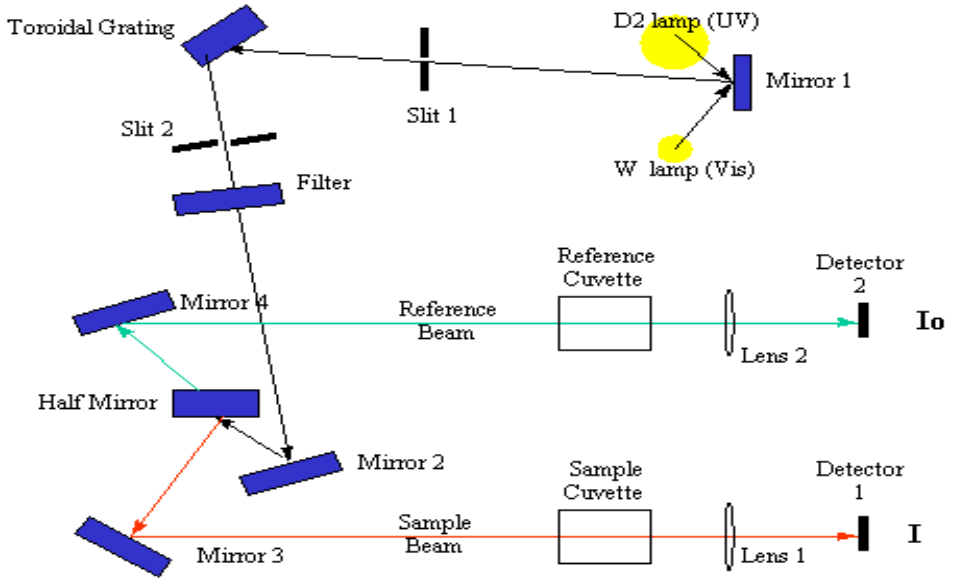

Figure 2.7. Schematic layout of ultraviolet-visible (UV-$_{Vis}$) absorption spectroscopy

These measurements allow obtaining optical absorption spectra, which can be useful to identify the character of electronic transitions inside the material [9]. In particular, they give insightful data regarding the optical bandgap energy that plays a critical role in the description of the electronic structure of glassy systems. Electronic transitions in amorphous materials may be direct or indirect, and the more frequently seen near the onset of fundamental absorption [11,13].

To obtain optical bandgap energy (E_{opt}), the absorption coefficient (α) was plotted against photon energy ($h\nu$) and the resulting data were plotted on the Tauc method of indirect transitions. With this method, it is possible to find out E_{opt} through extrapolation of the linear segment of the $(\alpha h\nu)^2$ versus $h\nu$ to the energy axis.

Fig. 2.8. Pictorial representation of ultraviolet-visible (UV-$_{Vis}$) absorption spectrometer (PerkinElmer Lambda 750 spectrophotometer)

The Davis and Mott model provides a framework to explain the variation in the bandgap of amorphous materials theoretically; thus, the changes are owed to the presence of low-lying resonant states on the band scheme [9]. E_{opt} on the existence and development of localized states and defect states as well as localized energy levels in the band structure. The aforementioned properties are the results of the intrinsic structural disorder of glassy matrices. An increased level of disorder usually leads to an increased localized state density, which further affects the optical absorption edge and broadens or narrows the optical bandgap depending on the given type and distribution of the defects [8].

Energy of incident photons, when measured, is referred to as $h\nu$, a fundamental quantity in optical spectroscopy, and it is used in evaluating electronic transitions taking place within a material. It may be computed based on the relation [8]:

$$h\nu = \frac{hc}{\lambda} \tag{2.9}$$

Where h is Planck's constant (4.14×10^{-15} eVs),

c is the speed of light in a vacuum (2.9979×10^{8} m/s),

λ is the wavelength of the incident light in meters.

E_{opt} has been quantified as the absorption coefficient of the ultraviolet-visible (UV-Vis) electromagnetic waves using the following formulae [12]:

$$\alpha hv = [A\,(hv - E_{opt})]^{n} \quad (2.10)$$

In this, A represents the constant value of the band-tailing parameter. The value of the exponent (n) is dependent on the electronic character of the band gap, i.e., directly allowed (DA), indirect allowed (IA), direct forbidden (DF) and indirect forbidden (IF) electronic transition is represented by the value of p as 1/2, 2, 3/2, and 3, respectively.

According to Davis and Mott, the denoted optical bandgap energy is often associated with the density of the defects or localized states in low crystalline or amorphous solids [9]. Along with the proposal that in the amorphous glass structure the number of states of defects and disorder gave rise to localized or extended states within the optical bandgap or mobility gap, Davis and Mott had also hypothesized ionic conductivity involving the hopping of various defect states using states of the disorder in the landscape of amorphous glass [9]. At the edge of the optical bandgap of the absorption coefficient (lnα) an exponentially decreasing band tail is observed, which can be described as Urbach energy (E_U) or band tail energy [12]. The degree and character of disorder within the glass matrix are usually associated with E_U. The time obtained using the subsequent equation of the Urbach empirical rule is used in measuring the values of E_U of all the amorphous glass nanocomposites [12]:

$$\alpha = \alpha_0 \exp\left(\frac{hv}{E_U}\right) \quad (2.11)$$

In this case, the default parameter of band tailing is represented as α_0 . E_U value is indicated by the value of the reciprocal of the slope of the straight line of the linear part of the graph of ln (α) versus hv[12].

2.6. Electrical and dielectric measurement

The measurements of several electrical and dielectric parameters are performed using an LCR meter (model: IM3536), applying the well-known two-probe technique in the frequency range from 40 Hz to 5 MHz at several temperatures(**Fig.2.9**). Small pieces of all five glass samples are finely polished to attain a thin slab shape with flat faces. Highly conductive silver paste is painted on both faces of thin glass slabs, acting as an electrode [14-16]. A Eurotherm temperature controller regulates the temperature within the furnace.

To conduct dielectric measurements, silver paste with high conductivity and resistance to elevated temperatures was uniformly applied to both surfaces of the meticulously polished, bulk glassy circular pellets to serve as electrodes. Subsequently, these silver-coated glass specimens underwent a drying process in a furnace at 120°C to prevent silver diffusion throughout the experimental procedure [15-16]. Dielectric parameter values were measured across a range of temperatures using a programmable, highly accurate LCR Hi-Tester (Model No: 3532-50; Hioki) within the 20 Hz to 5×10^6 Hz frequency range and in a temperature range of 353 K - 533 K. The experiments involved placing glass samples in a cryostat chamber, which was kept under a constant vacuum for controlled conditions. Temperature regulation within the chamber was managed using a Eurotherm device, ensuring that the temperature remained at the specified conditions [15-16].

Fig. 2.9. Pictorial representation of LCR Hi-Tester (Model No: 3532-50; Hioki)

The investigational measurements of parallel capacitance (C_p), conductance (G), and loss tangent ($tan\ \delta$) were meticulously documented to evaluate the varied dielectric properties of the glasses. Additionally, the complex dielectric permittivity (ε^*), which is an essential parameter for characterizing the transmission speed of AC signals and parallel capacitance in the material, is mathematically expressed as follows [17]:

$$\varepsilon^* = \varepsilon^{/} - j\varepsilon^{//} \tag{2.12}$$

where $\varepsilon^{/}$ denotes the real part (dielectric constant) and $\varepsilon^{//}$ represents the imaginary part (dielectric loss) of the complex dielectric permittivity.

The dielectric constant ($\varepsilon^{/}$) was determined by employing an equation that takes into account the parallel capacitance (C_p), the permittivity of free space (ε_o), the thickness (t), and the surface area (A) of the glass samples [17]:

$$\varepsilon^{/} = \frac{C_P t}{\varepsilon_0 A} \tag{2.13}$$

To calculate the Dielectric loss ($\varepsilon^{//}$), the dielectric loss tangent (tanδ) and dielectric constant ($\varepsilon^{/}$) were used in the formula [17]:

$$\varepsilon^{//} = \varepsilon^{/} \tan\delta \tag{2.14}$$

The complex electric modulus (M^*) methodology is employed to distinguish between the impacts of dipole relaxation and interfacial polarization within the conductivity process. Additionally, it serves to characterize the comprehensive conductivity or dielectric relaxation behaviour. The complex electric modulus (M^*) is given by [17]:

$$M^* = \frac{1}{\varepsilon^*} = M^{/} + iM^{//} = \frac{\varepsilon^{/}}{(\varepsilon^{/})^2 + (\varepsilon^{//})^2} + i\frac{\varepsilon^{//}}{(\varepsilon^{/})^2 + (\varepsilon^{//})^2} \tag{2.15}$$

In this context, $M^{/}$ and $M^{//}$ are the real and imaginary components of the complex electric modulus, respectively. The frequency dependence of $M^{/}$ and $M^{//}$ provides valuable insights into the relaxation mechanisms occurring within the material [18-20].

2.7. Mechanical Property Measurement

2.7.1. Microhardness Measurement

Microhardness measurement is a fundamental process for determining the mechanical strength and resistance of materials to localised deformation based on microscopic properties. It consists of placing a small, well-controlled force on a sharp indenter onto the material, usually of diamond, leaving a mark on the surface of the material. An optical microscope is used to measure the dimensions of the resulting indentation, and the hardness is computed based on the applied load and depth of the impression. This technique has the great advantage when used with brittle, layered, or in-house small quantities of materials. It is particularly suited to characterize fine-scale material properties; its non-destructive character and high spatial resolution is particularly suitable in this case.

In the scope of the glasses in terms of the materials, microhardness testing is a valuable means to determine the mechanical sustainability and the internal strengthening of the structure. Glasses are highly non-crystalline in structure and brittle in nature, and their mechanical

properties are highly dependent on the structure of their atomic bond formation and network connectivity. The microhardness values may correspond to the packing density of the glass network and also to the resistance to surface damage or crack generation. Increasing hardness is, in general, a sign of a stronger, more polymerized glass network, whereas low hardness can be caused by depolymerisation or presence of structural modifiers, which also lead to non-bridging oxygen sites weaking the network.

Fig.2.10 Micro-Vickers hardness tester (UHL VMHT; model no: VMH-002V)

The methodology for microhardness characterization involves a series of precise steps to ensure accurate measurement of the material's hardness. The process begins with meticulous sample preparation, where glass samples are cut into small, flat pieces having dimensions 5 mm × 5 mm and a thickness of approximately 1.2 mm, and mounted in cold-setting resin or epoxy for stability. The samples are then ground using silicon carbide abrasive paper of successively decreasing grit from 800 to 2000 and finally polished using diamond paste. After washing the sample, most of the debris and other unwanted parts are removed to prepare it for the test. I have used the UHL VMHT-VMH-002V Micro-Vickers hardness tester (**Fig.2.10**), which normally employs a Vickers diamond pyramidal indenter having an elastic modulus of 1140 GPa, and its Poisson's ratio is around 0.07, and a standard, whose hardness characteristic is well known, is used to check the tester. The correct load is chosen, ranging from 10g to 1kg based on the hardness expected, and the dwell time for the indentation is around 10-15 seconds. The polished sample is put on the tester stage, and the indenter is brought to bear on the surface of the sample to the specified load. The indenter penetrates the sample for the same dwell time, and then the load is released slowly. The final indentation mark is then viewed with a high-power optical light microscope, and the length of the diagonals is measured with considerable precision.

The Vickers Hardness of all prepared glassy systems is estimated using the following equation [21]:

$$H_V = \frac{1.854 \times F}{d^2} \tag{2.16}$$

where *F* represents the applied load in kgf and d is the average length of the two diagonals in mm. All the values of micro-hardness are directly converted to Hv as Hv or Vickers hardness number is well accepted as a representative of hardness unit.

Indentation is carried out several times on different sites of the sample so that at least five measurements should be taken, and then the average microhardness is calculated. Any variation is simulated to evaluate the actual hardness of the given material correctly. Sources of possible errors, including sample roughness, indentation damage, or sharpness and alignment of the indenter, are controlled by using well-prepared samples and checking the indenter's sharpness and alignment. The obtained graphics of average hardness values, standard deviations, and the images of indentation marks are then used to study the hardness characteristics of the material. This multi-faceted approach guarantees that microhardness testing gives proper information on

the mechanical attributes and atomic structures of the glass and other materials at the microscopic level.

2.7.2. Measurement of Nano-hardness

Nanoindentation is a sophisticated form of mechanical characterization which is specially engineered to measure the hardness, elastic modulus and other mechanical qualities of materials on a nano level. Nanoindentation is in contrast to the conventional or microhardness tests, wherein the very low (usually between micro- to millinewtons) loads are being used and continuously monitored by the amount of penetration on the sample surface by a sharp, calibrated indenter such as a three-sided Berkovich diamond tip. The resulting load-displacement curve delivers really accurate inputs on localized deformation response of a material in terms of its elastic and plastic response. Nanoindentation can be particularly more useful in the cases of thin films, coatings, heterogeneous materials and the micro/nanoscale devices where general mechanical testing will not be applicable.

Nanoindentation of glassy materials is useful in investigating properties on the surface and near-surface because these properties cannot be determined by bulk measurements. With the brittle and non-crystalline character of glass, it is crucial to know the means through which it deforms over a very small scale so as to evaluate strength with regard to the suitable failures in higher applications. Nanoindentation enables an investigator to study local changes in stiffness and hardness that can occur either as a result of compositional fluctuations or as a result of structural heterogeneities inside a glass matrix. Glasses do not have a crystalline lattice and it is the extent to which the atoms are networked, the degree of atomic packing, and existence of non-bridging oxygen atoms determine their mechanical response. Nanoindentation observation can sensitively probe these factors giving a depth-resolved profile of mechanical properties.

Even more powerful (at least in principle) in the case of glass nanocomposites is nanoindentation, which gives spatially resolved information in how the nanoscale inclusions interact with the host glass matrix [22]. Nanoparticles or nanocrystals dispersion into the glass may increase its stiffness, hardness and crack propagation resistance. Nanoindentation can be used to locally determine the extent of such enhancements and distinguish the mechanical behavior of the matrix, the filler and the interfacial zones. It is especially useful at picking up mechanical gradients, e.g. those that exist in functionally graded glasses or phase-separated glasses. Moreover, the ability of the load to transfer between the matrix and filler phases of the

composite can be assessed with nanoindentation, and this can be used as a quantitative measure to optimize the design of any nanocomposite systems.

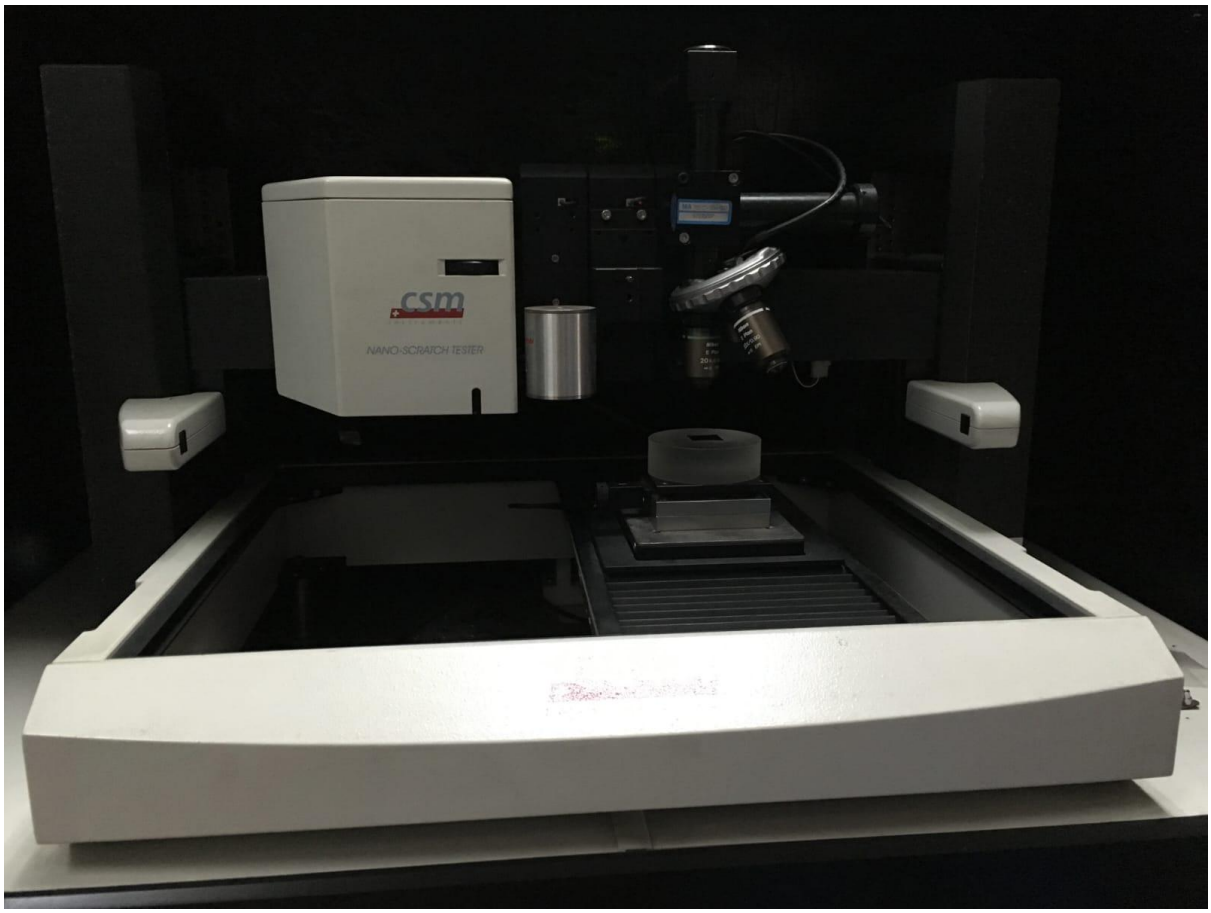

Fig.2.11 Pictorial representation of Continuous Stiffness Measurement (CSM) Nano Indenter (NHTX S/N: 55-0019)

The nano-hardness measurements were conducted using a Continuous Stiffness Measurement (CSM) Nano Indenter (NHTX S/N: 55-0019) [**Fig. 2 .11**], which is highly precise for evaluating the nano-scale hardness and elastic modulus of materials. The equipment's setup involved an approach speed of 3000 nm/min with the D_z sensor set in a fine range, and the Delta Slope Contact at 80% to accurately detect the initial contact. The indenter's position was configured at X = 101.20 mm and Y = 88.65 mm. The measurement settings included an acquisition rate of 10.0 Hz, a linear loading method with a maximum load (F_m) of 10.00 mN, loading and unloading rates of 20.00 mN/min, and a 2.0-second pause at peak load. During testing, the glass samples were first polished to ensure smoothness and mounted onto the indenter stage, followed by the indenter approaching the sample surface until contact was detected. The load was applied linearly until reaching the maximum, where it was held for 2.0 seconds before unloading began, and this load-displacement data was analyzed using the Oliver-Pharr method

to determine hardness [23]. The results are calculated with the help of CSM Indentation 3.71 software. All the values of nanohardness are directly computed by the software and converted to Hv [1Hv = 0.009807Gpa], as Hv or Vickers hardness number is a well-accepted unit for hardness in the micro and nanohardness community [25].

2.7.3. Elastic Modulus Study

The Oliver-Pharr method encompasses a series of critical computations: the contact stiffness (*s*) is calculated by determining the slope of the unloading curve at the point of maximum displacement (h_m), where it is expressed as [22-24]:

$$s = \frac{d_P}{d_h} \tag{2.17}$$

Here, P represents the applied load, and *h* is the displacement (or indentation depth).

The contact depth (h_c) is calculated using the equation [22-24]:

$$h_C = h_m - \epsilon \frac{F_m}{s} \tag{2.18}$$

where ϵ (geometrical constant) is 0.75 for a Berkovich indenter. The projected contact area (A_p) is estimated from [22-24]:

$$A_p = 24.5h_c^2 \tag{2.19}$$

The nano-hardness (*H*) is then calculated by [22-24]:

$$H = \frac{Fm}{Ap} \tag{2.20}$$

Additionally, the reduced modulus (E_r) was derived using [22-24]:

$$E_r = \frac{1}{2}\frac{s}{\sqrt{Ap}} \tag{2.21}$$

The actual elastic modulus (*E*) was obtained by incorporating the indenter's properties using the relationship [22-24]:

$$\frac{1}{E_r} = \frac{1-v^2}{E} + \frac{1-v_i^2}{E_i} \tag{2.22}$$

In the given expression, (v) represents the Poisson's ratio of the sample, whereas (E_i) and (v_i) denote the modulus and Poisson's ratio of the indenter(commonly E_i = 1141 GPa, v_i = 0.07 for diamond).

Generally, the process employing the CSM Nano Indenter and Oliver-Pharr method of analysis gives a complete and accurate value of the nano-hardness of the glass samples under investigation, including all the facets of indentation behaviour and material response [16]. Calibration of the Berkovich indenter was carried out by indentation against fused silica, where the stiffness of the indenter can be measured against the fused silica and the stiffness values for different displacements are depicted in **Table 2.1,** which adheres to the known value from one of the pioneer literatures in this domain [23]

Table 2.1 Stiffness values against various displacement procured while calibrating the prob (Berkovich indenter)

Displacement (nm)	**0**	**500**	**1000**	**1500**	**2000**	**2500**
Stiffness (mN/nm)	0	137.0	287.0	443.0	558.0	676.0

Fracture toughness (K_{IC}) was assessed through indentation-induced cracking. Crack lengths were measured using an optical microscope (50X magnification) integrated into the microhardness tester. The Anstis equation was employed to calculate K_{IC}, incorporating the measured hardness and modulus values [30]:

$$K_{IC} = \propto \left(\frac{E}{H}\right)^{\frac{1}{2}} \left(\frac{P}{c^{\frac{3}{2}}}\right) \quad (2.23)$$

The classical theory of brittle fracture put forward by Griffith further refined by Irwin (1957) is used to determine the strain energy released as [31]:

$$U_r = \frac{K_{IC}^2}{E} \quad (2.24)$$

In this **Eq. (2.24)**, K_{IC} is fracture toughness, and E is elastic modulus.

2.7.4. Elastic Property Evaluation Using Ultrasonic Pulse-Echo Technique

The elasticity of glass and glass-based products provides crucial knowledge and information towards structural stiffness, force of bonding and mechanical stability in a diverse range of stress parameters. The elastic characteristics of the prepared samples in the present investigation were systematically conducted at ambient conditions through the ultrasonic pulse-echo technique which is a popular and non-destructive technique used in determining

the mechanical moduli of solids.

This procedure was carried out with the help of the digital ultrasonic flaw detector that can work in the pulse-echo regime and allows one to measure not only longitudinal wave velocity (v_L) but also transverse/shear wave (v_T) velocity. Piezoelectric transducers, which have a resonance at a frequency of 5 MHz were used to create and receive the ultrasonic pulses. Ultrasonic transducers were coupled acoustically to the sample surfaces using an appropriate coupling medium (usually silicone grease or glycerin), to allow efficient transmission of ultrasonic waves, and to keep signal loss to a minimum.

With the flaw detector, the time-of-flight (TOF) of the ultrasonic pulses, which are reflected off the other side of the sample, is measured. Normal velocities were obtained using the basic relation in which the known thickness (d) of each of the samples was used instead of the known depth [26].

$$v = \frac{2d}{t} \tag{2.25}$$

where v is the velocity of the respective wave, d is the sample thickness, and t is the measured transit time of the ultrasonic pulse.

The velocities that arose experimentally and the measured bulk density (ρ) of the glass samples (measured through Archimedes' principle) were applied to calculate the following elastic moduli through standard mathematical formulas [27,28]:

1. Longitudinal Modulus (L):

$$L = \rho V_l^2 \tag{2.26}$$

2. Shear modulus (S):

$$S = \rho V_T^2 \tag{2.27}$$

3. Bulk modulus (K):

$$K = L - \frac{4}{3}S \tag{2.28}$$

4. Young's modulus (Y):

$$Y = 2S(1+\sigma) \tag{2.29}$$

5. Poisson's ratio (σ):

$$\sigma = \left(L - 2S\right)2(L - S)^{-1} \tag{2.30}$$

The parameters indicate the resistance of the material to deformation under longitudinal, volumetric and shear stresses and as a set provide a quantitative measure of the bonding properties and network-stiffness of the material of the glass matrix.

The non-destructive, high-precision character of the methodology is also a major benefit in the case of amorphous systems (glasses and glass ceramics) since it can test the mechanical integrity of such materials without creating microstructural damage. Moreover, the large sensitivity of ultrasonic wave velocities to atomic level variations can make this method very useful to investigate minute structural changes such as caused by compositional difference, nanocrystals incorporation, or temperature treatment in glass nanocomposites.

2.8. Thermal Property Measurement

Thermal analysis is especially critical in interpreting the structural relaxation, phase stability and the crystallisation behaviour of the glass and glass-ceramic materials. Differential Scanning Calorimetry (DSC) is particularly powerful, sensitive and efficient in the study of the critical thermal transitions, which include the glass transition temperature (T_g), onset crystallisation temperature (T_c) and the peak crystallization temperature (T_p) [28]. Such a transition can be interpreted as a transition to molecular mobility in the amorphous host and is of direct relevance to comprehending the thermal stability and processing window of the glass.

The crystallization temperature (Tc) is recorded as an exothermic peak subsequent to the glass transition in DSC curve, designating the beginning of structural rearrangement and crystal nucleation. The max crystallization temp (T_p), the highest temperature that the rate of crystallization attains, is defined by the point of this signal. The location, the stiffness and the structure of this maximum give much information about the kinetics and thermodynamics of crystallization. These characteristic temperatures, these T_g, T_c, T_p, will offer a complete thermal signature of the glass system. Their values are useful in streamlining thermal therapy (including controlled heat therapy to effect glass-ceramic formation implicitly), in the assessment of process safety and in terms of compositional restraint on the thermal behaviour.

Moreover, thermal stability was determined and measured by DSC data, which is normally measured by the thermal stability factor ($\Delta T = T_c - T_g$), where Tc is the crystallization temperature (T_c)and T_g is the glass transition temperature [29]. The higher the ΔT, the higher the resistance of the glass to spontaneous crystallization, a desirable attribute in cases where there is a need to have a high thermal resistant glass or a glass that can undergo a controlled crystallization in order to develop glass-ceramics. For my research, the thermal measurements were carried out using a NETZSCH DSC 214 instrument (**Fig.2.12**), which offers a temperature precision of ±0.1 °C and a heating rate accuracy of ±0.1 °C/min. Each sample was analyzed at least twice to ensure the reproducibility of the results.

Fig.2.12 NETZSCH DSC 214 instrument

2.9. Summary

In conclusion, this chapter has discussed the detailed experimental methods used to characterize the structural, optical, electrical, dielectric, mechanical and thermal properties of the synthesized glass nanocomposites. All the techniques exhibit critical insight into various

aspects of the behavior of the materials and ultimately help in a better understanding of the composition-structure-property correlations.

The analysis that takes place through structure analyses can provide a view into the amorphous or partially crystalline character of the samples, which is necessary for the stability and network connection of the glass matrices. Concurrently, the thermal tests, including DSC, allow recognizing important points of transition and thermal stability of the systems. Mechanical parameters such as hardness and elastic moduli are a good indication of structural compactness and integrity, whereas electrical and dielectric studies further confirm the compatibility of the glass systems towards potential electronic or energy storage uses.

Finally, this combined experiment-fitting gives the opportunity to accurately chart the role that nano-crystallinity, compositional changes and internal disorder play in affecting the physics of the glasses. This all-encompassing practice provides a firm basis for the selection and optimization of the glass nanocomposites in the envisaged high-technology applications.

2.10. References

1. Brow, R. K., Click, C. A., & Alam, T. M. (2000). Modifier coordination and phosphate glass networks. Journal of Non-Crystalline Solids, 274(1–3), 9–16. https://doi.org/10.1016/S0022-3093(00)00178-2
2. Xia, Y., Calahoo, C., Poletto Rodrigues, B., Griebenow, K., Graewe, L., & Wondraczek, L. (2022). Structure and properties of cerium phosphate and silicophosphate glasses. Journal of the American Ceramic Society, 106(1), 1–14. https://doi.org/10.1111/jace.18936
3. Biswas, D., Das, A. S., Mondal, R., Banerjee, A., Deb, D., Dutta, A., Bhattacharya, S., Kabi, S., & Singh, L. S. (2020). Study of microstructure and electrical conduction mechanisms of quaternary semiconducting glassy systems: Effect of mixed modifiers. Journal of Non-Crystalline Solids, 542, 120104. https://doi.org/10.1016/j.jnoncrysol.2020.120104
4. Ihyadn, A. (2022). Structural, dielectric, and energy storage properties of $BaO–Na_2O–Nb_2O_5–P_2O_5$ glass-ceramics. European Journal of Glass Science and Technology Part B: Physics and Chemistry of Glasses, 63(2), 33–42. https://doi.org/10.13036/17533562.63.2.20
5. Stoch, P., Stoch, A., Ciecinska, M., Krakowiak, I., & Sitarz, M. (2016). Structure of phosphate and iron-phosphate glasses by DFT calculations and FTIR/Raman spectroscopy. Journal of Non-Crystalline Solids, 450, 48–60. https://doi.org/10.1016/j.jnoncrysol.2016.07.027
6. Alsaif, N., Alfryyan, N., Al-Ghamdi, H., Rammah, Y., Mahdy, E., Abo-Mosallam, H. A., & Talaat, S. (2025). Impact of Sm ions on the structure, physical, FTIR spectroscopy and mechano-radiation shielding capabilities of high dense $CdO–Bi_2O_3–SiO_2$ glasses. Applied Physics A, 131(2), Article 83. https://doi.org/10.1007/s00339-025-08385-2
7. Mysen, B. O., & Frantz, J. D. (1992). Raman spectroscopy of silicate melts at magmatic temperatures: $Na_2O–SiO_2$, $K_2O–SiO_2$ and $Li_2O–SiO_2$ binary compositions in the temperature range 25–1475 °C. Chemical Geology, 96(3–4), 321–332. https://doi.org/10.1016/0009-2541(92)90062-A
8. Azlam, M. N., Halimah, M. K., Shafinas, S. Z., & Daud, W. M. (2013). Effect of erbium nanoparticles on optical properties of zinc borotellurite glass system. Journal of Nanomaterials, 2013, 1–8. https://doi.org/10.1155/2013/940917
9. Davis, E. A., & Mott, N. F. (1970). Conduction in non-crystalline systems V. Conductivity, optical absorption and photoconductivity in amorphous semiconductors.

Philosophical Magazine, 22(179), 903–922. https://doi.org/10.1080/14786437008221061

10. Anigrahawati, P., Sahar, M. R., & Ghosal, S. K. (2015). Influence of Fe_3O_4 nanoparticles on structural, optical and magnetic properties of erbium doped zinc phosphate glass. Materials Chemistry and Physics, 155, 155–161. https://doi.org/10.1016/j.matchemphys.2015.02.014
11. Ahmadi, F., Hussin, R., & Ghoshal, S. K. (2017). Structural and physical properties of Sm^{3+} doped magnesium zinc sulfophosphate glass. Bulletin of Materials Science, 40(6), 1097–1104. https://doi.org/10.1007/s12034-017-1462-5
12. Urbach, F. (1953). The long-wavelength edge of photographic sensitivity and of the electronic absorption of solids. Physical Review, 92(5), 1324. https://doi.org/10.1103/PhysRev.92.1324
13. Lopez-Iscoa, P., Petit, L., Massera, J., Janner, D., Boetti, N., Pugliese, D., Fiorilli, S., Novara, C., & Milanese, D. (2017). Effect of the addition of Al_2O_3, TiO_2 and ZnO on the thermal, structural and luminescence properties of Er^{3+}-doped phosphate glasses. Journal of Non-Crystalline Solids, 460, 161–168. https://doi.org/10.1016/j.jnoncrysol.2017.01.030
14. Chou, C.-C., Chang, C.-Y., Chen, G.-Y., Liao, W.-J., Feng, K.-C., & Tsao, C.-Y. (2018). Control of silver diffusion in low-temperature co-fired diopside glass-ceramic microwave dielectrics. Materials, 11(1), 55. https://doi.org/10.3390/ma11010055
15. Jlassi, I., Sdiri, N., & Elhouichet, H. (2017). Electrical conductivity and dielectric properties of MgO-doped lithium phosphate glasses. Journal of Non-Crystalline Solids, 466–467, 45–51. https://doi.org/10.1016/j.jnoncrysol.2017.03.042
16. Choudhary, B. (2017). Electrical and dielectric behavior of zinc phosphate glasses. Materials Today: Proceedings, 4(4), 5706–5714. https://doi.org/10.1016/j.matpr.2017.06.034
17. Marzouk, M. A., ElBatal, F. H., & Abdelghany, A. M. (2013). Ultraviolet and infrared absorption spectra of Cr_2O_3 doped-sodium metaphosphate, lead metaphosphate and zinc metaphosphate glasses and effects of gamma irradiation: A comparative study. Spectrochimica Acta Part A: Molecular and Biomolecular Spectroscopy, 114, 658–667. https://doi.org/10.1016/j.saa.2013.05.093
18. Ningthemcha, R. K. N., Biswas, D., Singh, Y. B., Sarkar, D., Mondal, R., Mandal, D., & Singh, L. S. (2020). Temperature and frequency dependent electrical conductivity and dielectric relaxation of mixed transition metal doped bismuth-phosphate

semiconducting glassy systems. Materials Chemistry and Physics, 249, 123207. https://doi.org/10.1016/j.matchemphys.2020.123207

19. Bergo, P., Pontuschka, W., & Prison, J. M. (2008). Dielectric properties and physical features of phosphate glasses containing iron oxide. Materials Chemistry and Physics, 108(1), 142–146. https://doi.org/10.1016/j.matchemphys.2007.09.021
20. Battisha, I., Ismail, M., Ahmed, H., Żur, L., Chiasera, A., Ferrari, M., Lukowiak, A., Ashery, A., & Salem, M. (2020). Optical, structure and dielectric properties of Er^{3+} ions doped Al–Na–K–Ba phosphate glasses. Egyptian Journal of Chemistry, 63(3), 1–10. https://doi.org/10.21608/ejchem.2020.27059.2578
21. Šantić, B., Moguš-Milanković, A., & Day, D. E. (2001). The DC electrical conductivity of iron phosphate glasses. Journal of Non-Crystalline Solids, 296(1–2), 65–73. https://doi.org/10.1016/S0022-3093(01)00873-0
22. Yamane, M., & Mackenzie, J. D. (1974). Vicker's hardness of glass. Journal of Non-Crystalline Solids, 15(2), 153–164. https://doi.org/10.1016/0022-3093(74)90044-1
23. Kim, J. J., Cho, Y., Suresh, S. A., & Argon, S. (2002). Nanocrystallization during nanoindentation of a bulk amorphous metal alloy at room temperature. Science, 295(5555), 654–657. https://doi.org/10.1126/science.1067453
24. Oliver, W. C., & Pharr, G. M. (2004). Measurement of hardness and elastic modulus by instrumented indentation: Advances in understanding and refinements to methodology. Journal of Materials Research, 19(1), 3–20. https://doi.org/10.1557/jmr.2004.19.1.3
25. Vaidyanathan, R., Dao, M., Ravichandran, G., & Suresh, S. (2001). Study of mechanical deformation in bulk metallic glass through instrumented indentation. Acta Materialia, 49(18), 3781–3789. https://doi.org/10.1016/S1359-6454(01)00263-4
26. Guo, Y., Li, J., Zhang, Y., Feng, S., & Sun, H. (2021). High-entropy R_2O_3–Y_2O_3–TiO_2–ZrO_2–Al_2O_3 glasses with ultrahigh hardness, Young's modulus, and indentation fracture toughness. iScience, 24(7), 102735. https://doi.org/10.1016/j.isci.2021.102735
27. Saddeek, Y. B., Aly, K. A., & Bashier, S. A. (2010). Optical study of lead borosilicate glasses. Physica B: Condensed Matter, 405(11), 2407–2412. https://doi.org/10.1016/j.physb.2010.02.055
28. Saddeek, Y. B., Issa, S. A. M., Alharbi, T., Aly, K., Ahmad, M., & Tekin, H. O. (2020). Mechanical and nuclear shielding properties of sodium cadmium borate glasses: Impact of cadmium oxide additive. Ceramics International, 46(2), 2661–2669. https://doi.org/10.1016/j.ceramint.2019.09.254

29. Ibrahim, S., Khattari, Z., & Mahdy, E. (2025). Impact of In_2O_3 content on the structural, thermal, and mechanical hallmarks of Na_2O–BaO–ZnO–Fe_2O_3–P_2O_5 glass systems. Journal of Materials Science: Materials in Electronics, 36(1), 1–12. https://doi.org/10.1007/s10854-025-14680-8
30. Anstis, G.R., Chantikul, P., Lawn, B.R. and Marshall, D.B. (1981) A Critical Evaluation of Indentation Techniques for Measuring Fracture Toughness: I, Direct Crack Measurements. Journal of the American Ceramic Society, 64, 533-538. https://doi.org/10.1111/j.1151-2916.1981.tb10320.x
31. Qiao, Y., Zhang, Z.-X., & Zhang, S. (2023). An Experimental Study of the Relation between Mode I Fracture Toughness, KIc, and Critical Energy Release Rate, GIc. Materials, 16(3), 1056. https://doi.org/10.3390/ma16031056

Chapter 3

Analysis of Physical and Structural Properties of Glass Nanocomposite Systems.

3.1. Introduction

Physical and structural characteristics of glass and glass nanocomposites create a fundamental stepping stone in characterizing their feasibility in optical, electrical, thermal and energy related realms. The thorough knowledge of these properties is of particular concern to the multicomponent glass systems because the addition of the network formers and modifiers implies significant changes to the glass network, which, in turn, directly affect the performance characteristics. It was the responsibility of this chapter to engage in the systematic exploration of the most important physical and structural parameters of three systems of quaternary glasses mixed with Transition metal oxides like V_2O_5 and Fe_2O_3 and Heavy metal oxides like Bi_2O_3 and BaO: V_2O_5–Na_2O–ZnO–P_2O_5 (VNZP), Bi_2O_3 -BaO -V_2O_5-P_2O_5 (BBVP), and Bi_2O_3 - Fe_2O_3 -V_2O_5 -P_2O_5 .Density (ρ) and molar volume (V_M) are some of the most insightful physical parameters, which essentially provide molecular ways of packing on the atomic scale and compactness of the network in glasses. These parameters present an indirect but significant insight into the amount of connectivity and openness of the glass architecture. The replacement or inclusion of individual oxides like Bi_2O_3, BaO, ZnO, and Fe_2O_3 does not just bring transformations in the molar mass as well as coordination number, but also instils serious moving around and rearrangements in the phosphate structure and the density of the general glass matrix.Also, the oxygen packing density (OPD), which is one of the measures of the number of oxygen atoms in the glass per unit volume, can provide great insight about the rigidity of the glass network and the degree of polymerization. The increase in OPD is then normally related to a less depolymerized, more tightly bound structure with direct proportionality of increased mechanical integrity and thermal stability. It can be further analyzed how various modifying oxides affect OPD, which can explain the structural role of each component and how it affects glass stability.

The amorphous state of the prepared glass specimens is ascertained by x-ray diffraction (XRD) analysis in order to identify the presence of any possible nanocrystalline structures within the composite systems which is likely due to its low crystallinity. The XRD is used as a key instrument to determine whether a long-range order exists, as well as the presence of a phase separation and/or crystalline inclusions, which may be introduced by differences in thermal treatment or through any of its compositional design. Lack or presence of sharp diffraction peaks is useful in grouping the materials under fully amorphous, partially crystalline or nanostructured categories thereby forming a key structure property relationship.

In addition to these physical parameters some selective vibrational spectroscopic tractions are used together with Fourier-transform infrared (FTIR) spectroscopy and Raman spectroscopy to examine short-range structure environment especially on individual compositions. These methods are particularly suited to determine the type of structures units of phosphate (e.g. Q_n species) metal-oxygen bonding and the extent of polymerization that exists within the glass network. Vibration of fundamental phosphate groups ($PO4^{3-}$), V-O, Bi-O, and other metal oxygen bonds is shown by FTIR spectra, and Raman spectrum of deeper explanation about the property of network symmetry and modes of bonding are done by polarizable vibration modes.

It is noted that FTIR and Raman Analyses were not standardized applicable to all compositions and they were subjectively applied in representative samples of each composition in each type of glass to bring out specific structural changes and to maximize experimental relevance.

It is expected that the analysis of the data retrieved using these complementary methods of investigation (molar calculations, density-based analysis, XRD, FTIR, and Raman spectroscopy) will lead to the creation of a holistic picture of the physical construction as well as network arrangement of the prepared glass nanocomposites this chapter seeks to develop. The integrated design is crucial in customising the properties of materials for advanced functional applications.

3.2. Quaternary V_2O_5–Na_2O–ZnO–P_2O_5 glass system

3.2.1. Physical parameters analysis

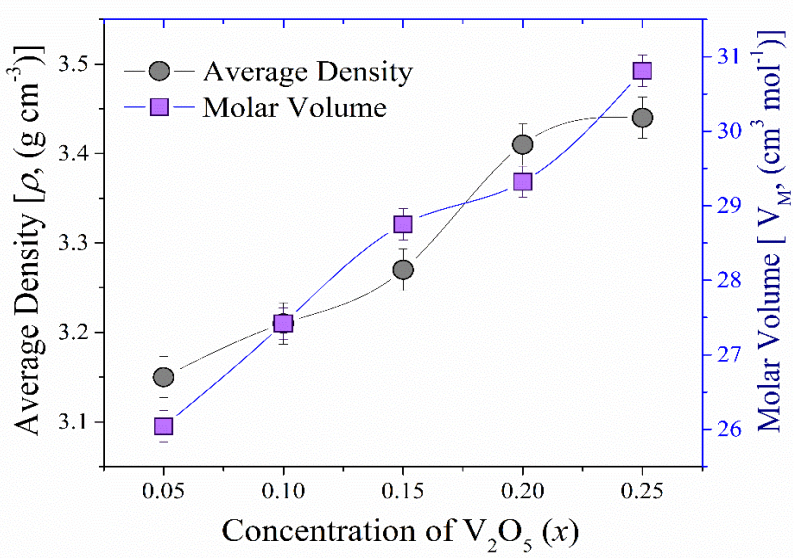

Fig. 3.1 Compositional dependence of average density (ρ) and molar volume (V_m) for $x$$V_2O_5$–(0.40-$x$)$Na_2O$–0.35ZnO–0.25$P_2O_5$ glassy samples

Fig. 3.1 illustrates the dependence of estimated density (ρ) and molar volume (V_M) of the glass samples on V_2O_5 concentration (x), where both parameters are shown increasing with the increasing content of V_2O_5The compactness of the glass sample is reduced, as the ρ and V_M values increase, by substituting the alkali oxide Na_2O, with its lower molar mass of 61.97 g/mol, with the transition metal oxide V_2O_5, which possesses a higher molar mass of 181.88 g/mol.

The increment in V_M implies that these glass composites have a disordered structure owing to the enlargement in the free volume. The increment of V_M can be attributed to modifications in structure as a result of the increased interatomic spacing, which reduces the stretching force constant of the bonds within the glassy network, resulting in less compaction of the glass sample. The increase in ρ and V_M can be described by the concept of non-bridging oxygen ions (NBOs) within the glassy network, which reveals changes in volume concentration [30]. The addition of V_2O_5 causes an increment in NBOs, revealing that VO_4 (NBOs) grow faster than V_2O_5 (BOs) and randomizes the glass structure, and, therefore, the glass network becomes more open. For the present system, the modifier becomes less abundant than the glass former and plays a secondary role in depolymerizing the glass network, i.e., the formation of non-bridging oxygens (NBOs) by replacing a covalent bond with an ionic bond [1].

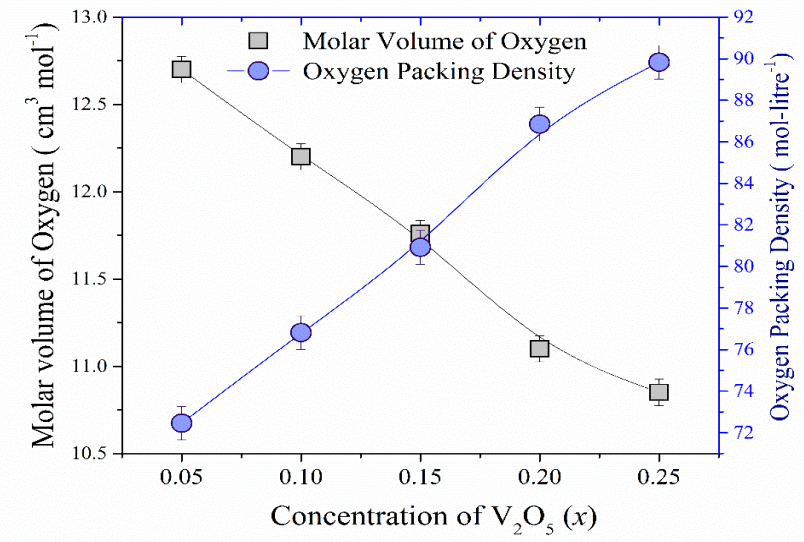

Fig. 3.2 Compositional dependence of oxygen molar volume (V_o) and oxygen packing density (OPD) for xV_2O_5–(0.40-x) Na_2O–0.35ZnO–0.25P_2O_5 glass nanocomposites

Finally, to understand more deeply the compactness of the glass network structure, the oxygen molar volume (V_O) and oxygen packing density (OPD) were determined according to the value of corresponding density and molar volume using **Eq. (3.1)** [2].

$$V_O = \frac{V_M}{\sum_i x_i n_i} \quad \text{and} \quad OPD = 1000\, C \left(\frac{\rho}{M}\right) \tag{3.1}$$

The parameter C in **Eq. (3.1)** is the total number of oxygen atoms per formula unit. **Fig.3.2** shows the changes of V_O as well as the OPD when the concentration of V_2O_5 increases (x). Dense packaging of oxygen within the glass framework is observed, where a significant increment in V_O and OPD is observed, corresponding to an increment in V_2O_5 contents. These trends depend on a number of features of composition, such as the oxygen content, the cation coordination environments, the ionic radii, and the molecular weights of the oxides involved. Reduced V_O implies the arrangement of structural units within the glass network and increased OPD, a measure of how tightly the oxide network is packed. The glass structure becomes more tightly packed when more V_2O_5 is incorporated into the glass matrix as OPD increases (**Fig. 3.2**). The decrement in V_O value is associated with an expansion in OPD, confirming the appearance of non–bridging oxygen bonds by replacement of Na_2O with V_2O_5 content, which leads to the formation of VO_4 tetrahedral units by conversion of VO_5 structural units to VO_4 units, responsible for increasing the non–bridging oxygen bonds [2]. The gradual conversion of VO_5 units to VO_4 units enables VO_4 to act as a network-modifying agent and breaks local symmetry, creating coordinated defects in the made glass [2].

The increasing trend of V_M (**Fig. 3.2**) with the incorporation of V_2O_5 predicts that the bond length is increasing consistently. The average vanadium-vanadium ions separation ($<d_{V-V}>$) and the average sodium-sodium ions separation ($<d_{Na-Na}>$) have been calculated to verify the increment in the density values of the glassy structures due to replacing alkali oxide Na_2O with transition metal oxide V_2O_5 [31].To determine the average interatomic separations $<d_{V-V}>$ and $<d_{Na-Na}>$, the molar volumes of vanadium (V_M^V) and sodium (V_M^{Na}) were first calculated using their respective compositional ratios through the following expression [2]:

$$V_M^V = \frac{V_M}{2\,(1 - x_{V-ion})} \quad \text{and} \quad V_M^{Na} = \frac{V_M}{(1 - x_{Na-ion})} \tag{3.2}$$

The average interatomic distances $<d_{V-V}>$ and $<d_{Na-Na}>$ were then computed from the calculated V_M^V and V_M^{Na} values using the following expressions [3].

$$< d_{V-V} > = \left(\frac{V_M{}^V}{N_A} \right)^{1/3} \quad \text{and} \quad < d_{Na-Na} > = \left(\frac{V_M{}^{Na}}{N_A} \right)^{1/3} \tag{3.3}$$

The outcomes of **Eq. (3.2)** and **(3.3)** are depicted in **Table 3.1**. With increasing V_2O_5 concentration (decreasing Na_2O), $<d_{V-V}>$ increases, whereas $<d_{Na-Na}>$ also decreases as expected (because of compositional replacement). As a result, the molar volume (V_M) of glass nanocomposite systems falls with the replacement of alkali metal oxide Na_2O by the transition metal oxide V_2O_5. The expression below shows the effect of the changes in the concentration of the V-ion and the Na-ion on the structural alteration in the glass network [3]:

$$N_{V/Na-ions} = \frac{\text{mol \% of oxide} \times N_A \times \rho}{\text{Molecular weight of composition (M)}} \tag{3.4}$$

The values inter-nuclear separation of V-ions (R_V) and Na-ions (R_{Na}) are derived from the calculated values of $N_{V/Na\ ions}$ as follows [3]:

$$R_{V/Na} = \left(\frac{1}{N_{V/Na-ions}} \right)^{1/3} \tag{3.5}$$

It is observed in **Table 3.2** that $N_{V\text{-}ions}$ value increases, and $N_{Na\text{-}ions}$ value decreases with the incorporation of V_2O_5 (x). Whereas R_V value decreases, and R_{Na} increases with the inclusion of V_2O_5 content (x).

Table 3.1

All corresponding physical parameters of xV_2O_5–(0.40-x) Na_2O–0.35ZnO–0.25P_2O_5 glass nanocomposite systems.

x	$V_M{}^V$ (gm/cm^2) (±1.50)	$V_M{}^{Na}$ (gm/cm^2) (±1.50)	$<d_{V\text{-}V}>$ (Å) (±0.02)	$<d_{Na\text{-}Na}>$ (Å) (±0.02)	$N_{V\text{-}ions}$ ($\times 10^{21}$) (ions/cm^2) (±0.01)	$N_{Na\text{-}ions}$ ($\times 10^{21}$) (ions/cm^2) (±0.01)	R_V (Å) (±0.15)	R_{Na} (Å) (±0.15)	OPD
0.05	14.70	21.49	2.90	3.29	1.07	7.54	9.75	5.09	72.46
0.10	16.26	20.92	3.00	3.26	2.05	6.16	7.86	5.45	76.82
0.15	17.99	20.38	3.10	3.23	2.95	4.92	6.96	5.87	80.92
0.20	19.42	19.41	3.18	3.18	3.87	3.87	6.36	6.36	86.85
0.25	21.70	19.15	3.30	3.16	4.62	2.77	6.02	7.11	89.83

3.2.2. XRD analysis

The X-ray diffraction (XRD) patterns of the as-quenched glass nanocomposites were recorded, as shown in **Fig.3.3**. Each sample displays a diffuse hump at a low diffraction angle

(< 15°) consistent with the predominantly amorphous character and lack of long-range structural order. Evidently, the sample at x = 0.05 is fully amorphous, but as the concentrations of V_2O_5 rise, individual diffraction peaks appear on top of the amorphous curve. These peaks indicate that nanocrystalline phases can be developed in the glass. All the crystalline phases identified included $NaV_{0.66}P_{0.34}O_3$ [4], $Na_2V_2O_6$ [5], $NaPO_3$ [6], $Na_2(P_2VO_8)$ [7], $ZnNa\ (PO_3)_3$ [8], and $Na_2(VPO_6)$ [9] nanocrystallites over the amorphous structure have been identified from the available authentic literature data and tabulated in **Table 3.2**.

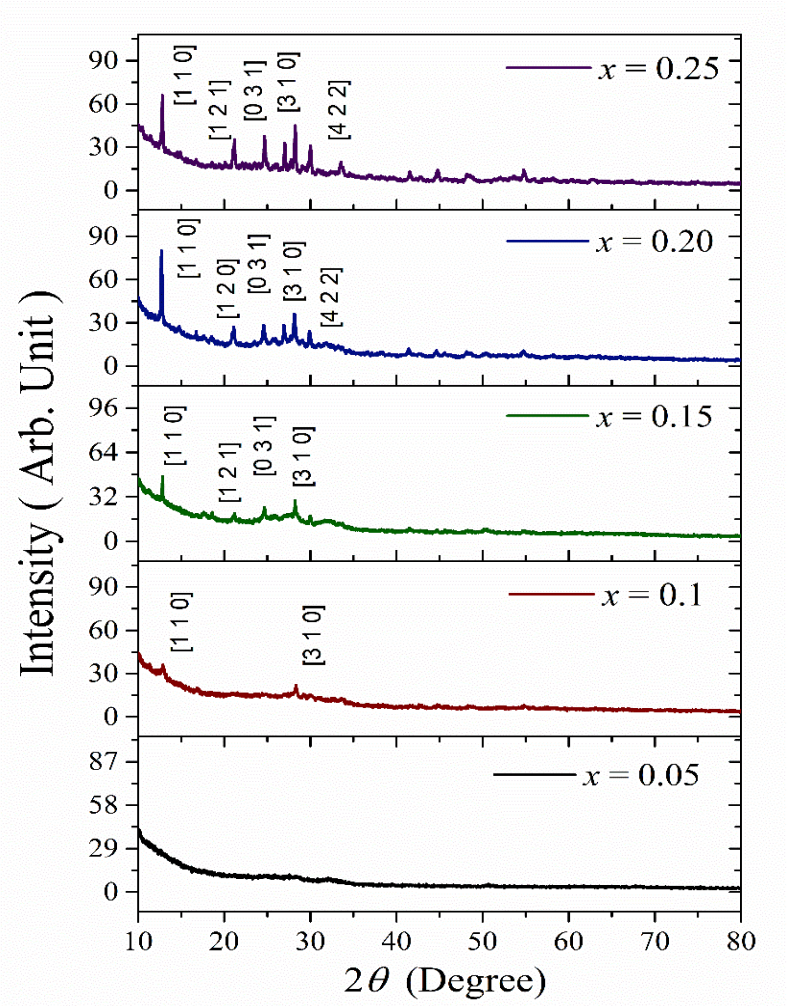

Fig. 3.3. X-ray diffraction (XRD) patterns for all nanocomposite samples.

The nanocrystallite size (d_C) of each identified phase was determined through the Scherrer equation (**Eq. 3.6**) based on the Full width at half maximum (FWHM) of the corresponding diffraction peaks as presented in **Fig.3.3**. The resulting values explaining the crystallite size can be found in **Table 3.2**.

Each nanocrystallite size (d_C) is calculated using the renowned Scherrer formula (**Eq. (3)**) by applying the full width at half maxima (FWHM) value of the corresponding diffraction peak (**Fig. 3.6**), and the d_C values are summarized in **Table 3.2** [10].

$$d_C = \frac{0.89\ \lambda}{\beta_{correct}\ \cos\theta} \tag{3.6}$$

In the above, θ is the Bragg angle, λ is the wavelength of the incident X-rays (0.15418 nm), and $\beta_{correct}$ is the corrected full width at half maxima (FWHM) of each diffraction peak. The mean particle size of the nanocrystallite grows steadily as the content of V_2O_5 rises, as has been outlined in **Table 3.2**.

Table 3.2 The values of Bragg's diffraction angle (2θ), the identified nanocrystalline phases, nanocrystallite sizes (d_C) calculated using the Scherrer equation, and the Miller indices(*h-k-l)* of all the nanocomposite samples.

x	2θ	Phase	Nanocrystallite size (d_C) (nm) (± 0.2)	*h*	*k*	*l*	Percent Crystallinity
0.10	12.9	$NaV_{0.66}P_{0.34}O_3$	23.55	1	1	0	0.24
	28.29	$Na_2V_2O_6$	32.10	3	1	0	0.15
			27.83 (avg.)				0.39
0.15	12.9	$NaV_{0.66}P_{0.34}O_3$	38.28	1	1	0	0.23
	21.21	$NaPO_3$	33.29	1	2	1	0.05
	24.62	$Na_2(P_2VO_8)$	49.83	0	3	1	0.07
	28.16	$Na_2V_2O_6$	27.75	3	1	0	0.12
	30	$ZnNa(PO_3)_3$	29.87	4	2	2	0.05
			35.81 (avg.)				0.52
0.20	12.9	$NaV_{0.66}P_{0.34}O_3$	59.04	1	1	0	0.64
	20.78	$Na_2(VPO_6)$	23.83	1	2	0	0.40
	24.62	$Na_2(P_2VO_8)$	31.65	0	3	1	0.40
	26.92	$Na_2(P_2VO_8)$	41.98	2	2	0	0.20
	28.16	Na_2V2O_6	36.94	3	1	0	0.42
	30	$ZnNa(PO_3)_3$	45.47	4	2	2	0.18
			39.82 (avg.)				2.25
0.25	12.9	$NaV_{0.66}P_{0.34}O_3$	28.66	1	1	0	0.42
	21.21	$NaPO_3$	42.65	1	2	1	0.95
	24.62	$Na_2(P_2VO_8)$	73.46	0	3	1	0.37
	27.16	$Na_2(VPO_6)$	36.79	1	3	1	0.11
	28.16	$Na_2V_2O_6$	30.40	3	1	0	0.88
	30	$ZnNa(PO_3)_3$	37.07	4	2	2	0.05
	33.64	$ZnNa(PO_3)_3$	40.71	5	2	1	0.06
			41.39 (avg.)				2.83

These observations are an indicator that V_2O_5 catalyses the facilitation of the emergence of nanocrystalline phases in the glassy structure. The degree of crystallinity was determined by [10]:

$$\% \text{ crystallinity} = \frac{Area\ under\ the\ crystalline\ peak}{Total\ area} \times 100 \qquad (3.7)$$

through the ratio of the crystalline peak area to the total diffraction area. Since higher V_2O_5 content involves decreased amorphousness, as shown in **Table 3.2**, more crystalline phases have appeared. It is worth noting that even with the rapid quenching procedure, partial crystallization can be seen in every sample which has $x \geq 0.10$.

3.2.3. FTIR spectra

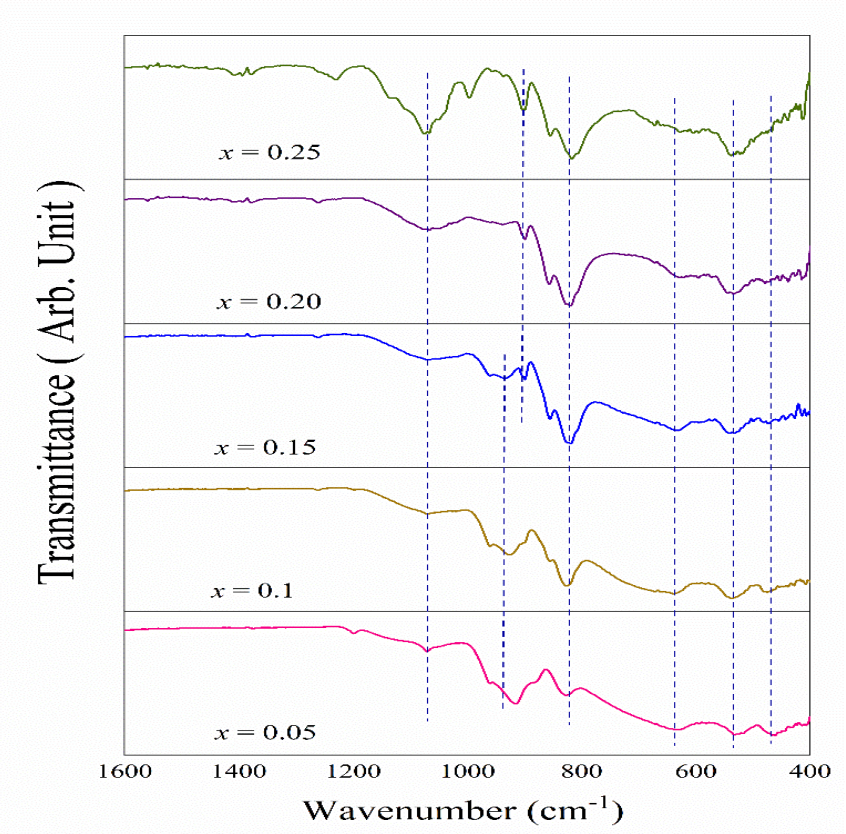

Fig. 3.4. FTIR spectra of all the nanocomposite samples.

The as-quenched glass composites FTIR spectra have been presented in **Fig. 3.4**, between 400 cm^{-1} to 1600 cm^{-1}, to discuss important vibrational modes (interpretation) related to different units within the structure. A broad absorption band near 1230 cm^{-1} is attributed to the asymmetric stretching vibrations of $(PO_2)^-$ groups and O–P–O bond coordination in Q^2 type phosphate tetrahedra, which contain two non-bridging oxygens bonded to phosphorus atoms.

This was a confirmation of the existence of non-bridging oxygen (NBO), where arrangement has a vital role in ionic conduction throughout the glass matrix [11,12]. A large band around 1080 cm^{-1} is associated with the terminal PO_3 groups, which shows that there was chain termination in the phosphate net. Also, the band at ~1000 cm^{-1} is interpreted as $P–O^-$ with depolymerized phosphate structures being found commonly with this band.

The 920–880 cm^{-1} region shows the characteristics of asymmetric stretching of P–O–P bridges, indicating that the molecules have bridging oxygen atoms that add to the connectivity of the network. The advancing absorption at caution 820 cm^{-1} is stronger with increasing abundance of V_2O_5, due to the extension to the vanadate units (VO_2 or VO_3), taking into consideration the insertion of vanadium into the phosphate structure. A clear peak at ca 640 cm^{-1} is related to the stretching of polymerized vanadate species, probably $(VO_3)_n$ chain entities.

The allocation of zinc oxide in the glass network structure is reflected by the existence of assemblies of P–O–Zn vibrations in the range of 510 to 540 cm^{-1}, indicating the formation of ZnO_4 structures through the P–O–Zn bonds. In addition, the band at a lower frequency of 430-440 cm^{-1} is explained by the band of the stretching exercise of ZnO bonds in tetrahedral bonding, that is substantiates the structural role of Zn^{2+} to the structure of the glass [13,14].

3.2.4. Raman Spectra

The Raman spectra of the phosphate-containing glasses display a few features of typical vibrational modes that are influenced by the structural modification of the glass network with the increasing amount of V_2O_5. Another band around 348 cm^{-1} that was seen in samples with values of x between 0.10-0.25 is related to the bending of tetrahedra of phosphate (PO_4). The formation of this band is linked with the depolymerization of longer chains of phosphate, and it implies the distribution of a structural rearrangement by the addition of a vanadium species into the viscous glass [15].

A strong band at 513 cm^{-1} is always seen in all the samples, and this is attributed to the vanadium cation vibrational motions and formation of vanadium and oxygen chains. This is an indication of the formation of a sub-network of vanadate in the phosphate glass. In all the compositions, another important band has been observed at 648 cm^{-1}, which is assigned to

symmetric stretching vibrations of Q_0 orthophosphate units. The occurrence of such species of Q_0 supports the greater depolymerization in the network and the generation of free phosphate groups.In the x = 0.05 composition, an isolated band is also picked up at 743 $cm^{-1,}$ which has been attributed to symmetric P–O–P stretch over bridging oxygen atoms (Q_2 units). With an increase in V_2O_5 content, the intensity of the band decreases it would suggest that there is a gradual loss of P–O–P linkages and the bridging to non-bridging oxygens. There is a band at 920 cm^{-1}, which is observed in compositions up to x = 0.15, assigned to the symmetric stretching of V–O–V and O–V–O bonds. The trend toward an even stronger peak as the vanadium content rises is an indication of the formation of vanadate groups and an increasing connection of the vanadium network [16].

In the x = 0.05 glass, a Raman band at 942 cm^{-1} is ascribed to symmetric P–O stretching vibrations in PO_4 units. Over the range of growing V_2O_5 content, there also occurs a new band (around 955 cm^{-1}) due to the stretch vibration of terminal V–O. Such a shift is associated with the substitution of phosphate structural units by vanadate and the growing concentration of Vanadium-Oxygen bonds.Other weak Raman bands at 166 cm^{-1}, 243 cm^{-1} and 270 cm^{-1} are skeletal vibrations of VPO_5 phases. Particularly, the 166 and the 243 cm^{-1} bands represent the β-phase, and the 270 cm^{-1} band represents the α-phase of VPO_5. These bands indicate that there are very small crystalline domains inside the glass matrix. The band at 554 cm^{-1}, which is associated with P–O bonds being vibrated in the α-phase, and the 897 cm^{-1} band, a symmetric P–O stretching in the β-phase, are further assurances of the VPO_5-related phases. The presence of those crystalline details in an amorphous background show that the phase separation is not complete or that they form nanocrystalline inclusions at increasing vanadium loading [17].

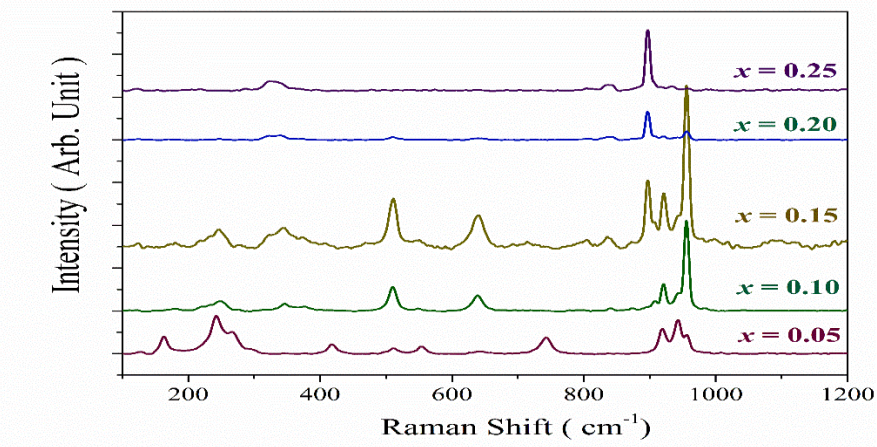

Fig. 3.5. Raman Spectra of all glass samples

3.3. Quaternary Bi_2O_3-BaO-V_2O_5-P_2O_5 glass system

3.3.1. Study of several physical parameters

An elementary physical parameter to evaluate the structural peculiarities of the glass nanocomposites is density (ρ). The density of all the samples of glasses that have been prepared was measured with the help of Archimedes' principle, as it applies the principle of displacement to deliver a trustworthy estimation [18]. In conjunction with this, the calculation of the molar volume (V_M) is performed by use of the measured density and by use of the molecular weight of each composition. **Fig.3.6 (a)** indicates how ρ and V_M change with different compositions, especially including how the replacement of Bi_2O_3 with BaO in the glass system of vanadium-phosphate affects them. It has been noted that an increase in both ρ and V_M of the glass may be a matter of the significant molecular weight of Bi_2O_3 (465.96 g/mol) in comparison to BaO (197.34 g/mol), which ultimately causes overall densification of the glassy matrix.

The parameters used were subsequently used to derive the oxygen molar volume (V_O) and oxygen packing density (OPD) via given relations (**Eq. 3.1**) to give more information on how the glasses are networked. The secondary parameters are important to learn the extent of the tightness of packing the oxygen atoms in the glass network, and also the change in connectivity of the glass upon a change in composition [3].

The plot of the molar volume of oxygen (V_O) and oxygen packing density (OPD) according to **Fig.3.6(b)** is calculated concerning Bi_2O_3 concentration (x). When the content of Bi_2O_3 increases obviously V_O would drop and OPD would increase as a sign of progressive formation of non-bridging oxygen (NBO) sites in the BaO–V_2O_5–P_2O_5 glass structure. Such rearrangement indicates increased compactness and rigidity of networks because of stronger fields and polarizability of Bi^{3+} ions [2].

To measure further the role of Bi_2O_3 substitution on the compactness of glass, the mean interatomic distances between Bi-Bi and Ba-Ba atoms were determined, denoted as $<d_{Bi-Bi}>$ and $<d_{Ba-Ba}>$, respectively. They were obtained based on the approximate molar volumes of bismuth and barium (V_M^{Bi} and V_M^{Ba}) by making use of the well-known models of structure. The differences in these separations will help us understand how the addition of Bi_2O_3 affects the spatial distribution of the cations and assists in the densification of the glassy matrix [3].

$$V_M^{Bi} = \frac{V_M}{2\times(1-x_{Bi-ion})} \quad \text{and} \quad V_M^{Ba} = \frac{V_M}{(1-x_{Ba-ion})} \tag{3.8}$$

The molar fractions of Bi_2O_3 and BaO are signified here by the ions $x_{Bi\text{-}ion}$ and $x_{Ba\text{-}ion}$, respectively. The calculated values of $<d_{Bi\text{-}Bi}>$ and $<d_{Ba\text{-}Ba}>$ from the following equations are tabulated in **Table 3.3** [3].

$$\langle d_{Bi-Bi}\rangle = \left(\frac{V_M^{Bi}}{N_A}\right)^{1/3} \quad \text{and} \quad \langle d_{Ba-Ba}\rangle = \left(\frac{V_M^{Ba}}{N_A}\right)^{1/3} \tag{3.9}$$

Here N_A is Avogadro's number ($N_A = 6.0228 \times 10^{23}$ mol^{-1}). With the use of Bi_2O_3 in place of the BaO in the vanadium-phosphate glass matrix, the value of $<d_{Bi\text{-}Bi}>$ drops, as illustrated in **Table 3.3**.

The gradual increase in density implies that the glass network becomes more compact through the incorporation of Bi_2O_3. Such structural densification can also be considered through assessing the number densities of Bi-ion and Ba-ion ($N_{Bi/Ba\text{-}ions}$), the concentration of these cations expressed per single volume. The calculation of these values is made through the following equations, which provide an understanding of the way of adaptation of different ionic populations to the structure of rearrangement in the phosphate glass matrix [3].

$$N_{Bi/Ba-ions} = \frac{mol\ \%\ of\ oxide \times N_A \times \rho}{Molecular\ weight\ of\ Composition\ (M)} \tag{3.10}$$

The values of inter-nuclear separation of Bi-ions (R_{Bi}) and Ba-ions (R_{Ba}) are independently estimated using a subsequent equation, knowing the value of $N_{Bi/Ba\text{-}ions}$ (**Eq. (3.10)**).

$$R_{Bi/Ba} = \left(\frac{1}{N_{Bi/Ba-ions}}\right)^{\frac{1}{3}} \tag{3.11}$$

With more content of Bi_2O_3 in the glass matrix, the change in Bi-Bi interionic distance (R_{Bi}) is noticeable since the glass has a denser cationic packing. Contrastingly, there is an increasing trend of the Ba-Ba separation (R_{Ba}) that can be seen summarised in **Table 3.3**, to show the differences in the structural roles of the two ions, Bi^{3+} and $Ba^{2+,}$ in the network as against each other.

Table 3.3: Several estimated physical parameters

x	V_M^{Bi} (g/cm^2) (±1.50)	V_M^{Ba} (g/cm^2) (±1.50)	$<d_{Bi\text{-}Bi}>$ (Å) (±0.02)	$<d_{Ba\text{-}Ba}>$ (Å) (±0.02)	$N_{Bi\text{-}ions}$ ($\times 10^{20}$) (ions/cm^2) (±0.01)	$N_{Ba\text{-}ions}$ ($\times 10^{20}$) (ions/cm^2) (±0.01)	R_{Bi} (Å) (±0.12)	R_{Ba} (Å) (±0.15)
0.05	59.04	86.29	12.30	06.43	5.37	37.5	12.30	06.43
0.15	68.44	77.57	08.63	07.28	15.5	25.8	08.63	07.28
0.25	78.18	68.98	07.30	08.65	25.7	15.4	07.30	08.65
0.35	94.03	64.34	06.68	12.66	34.5	4.92	06.61	12.67

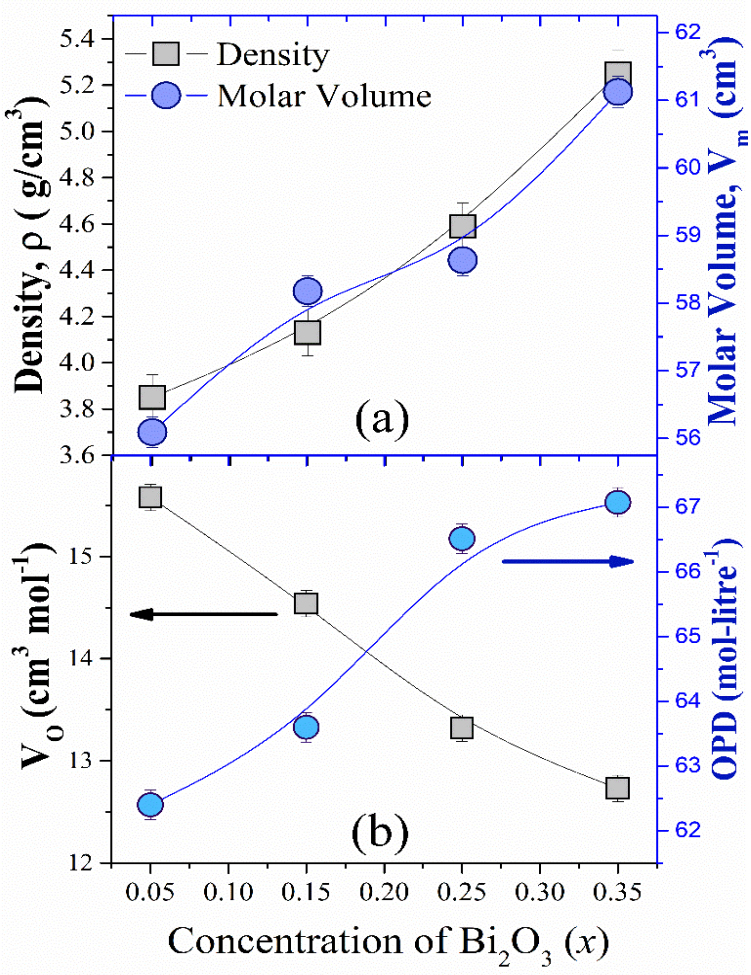

Fig. 3.6. Estimated values of (a) Average values of ρ and V_M, and (b) V_o and OPD against Bi_2O_3 content (x).

3.3.2. Investigation of X-Ray Diffraction spectra

The XRD patterns of the quaternary glass systems were measured at room temperature, as shown in **Fig.3.7**. The broad hump in the range 25-35º, as well as the absence of sharp Bragg

peaks, reveals the amorphous structure of all the prepared glass samples, i.e. there was no long-range crystalline order [1].

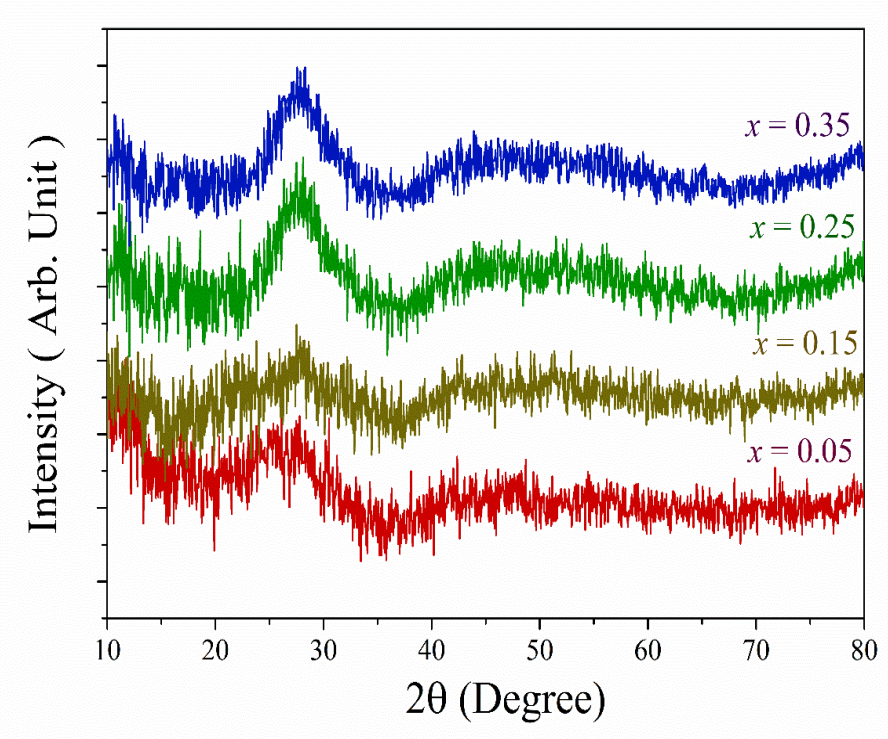

Fig. 3.7. Recorded XRD patterns of Bi_2O_3-doped glassy systems

3.3.3. Analysis of Raman Spectroscopy

As indicated in the Raman spectra of the investigated glass samples in **Fig. 3.8**, there exist characteristic vibrational modes that are attributed to the introduction of Bi_2O_3. These bands are mainly ascribed to structural units that contain the heavy cation of Bi^{3+}. It can be described that the spectral features are classifiable in two regions, viz., low-frequency domain (170-250 cm^{-1}) in connection with Bi-related cationic vibrations and intermediate region (300-606 cm^{-1}) in association with anion-related modes. Because of the increased atomic mass of bismuth, these vibrations occur at low wavenumbers relative to phosphate units, and thus it is definite that the observed features are primarily due to the Bi-O structure pattern. The Bi^{3+} ions occupy a position in the [BiO_3] pyramid and in the [BiO_6] octahedron, changing the local coordination environment. A small peak at 170 cm^{-1} is attributed to symmetric stretching of Bi-O-Bi bonds within [BiO_3] and [BiO_6] units [19], and a strong peak at 243 cm^{-1} to O-Bi-O bend in [BiO_7] polyhedral structure [20]. It is seen that these vibrational assignments are indicative of Bi_2O_3

contributing to controlling the glass structure by changing polyhedra symmetry and network connectivity.

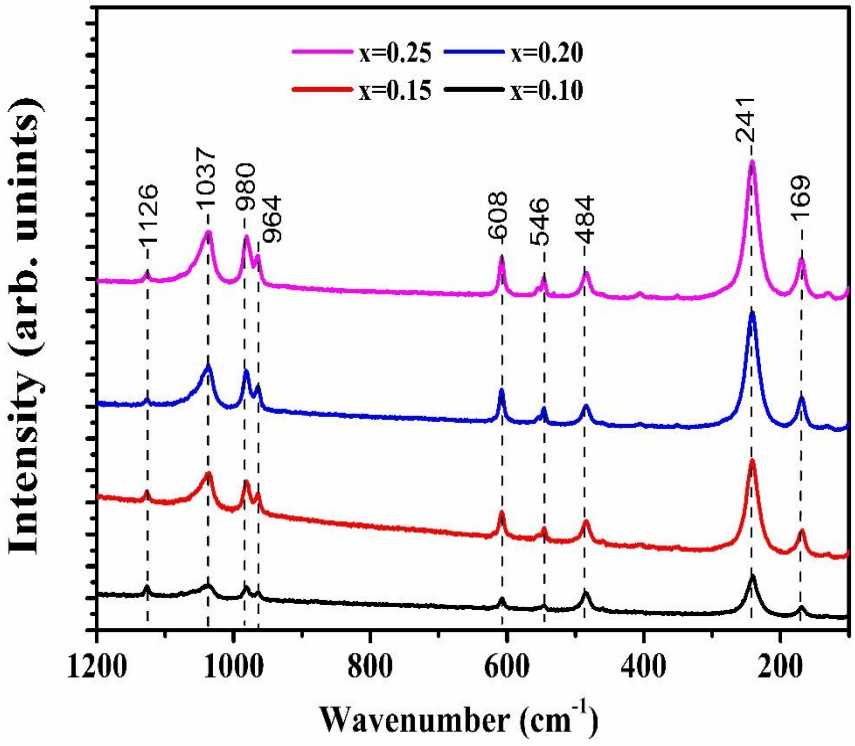

Fig. 3.8 FTIR spectra of the studied glass samples

The characteristic peak at 486 cm^{-1} in the Raman spectra of all the analyzed samples is located by Bi-O bond vibration in distorted octahedra BiO_6 [21]. There are also bands assigned to stretching of BiO bonds at 543 cm^{-1} and 606 cm^{-1} attributed to the progressively distorted BiO_6 groups [22,23]. A sharp feature around 964 cm^{-1} is linked to Ba–O bond vibrations, while a nearby band near 980 cm^{-1} is associated with VO_2 groups in VO_4 tetrahedra and/or VO_5 pyramidal configurations [24]. The phosphate network is also depolymerized in the process of replacing BaO by Bi_2O_3 and turns Q_2 into Q_1 (symmetric stretching mode of diphosphate groups exhibits around 1036 cm^{-1} [25]. This band signifies the augmented amount of pyrophosphate species. Moreover, the high band approximately at 1126 cm^{-1} is attributed to symmetric P-O stretching vibrations of Q_2 phosphate tetrahedra, which proves again that the presence of different phosphate units is present in the modified glass structure [26].

Table 3.4: Raman peak positions (cm^{-1}) of studied glass ceramics

Assignments	x = 0.10	x = 0.15	x = 0.20	x = 0.25	References
Symmetric stretching vibrations of Bi—O—Bi bonds in the BiO_6 octahedron units	170	170	170	169	[22]
Bending vibrations of Bi–O-Bi bonds in BiO_6 octahedron units	243	243	243	243	[23]
Stretching vibrations of Bi–O^- bonds in BiO_6 octahedron units	486	486	486	486	[24]
Stretching vibrations of Bi–O^- bonds in BiO6 octahedron units	543	543	543	544	[25]
Bi–O–Bi, Bi–O^- in [BiO_6] octahedra	606	606	606	606	[26]
Stretching vibrations of Ba—O bonds	961	960	960	961	[26]
VO_2 groups in VO_4 tetrahedra and/or in VO5 pyramids	980	980	981	980	[27]
Asymmetric vibrations of P-O-P bonds	1036	1036	1036	1036	[28]
Symmetric stretching of P-O bonds in Q^2 units.	1124	1124	1124	1124	[29]

3.4. Quaternary Bi_2O_3-Fe_2O_3-V_2O_5-P_2O_5 glass system

3.4.1. Analysis of physical parameters

Density (ρ) can be a crucial structural parameter to be used in assessing the internal structure of crystalline and amorphous solids and glass systems. The value of density and molar volume (V_M) was obtained in the present study based on **Eq. (3.1)**. As shown in **Fig. 3.10(a)**, the results have shown that ρ and V_M will rise progressively as the composition of the glass matrix is increased with Bi_2O_3. The major cause of this trend is, however, due to the gross molecular weight size of Bi_2O_3 (465.96 g/mol) being much bigger than other glass constituents like Fe_2O_3 (159.69 g/mol), V_2O_5 (181.88 g/mol) and P_2O_5 (283.88 g/mol). Also, this growth is subject to some factors such as the decrease of the free volume, the modification of the coordination number and the glass networks densification.

Structurally, the replacement of the lighter oxides by Bi_2O_3 is the reason behind the modification of the phosphate backbone because the formation of P = O double bonds in [PO_4] tetrahedral units gets interfered with in the [PO_4] tetrahedral units. This causes the creation of

several Q_n units, with n representing the number of bridging oxygen atoms. Based on the nomenclature put forth by Mogu-Milankovic et al. [27], the Q_3 units have three bridging and one non-bridging oxygen and Q_2 units have two bridging oxygens (and would be characteristic of metaphosphates), Q_1 units have one bridging oxygen (and would be characteristic of pyrophosphates) and Q_0 units consist of purely non-bridging oxygens (and would be representative of orthophosphates). The more the concentration of Bi_2O_3, the higher the level of non-bridging oxygen atoms [28], which causes the glass network to shrink, and hence a rise in bulk density. Such modifications verify the structural rearrangement of the glass system, and they evince the functionality of Bi_2O_3 as a densification compound in the phosphate glass network.

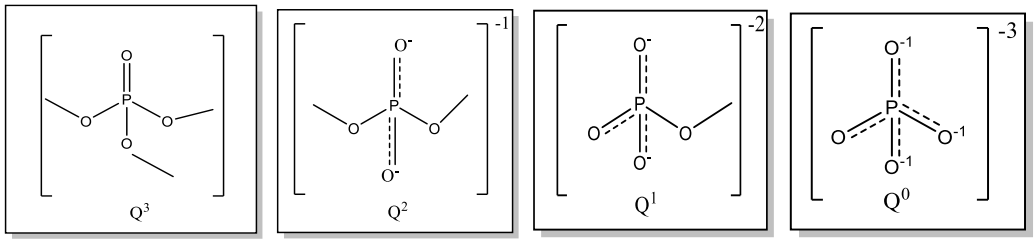

Fig. 3.9 Possible tetrahedral structure units in a phosphate glass system.

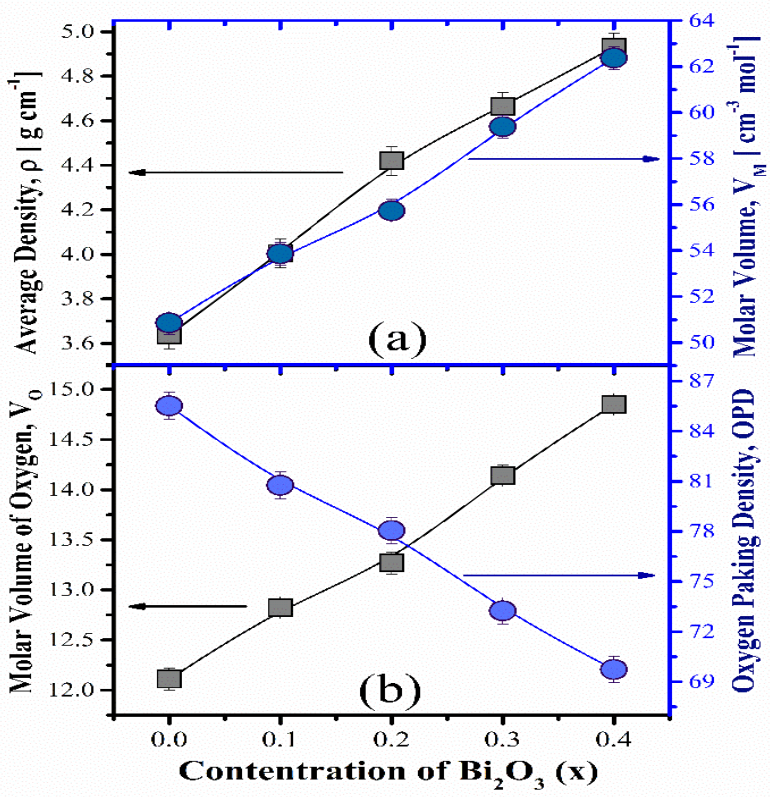

Fig. 3.10 Evaluated values of(a)Average density and Molar Volume and (b) Molar Volume of oxygen and Oxygen packing density against Bi_2O_3 content (x).

Fig. 3.10 (b) illustrates the evaluated values of oxygen molar volume (V_O) and oxygen packing density (OPD) as a plot of rising Bi_2O_3 composition (x). A low increase in V_O and a cross-drop of OPD are also observed as the proportion of Bi_2O_3 increases. This tendency implies that there are more non-bridging oxygen (NBO) sites in the glass structure [29]. This is manifested by an apparent increase in V_M (molar volume) that is mainly affected by extension of bond lengths [27] and lessened stretching force constant of structural units [30,31]. Incorporation of Bi_2O_3 leads to covalent bonding to alter the phosphate network that breaks the bridging oxygen relationships and facilitates the production of NBOs. Such changes in structure, in combination, increase the free volume and decrease its packing density of oxygen atoms, indicating a simpler glass network.

To conduct a more in-depth analysis of the spatial distribution of Bi atoms within the network, the molar volume corresponding to one mole of Bi was calculated using the correct conditions for determining volumetric dependence[32].

$$V_M^{Bi} = \frac{V_M}{2 \times (1 - x_{Bi-ion})} \tag{3.12}$$

The symbol $x_{Bi\text{-}ion}$ represents the molar fractions of Bi_2O_3. **Table 3.5** displays the calculated values of $<d_{Bi\text{-}Bi}>$ using the given equation [32].

$$\langle d_{Bi-Bi} \rangle = \left(\frac{V_M^{Bi}}{N_A} \right)^{1/3} \tag{3.13}$$

The $<d_{Bi\text{-}Bi}>$ value shows a steady increase as Bi_2O_3 is added to the iron-vanadium-phosphate amorphous matrix, as shown in **Table 3.6**. Using the relationship to estimate $N_{Bi\text{-}ion}$ values allows for the analysis of how Bi-ion concentrations affect the glass structure.

$$N_{Bi-ions} = \frac{mol\,\%\,of\ oxide \times N_A \times \rho}{Molecular\ weight\ of\ Composition\ (M)} \tag{3.14}$$

Using **Eq. (3.15)** to determine the $N_{Bi\text{-}ion}$ values, the inter-nuclear separation of Bi-ions (R_{Bi}) is calculated through the equation [33]:

$$R_{Bi} = \left(\frac{1}{N_{Bi-ions}} \right)^{\frac{1}{3}} \tag{3.15}$$

The results of the estimation of the inter-nuclear separation of Bi-ion (R_{Bi}) are tabulated in **Table 3.5.** There is a steady decrease in R_{Bi} observed as the Bi_2O_3 content is increased in the

material, and this can be taken to probe the evidence that the bismuth ions are much closer in the glass structure. The decrease in inter-ionic distance enables the building up of small polarons, localized charge carriers that play a major role in increasing the electrical conductivity with increasing concentration of Bi_2O_3 (x). The respective small polaron radius (R_p) is estimateable with the help of the following well-known formula [33], which has been based on the calculated value of R_{Bi} :

$$R_P = \left(\frac{R_{Bi}}{2}\right)\left(\frac{\pi}{6}\right)^{1/3} \tag{3.16}$$

The calculated radius of a small polaron (R_P) that is approximated, with an estimated radius of each allocated Bi-ion, decreases as the concentration level of the Bi_2O_3 material elevates. This decrease complies with the known fact that the lowest polaron radii can lead to better DC conductivity. Therefore, Bi_2O_3 is considered a network modifier in the glass matrix that enhances the electrical conduction of the present system [34-36].

Table 3.5 The magnitudes of various physical parameters

x	V_M^{Bi} (g/cm^2) (±1.50)	V_M^{Fe} (g/cm^2) (±1.50)	$<d_{Bi-Bi}>$ (Å) (±0.02)	$<d_{Fe-Fe}>$ (Å) (±0.02)	$N_{Bi\text{-}ions}$ (×10^{21}) (ions/cm^2) (±0.01)	$N_{Fe\text{-}ions}$ (×10^{21}) (ions/cm^2) (±0.01)	R_{Bi} (Å) (±0.15)	R_{Fe} (Å) (±0.15)	$R_{P\text{-}Bi}$ (Å) (±0.15)
0.00	25.43	84.76	1.280	1.912	-	4.736	-	5.954	-
0.10	29.92	76.94	1.326	1.817	1.118	3.354	9.634	6.680	3.88
0.20	34.83	69.66	1.379	1.738	2.161	2.161	7.734	7.734	3.12
0.30	42.42	65.98	1.442	1.671	3.042	1.014	6.901	9.953	2.78
0.40	51.97	62.37	1.518	1.613	3.862	-	6.373	-	2.57

3.4.2. Analysis of X-ray diffractograms (XRD)

The X-ray diffraction (XRD) spectra plot of the series of xBi_2O_3-(0.40-x) Fe_2O_3-$0.35V_2O_5$-$0.25P_2O_5$ glass nanocomposites are shown in Fig. 3.11. The patterns have wide humps typical of amorphous structures, as well as several overlying sharp diffraction peaks, which means a partial lack of crystallinity. These crystalline reflections also prove the formation of nanocrystalline phases embedded in the glass matrix. To determine the level of amorphousness of each sample, the percentage of crystallinity was obtained through a standard **Eq. (3.7)**[36]. The approximate percentages of the crystallinity in the glass systems as x = 0.0, 0.10, 0.20,

0.30, and 0.40 are 6.32%, 7.14%, 7.78%, 9.66%, and 11.12% respectively. These values are clear indications of the progressive development of nanocrystalline phases in the glass matrix with an increase in Bi_2O_3 content. Therefore, the general amorphous character of the glasses reduces with increased Bi_2O_3 substitution in the base of Fe_2O_3-V_2O_5-P_2O_5 composition.

The diffraction peaks that are identified in **Table 3.6** were consistent with the known crystalline phases of $Fe_3(PO_4)_2$ [JCPDS card No. 49-1087], Fe_2VO_4 [JCPDS card No. 01-075-1519], $BiPO_4$ [JCPDS card No. 15-0767] and Bi_2VO_5 [JCPDS card No. 51-0032]. The Scherrer equation (**Eq.3.6**) that was used to obtain the average crystallite sizes (d_c) of these nanophases Based on the predetermined crystallite size (d_c), the estimated average crystallite sizes of each nanocomposite glass sample are immortalised in **Table 3.6**. As indicated, there is an evident rising order to the average values of d_c with an increase in Bi_2O_3 (x), meaning that there is promotion of crystal growth in the glass matrix with an increase in the amount of bismuth.

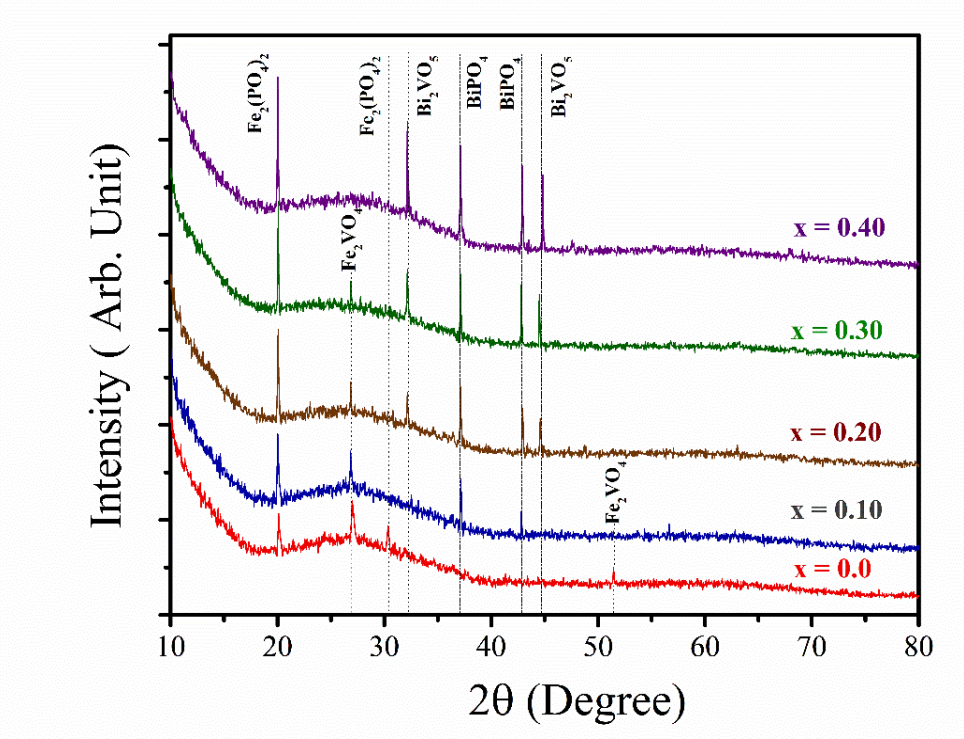

Fig. 3.11 Recorded XRD patterns of Bi_2O_3 doped glassy systems

Table 3.6 Several estimated physical parameters

Sl No	2θ (Degree) (±0.05)	β (±0.002)	Individual Particle Size (nm) (±0.12)	Average Particle Size (d_c) (nm) (±0.15)	h	k	l	Nanophase
x = 0	20.004	0.2378	33.54	50.61	3	1	0	$Fe_3(PO_4)_2$
	26.868	0.2446	33.02		4	0	0	Fe_2VO_4
	30.258	0.2222	36.62		0	2	2	$Fe_3(PO_4)_2$
	51.525	0.0879	99.23		6	4	2	Fe_2VO_4
x= 0.10	20.004	0.1693	47.12	67.94	3	1	0	$Fe_3(PO_4)_2$
	26.868	0.1731	46.66		4	0	0	Fe_2VO_4
	37.115	0.099	83.71		2	2	2	$BiPO_4$
	42.839	0.0895	94.29		4	0	2	$BiPO_4$
x = 0.20	20.004	0.1052	75.83	78.85	3	1	0	$Fe_3(PO_4)_2$
	26.868	0.1083	74.58		4	0	0	Fe_2VO_4
	32.156	0.0958	85.34		1	3	1	Bi_2VO_5
	37.115	0.0833	99.48		2	2	2	$BiPO_4$
	42.839	0.1193	70.73		4	0	2	$BiPO_4$
	44.504	0.1264	67.15		3	3	1	Bi_2VO_5
x =0.30	20.004	0.1054	75.67	86.12	3	1	0	$Fe_3(PO_4)_2$
	26.868	0.1223	66.04		4	0	0	Fe_2VO_4
	32.156	0.0929	88.01		1	3	1	Bi_2VO_5
	37.115	0.0743	111.53		2	2	2	$BiPO_4$
	42.839	0.0765	110.31		4	0	2	$BiPO_4$
	44.504	0.1303	65.145		3	3	1	Bi_2VO_5
x = 0.40	20.004	0.1077	74.03	92.41	3	1	0	$Fe_3(PO4)_2$
	26.868	0.1131	71.39		4	0	0	Fe_2VO_4
	32.156	0.0834	97.99		1	3	1	Bi_2VO_5
	37.115	0.0752	110.08		2	2	2	$BiPO_4$
	42.839	0.0863	97.69		4	0	2	$BiPO_4$
	44.504	0.0821	103.29		3	3	1	Bi_2VO_5

3.5. Summary

The chapter has demonstrated the structural and physical analysis of three pseudo-quaternary and quaternary glass systems, V_2O_5-Na_2O-ZnO-P_2O_5 (VNZP), Bi_2O_3-BaO-V_2O_5-P_2O_5 (BBVP) and Bi_2O_3-Fe_2O_3-V_2O_5-P_2O_5 (BFVP), which incorporate VO_5 nanoparticles. The physical data of density (ρ), molar volume (V_M), oxygen molar volume (V_o), and oxygen packing density (OPD) disclosed crucial differences in structural compression, bonds, and permeability in association with considerable TMO and heavy metal oxide accounts. An increase in V_2O_5 tended to add non-bridging oxygen (NBO) species, depolymerised phosphate networks, and affected the rigidity of glasses, in part by inducing the VO_4 tetrahedral unit.

Bi_2O_3, heavy metal oxide, and high molecular weight fillers the role doubly increasing density, and engage in network modification as a result of forming Bi-O bonds (BiO_3 and BiO_6 structural units), which FTIR and Raman measurements confirmed. Such an addition advanced the OPD and diminished internuclear separations (R_{Bi}), suggesting that a more condensed and polarizable organization (compatible with smaller polarons development) was being formed, which possibly contributes to electrical conductivity.

Likewise, BaO (one of the members of the BBVP series), which is partially substituted by Bi_2O_3, exhibited rising density and OPD patterns. Its reduced polarizing field and increased ionic radius caused Ba^{2+} to be more of a network modifier, locally distorting structure without providing an overall rise in connectivity. Conversely, the presence of Fe_2O_3 in the BFVP system disturbed the phosphate network by the addition of FeO coordination units that disrupted not only the glassy structure but also generated nanocrystalline products like $Fe_3(PO_4)_2$ and Fe_2VO_4 that were additionally established by XRD.

The depolymerization of phosphate groups (Q_3 - Q_1) and the formation of V-O-V, Bi-O-Bi, and Fe-O-P linkages were also proved by Raman and FTIR spectroscopy and further support the role of oxides in the local structure. XRD profiles showed that with increased amounts of dopant, entire nanocrystallites were formed, and a premature crystalline increase was observed with the addition of Bi and Fe elements as oxides.

3.6. References

1. Elliott, S. R. (1986). Physics of amorphous materials. John Wiley & Sons. https://isbnsearch.org/isbn/9780470204726
2. Singh, D. P., & Singh, G. P. (2013). Conversion of covalent to ionic behavior of Fe_2O_3–CeO_2–PbO–B_2O_3 glasses for ionic and photonic application. Journal of Alloys and Compounds, 546, 224–228. https://doi.org/10.1016/j.jallcom.2012.08.105
3. Biswas, R. K. N., Ningthemcha, L. S., & Singh, A. S. D. (2019). Structural characterization and electrical conductivity analysis of MoO_3–SeO_2–ZnO semiconducting glass nanocomposites. Journal of Non-Crystalline Solids, 515, 21–33. https://doi.org/10.1016/j.jnoncrysol.2019.04.002
4. Biswas, D., Chakrabarti, C., Das, A. S., Ahmed, M., Mukherjee, S., & Nambissan, P. M. G. (2022). Microstructure and defects of $0.1P_2O_5$–0.65ZnO–0.25($xTeO_2$–(1–x) MoO_3) quaternary glass nanocomposites using positron annihilation and correlated experimental methods. Journal of Physics and Chemistry of Solids, 163, 110598. https://doi.org/10.1016/j.jpcs.2022.110598
5. Idler, K. L., Calvo, C., & Ng, H. N. (1978). Crystallographic studies on cation substitutions in the system (Na,K)(V,P)O_3. Journal of Solid State Chemistry, 25, 285–294. https://doi.org/10.1016/0022-4596(78)90113-5
6. Bubnova, R. S. (1982). Kristallografiya, 27, 1094. https://doi.org/10.17188/1193868
7. Immirzi, A., & Porzio, W. (1982). Acta Crystallographica Section B: Structural Science, Crystal Engineering and Materials, 38, 2788. https://doi.org/10.1107/S0567740882009960
8. Benhamada, L. (1992). $Na_2VP_2O_8$: A tetravalent vanadium diphosphate with a layered structure. Journal of Solid State Chemistry, 101, 154–160. https://doi.org/10.1016/0022-4596(92)90211-D
9. Averbuch-Pouchot, M. T., & Durif, A. (1983). Crystal chemistry of MIIAg$(PO_3)_3$ polyphosphates for MII = Zn, Co, Ni, Mg and $MII_4Na_4(P_4O_{12})_3$ tetrametaphosphates for MII = Zn, Co, Ni: Crystal structures of ZnAg$(PO_3)_3$ and $Zn_4Na_4(P_4O_{12})_3$. Journal of Solid State Chemistry, 49, 341–352. https://doi.org/10.1016/S0022-4596(83)80012-7
10. Korthuis, V. C., Hoffmann, R. D., Huang, J., & Sleight, A. W. (1993). Synthesis and crystal structure of potassium and sodium vanadium phosphates. Chemistry of Materials, 5, 206–209. https://doi.org/10.1021/cm00026a009

11. Biswas, D., Rajan, A., Kabi, S., Das, A. S., Singh, L. S., & Nambissan, P. M. G. (2019). Structural defects characterization of silver–phosphate glass nanocomposites by positron annihilation and related experimental studies. Materials Characterization, 158, 109928. https://doi.org/10.1016/j.matchar.2019.109928
12. Shih, P. Y., Ding, J. Y., & Lee, S. Y. (2003). ^{31}P MAS–NMR and FTIR analyses on the structure of CuO–containing sodium poly– and meta–phosphate glasses. Materials Chemistry and Physics, 80, 391–396. https://doi.org/10.1016/S0254-0584(03)00098-1
13. El-Hezzat, M., Et-tabirou, M., Montagne, L., Bekaert, E., Palavit, G., Mazzah, A., & Dhamelincourt, P. (2003). Structure and AC conductivity of sodium–lead–cadmium metaphosphate glasses. Materials Letters, 58, 60–66. https://doi.org/10.1016/S0167-577X(03)00415-4
14. Biswas, D., Das, A. S., Kabi, S., Singh, L. S., Ahmed, M., Mukherjee, S., & Nambissan, P. M. G. (2021). Positron annihilation and correlated dielectric property studies of a transition metal oxide–modified quaternary nanocomposite $0.1P_2O_5$–$0.4ZnO$–$0.5(xV_2O_5$–$(1–x)MoO_3)$. Journal of Alloys and Compounds, 864, 158395. https://doi.org/10.1016/j.jallcom.2020.158395
15. Zandi, S., Kameli, P., Salamati, H., Ahmadvand, H., & Hakimi, M. (2011). Microstructure and optical properties of ZnO nanoparticles prepared by a simple method. Physica B: Condensed Matter, 406(17), 3215–3218. https://doi.org/10.1016/j.physb.2011.05.026
16. Magdas, D. A., Vedeanu, N. S., & Toloman, D. (2015). Study on the effect of vanadium oxide in calcium phosphate glasses by Raman, IR and UV–vis spectroscopy. Journal of Non-Crystalline Solids, 428, 151–156. https://doi.org/10.1016/j.jnoncrysol.2015.08.012
17. Anderson, G. W., & Verble, J. L. (1979). Raman spectra of vanadium phosphate glasses. Journal of Applied Physics, 50(4), 2765–2769. https://doi.org/10.1063/1.326239
18. Bhargava, R. N., & Condrate, R. A. (1977). The vibrational spectra of VPO_5 crystal phases and related glasses. Applied Spectroscopy, 31(3), 230–236. https://doi.org/10.1366/000370277774463742
19. Singh, B., Chatterjee, P., Ningthemcha, R. K. N., Adhikari, S., Mondal, R., Das, A. S., Kabi, S., Singh, L. S., & Biswas, D. (2021). Compositional dependence of structural, physical, and optical parameters of $Se_{50–x}Te_{30}Sn_{20}Sbx$ chalcogenide glassy systems. Materials Chemistry and Physics, 274, 125153. https://doi.org/10.1016/j.matchemphys.2021.125153

20. Baia, L., Stefan, R., Kiefer, W., Popp, J., & Simon, S. (2002). Structural investigations of copper doped B_2O_3–Bi_2O_3 glasses with high bismuth oxide content. Journal of Non-Crystalline Solids, 303(2), 379–386. https://doi.org/10.1016/S0022-3093(02)01042-6
21. Kharlamov, A. A., Almeida, R. M., & Heo, J. (1996). Vibrational spectra and structure of heavy metal oxide glasses. Journal of Non-Crystalline Solids, 202(3), 233–240. https://doi.org/10.1016/0022-3093(96)00192-5
22. Chahine, A., Et-tabirou, M., & Pascal, J. L. (2004). FTIR and Raman spectra of the Na_2O–CuO–Bi_2O_3–P_2O_5 glasses. Materials Letters, 58(22–23), 2776–2780. https://doi.org/10.1016/j.matlet.2004.04.010
23. Bale, S., Rahman, S., Awasthi, A. M., & Sathe, V. (2008). Role of Bi_2O_3 content on physical, optical and vibrational studies in Bi_2O_3–ZnO–B_2O_3 glasses. Journal of Alloys and Compounds, 460(1–2), 699–703. https://doi.org/10.1016/j.jallcom.2007.06.090
24. He, F., He, Z., Xie, J., & Li, Y. (2014). IR and Raman spectra properties of Bi_2O_3-ZnO-B_2O_3-BaO quaternary glass system. American Journal of Analytical Chemistry, 5(16), 1142–1150. https://doi.org/10.4236/ajac.2014.516121
25. Hayakawa, S., Yoko, T., & Sakka, S. (1995). IR and NMR structural studies on lead vanadate glasses. Journal of Non-Crystalline Solids, 183(1–2), 73–84. https://doi.org/10.1016/0022-3093(94)00652-0
26. Ilieva, D., Jivov, B., Bogachev, G., Petkov, C., Penkov, I., & Dimitriev, Y. (2001). Infrared and Raman spectra of Ga_2O_3–P_2O_5 glasses. Journal of Non-Crystalline Solids, 283(1–3), 195–202. https://doi.org/10.1016/S0022-3093(01)00361-1
27. Brow, R. K. (2000). Review: The structure of simple phosphate glasses. Journal of Non-Crystalline Solids, 263–264, 1–28. https://doi.org/10.1016/S0022-3093(99)00620-1
28. El-Desoky, M. M., Gazouly, N. A., Hannor, A. E., & Yousef, H. A. (2023). Adiabatic small polaron hopping conduction in nanostructured Bi_2O_3–Fe_2O_3–$PbTiO_3$ prepared by high energy planetary ball mill. Journal of Materials Science: Materials in Electronics, 34(2), 829–836. https://doi.org/10.1007/s10854-023-10243-x
29. Mott, N. F. (1967). Electrons in disordered structures. Advances in Physics, 16(61), 49–144. https://doi.org/10.1080/00018736700101265
30. Austin, I. G., & Mott, N. F. (1969). Polarons in crystalline and non-crystalline materials. Advances in Physics, 18(71), 41–102. https://doi.org/10.1080/00018736900101267

31. Moguš-Milanković, B., Šantić, B., Day, D. E., & Ray, C. S. (2001). Electrical conductivity in mixed-alkali iron phosphate glasses. Journal of Non-Crystalline Solids, 283(1–3), 119–128. https://doi.org/10.1016/S0022-3093(01)00355-6
32. Moguš-Milanković, B., Ličina, V., Reis, S. T., & Day, D. E. (2007). Electronic relaxation in zinc iron phosphate glasses. Journal of Non-Crystalline Solids, 353(26–27), 2659–2666. https://doi.org/10.1016/j.jnoncrysol.2007.05.001
33. Reis, S. T., Moguš-Milanković, A., Ličina, V., Yang, J. B., Karabulut, M., Day, D. E., & Brow, R. K. (2007). Iron redox equilibrium, structure and properties of zinc iron phosphate glasses. Journal of Non-Crystalline Solids, 353(2), 151–158. https://doi.org/10.1016/j.jnoncrysol.2006.10.002
34. Ghosh, B. K., Biswas, D., Ganguly, S., Debnath, A., Mandal, D., Shaharukh, S., Adhikari, S., Mondal, R., Kabi, S., & Das, A. S. (2024). Effect of the inclusion of Fe_2O_3 on the optical and electrical transport properties into sodium-zinc-phosphate quaternary glassy systems. Materials Today Communications, 38, 107785. https://doi.org/10.1016/j.mtcomm.2023.107785
35. Rahman, R. S., Shoab, M., Khan, Z. M. S. H., Aslam, Z., Asokan, K., & Zulfequar, M. (2020). Bandgap tunability endowed by isovalent sulphur doping in SeTe glassy films: Correlation with Kastner's and single oscillator models. Journal of Alloys and Compounds, 835, 155441. https://doi.org/10.1016/j.jallcom.2020.155441
36. Biswas, D., Hota, S. B., Mondal, R., Mukherjee, S., Chandra, P. C., Das, A. S., Kabi, S., & Roy, D. (2023). Effect of heavy metal and alkaline earth oxides on the optical and electrical mechanism of vanadium-phosphate amorphous glassy systems. Journal of Non-Crystalline Solids, 620, 122593. https://doi.org/10.1016/j.jnoncrysol.2023.122593

Chapter 4

Analysis of Optical Properties of Glass Nanocomposite Systems

4.1. Introduction

Optical characterization of glass and glass nanocomposites is necessary to understand their relevance in optoelectronic, photonic, and solar energy to conversion. Their composition, electronic structure and the short-range order in glass matrix play a strong role in control of the optical properties of these end materials. This chapter discusses how the optical properties of three systems of glass nanocomposites of vanadium phosphate (including V_2O_5 -Na_2O -ZnO-P_2O_5 (or VNZP), Bi_2O_3-BaO-V_2O_5-P_2O_5 (or BBVP), and Bi_2O_3-Fe_2O_3-V_2O_5-P_2O_5(or BFVP)) can be studied via ultraviolet-visible. UV-$_{Vis}$ absorption spectrometry is an extremely delicate and non-destructive method of analysis to analyze the electron transitions between glassy materials. The absorption spectra of the oxide glasses that contain transition metal ions ($V^{5+/V4+}$, Bi^{3+}, Fe^{3+}, and Zn^{2+}) can be useful in terms of the information regarding the localized states of electrons, ligand fields, and the oxidation states of the components. Such transitions, and especially in UV and visible, are strongly linked with the band structure of the energy of the glass and give a clue to the electronic structure.

Optical absorption spectra of the synthesized samples were taken within a wavelength range of 200 to 1100 nm. Using these spectra, important optical data were obtained, including the optical band gap energy (E_{opt}) and Urbach energy (E_U). The band gap energy that denotes the minimum energy to excite an electron in the valence band to the conduction band is determined by the application of the Tauc plot using both direct and indirect transitions allowed by the absorption edge perusal. The Urbach energy, which is the exponentially increasing part of the absorption edge, signifies the proximity to disorder and defect states in the glassy matrix. Inclusion of other modifiers and transition metal oxides leads to unique shifts of the optical absorption edges and spectral properties, thereby affecting the electronic polarizability and band structure. As an example, ZnO in the VNZP system would tend to increase transparency and the band gap, whereas Fe_2O_3 and Bi_2O_3 local states and reduce the gap since they are multivalent and electronic transition in nature. On the same note, the non-bridging oxygen content and interfering with the optical behaviour may be an effect of the Ba^{2+} ion in the series of the BBVP. Such optical studies are essential towards understanding the structure-property relationship but are also the building blocks of tuning the electronic and optical response of these materials towards device level applications like UV blocking coatings, photonic switches and electrochromic devices.

Conclusively, the general objective of this chapter is to provide a comparison optical probe of the synthesized glass nanocomposites using UV-$_{Vis}$ absorption spectroscopy to highlight the impact of compositional customization in the band structure variations and negligible deviations linked with defect transfers in the related electronic transitions. The results gleaned from these optical studies play a crucial role in comparing the physical and structural properties of the systems for the electronic behavior of the glass system.

4.2. Quaternary V_2O_5–Na_2O–ZnO–P_2O_5 glass system

4.2.1. UV-$_{Vis}$ absorption spectra

Optical absorption-based spectra are an excellent property to assess when there is a change in the structure of the amorphous glass material due to optically induced electronic transitions. They are important in estimating the character of the optical band gap, either direct or indirect; they are affected by various factors in the form of dopant type, elemental constitution, and the synthesis methodology. The absorption properties of the semiconductor glass materials are of great benefit in terms of illuminating the electronic transitions, localized vibrational and localized states, as well as the vibrational dynamics. **Fig. 4.1** shows the absorption of the glass samples in which the concentration of V_2O_5 was varied. There is an evident trend for the absorbance to rise as the wavelength rises in the ultraviolet range. The absorption in all the samples is intense in the region 240-320 nm, which is a sign of substantial electronic transitions. After the peak absorbance of around 330 nm, the absorbance decreases and finally levels off, which means that there is little absorption occurring in the visible regime and that optical transparency is excellent.

Particular interest in this study gravitates around the analysis of the optical absorption coefficient (α) in order to determine the character of the electronic transition as well as to determine the optical band gap energy of the glass systems. Absorption coefficient is important because it provides important information on levels of electromagnetic radiation energy that is attenuated after traversing through the material. This parameter goes directly to the interaction of the incident photons and the electronic structure of the glass. By employing a simple mathematical relationship, the absorption coefficient (α) of the synthesized samples has been determined, giving a good opportunity to make an in-depth analysis of the optical behavior and transition dynamics of the glass matrix [1].

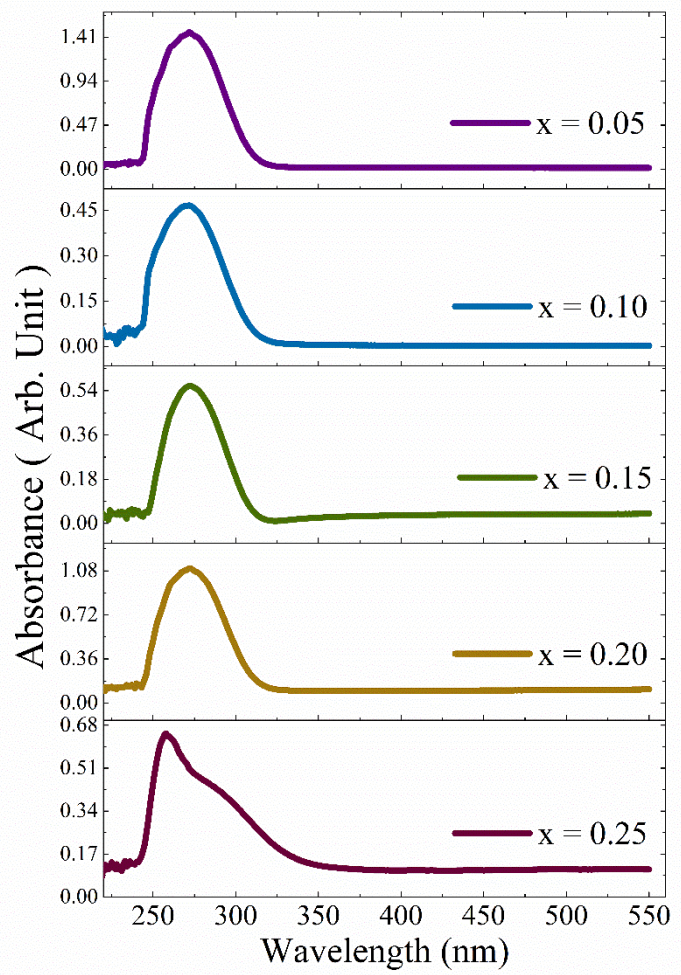

Fig. 4.1 Dependence of Absorbance on the wavelength

$$\alpha = 2.303\frac{A}{d} \tag{4.1}$$

Where A represents the absorbance and d is the thickness. The dependence of α on the wavelength for different V_2O_5 concentrations has been depicted in **Fig. 4.2.**

The range of absorption coefficient on all the samples studied reflects an absorbance trend with them. It is also noticeable that the absorption coefficient shows high values in the wavelength area of 250-320 nm, and this can be attributed to the incidence of photons, which leads to the occurrence of the resonance effects. The red shift of the absorption edge is also evident in the absorption edge as it shifts between 270 nm and 300 nm with changes in the composition, implying a change in the optical band structure.

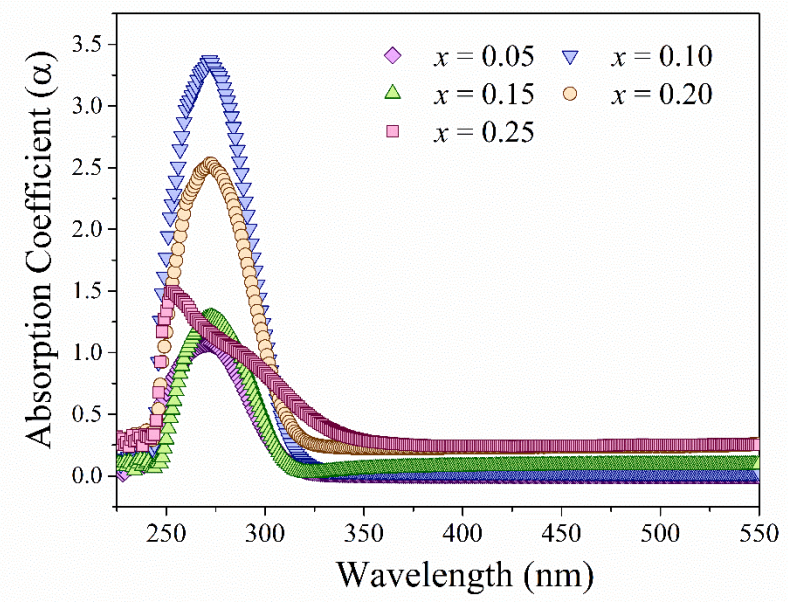

Fig.4.2 Dependence of absorption coefficient on wavelength.

The extinction coefficient (k) that is intrinsically connected with the absorption coefficient (α) gives one more knowledge about the interaction of electromagnetic waves with the glass medium. The extinction coefficient is used for the assessment of the patterns of propagation of electromagnetic waves within the material. The value of k is computed by a standard expression which takes into consideration the absorption coefficient, which provides more insight about the optical losses in the material and the propagation character of light in the material [2].

$$k = \frac{\alpha\lambda}{4\pi} \tag{4.2}$$

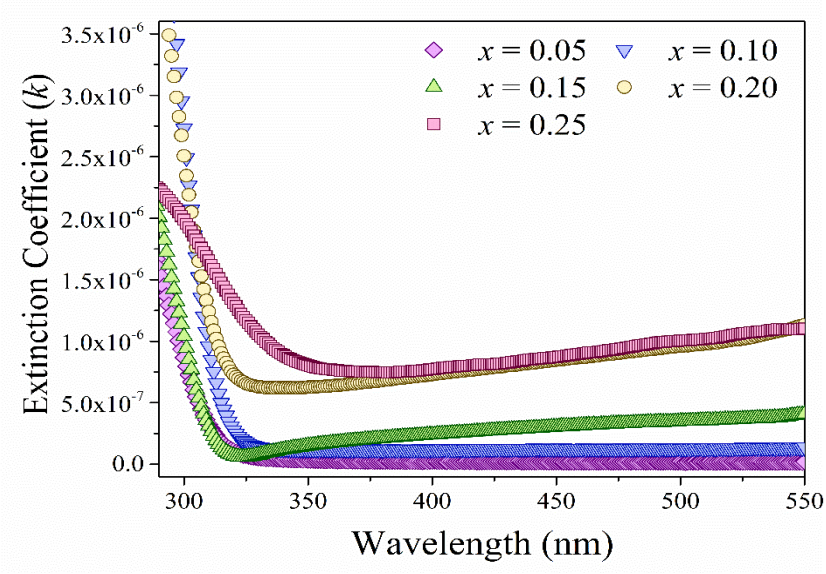

Fig.4.3 Variation of the Extinction coefficient with the wavelength

It is noted that the extinction coefficient (*k*) is reduced substantially till around 340nm in the samples that have an x = 0.05 and x = 0.10 composition, after which it becomes constant. In the other compositions, an increment in '*k'* is observed, but in a weak amount above 350 nm. However, at longer wavelengths, all samples have very low *k* values, indicating little light is absorbed at this part. The latter is an indication of the high optical transparency character of the glass samples, and therefore, they can be used as transparent optical materials [3].

Based on this transparency and the essence of the electronic transition, there is a need to look into the optical band gap of the samples. To achieve this, plots of $(\alpha h\upsilon)^2$ versus photon energy (hν) are analyzed, as shown in **Fig. 4 .4 (a)**, assuming a direct allowed band-to-band electronic transition.

It is noticed that the *k* values decrease dramatically up to 340 nm; afterwards, they attain an almost constant value of *x* = 0.05 and *x* = 0.10 composition. At the same time, the *k* values have a slightly increasing trend after 350 nm for the rest of the three samples. As the *k* values remain extremely small for all the studied samples after 350 nm, indicating the absorption of light is minimum, and these samples can be used as transparent material [3].

In this context, by considering the band-to-band transition, inspecting the optical band gap of these as-prepared samples is important. To estimate the optical band gap $(\alpha h\upsilon)^2$ is plotted vs the incident photon energy hν as depicted in **Fig. 4 .4 (a).**

The energy value of the optical band gap (E_{opt}) is obtained by locating the intercepts of the extrapolated straight, line segments of the Tauc plot with axes of photon energy. Variation of E_{opt} with different levels of V_2O_5 is shown in **Fig. 4.4 (b)**. As V_2O_5 content increases, a definite negative trend in E_{opt} is measured. This decrease in band gap can be explained by the structural role of vanadium ions, which partially replace the P–O–P bridges in the phosphate network by the P–O–V linkages [3]. This replacement balances the presence of non-bridging oxygen atoms more strongly and gives rise to localized states of the band structure and a red shift of the absorption edge.

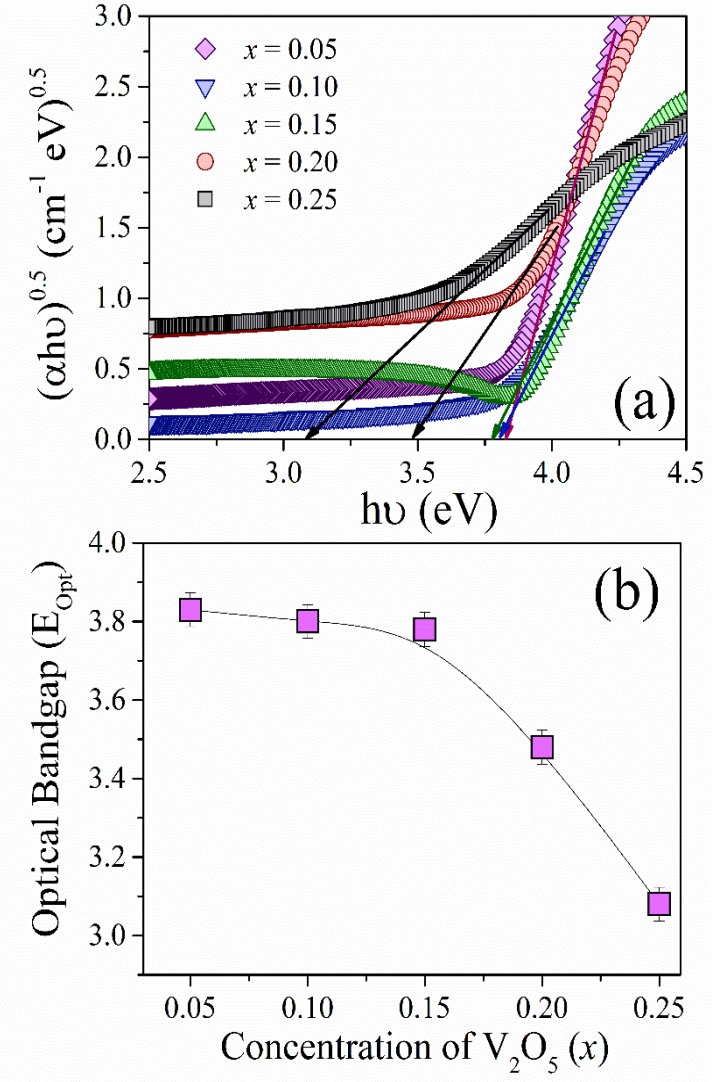

Figs. 4.4 (a) Tauc's plot $(\alpha h\upsilon)^2$ vs the photon energy (hν) **(b)** Dependence of E_{opt} on V_2O_5 content (x).

Such transformations denote enhanced structural chaos that can be measured quantitatively by calculating Urbach energy (E_U), as introduced in the relation below [4,5].

$$\alpha(\upsilon) = \alpha_0 \exp\left[\frac{h\upsilon}{E_U}\right] \tag{4.3}$$

The values of Urbach energy can be attained by taking the reciprocal of the slope of the linear part of the plot of ln (α) versus hυ, as depicted in **Fig. 4.5(a).**

It is noted that the values of Urbach energy (E_U) have a consistent increase with the increase in the concentration of V_2O_5 in glass matrix [**Fig. 4.5(b)**]. This tendency shows gradual increase of the structural disorder or fault density, which is implicated in the creation of the localized states in the band structure.

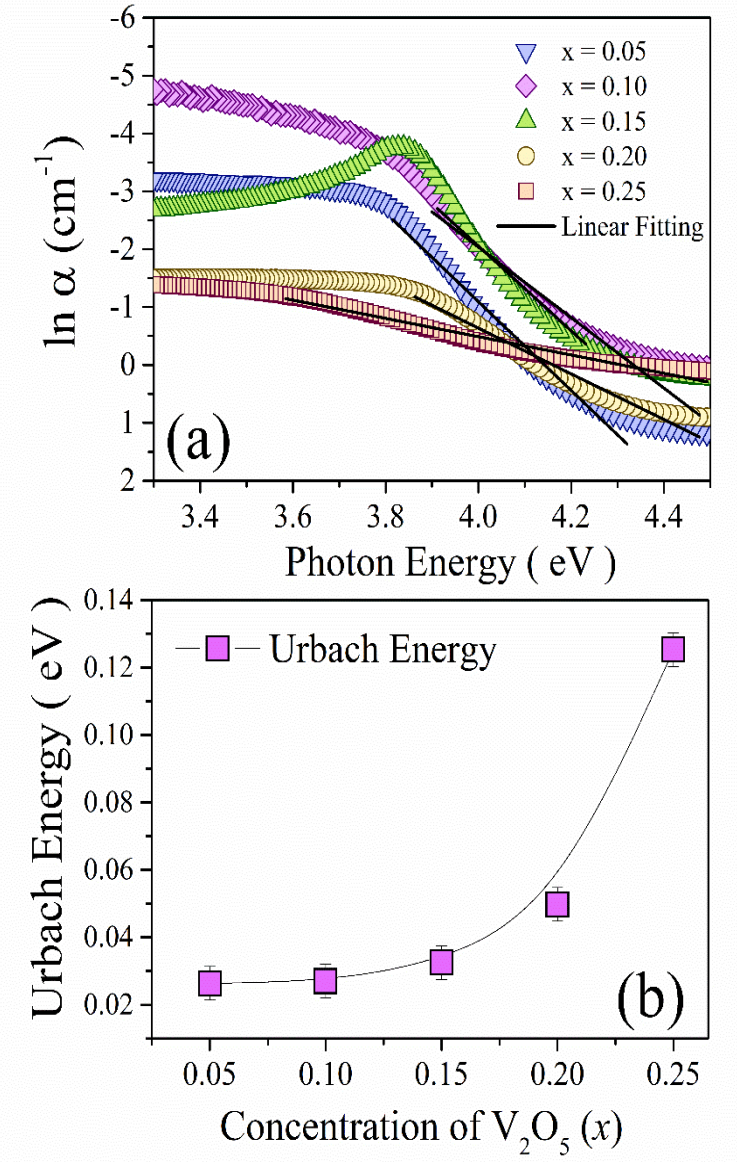

Fig. 4.5 (a) Urbach energy plot and **(b)** Variation of E_U with V_2O_5 content (x)

The red shift in the absorption edge corresponds with the narrowing of the optical band gap, as the increase in E_U. This inverse correlation between the variables E_{opt} and E_U is consistent with the results posted in past literatures [6,7].

Table 4.1 Several calculated optical parameters of the glassy system having chemical composition 0.35ZnO-O.25P_2O_5-(0.4-*x*) Na_2O-*x*V_2O_5

x	Optical band gap energy (E_g) in eV	Urbach energy in eV	Refractive index (n)	Polarizability (α_e) x 10^{-24}
0.05	3.84	0.024	2.19	6.27
0.10	3.81	0.026	2.20	6.33
0.15	3.79	0.030	2.21	6.44
0.20	3.46	0.050	2.27	6.56
0.25	3.12	0.124	2.37	6.86

4.2.2. Study of R-T spectra

Figs. 4.6(a-b) presents the optical transmission of absorption spectra of five quaternary glass samples with the composition 0.35ZnO-0.25P_2O_5-(0.4-x)-Na_2O-xV_2O_5, that have been measured over the range 200-550 nm. By increasing the value of x (concentration of the V_2O_5), the fundamental absorption edge is red-shifted to a longer wavelength, just above 250 nm. When this happens, there is a related decrease in the optical band gap of the materials [8]. The optical transmission and absorption spectra of five quaternary glass samples having chemical composition 0.35ZnO-O.25P_2O_5-(0.4-*x*) Na_2O-*x*V_2O_5 ($0.05 \le x \le 0.25$) measured in the wavelength region 200-550 nm are depicted in **Figs. 4.6(a-b)**. The absorption edge observed at 250 nm is noticed to be shifted to the higher wavelength, resulting in a redshift with the rise of the V_2O_5 content (*x*). The observed fundamental absorption edge allows us to estimate the optical band gap of the studied materials [8].

Remarkably, the x = 0.25 sample exhibits an unstable transmission spectrum above 350 nm, while the other samples have stabilised above 320 nm. This difference can be attributed to structural variations caused by the incorporation of vanadium, which affects the electronic structure and optical transparency. Additionally, the transmission spectra display behaviour opposite to that of the reflectance spectra during the examined period.

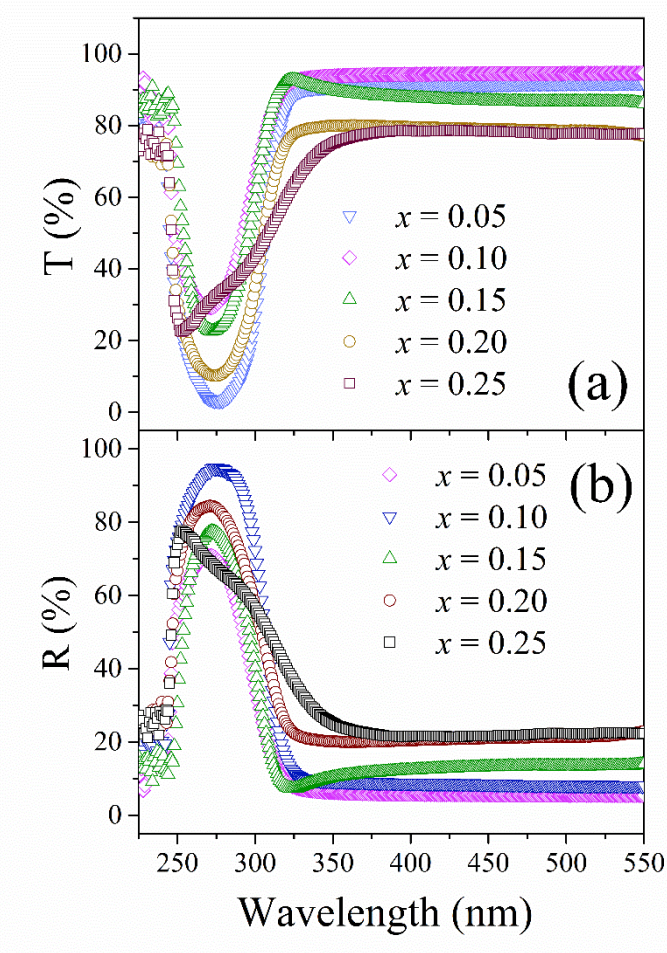

Figs. 4.6 (a-b) T (%) and R (%) spectra of the studied samples

4.2.3. Study of linear refractive index (n) and polarizability

The refractive index (n) is one of the most significant optical properties of the material. The value of n is obtained by using the following expression [9]

$$n = \left[\frac{(1+R)}{(1-R)}\right] + \sqrt{\frac{4R}{(1-R)^2} - k_{ex}^2} \tag{4.4}$$

The variation of refractive index (n) with wavelength (λ) for all the investigated samples has been depicted in **Fig. 4.7.**

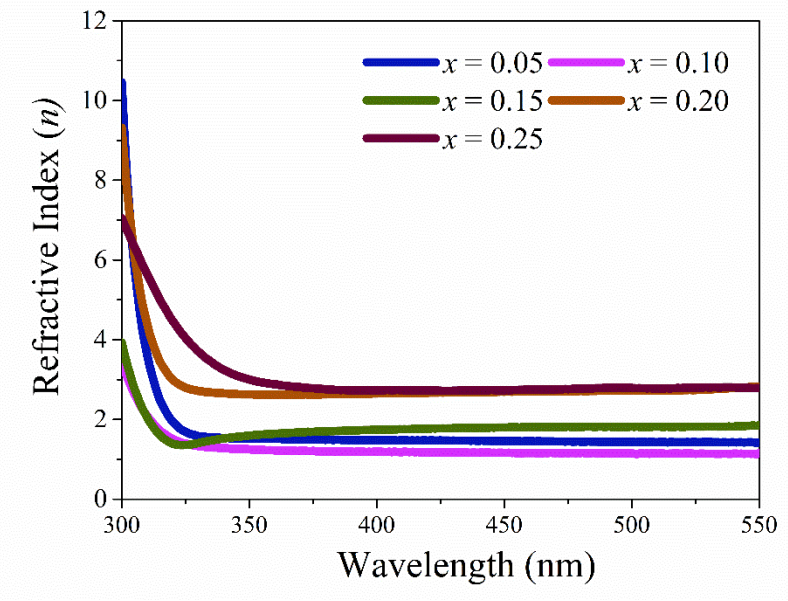

Fig. 4.7. Dependence of refractive index (*n*) on wavelength

The **Fig.4.7** gives the wavelength dependent change of the refractive index (n) of all the investigated glass samples. The behavior of all compositions is to show typical of normal dispersion, that is, a rapid decrease in the refractive index up to about 350 nm. Further on the refractive index values will not be so much changed and will be almost constant in the range of the spectrum up to 550 nm. Moreover, in order to evaluate the influence that composition has on the refractive index, the empirical formula proposed by Dimitrov and Sakka [10] has been utilised.

$$\frac{n^2-1}{n^2+2}=1-\left(\frac{E_{opt}}{20}\right)^{0.5} \tag{4.5}$$

These refractive index values (n), as indicated in **Table 4.1,** have been increasing steadily (2.19--2.37) as more V_2O_5 was being added to the glass matrix. Such a trend indicates that vanadium is a network modifier and it has a direct effect on the optical density and bonding surrounding the structure.

As the nonlinear optical response of a material is determined mainly by its electronic polarization, it is vital to be able to consider polarizability, which can determine the

optoelectronic properties of a material [10]. The electronic polarizability (α_e) of the glass systems was determined in the Lorentz-Lorentz equation [11].

$$\frac{n^2-1}{n^2+2}(V_m)=\frac{4}{3}\pi N\alpha_e \tag{4.6}$$

Here, N displays the Avogadro number. The obtained results of electronic polarizability are provided in **Table 4.1**. The greater polarizability in the V_2O_5-rich samples of the glass is explainable by the introduction of non-bridging oxygens (NBOs) in the glass. When the amount of V_2O_5 is high, it favours the generation of NBOs, and this promotes an increased electron displacement, and this enhances the polarizability of the system [11]. It is found that polarizability and refractive index have a direct correlation; that is, the more the polarizability of a substance, the higher its refractive index, and this goes in line with findings on all the samples [12]. Polarizability, being inherently part and parcel of the dielectric behavior of materials, necessitates the evaluation of the complex dielectric constant to have a more complete picture of optical response.

4.3 Quaternary Bi_2O_3-BaO-V_2O_5-P_2O_5 glass system

4.3.1. Optical Energy band gap and Urbach Energy

Optical absorption spectrum is an important component in evaluating any structural alterations due to optically excited transition, as well as the establishment of the bandgap energy as either direct or indirect [13]. The evidence of indirect electronic transitions at the band edge of the glass nanocomposites has been realized in the present study. The optical bandgap is estimated by estimating the energy E_{opt} against the absorption coefficient (α) versus the photon energy [hν]. The Davis and Mott model was estimated to estimate E_{opt}, through the following expression: the Davis and Mott model [13].

$$\alpha(h\upsilon)=[A(h\upsilon-Eopt)]^p \tag{4.7}$$

In the Tauc method, the band tailing constant A is independent, and the exponent p depends on the character of the interband transition. In particular, p = 2 corresponds to indirect allowed transitions and p = 1/2 to direct allowed transitions. To detect the optical bandgap in case of indirect transitions, Eq. (4.6) will be used, and the trend of the plotted graph will be extrapolated into the y-axis where $(\alpha h\upsilon)^{1/2} = 0$. This approach will result in the E_{opt} (indirect) values as shown in **Fig. 4.8** (a) by the Tauc formalism.

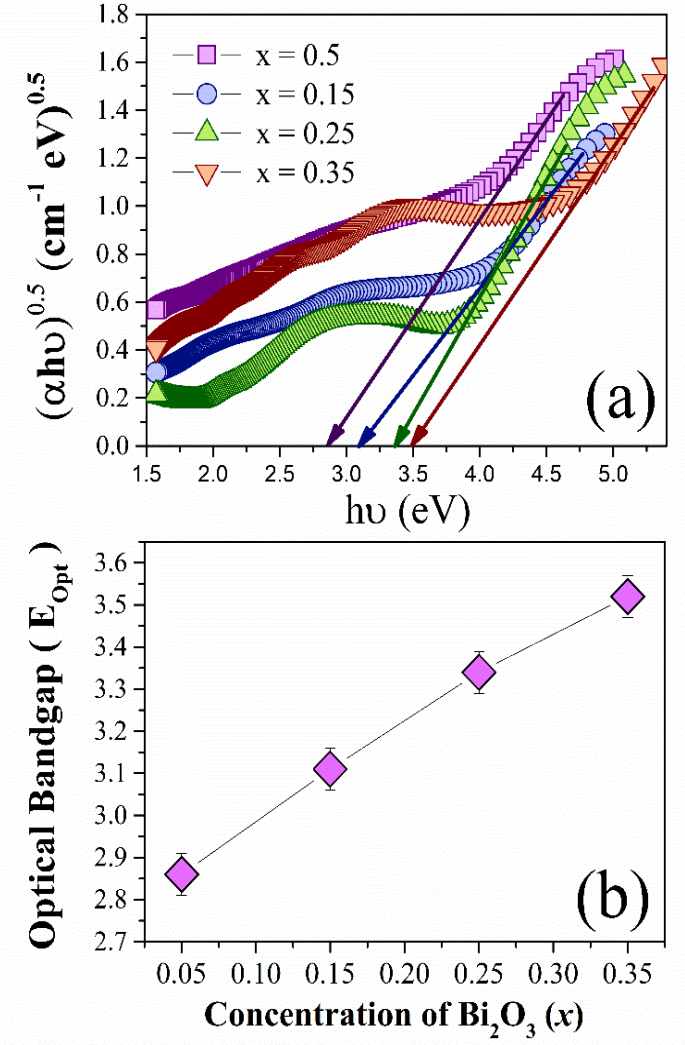

Fig. 4.8 (a) Plot of $(\alpha h\upsilon)^{1/2}$ versus energy and **(b)** deviation of composition-dependent $E_{opt.}$

Fig. 4.8(b) shows the variation of optical band gap energy (E_{opt}) with rising concentration of Bi_2O_3 (x) as a line graph. Addition of Bi_2O_3 in the glass matrix brings in the structural changes, which affect the value of E_{opt}. A clear upward trend in E_{opt} is observed with the increase in Bi_2O_3 content, which suggests a widening of the optical band gap. Such a behaviour is explained by the decrease in the amount of non-bridging oxygen (NBO) in the glass network that changes the electronic band structure by increasing the gap between the valence and conduction bands. In contrast to crystalline semiconductors, which exhibit a sharp absorption edge near the band gap, amorphous materials show a tailing effect into the band gap due to the presence of localized defect states and structural disorder.[14]

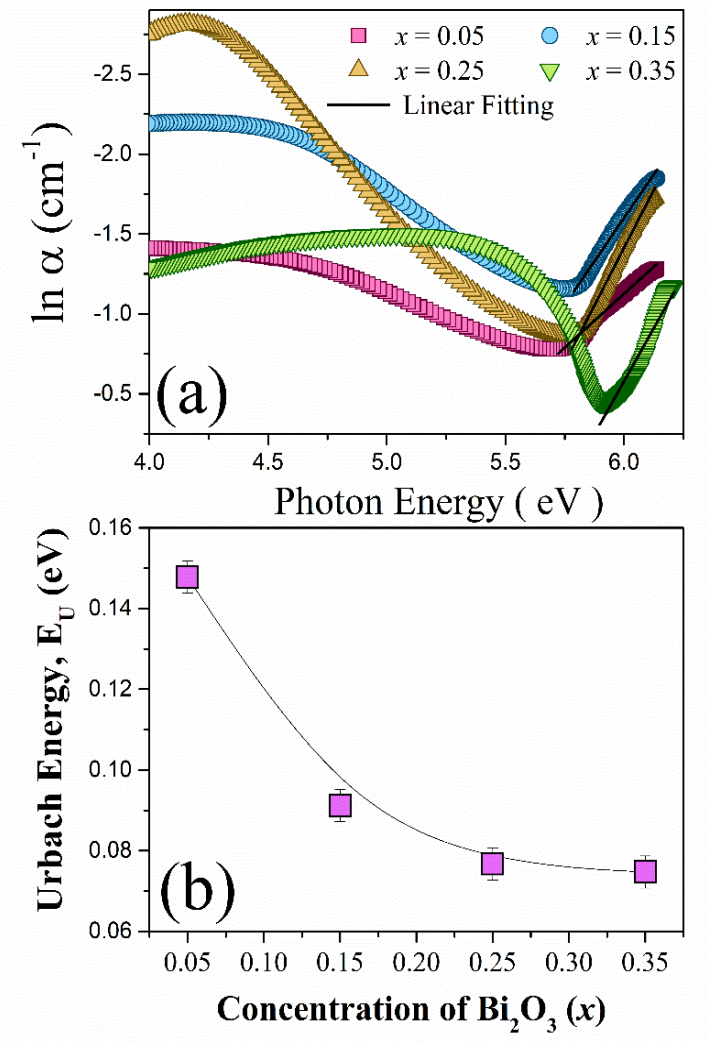

Fig. 4.9 (a) The dependence of ln (α) on hν, and **(b)** variation of composition-dependent E_U.

A comprehensive evaluation of Urbach energy (E_U) provides insight into the degree of structural disorder and the presence of defect states within the glass matrix. These localized states near the optical band edge (E_{opt}) are commonly characterized by the Urbach energy, which serves as a reliable indicator of the extent of disorder in amorphous systems. The value of the E_U can be determined using Urbach's empirical relation [15], which describes the exponential tail of the absorption edge associated with electronic transitions in disordered materials (**Eq.4.2**). Urbach energy (E_U), also referred to as the band tail energy, corresponds to the exponential edge extending near the optical band gap and is indicative of localized states and structural imperfections. The values of E_U are derived from the inverse of the slope

obtained by fitting the linear region of the absorption edge in the low photon energy range, as illustrated in **Fig. 4.9(a)** [15]. As shown in **Fig. 4.9(b)**, E_U gradually declines from 0.148 eV to 0.071 eV with increasing Bi_2O_3 content. A higher value of E_U signifies a greater presence of defects and disorder, while a lower value indicates improved structural ordering. The decreasing trend of the E_U suggests that Bi_2O_3 incorporation promotes network repolymerization, thereby reducing structural disorder. This structural improvement is also consistent with the rise in glass density (ρ), as previously discussed in **Chapter 3** and shown in **Fig. 3.6**.

4.3.2. Optical Refractive index (n) and related optical parameters

One of the fundamental optical characteristics of a glassy material is the refractive index (n), and this is very critical in the application of the material in optical and photonic applications. It is an indication of how light becomes slower as it goes through the material. This, in the context of the glass nanocomposites, directly affects the value of "n", which is a direct consequence of the structure and type of bonding that is present in the glass network. The refractive index is an essential device parameter when deploying optical material and in the manufacture of devices. An empirical relationship of practical value exists between optical band gap energy (E_{opt}) and the refractive index, which is usually used to estimate the n values of well-measured E_{opt} through the following expression [4]:

$$n = \sqrt{\frac{12.417}{E_g - 0.365}} \tag{4.9}$$

Table 4.2 contains the values of refractive index (n) of various compositions. These variations in *"n"* are closely linked to the structural modifications occurring within the glass matrix. In particular, the electronic polarizability of the material (α_m) plays a very important role in alterations of the refractive index. Since "*n"* is a direct indicator of how easily the electron cloud of the material can be distorted under an applied optical field, assessing the polarizability becomes essential. Molar polarizability (α_m) of the samples of the glass is consequently estimated through the following empirical relation [16] as depicted in **Eq.4.5**.

In **Table 4.2**, the calculated quantities of molar polarizability (α_m) are found. It was seen earlier that the addition of Bi_2O_3 in the glass increases the density and therefore also increases compactness and thus the subsequent preference for few non-bridging oxygen (NBO) sites. Such an effect of compaction is in agreement with the measured reduction in Urbach energy (E_U), which implies the reduction of structural defects and localize disorder. Therefore, there

is a tendency for a decrease in the total refractive index (n) of the glass systems as Bi_2O_3 content is increased. To go further into the optical behavior, the molar refraction (R_m) of the glass system is determined with the help of the following relation [10].

$$R_m = \frac{4}{3}\pi\alpha_m N_A \tag{4.10}$$

Table 4.2 shows how molar refraction (R_m) and electronic polarizability (α_e) change with each of the glass systems as adjustment with Bi_2O_3 (x) concentration changes. Reflectivity (R) is one of the meaningful optical properties of glass, which reflects the amount of incident light at the surface. Generally, glass is highly transparent in the wavelength of near ultraviolet to near infrared [17]. But some atoms in the glass structure, especially those containing strongly held electrons, may also make part of the reflection loss by interaction with incident light. The value of R depends on the refractive index (n) of the material, where it can be calculated by the Fresnel formula, which means that R is related to the refractive index of the material (n).

$$R = \left(\frac{n-1}{n+2}\right)^2 \tag{4.11}$$

The subsequent formula can be used to estimate the reflection factor (P) [17].

$$P = \frac{2n}{n^2+1} \tag{4.12}$$

In **Table 4.2**, the calculated reflectivity (R) and the molar polarizability (P) of all the glass samples are given. It is noted that the higher the amount of Bi_2O_3 used, the lower the value of reflectivity (R). The trend shows a negative relationship between R and P as observed in the past literature [20]. In order to evaluate more specifications of the electronic nature of the glasses, the metallization factor (M) is determined. This parameter assists in the classification of materials according to their optical response, which points out whether a glass is metallic or not. The standard M value is obtained by using a conventional empirical expression that includes refractive index values and values of molar refractions [18].

$$M = 1 - \frac{R_m}{V_m} \tag{4.13}$$

A conductor typically has a metallization factor (M) value near 0, but insulators tend toward values of M close to unity [19]. The actual values (**Table 4.2**) of M of the current glass systems are between 0.379 and 0.422. It is interesting to see that the M value is minimum at x = 0.05,

and this means a lower optical band gap (E_{opt}). This indicates a smaller energy gap between the valence and conduction band, according to **Fig. 4.9(b)**, keeping up with the trend that electronic polarizability becomes stronger and its insulating strength weakens at lower levels of Bi_2O_3.

4.3.3. *Non-linear optical parameters*

An important parameter to evaluate the capability of a material in nonlinear optoelectronics is the third-order nonlinear optical susceptibility (χ^3). It analyses the behaviour response of the material under a strong intensity light source, and it plays a crucial role in the design of devices such as optical switches, modifications, as well as frequency changers. To calculate the nonlinear refractive index, a dozen semi-empirical models can be used, the most common ones being Miller and Wang's rule [20]. In the determination of the nonlinear refractive index(n_2), the linear susceptibility (χ^1) and the nonlinear susceptibility (χ^3) were determined by use of the following expressions [21].

$$\chi^3 \cong A\left(\chi^{(1)}\right)^4 \tag{4.14}$$

Here A= 1.7×10^{-10} (χ is measured in e.s.u)

and, $$\chi^1 = \frac{\left(n^2-1\right)}{4\pi} \tag{4.15}$$

The values of the third-order nonlinear optical susceptibility (χ^3) have been obtained with the help of **Eq.4.15**. They are listed in **Table 4.2**. In addition, the calculation of an estimate of the nonlinear refractive index (n_2) has also been determined by using the theoretical method as proposed by Ticha and Tichy, which is a confident way to analyse nonlinear optical properties in amorphous glass materials [22].

$$n_2 = \frac{12\pi\chi^3}{n} \tag{4.16}$$

The determination of the nonlinear refractive index (n_2) was calculated and presented in **Table 4.2**. Similar to that of 3rd-order nonlinear susceptibility (χ^3) and n_2 (both an increasing order) as the concentration of Bi_2O_3 (x) goes up. Remarkably, the maximum value of n_2 can be seen in the case of x = 0.05, which means that this composition can be applied in nonlinear optoelectronics. The decrease in n_2 as more Bi_2O_3 is added is probably attributable to a

reduction in structural defects in the glassy substance, which agrees with the results in the past literature [22,23].

Table 4.2: Optical parameters of glass samples

Optical Parameters	**Concentration of Bi_2O_3 (*x*)**			
	0.05	**0.15**	**0.25**	**0.35**
Optical Bandgap (E_{opt}) (eV)	2.86	3.11	3.34	3.52
Urbach Energy (E_U)	0.147	0.091	0.076	0.074
Refractive index (n)	2.26	2.20	2.11	1.98
Molar refractivity (R_m) ($cm^3\ mol^{-1}$)	32.41	32.66	31.37	30.15
Molar Polarizibility (α_m) x 10^{-23}	1.285	1.295	1.244	1.195
Reflectivity (R)	0.149	0.140	0.127	0.108
Reflection factor (P)	0.740	0.753	0.774	0.804
Metallization (M)	0.422	0.438	0.464	0.506
Third-order susceptibility $\chi^{(3)} \times 10^{-11}$ (e.s.u)	0.16	0.10	0.06	0.04
Non-linear refractive index (n_2) $\times 10^{-11}$ [e.s.u]	2.70	1.77	1.10	0.76

4.4. Quaternary Bi_2O_3-Fe_2O_3-V_2O_5-P_2O_5 glass system

4.4.1. Optical Study

Optical absorption spectroscopy is a vital method for determining the band gap energy and analysing optically induced electronic transitions in glassy materials. By using measured UV-visible absorption spectra, key optical parameters such as the absorption coefficient (α), extinction coefficient (k), refractive index (n), optical band gap energy (E_{opt}), Urbach energy (E_U), and others can be systematically calculated.

4.4.2. Analysis of absorption coefficient (a), and extinction coefficient (k)

Fig. 4.10 demonstrates the absorption coefficients of the spectra of glass samples at 300K. The amount of light which can be swept into a material before absorption is the absorption coefficient. Every sharp absorption edge in the spectra signifies that photons having energies less than the band gap optical are no longer able to eject electrons in the valence band to the conduction band and thus restrict the absorption at respective energies[24,25]. In the figure, it

can be seen that the value of the absorption coefficient (α) gets lower as photons increase in terms of energy value ($h\nu$). The values of α were computed using the appropriate theoretical expression as per **Eq.4.1** cited in the literature [26].In this regard, alpha (α) is the absorbance, and d is the thickness of the glass sample under examination. Most significantly, and characteristic feature is that the absorption coefficient (α) decreases with increasing wavelength above a wavelength of about 260 nm, a trend normally associated with effects of electron-electron coupling. This point can be well linked to the previous literature results [27, 28]. The parameter of extinction coefficient (k) is an important parameter, and it gives a measure of the ability of a material to absorb the incident electromagnetic radiation of a particular wavelength.

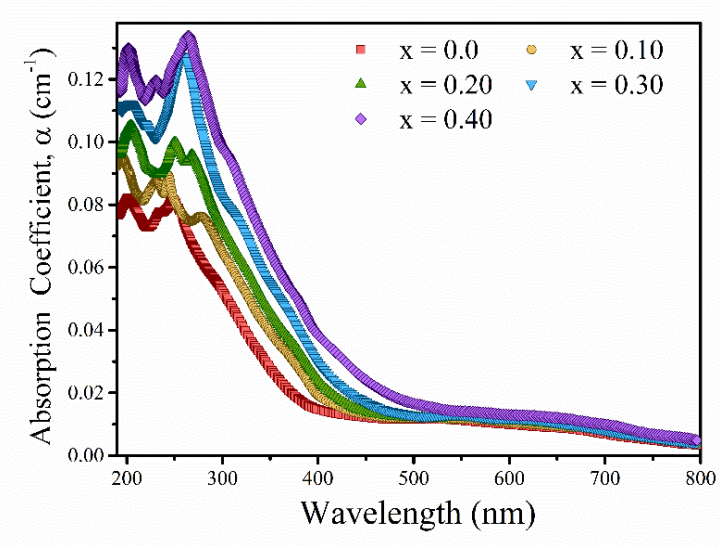

Fig. 4.10. Variation of absorption coefficient with the wavelength (nm)

The extinction coefficient for a given specimen can be calculated using the **Eq. 4.2** [29].Here, α represents the coefficient of absorption, whereas λ is the wavelength of the light that is incident on the glass. The figure of spectral variation of the extinction coefficient (k) against wavelength is as shown in **Fig. 4.11**. The values of *k* decrease continuously until about 450 nm, thereafter, they seem to approach stability and almost stay constant between 450 and 800 nm. This decreasing behaviour of k is an indication of the wavelength-dependent characteristic of light attenuation within the substance. The values of *k* depend on the wavelength in the same way as the values of α and thus show almost the same spectral behaviour. The value of parameter *k* shows the degree to which incident electromagnetic waves are attenuated. Hence, the lower *k* values result promotes that these materials being perfectly applicable in Near-Infrared (NIR) optical use.

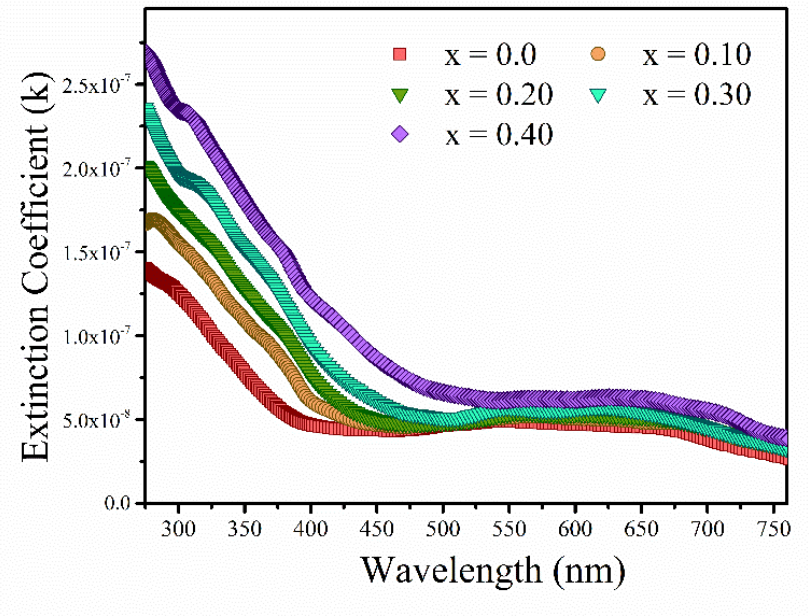

Fig. 4.11. Variation of the extinction coefficient with wavelength (nm)

4.4.3. *Analysis of optical bandgap energy and Urbach energy*

Optical absorption spectrum is a very crucial means of assessment of optical band gap and structural developments caused by optically stimulated electronic transitions [30]. According to the Davis-Mott model, localized electronic states as well as structural defects at the band gap region can largely affect the optical band gap (E_{opt}) in the amorphous glass systems [29]. To determine the effect of bismuth (Bi) incorporation on the optical band gap, the plots of $(\alpha h\nu)^{1/n}$ against hν were generated, where n denotes the type of electronic transition. In the case of indirect allowed transition, the value of 2 is taken, according to Tauc relation [30,31] and used to calculate the corresponding optical band gap energies.

$$(\alpha h\nu)^{\frac{1}{2}} = B\left(h\nu - E_{opt}\right) \tag{4.17}$$

Here, E_{opt} is the optical band gap energy, hν is the incident photon energy, and B is a constant that is specific to the material. The optical band gap may be determined by extrapolating the linear portion of the Tauc plot so as to cross the energy axis. All the samples under study have these Tauc plots as shown in **Fig. 4.12**. As indicated in **Fig. 4.12(a)**, values of E_{opt}, computed using the above formula, continuously decline between 2.42 eV and 2.00 eV as the content of

Bi_2O_3 increases. The reduction of band gap energy is credited to the changes in the structure of the glass network, specifically, the change in defect states that lower the energies difference between the valence and conduction bands. Further, the shrinking of the band gap implies the escalating formation of non-bridging oxygen atoms (NBOs) as the concentration of Bi_2O_3 augments [10].

The cause of this drop in E_{opt} could be an increase in localized or disordered states, so the degree of disorder or defect state in the material must now also be investigated.

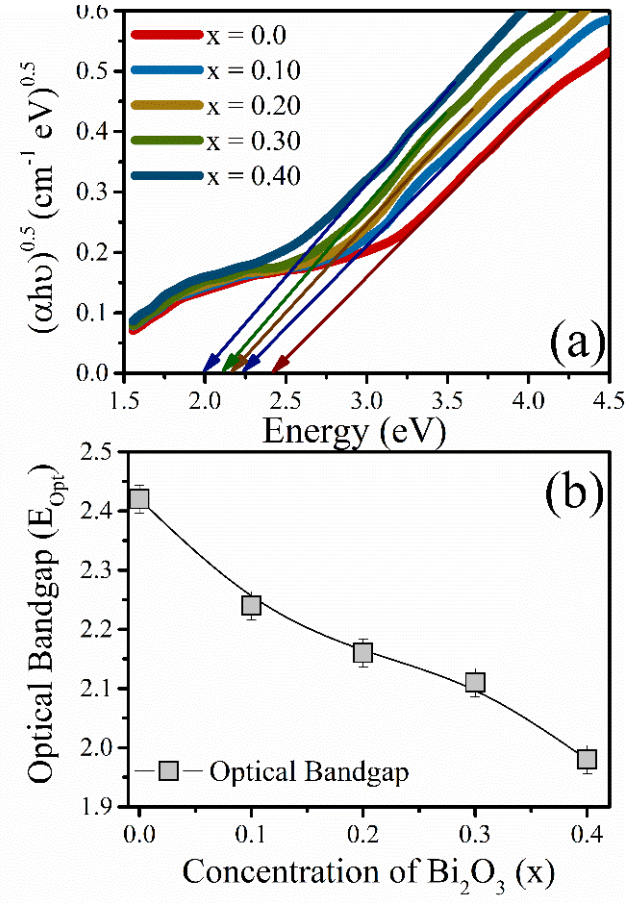

Fig. 4.12. Tauc's plot optical band gap

In order to evaluate the level of disorder that exists within the glassed matrix, Urbach energy (E_U) is the most important diagnostic parameter. It is an energy of the exponential tail of the localized states extending into the band gap, which appear because of the structural or compositional disorder. The expansion of the valence and conduction band edges reported by the width of the Urbach tail has added electronic transitions between these localized defect states. Such tails are caused by random fluctuations of the internal potential, also typical of disordered (or amorphous) materials. Specifically, it is important to mention that the existence of such exponential tails is a universal phenomenon and reflects the density of states

distribution in the gap. The quantity of the Urbach energy can be calculated with the help of a well-known empirical formula as depicted in **Eq.4.2** [32], and the linear fit (shown in **Fig. 4.13(a)**) allows obtaining the value of E_U.It is important to highlight that the Urbach energy values rise from (0.25-0.56) eV with the addition of Bi_2O_3 to the host matrix.

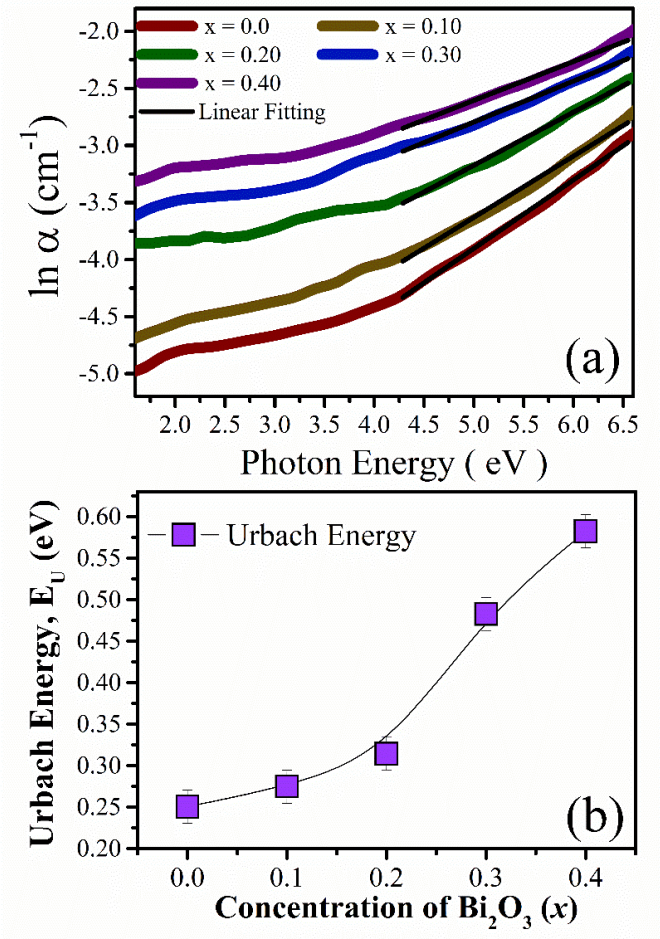

Fig. 4.13 (a) Natural logarithm of α plotted against photon energy and (b) Urbach energy (E_U) plotted against Bi_2O_3 content (x).

Fig. 4.13(b) shows the Urbach energy (E_U) values calculated for the studied glass systems. As the data show, the addition of Bi_2O_3 causes a gradual increase in Urbach energy, which is attributed to a higher density of localised states and increased disorder in the glass network structure. This positive correlation between the E_U and the Bi_2O_3 percentage is proportional and inversely related to the optical bandgap energy (E_{opt}), which decreases as the Bi_2O_3 content rises. Such an inverse relationship between E_U and E_{opt} aligns with previous reports in similar

disordered systems [4, 33], confirming that as the defect concentration increases, the bandgap narrows due to a broader tail of electronic states extending into the forbidden zone of the band structure.

4.4.4. Estimation of optical refractive index (n) and other associated optical parameters

Every glassy system has a unique refractive index (n), and the refractive index differs with composition. This is one of the critical parameters in determining the optical properties of materials used in optoelectronic and photonic products [34]. The refractive index measures the interaction of light incident upon a material, and is the key in judging the ability of a material to disperse or focus light, which is essential in designing optical lenses, optical coatings, prisms, and lenses. Moreover, it has a great influence on such properties as reflectivity and chromatic dispersion. It is worth noticing that there is a long-standing relationship between the refractive index (n) and the optical bandgap energy (E_{opt}) that is commonly characterized by such empirical correlations as that suggested in previous studies and stated as **Eq.4.4** [24,31].

The irregularities in refractive index of varied Bi_2O_3 concentrations are directly attributed to the altered structures in the glass matrix, as shown in **Table 4.3**. It showed an upward trend, whereupon refractive index values increased by about 0.19 (2.564 vs 2.754), as Bi_2O_3 was added to the mixture, in the form of an increasing value of x. Among the main factors which contribute to this tendency is the electronic polarizability (α_m) is a large component of the interaction of the material with the incoming electromagnetic radiation. It would therefore be important to gauge the polarizability of the constituent oxides in comprehending these optical shifts. Electronic polarizability (α_e) of each composition is calculable by **Eq.4.5** [24,25].As **Table 4.3** shows, the determined values of polarizability (α_m) demonstrate the increasing tendency with a corresponding growth of Bi_2O_3 concentration. This is occasioned by a similar increase in molar volume due to the incorporation of Bi_2O_3, which leads to the formation of non-bridging oxygen (NBO) atoms in the glass matrix. These NBOs help to increase the electron polarizability of the glass system, therefore increasing the refractive index (n) of the glass system. The change of these optical parameters takes place with the help of changing the structure of the glass network by adding Bi_2O_3.

The second optical property of glass materials that is extremely relevant is the reflectivity (R), expressing the degree to which the light is reflected back by the surface. The electrons confined within the shell of the atom can cause partial reflection of incident light in transparent glass systems, and this happens mostly within the near-ultraviolet to near-infrared range. The reflectance or reflection loss is usually calculated with the help of the Fresnel equation (**Eq.4.10**) that links the reflectivity and the refractive index of the substance [24,25].From **Table 4.3**, it is noted that the reflectivity rises from 0.192 to 0.218 with the incorporation of Bi_2O_3 content. Additionally, **Eq.4.11** [24] has been used to determine the reflection factor (P). The highest reflectivity (R) is measured at 0.677 in the glass sample when x = 0.0, while the lowest molar polarizability ratio (P), calculated as 0.641, is also observed in the same sample. This trend indicates that as the concentration of Bi2O3 in the glass matrix increases, the reflectivity of the glass decreases. **Table 4.3** demonstrates that an inverse relationship exists between reflectivity (R) and the polarizability ratio (P), which is also consistent with previous research [24,25].

The metallization factor (M) has been used to assess whether the prepared glass samples are metallic or non-metallic by analysing the measured molar refraction (R_m) and molar volume (V_m). This parameter is calculated using **Eq.4.12** and effectively indicates the potential of a material to be either a metallic conductor or an insulator [24,25]. Generally, the metallization factor (M) of insulating materials is high, which is also close to unity, whereas the conductive materials have a value of metallization factor (M) that is approaching "0" [25]. The M values of the respective glass samples in the study continue to drop proportionately to the concentration of Bi_2O_3 (x), ranging between 0.349 to 0.313 as shown in **Table 4.3**. Such a negative trend in M indicates a smaller optical band gap (E_{opt}), most probably a decrease in the difference in energy between the conduction and valence bands. The increasing T values imply that the shift of the glass system toward semiconducting tendency. Consequently, with the progressive substitution of Bi_2O_3, the samples exhibit an increasing tendency toward metallization. This observation corresponds well with the simultaneous decrease in E_{opt} from 2.42 eV to 2.00 eV, confirming the structural and electronic evolution within the glass matrix.

Table 4.3 The glass sample was analyzed using a range of physical and optical parameters.

Parameters	**x = 0.0**	**x = 0.10**	**x = 0.20**	**x = 0.30**	**x = 0.40**
Average Density(ρ)	3.63	4.04	4.42	4.68	4.92
Molar Volume(Vm)	51.23	54.21	55.12	59.34	61.61
Optical band gap energy (E_{opt}) (eV)	2.42	2.24	2.20	2.17	2.00
Urbach energy (E_U)(eV)	0.25	0.27	029	0.47	0.56
Refractive Index(n)	2.564	2.632	2.663	2.689	2.754
Polarizability(α_e) x 10^{-23}	1.320	1.427	1.464	1.588	1.678
Molar refraction (Rm)	33.305	35.9931	36.930	40.054	42.325
Metallization constant(M)	0.349	0.336	0.329	0.325	0.313
Reflection factor(P)	0.677	0.664	0.658	0.653	0641
Reflectivity (R)	0.192	0.201	0.206	0.209	0.218

4.5. Summary

The optical investigations carried out in this chapter offer critical insights into the effect of compositional tuning on the electronic structure and localized defect states within vanadium-phosphate-based glass nanocomposites. By employing UV-$_{Vis}$ absorption spectroscopy, key parameters such as the optical band gap energy (E_{opt}) and Urbach energy (E_U) were systematically evaluated across the VNZP, BBVP, and BFVP series. The observed variations in absorption edges and band gap energies directly reflect the influence of doped transition metal oxides (such as Fe_2O_3, Bi_2O_3, and ZnO) and alkaline earth modifiers (like BaO and Na_2O) on the short-range structural order and degree of electronic disorder within the glass network.

In the VNZP system, ZnO incorporation was found to enhance transparency and widen the band gap due to its role as a stable network modifier. Conversely, the BBVP and BFVP systems showed reduced band gap values, attributed to the multivalent nature of Bi^{3+} and Fe^{3+} ions, which introduce additional localized states and increase the density of defect-related transitions. The shifting Urbach energies across all systems further indicate the presence of varying degrees of structural disorder and non-bridging oxygen content.

The comparative analysis confirms that UV-$_{Vis}$ spectroscopic parameters are sensitive indicators of glass structure evolution, particularly in identifying the interplay between electronic transitions, defect states, and bonding configurations. These findings establish the

compositional dependency of optical properties and affirm the feasibility of tailoring band structures through strategic dopant engineering. Ultimately, this study supports the broader vision of designing phosphate-based glasses with tunable optical features for targeted applications in UV shielding, photonics, and optoelectronic device platforms.

4.6. Reference

1. Wahab, E. A. A., Shaaban, K. S., & Yousef, E. S. (2020). Enhancement of optical and mechanical properties of sodium silicate glasses using zirconia. Optical and Quantum Electronics, 52(1), 458. https://doi.org/10.1007/s11082-020-02575-3
2. Abdelghany, A. M., & Hammad, A. H. (2015). Impact of vanadium ions in barium borate glass. Spectrochimica Acta Part A: Molecular and Biomolecular Spectroscopy, 137, 39–44. https://doi.org/10.1016/j.saa.2014.08.012
3. Hamad, A. H., & Abdelghany, A. M. (2016). Optical and structural investigations of zinc phosphate glasses containing vanadium ion. Journal of Non-Crystalline Solids, 433, 14–19. https://doi.org/10.1016/j.jnoncrysol.2015.11.016
4. Urbach, F. (1953). The long-wavelength edge of photographic sensitivity and of the electronic absorption of solids. Physical Review, 92(5), 1324. https://doi.org/10.1103/PhysRev.92.1324
5. Ghobadi, N., Sohrabi, P., & Hatami, H. R. (2020). Correlation between the photocatalytic activity of CdSe nanostructured thin films with optical band gap and Urbach energy. Chemical Physics, 538, 110911. https://doi.org/10.1016/j.chemphys.2020.110911
6. Haily, E. M., Bih, L., Jerroudi, M., & El Bouari, A. (2021). Optical properties and frequency-dependent conductivity of K_2O–BaO–TiO_2–P_2O_5 glasses. Materials Today: Proceedings, 51(6), 2027–2031. https://doi.org/10.1016/j.matpr.2021.06.082
7. Biswas, D., Das, A. S., Mondal, R., Banerjee, A., Dutta, A., Kabi, S., Roy, D., & Singh, L. S. (2020). Structural properties and electrical conductivity mechanisms of semiconducting quaternary nanocomposites: Effect of two transition metal oxides. Journal of Physics and Chemistry of Solids, 144, 109505. https://doi.org/10.1016/j.jpcs.2020.109505
8. Boudaoud, L., Banramdane, N., Bouzidi, A., Nekerala, A., & Desfeux, R. (2016). $(MoO_3)_{1-x}(V_2O_5)_x$ thin films: Elaboration and characterization. Optik, 127(2), 852–854. https://doi.org/10.1016/j.ijleo.2015.10.105
9. Dimitrov, V., & Sakka, S. (1996). Electronic oxide polarizability and optical basicity of simple oxides. Journal of Applied Physics, 79(3), 1736–1740. https://doi.org/10.1063/1.360962
10. Mondal, R., Biswas, D., Das, A. S., Ningthemcha, R. K. N., Deb, D., Bhattacharya, S., & Kabi, S. (2020). Influence of samarium content on structural, thermal, linear and non-

linear optical properties of ZnO–TeO_2–P_2O_5 glasses. Materials Chemistry and Physics, 255, 123561. https://doi.org/10.1016/j.matchemphys.2020.123561

11. Noorazlan, A. M., Kamari, H. M., Zulkefly, S. S., & Mohamad, D. W. (2013). Effect of erbium nanoparticles on optical properties of zinc borotellurite glass system. Journal of Nanomaterials, 2013, 940917. https://doi.org/10.1155/2013/940917
12. Azlam, M. N., Halimah, M. K., Shafinas, S. Z., & Daud, W. M. (2013). Effect of erbium nanoparticles on optical properties of zinc borotellurite glass system. Journal of Nanomaterials, 2013, 1–8. https://doi.org/10.1155/2013/940917
13. Davis, E. A., & Mott, N. F. (1970). Conduction in non-crystalline systems V. Conductivity, optical absorption and photoconductivity in amorphous semiconductors. Philosophical Magazine, 22(179), 903–922. https://doi.org/10.1080/14786437008221061
14. Anigrahawati, P., Sahar, M. R., & Ghosal, S. K. (2015). Influence of Fe_3O_4 nanoparticles on structural, optical and magnetic properties of erbium doped zinc phosphate glass. Materials Chemistry and Physics, 155, 155–161. https://doi.org/10.1016/j.matchemphys.2015.02.014
15. Ahmadi, F., Hussin, R., & Ghoshal, S. K. (2017). Structural and physical properties of Sm^{3+} doped magnesium zinc sulfophosphate glass. Bulletin of Materials Science, 40(6), 1097–1104. https://doi.org/10.1007/s12034-017-1462-5
16. Reddy, R. R., Nazeer Ahammed, Y., Rama Gopal, K., & Raghuram, D. V. (1998). Optical electronegativity and refractive index of materials. Optical Materials, 10(2), 95–100. https://doi.org/10.1016/S0925-3467(97)00171-7
17. Cheng, Y., Xiao, H., Shuguang, C., & Tang, B. (2009). Structure and crystallization of B_2O_3–Al_2O_3–SiO_2 glasses. Physica B: Condensed Matter, 404(8–11), 1230–1234. https://doi.org/10.1016/j.physb.2008.11.198
18. Hussain, S., Ahmed, R. J., Tanveer, M., Nadeem, M., Mahmood, H., Sattar, A., Iqbal, A., Hussain, I., Amjad, Z., Hussain, S. Z., Siddique, S. A., & Dousti, M. R. (2017). Glass Physics and Chemistry, 43(6), 538–547. https://doi.org/10.1134/S1087659617060219
19. Al-Harbi, N., Sayyed, M. I., Al-Hadeethi, Y., Kumar, A., Elsafi, M., Mahmoud, K. A., Khandaker, M. U., & Bradley, D. A. (2021). A novel CaO–K_2O–Na_2O–P_2O_5 glass systems for radiation shielding applications. Radiation Physics and Chemistry, 188, 109645. https://doi.org/10.1016/j.radphyschem.2021.109645

20. Charbonnier, M., & Romand, M. (2002). Tin-free electroless metallization of glass substrates using different PACVD surface treatment processes. Surface and Coatings Technology, 162(1–2), 19–30. https://doi.org/10.1016/S0257-8972(02)00382-1
21. Wang, C. C. (1970). Empirical relation between the linear and third order nonlinear susceptibility. Physical Review B, 2(6), 2015–2018. https://doi.org/10.1103/PhysRevB.2.2045
22. Behera, M., Naik, R., Sripan, C., Ganesan, R., & Mishra, N. C. (2019). Influence of Bi content on linear and nonlinear optical properties of $As_{40}Se_{60-x}Bi_x$ chalcogenide thin films. Current Applied Physics, 19(8), 884–893. https://doi.org/10.1016/j.cap.2019.05.007
23. Zhang, B., Shi, G., Yang, Z., Zhang, F., & Pan, S. (2017). Fluorooxoborates: Beryllium-free deep-ultraviolet nonlinear optical materials without layered growth. Angewandte Chemie International Edition, 56(15), 3916–3919. https://doi.org/10.1002/anie.201700540
24. Rahman, R. S., Shoab, M., Khan, Z. M. S. H., Aslam, Z., Asokan, K., & Zulfequar, M. (2020). Bandgap tunability endowed by isovalent sulphur doping in SeTe glassy films: Correlation with Kastner's and single oscillator models. Journal of Alloys and Compounds, 835, 155441. https://doi.org/10.1016/j.jallcom.2020.155441
25. Biswas, D., Hota, S. B., Mondal, R., Mukherjee, S., Chandra, P. C., Das, A. S., & Kabi, S. (2023). Effect of heavy metal and alkaline earth oxides on the optical and electrical mechanism of vanadium-phosphate amorphous glassy systems. Journal of Non-Crystalline Solids, 620, 122593. https://doi.org/10.1016/j.jnoncrysol.2023.122593
26. Biswas, D., Das, A. S., Kabi, S., Singh, L. S., Ahmed, M., Mukherjee, S., & Nambissan, P. M. G. (2021). Positron annihilation and correlated dielectric property studies of a transition metal oxide-modified quaternary nanocomposite $0.1P_2O_5$–$0.4ZnO$–$0.5(xV_2O_5$–$(1-x)MoO_3)$. Journal of Alloys and Compounds, 864, 158395. https://doi.org/10.1016/j.jallcom.2020.158395
27. Singh, Y. B., Biswas, D., Mondal, R., Chattopadhyay, S., Das, A. S., Mandal, D., Kabi, S., & Singh, L. S. (2024). Effect of Zn doping on optical properties and electrical conductivity mechanism of Sb–Ge–Se chalcogenide glassy systems. Materials Today Communications, 38, 108002. https://doi.org/10.1016/j.mtcomm.2023.108002
28. Hassanien, A. S., & Akl, A. A. (2016). Effect of Se addition on optical and electrical properties of chalcogenide CdSSe thin films. Superlattices and Microstructures, 89, 153–169. https://doi.org/10.1016/j.spmi.2015.10.044

29. Hassanien, A. S., & Akl, A. A. (2018). Optical characteristics of iron oxide thin films prepared by spray pyrolysis technique at different substrate temperatures. Applied Physics A, 124, 752. https://doi.org/10.1007/s00339-018-2180-6
30. Biswas, D., & Mondal, R. (2024). Tailoring of physical, optical, and thermal properties of $Se_{50-x}Te_{30}Ge_{20}Sb_x$ chalcogenide glasses: Influence of metalloids. Materials Today Communications, 38, 108501. https://doi.org/10.1016/j.mtcomm.2024.108501
31. Anigrahawati, P., Sahar, M. R., & Ghoshal, S. K. (2015). Influence of Fe_3O_4 nanoparticles on structural, optical and magnetic properties of erbium doped zinc phosphate glass. Materials Chemistry and Physics, 155, 155–161. https://doi.org/10.1016/j.matchemphys.2015.02.014
32. Tsang, L., Kong, J., & Ding, K.-H. (2004). Scattering of electromagnetic waves: Theories and applications (Vol. 3). Wiley. https://doi.org/10.1002/0471224286.ch4
33. Hota, S. B., Roy, D., Ghosh, B. K., Das, A. S., Mondal, R., Kabi, S., Chakrabarti, C., & Biswas, D. (2023). Effect of transition metal and alkali oxides on structural, optical and dielectric properties in zinc-phosphate amorphous glassy systems. Journal of Non-Crystalline Solids, 609, 122235. https://doi.org/10.1016/j.jnoncrysol.2023.122235
34. Kaur, P., Singh, D., & Singh, T. (2016). Optical, photoluminescence and physical properties of Sm^{3+} doped lead alumino phosphate glasses. Journal of Non-Crystalline Solids, 452, 87–92. https://doi.org/10.1016/j.jnoncrysol.2016.08.020

Chapter 5

Analysis of Dielectric Properties of Glass Nanocomposite Systems

5.1. Introduction

The dielectric analysis is useful in investigating the polarization properties, the energy storage capability and frequency-dependent electrical behaviour of both glass and nanocomposites of glass. In oxide glasses and in particular glasses which have already been studied, including oxides of the transition and heavy metals, the dielectric properties are closely and, in fact, inseparably associated with the structural order, ionic mobility and local dynamical properties of the charged carriers in the glass structure. This chapter presents a discussion of the dielectric properties of three structurally engineered glass nanocomposites, namely V_2O_5-Na_2O-ZnO-P_2O_5 (VNZP), Bi_2O_3-BaO-V_2O_5-P_2O_5 (BBVP) and Bi_2O_3-Fe_2O_3-V_2O_5-P_2O_5 (BFVP).

Glassy materials behave as dielectrics due to a number of mechanisms, such as dipolar orientation, interfacial (Maxwell-Wagner) polarization, space charge accumulation, and hopping conduction of mobile ions or polarons. These mechanisms interact at different frequencies and temperatures to bring important insights about how the material behaves in alternating electric fields. Specifically, dependence on frequency and temperature of the dielectric constant ($\varepsilon^{/}$) and dielectric loss ($\varepsilon^{//}$) indicates the process of structural relaxation, the properties of defect states, and the activity of polarization processes.

The added V_2O_5 leads to mixed valence states (V^{5+} /V^{4+}), further an ease in conducting via polaron hopping, contributing to a large effect on the dielectric loss and conductivity of the material. The high polarizability and presence of $6s^2$ lone-pair electrons in Bi_2O_3 contribute significantly to enhanced dielectric dispersion, while Fe_2O_3 contains iron ions capable of changing their oxidation state (Fe^{3+}/Fe^{2+}), which enables localized charge hopping within the glass matrix. Equally, the addition of ZnO and BaO contributes to changing oxygen coordination environment, the addition of oxygen, non-bridging oxygen levels and influences of ionic mobility. The formalism of the electric modulus is utilised to further deconvolve the dielectric response and relaxation dynamics. This method separates the relaxation behavior, which is free of electrode polarization effects, and gives a clear picture of the bulk dielectric response. Real ($M^{/}$) and imaginary ($M^{//}$) components of the electric modulus yield parameters concerning characteristic relaxation times and the nature of conduction pathways: that is, whether conduction is via pathway involvement of either long-range ion migration or localized relaxations.

Notably, the dielectric behavior of these glass systems is extremely composition-centred. The different modifying oxides vary in cation field strength, molar mass, and bonding character and this leads to large variations in dielectric dispersion, loss tangent behavior, and relaxation peak shifting. Such attributes are essential in the development of glassy materials which are to be applied in frequency-stable capacitors, electrochemical devices and energy storage technologies, where a high dielectric constant with low loss at frequencies at which the material is used is preferred.

The chapter, thus, is dedicated to the examination and comparison of dielectric properties of the series VNZP, BBVP and BFVP with discussing the effects of chemical structure and oxide composition on the measured frequency-and temperature-dependent electrical behavior. This way, the chapter would have made an attempt to form a stronger awareness of the dielectric mechanisms involved and to distinguish the most potential compositions towards the accomplishment of high-performance dielectric and electronic meets.

5.2. Quaternary V_2O_5–Na_2O–ZnO–P_2O_5 glass system

5.2.1. Investigation of Frequency-Dependent Complex Dielectric Permittivity

Dielectric materials develop the ability to store electrical energy when subjected to external electric field. This effect is determined by the external electric field applied to the material and the internal electric field created within the dielectric glass, which induces polarisation. The real component of the dielectric constant ($\varepsilon^{/}$) measures the capacity of electrical energy that is collected in the glasses matrix as cured to the imposed field [1]. Conversely, one can view the imaginary part ($\varepsilon^{//}$) as dielectric loss, and hence the energy is converted mostly into heat as a result of delayed polarisation processes [2]. The $\varepsilon^{//}$ is in essence the measure of energy loss of delayed polarization processes like the dipolar and ionic relaxations [3].

This research paper shows that the values of 6 were measured at a wide frequency range and different temperatures of vanadium and sodium-doped zinc-phosphate glass nanocomposites. Figs. **5.1(a-b)** and **5.2(a-b)** show the frequency dependence of $\varepsilon^{/}$ and $\varepsilon^{//}$ at different temperatures for samples with compositions **x = 0.15** and **x = 0.25**, respectively. The observation of a sharp non-linear decrease in $\varepsilon^{/}$ and $\varepsilon^{//}$ in the low frequency ($f < 40$ kHz) gives

rise to the fact that at higher frequencies (f > 40 kHz) both these values tend to be stabilized, which shows that frequency diminishes its influence at higher regimes.

The loss in ε in low frequencies is mainly explained by interfacial polarization and the dipolar polarization mechanism. The process of dipolar polarization is associated with the orientation of the permanent dipoles due to the externally applied field, whereas the interfacial (Maxwell-Wagner) polarization is the build-up of mobile charge carriers at the interfaces generated by the heterogeneous structure of the glass [4,6]. In this regime, ionic migration also reduces the values of $\varepsilon^{//}$ exponentially, with consequences mainly of V^{4+} /V^{5+} transition metal ions contributing space charge polarization.

Reorientation of dipoles and movement of the charge carriers grow more slowly than the field that swings extremely fast, in frequency, across the electric field. This difference causes both the values of $\varepsilon^{/}$ and $\varepsilon^{//}$ to diminish drastically. At sufficiently high frequencies, orientational polarization is significantly suppressed, leading to a plateau in $\varepsilon^{/}$ and minimal dielectric loss ($\varepsilon^{//}$), indicating the dominance of instantaneous polarization processes (e.g., electronic or ionic).

Further evidences of the respective positive effect of adding V_2O_5 in both $\varepsilon^{/}$ and $\varepsilon^{//}$ are observed in **Figs. 5.3 (a-b)** where the solid circles indicate the temperature of 433 K. Such a boost is associated with the increase in polarizable centres, the presence of multivalent vanadium ions, which favour polaron hopping and localized shift of charges around. To quantify the dielectric relaxation process and the contributions to polarization losses and conduction losses, the Havriliak-Negami (HN) formalism is utilized [6]. The HN model presents a fully detailed account of the dielectric response of complex disordered systems, and the mathematical attitude of the complex dielectric function can be illustrated as below [6]:

$$\varepsilon^{*} = \varepsilon_{\infty} + \frac{\varepsilon_{s} - \varepsilon_{\infty}}{\left[1 + (i\omega\tau_{HN})^{\alpha_{HN}}\right]^{\gamma_{HN}}} \tag{5.1}$$

In the above equation, ε_s corresponds to the static permittivity at low frequencies, while ε_∞ corresponds to that at high frequencies. τ_{HN} and α_{HN} represent the relaxation time of permittivity and offset angle in the real and imaginary planes, respectively, whereas γ_{HN} represents high-frequency non-linearity. Furthermore, γ_{HN} and α_{HN} are recognized as the shape parameters that follow the conditions $0 \leq \gamma_{HN} \leq 1$ and $0 \leq \alpha_{HN} \leq 1$ [6]. Precisely, $\varepsilon^{/}(\omega)$ and $\varepsilon^{//}(\omega)$ are correspondingly defined by the succeeding relations following the HN formalism [6].

$$\varepsilon'(\omega) = \varepsilon_\infty (\varepsilon_s - \varepsilon_\infty) \mathrm{Re}\left[\frac{1}{\left[1+(i\omega\tau_{HN})^{\alpha_{HN}}\right]^{\gamma_{HN}}}\right] \tag{5.2}$$

and

$$\varepsilon'(\omega) = \varepsilon_\infty (\varepsilon_s - \varepsilon_\infty) \mathrm{Im}\left[\frac{1}{\left[1+(i\omega\tau_{HN})^{\alpha_{HN}}\right]^{\gamma_{HN}}}\right] + \frac{S}{\omega^p} \tag{5.3}$$

In this context, S indicates the conductivity component that does not vary with frequency, whereas p signifies the related frequency exponent. The conductivity of glassy systems with transition metal oxides (V_2O_5) can be elucidated by Small polaron hopping mechanism.

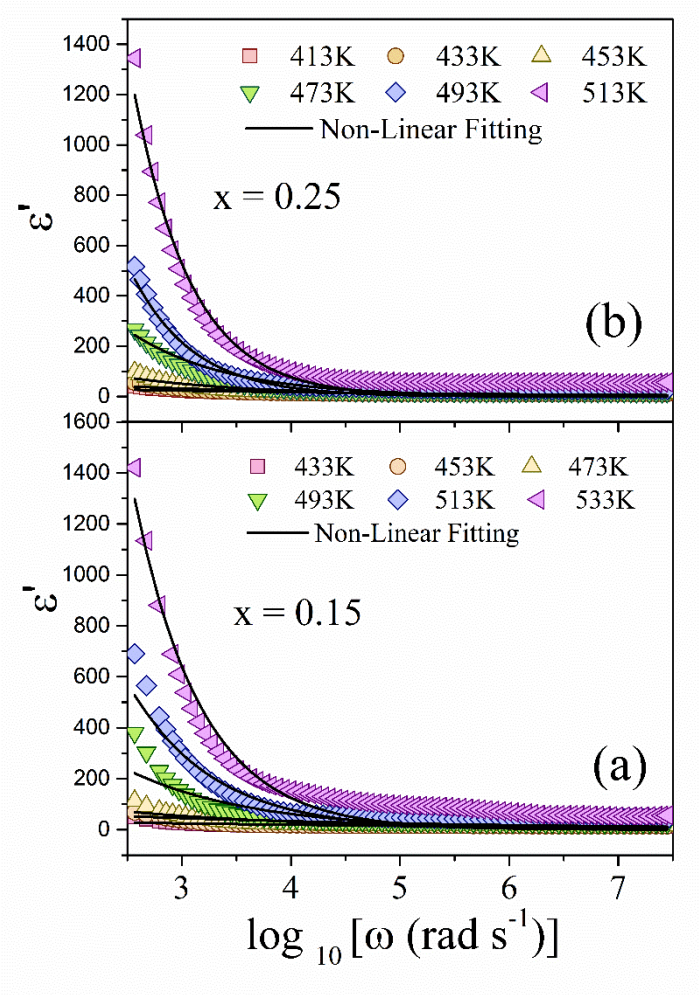

Figs. 5.1(a-b). Frequency-dependent dielectric constant for glass samples (x = 0.15 and 0.25) measured at various temperatures

The solid black lines in **Figs. 5.1(a-b)** and **5.2(a-b)** depict the outcomes of non-linear fitting applied to the experimental data, performed following the Havriliak–Negami (HN) model outlined in **Eq. (5.2)** and **(5.3)**. The fitted parameters in this model are tabulated appropriately in **Table 5.1**. The non-unity values of the exponent p and the fact that the calculated values of the shape parameters γ_{HN} and α_{HN} are not equal to unity indicate that the non-Debye-type dielectric relaxations are present in the studied glass systems [6]. Departures of such deviations to ideal Debye characteristics suggest a heterogeneous and asymmetric distribution of relaxation times, usually due to structural and compositional heterogeneity. Furthermore, **Table 5.1** lists the dielectric strength ($\Delta\varepsilon$), defined as the difference between the low-frequency static permittivity (ε_s) and the high-frequency limiting permittivity (ε_α). An increase in V_2O_5 concentration enhances the polarization of oxygen ions, thereby leading to higher dielectric strength values.[7]

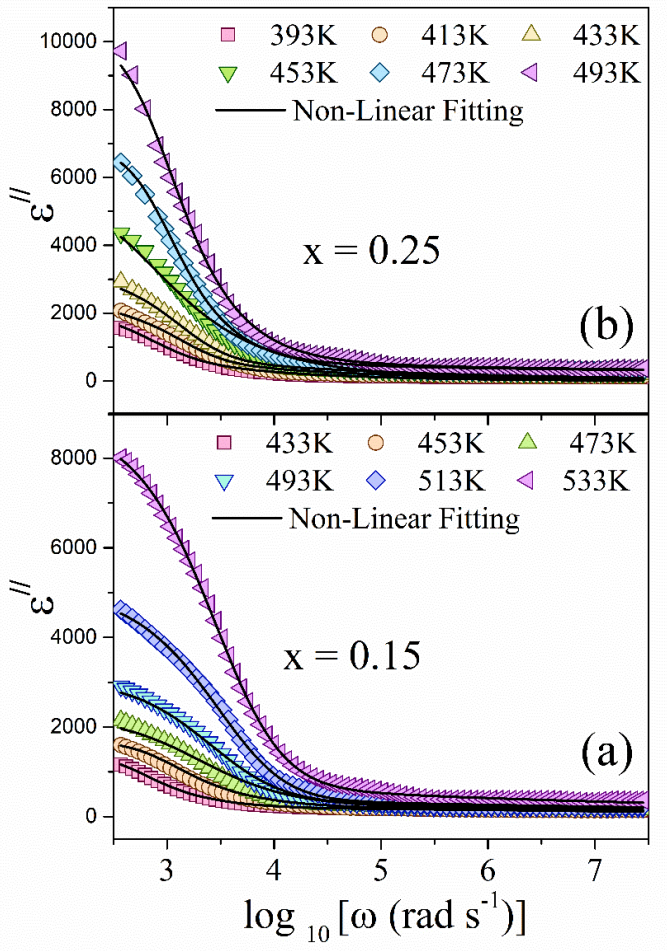

Figs. 5.2 (a-b). Variation of dielectric constant with frequency for glass samples with x = 0.15 and 0.25 at various temperatures

Table 5.1. Dielectric parameters estimated from Havriliak–Negami (HN) fitting at T= 453 K, along with E_τ for 0.35ZnO-O.25P_2O_5-(0.4-x) Na_2O-xV_2O_5 glass samples.

(% mol)	Δε (± 5.0)	α_{HN} (± 0.005)	γ_{HN} (± 0.005)	P (± 0.008)	E_τ (eV) (±0.03)
0.05	163.5	0.738	0.514	0.089	1.32
0.10	193.4	0.774	0.543	0.102	1.72
0.15	202.1	0.789	0.603	0.126	1.77
0.20	221.3	0.812	0.632	0.132	1.81
0.25	262.2	0.836	0.635	0.231	1.84

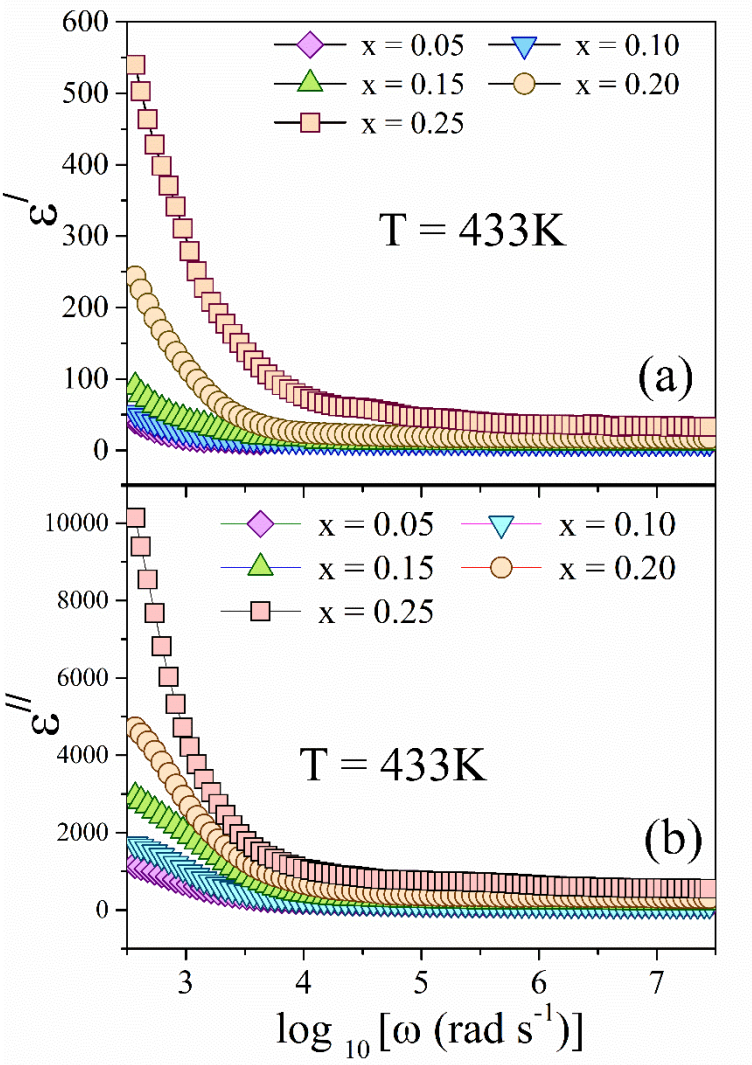

Figs. 5.3 (a-b). Frequency-dependent dielectric loss ($\varepsilon^{/}$) and dielectric constant ($\varepsilon^{//}$) at T = 433K.

5.2.2. Investigation of Temperature-Dependent Complex Dielectric Permittivity

The temperature dependence of real ($\varepsilon^{/}$) and imaginary ($\varepsilon^{//}$) components of the dielectric constant of the glass sample used in this study, that is, x=0.05 and x=0.20, has been investigated and systematically reported over different frequencies, shown in Figs 5.4(a-b) and 5.5(a-b), respectively. At the lower temperatures, both $\varepsilon^{/}$ and $\varepsilon^{//}$ show little temperature and frequency dependence, which implies that dipolar mobility is restricted and that thermal activation is low. But with rising temperature, the thermal energy makes the movement of the dipoles easy along the direction of the electric field being applied. Such an increment in alignment (enhanced by the increment in thermal agitation) causes a concurrent increase in both $\varepsilon^{//}$ values [8]. At low frequencies, the fact that the intermolecular forces become weaker at elevated temperatures further facilitates the dipolar orientation of electrons and polarization of the vibrations and adds to the overall increase in dielectric response, as present in the figures mentioned above [9]. In these materials, the dielectric loss ($\varepsilon^{//}$). exists as a result of three main mechanisms: the dipolar relaxation, the vibrational resonance, and the conduction loss. These include conduction loss, which is directly proportional to the AC conductivity of that system, which can be attributed to thermally activated hopping of charge carriers. Consistent with the expectation, the conduction losses are low at low temperatures as a consequence of the limited mobility of the carriers, but they become very high as the temperature rises, owing to the improved ability of the carriers to transport charge through the encompassing glassy material.

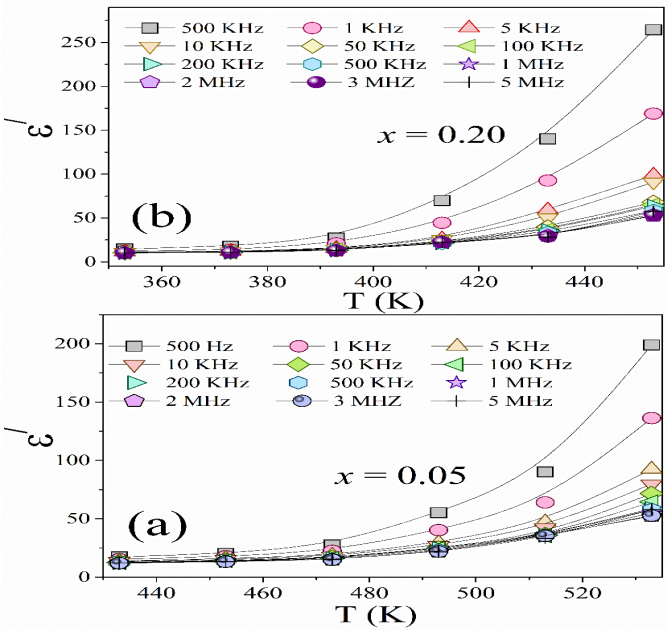

Figs. 5.4(a-b). Temperature-dependent dielectric loss ($\varepsilon^{/}$) of glass samples x = 0.05 and *x* = 0.20.

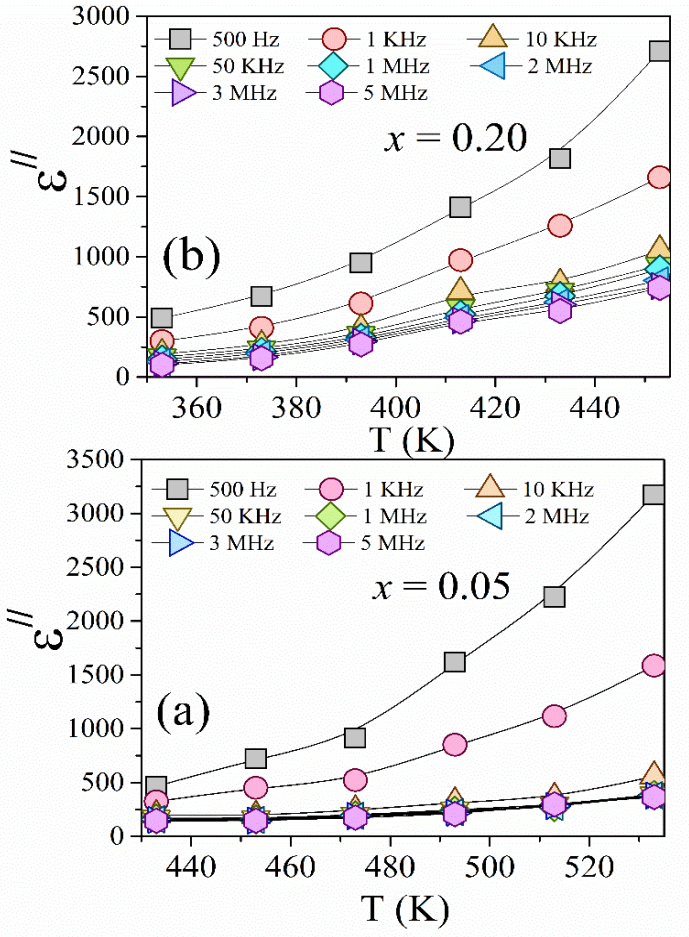

Figs. 5.5 (a-b). Temperature dependence of the dielectric constant ($\varepsilon^{//}$) for glass samples with compositions x = 0.05 and x = 0.20.

5.2.3. Analysis of Electrical modulus

The complex electric modulus (M^*) formulation can be used effectively in narrowing down the cause of interfacial polarization and dipolar relaxation during the electrical conductivity processes, as well as being a beneficial way of presenting an informative picture about the overall dielectric relaxation and charge transport activity of the material in question [10]. The real and imaginary components of M^*, $M^{/}$ and $M^{//}$ are calculated by the **Eq. 5.4** at various temperatures on the samples of glass under investigation. **Figs. 5.6 (a-b)** shows the frequency-dependent behaviour of the $M^{/}$ and $M^{//}$ when the sample of glass is at the temperature range 393-513 K and x = 0.15. The non-existence of the electrode effect or interfacial polarization may be seen in **Fig. 5.6(a)** as the value of $M^{/}$ decreases closely approaching zero at lower frequencies. The alteration in $M^{/}$ spectra is a specification of a variation in sample rigidity [11]. $M^{/}$ is frequency dependent, rising to a dispersive region, then peaking with

frequency followed by its loss peak across higher frequencies, which shift at an increasing temperature.

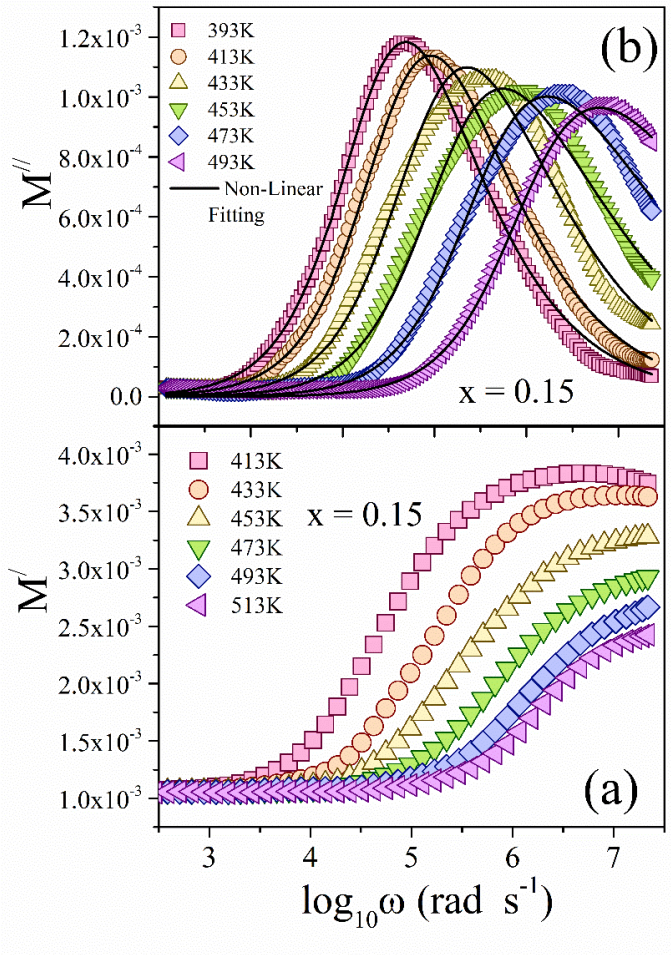

Figs. 5.6 (a-b). Frequency dependence of $M^{/}$ and $M^{//}$ for the glass sample with composition $x = 0.15$.

It is widely thought that the dispersiveness of the real part of the electric modulus ($M^{/}$) is mainly due to relaxation processes that play out within the whole frequency domain in a distributed manner, as previous studies also thought [12]. As shown in **Fig. 5.6(a)**, the maximum $M^{/}$ ($M^{/}_{max}$) values show a significant reduction with increasing temperature, and this means that ionic or polaronic short-range mobility plays an important role in the conduction mechanism of the glasses under study. The increased thermal energy, as the temperature is increased, allows more ready lining up of charge carriers and molecular dipoles, hence, increasing their mobility throughout the glass network [13]. **Fig. 5.6(b)** shows the imaginary component of electric modulus ($M^{//}$), as a parameter of the amount of energy dissipated through an external electric field, as a periodicity of the temperature. The low frequency part of the $M^{//}$ spectra has low values **(Fig. 5.6(b)),** and this is mainly as a result of the effects of capacitance in parallel

configuration and electrode polarization. This effect is the result of an extensive buildup of mobile charge carriers at the glass-electrode interface. These spectra ($M^{//}$) show a characteristic relaxation peak as a function of frequency (in this case, shifting the maximum relaxation peak) and move to higher frequencies (at ω_{max}) with temperature, indicating a thermally activated relaxation mechanism. The aspect of behavior implies that charge carriers attain a reasonable amount of thermal energy that facilitates jumping over localized potential barriers, hence decreasing the relaxation time and increasing the relaxation frequency [12]. Below the relaxation peak, the conduction process is explained by long-range small polaron hopping, though the situation changes above the peak frequency, where the process is dominated by localized short-range hopping. The two-mode conduction shows the dynamic behavior of the switchback of the localized motion and extended-range transport of charge carriers with temperature [13]. Moreover, one can define the electric modulus M^* as Fourier transform of an effective time-dependent relaxation function $\phi(t)$ providing a more sophisticated way of discussing the relaxation behavior in disordered media [5,14].

$$M^* = M_\infty \left[1 - \int_0^\infty \exp(-\omega t) \left(\frac{d\varphi}{dt} \right) dt \right] \tag{5.4}$$

In this formulation, $\phi(t)$ represents the Kohlrausch–Williams–Watts (KWW) function, which models how the electric field changes over time within the glass material [15].

$$\varphi(t) = \exp\left[-\left(\frac{t}{\tau_c} \right) \beta \right] \qquad \text{where} \quad 0 < \beta < 1 \tag{5.5}$$

Here, exponent β denotes the Kohlrausch-Williams-Watts (KWW) stretched exponential parameter that is a quantitative measure of how far the system is not behaving ideally as a Debye-type relaxation process; β = 1 indicates a perfect Debye relaxation process. ß values below unity mean there is non-Debye relaxation, which means that the relaxation times are more extended in the system. In the meantime, the value of τ_c is the characteristic conductivity relaxation time, nucleating the phenomenon that occurred on the time scale of returning equilibrium to the mobile charge carrier after being distorted. The KWW formalism has been modified by Bergman, which has characterized the behavior of the imaginary part of the electric modulus ($M^{//}$) better in improving the simplification in non-Debye dielectric relaxation. According to the model by Bergman, the mathematical formulation of $M^{//}$ considers the asymmetry and broadening of the relaxation peak, and it is given by [15]:

$$M^{//} = \frac{M^{//}_{\max}}{(1-\beta) + \frac{\beta}{1+\beta}\left[\beta\left(\frac{\omega_{\max}}{\omega}\right) + \left(\frac{\omega}{\omega_{\max}}\right)^{\beta}\right]} \tag{5.6}$$

The maximum value of $M^{//}$ is referred to as $M^{//}_{max}$ and the maximum angular frequency is ω_{max} in this case. The ability of the equation developed by Bergman to fit the experimental data can be depicted by solid black lines in **Fig. 5.6(b)**. It can be observed in **Fig. 5.7(a)** that one of the fitting parameters, i.e. β, depends on the temperature. The conductivity relaxation process is a non-Debye type and is denoted when the β values are less than unity [15,16]. The reciprocal of the extreme angular frequency is the relaxation time ($\tau_c = 1/\omega_{max}$).

The relaxation times (τ_c) at 453 K are shown in **Fig. 5.7(b)**. The activation energy (E_τ) associated with the conductivity relaxation process could be found using the formula given below.

$$\tau_c = \frac{1}{\omega_{\max}} = \tau_0 \exp\left(-\frac{E_\tau}{K_B T}\right) \tag{5.7}$$

K_B, in this equation, is the Boltzmann constant and τ_0 is a pre-exponential constant, and T = absolute temperature in Kelvin. The energy needed in such a condition, represented by the symbol E_τ, to initiate the molecules to be translated by the medium, is the one needed to invoke their conformation change to another steadier state. In the low activation energy (E_τ), temperature has very little influence on the rate of the conductivity relaxation process. It is related to the rotational movements of the side group of molecules on a molecular basis. The large activation energy is, however, connected with structural relaxation, where the activation energy deals with the local rearrangement of the environment of one molecule, rather than the interconversion of conformations. E_τ is also taken to correlate with the movement or softening of oxygen ions. **Table 5.1** provides the estimates of E_τ in each of the crossings. The results indicate clearly that E is affected by composition, and an increase occurs with the inclusion of V_2O_5.

The data can be further considered with the help of the empirical model of Cole-Davidson [52] according to the following expressions:

$$M^{/} = \frac{M_\infty M_s\left[M_s + (M_\infty - M_s)(\cos\phi)^{\gamma}\cos\gamma\phi\right]}{M_s^2 + (M_\infty - M_s)(\cos\phi)^{\gamma}\left[2M_s\cos\gamma\phi + (M_\infty - M_s)(\cos\phi)^{\gamma}\right]} \tag{5.8}$$

$$M'' = \frac{M_\infty M_s \left[(M_\infty - M_s)(\cos\phi)^\gamma \sin\gamma\theta \right]}{M_s^2 + (M_\infty - M_s)(\cos\phi)^\gamma \left[2M_s \cos\gamma\phi + (M_\infty - M_s)(\cos\phi)^\gamma \right]} \tag{5.9}$$

Where, $0 < \gamma \leq 1$, $tg\phi = \omega\tau$

$$\text{and, } \omega_{max}\tau = tg\left(\frac{1}{\gamma+1}\frac{\pi}{2}\right) \tag{5.10}$$

In this juncture, τ is the relaxation time. As the γ goes to unity, we end up in the pure Debye model having only a single relaxation time with the **Eqn. (5.8)** and **(5.9)**. Parameters of the relaxation are determined by the Cole-Davidson model of a representative temperature, the precision of the fitting procedure and a simulation of the M'' spectrum. It is established that relaxation times correspond nearly to the value of Eqn. (5.7).

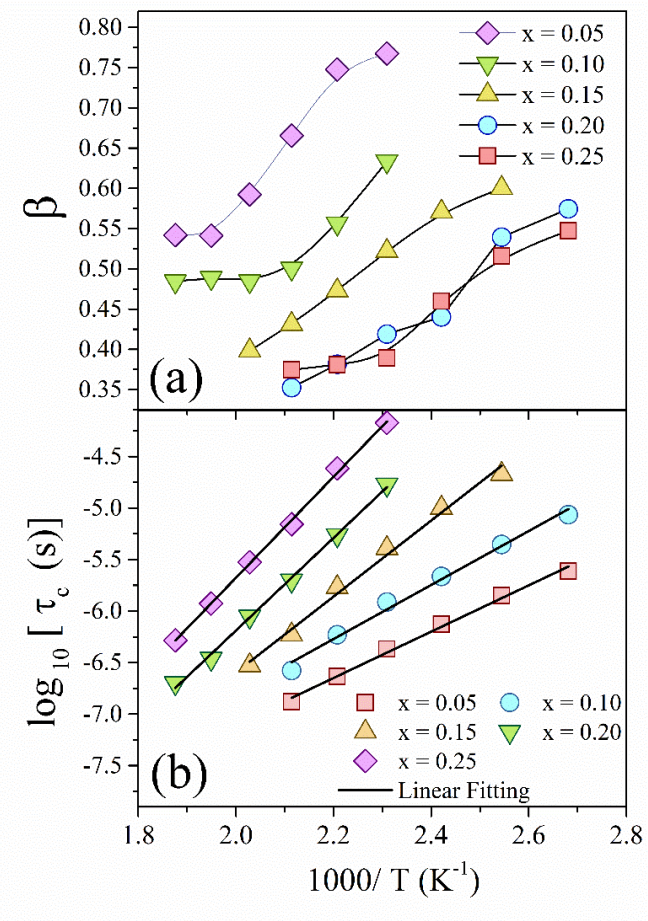

Figs. 5.7 (a) KWW stretched coefficient (β) and **(b)** conductivity relaxation time (τ_c) against the reciprocal of temperature.

For scaling analysis, each $M^{//}$ spectrum is normalized to its peak value ($M^{//}_{max}$) and the frequency is expressed relative to ω_{max}.[17]. **Fig.5.8 (a)** gives the scaled spectra of the glass sample x = 0.15 at a temperature range 413K to 473K. And the scaled spectra of all the glass samples at a constant temperature of 453K are shown in **Fig. 5.8 (b)**. The scaled spectra at all temperatures of the glass sample x = 0.15 [**Figs 5.7 (a)**] are shown to coalesce in the single master curve, showing that the conductivity relaxation process does not depend on the temperature. However, on the other hand, as shown in Fig.5.8 (b), the scaled spectra of all the glass samples at constant temperature do not overlap properly and hence validate the true nature of the compositional dependency of the conductivity relaxation process.

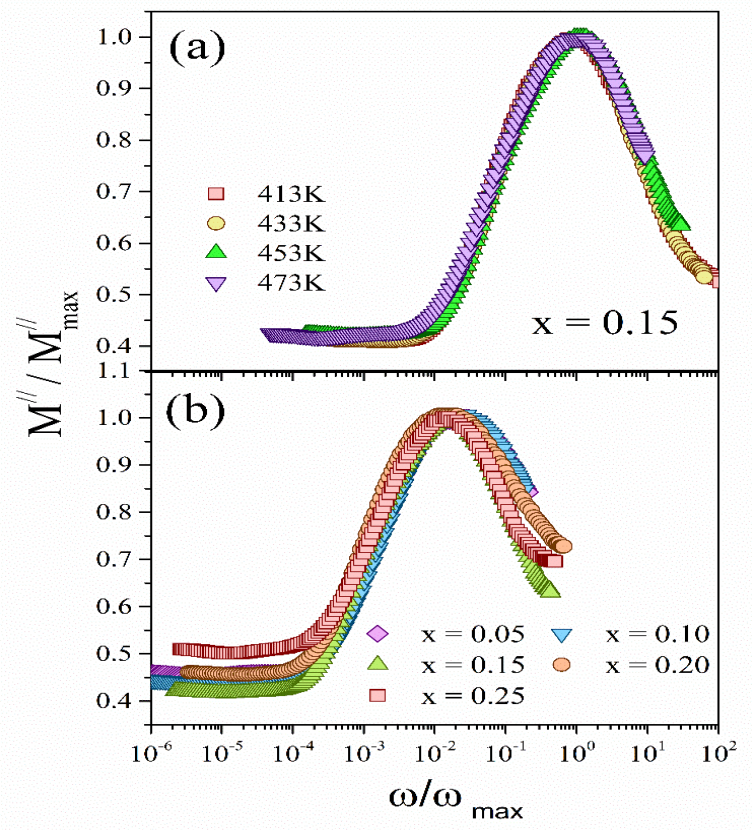

Figs. 5.8 (a) Electric modulus scaling spectra of the glass sample with composition x = 0.15 at different temperatures, and (b) compositional modulus scaling spectra of all glass samples.

5.3. Quaternary Bi_2O_3-BaO-V_2O_5-P_2O_5 glass system

5.3.1. Investigation of Frequency-Dependent Complex Dielectric Permittivity

The graph peovided investigates the dependency of dielectric permittivity upon frequency as well as temperature in the case of a sample of which whose composition parameter is x = 0.35.

Fig.5.9(a) and (b) are the real part and the imaginary part of the permittivity respectively, over a range of frequencies and various temperatures 413K to 533K.

As can be seen in **Fig. 5.9(a)**, the real part of the dielectric permittivity (ε') is decreasing with increasing frequency at any temperature that was recorded. In low frequencies, ε' is observed to take very high values, which in this case can be attributed to high polarization effects due to dipole orientation and the mobility of mobile charge carriers in the presence of the applied electric field. More commonly, these carriers and dipoles can no longer react effectively to the very quickly alternating electric field, and ε' drops off and eventually levels off. This positive thermal tuning of ε' is due to the creation of additional thermal energy and means greater dipole orientation and better polarisation.**Fig. 5.9(b)** demonstrates how the imaginary component of permittivity (ε'') changes with the level of frequency. There is a steady downward trend in the value of ε'' as frequency goes up. This is typical of the dielectric materials, where polarization mechanisms like interfacial and space charge polarization play an important role at low frequencies, resulting in increased dielectric loss. At the higher frequencies, these mechanisms are not able to keep up with the rapid field reversals, and therefore, there is less energy dissipated. Increase in ε'' with temperature shows that increased dielectric loss has occurred, which is probably due to thermally induced transport of dipoles and charge carriers.Space charge polarization and interfacial effects are mainly the causes of the high values of ε' and ε'' at low frequencies since mobile ions tend to accumulate at the interfaces and travel in accordance with the external field. At higher frequencies, the motion of these ions is not fast enough to follow the alternation of the field, and hence the polarization contribution decreases. Such a frequency-dependent dielectric is characteristic of amorphous glass systems with long-range ionic conduction dominating at lower frequencies and localized ion hopping becoming dominant at higher frequencies.

The existence of Bi_2O_3 and V_2O_5 in the glass skeleton plays an imperative role in the dielectric response. Such oxidations bring about structural changes that depolymerize the glass network (e.g. alteration of phosphate coordination and variations in valence states of vanadium) and consequently enhance free volume and ion mobility. As such, the dielectric response, including at lower frequencies, is increased as a result of the better ionic mobility and dipolar alignment. Experiments carried out in the literature have also shown similar trends in glasses doped by Bi_2O_3 corresponding to the respective two-way mixed ion-formation or polarization conduction and reinforcement in low frequency polarization [1-4]

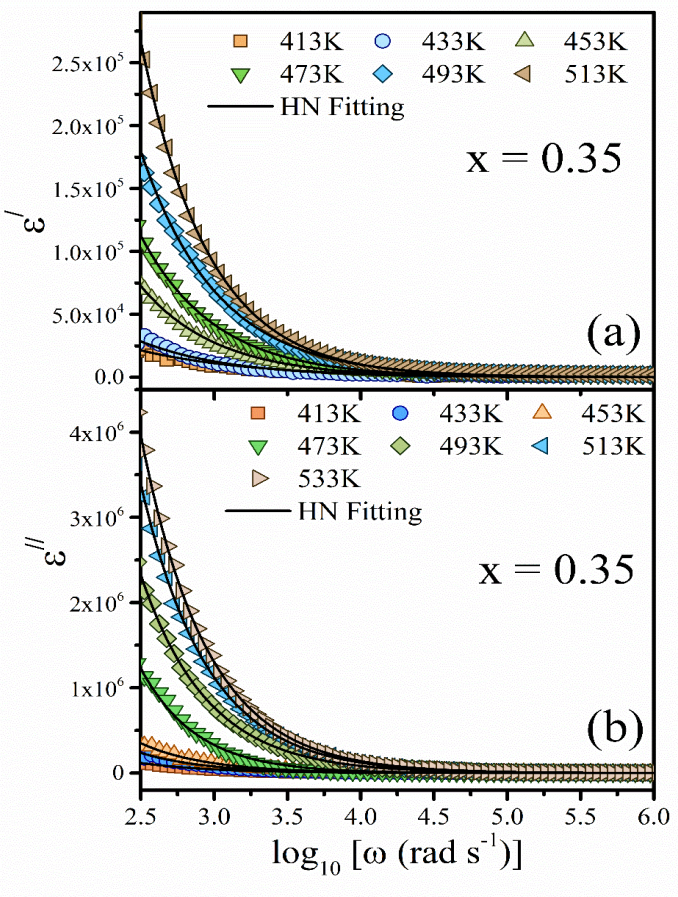

Figs. 5.9(a-b). The frequency-dependent dielectric constant(ε') and dielectric loss (ε'') of the glass sample $x = 0.35$ at different temperatures.

Regarding the description of the electrode polarization and conduction loss phenomena, it is possible to refer to the Havriliak–Negami (HN) method. This result furnishes a more accurate form of formulating dielectric functions using more formal mathematical methods using Eq.5.1 [6].The values of various parameters—namely, the relaxation time of the permittivity (τ_{HN}), the phase angle offset, α_{HN}, and the non-linearity factor γ_{HN}—are provided below, under their respective definitions. Furthermore, the shape parameters α_{HN} and γ_{HN} are referred to as being circumscribed by the constraints $0 \leq \gamma_{HN} \leq 1$ and $0 \leq \alpha_{HN} \leq 1$ [6]. The Havriliak-Negami model [6] represents the values of permittivity at the real and imaginary points, referred to as $\varepsilon'(\omega)$ and $\varepsilon''(\omega)$ [6]as described in *5.2.1*(Eq. 5.2 and 5.3).**Fig. 5.9(a)** and **Fig. 5.9(b)** indicate the solid black curves, which represent Havriliak-Negami (HN) fitting; it is an empirical model which is used to fit non-Debye-type dielectric relaxation. HN formalism can be used when broadened and asymmetric relaxation spectra are observed in disordered systems in an effective analytical way [6]. It provides parameters including the relaxation time (τ_{HN}), the shape parameters (α_{HN} and γ_{HN}) and the low and high-frequency limits of the permittivity (ε_s and ε_∞), providing a full

characterization of complex relaxation behavior. These parameters were derived using nonlinear least squares fitting, and the values obtained are shown in **Table 5.2**. The quality of the fit supports the idea that dielectric relaxation in the analysed glasses results from a combination of two processes, namely electrode polarisation at low frequencies and hopping conduction at intermediate and high frequencies. That is, heterogeneity of the glass matrix and a broad spectrum of relaxation times of constituent dipoles and charge carriers are reflected in the fact that the ideal Debye behaviour is not observed, as exemplified by the HN model.

All these results illustrate the complex interaction of frequency, temperature, and dielectric relaxation in these oxide glasses. The increase in both the real ($\varepsilon^{/}$) and imaginary ($\varepsilon^{//}$) components of permittivity with rising temperature is consistent and reflects a greater alignment of dipoles and increased mobility of thermally activated charge carriers. This process is essential for achieving and maximising the dielectric response in applications requiring thermal stability and efficient energy storage. Furthermore, the findings emphasise the importance of structural and compositional adjustments, including adding Bi_2O_3 and V_2O_5, when tailoring the dielectric properties to meet the requirements of modern electronic and energy-storage technologies.

Table 5.2. Dielectric parameters estimated from Havriliak–Negami (HN) fitting at T= 473 K, along with E_τ for xBi_2O_3−(0.4−x) BaO−$0.3V_2O_5$−$0.3P_2O_5$ glass samples.

(% mol)	$\Delta\varepsilon$ (± 5.0)	α_{HN} (± 0.005)	γ_{HN} (± 0.005)	P (± 0.008)	E_τ (eV) (±0.03)
0.05	354	0.63	0.51	0.076	0.76
0.15	412	0.60	0.57	0.081	0.63
0.25	443	0.78	0.67	0.101	0.58
0.35	612	0.81	0.73	0.122	0.51

5.3.2. Investigation of Temperature-Dependent Complex Dielectric Permittivity

The temperature-dependent behavior of the complex dielectric permittivity in BBPV glass-ceramic samples with composition x = 0.35 provides valuable insights into their dielectric response under varying thermal and frequency conditions. As illustrated in **Figs. 5.10(a)** and **5.10(b)**, both the real component of the dielectric constant ($\varepsilon^{/}$) and the dielectric loss ($\varepsilon^{//}$) show

a strong dependence on temperature and frequency. In the low-frequency region, ε' shows a pronounced increase with rising temperature, reflecting the influence of thermally activated polarization mechanisms—primarily dipolar orientation and interfacial (Maxwell–Wagner) polarization. This enhancement is particularly evident in the low-frequency regime, where charge carriers and dipoles are afforded sufficient time to align with the slowly oscillating external electric field, thereby contributing effectively to the overall polarization [7].

On the contrary, at higher frequencies, ε' tends to level off and becomes relatively insensitive to temperature variations. This behavior indicates that polarization processes at elevated frequencies are governed more by the inherent structural characteristics of the material than by thermal activation. The inability of dipolar entities and space charge carriers to follow the rapidly alternating field at such frequencies results in a diminished dielectric response. These observations are consistent with previously reported trends in glass-based dielectric systems, where high-frequency responses are primarily attributed to localized relaxation phenomena and short-range ionic movements [8].

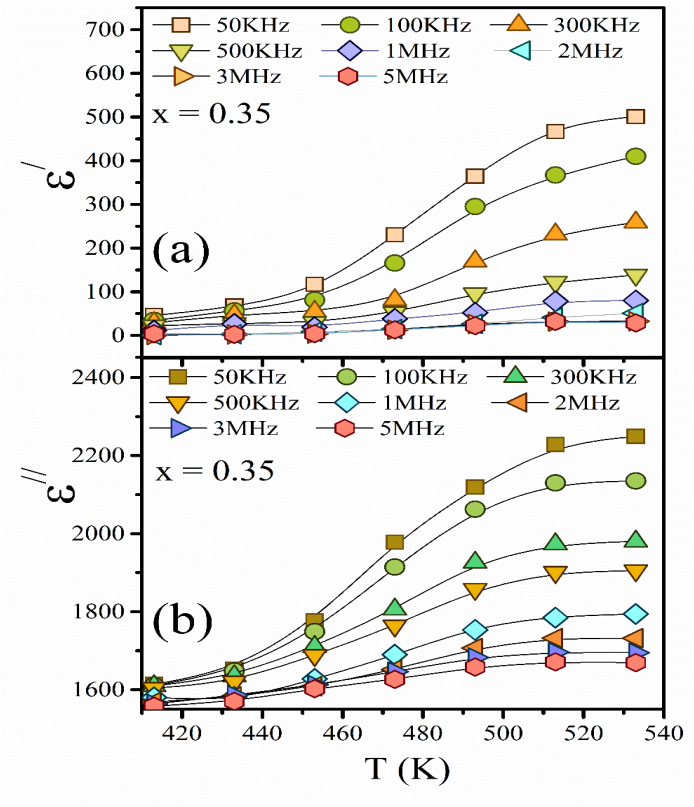

Figs. 5.10(a-b). Temperature-dependent dielectric loss (ε') and dielectric loss (ε'') of glass samples x = 0.35

Likewise, ε'', indicative of energy loss through heat, shows an upward trend with increasing temperature, especially noticeable at lower frequency ranges. Therefore, this trend has been explained by the fact that the mobility of dipoles and the charge carriers at high temperatures in the glass matrix increases, thereby enabling more energy to be absorbed. With higher thermal energy content, these entities can better respond to the applied electric field, thus giving higher dielectric losses at low frequencies.

Conversely at higher frequencies, the ε'' does not change too much with temperature. This implies that the unifying elements relaxations in this regime are identified with rapid dipolar reorientations, which are mostly determined by the natural structure of the glass and are minimally affected by thermal activation [18]. This behavior is caused in great part by the addition of Bi^{3+} ions in the mix of BBPV glass-ceramic. Having a greater ionic radius and polarizability, Bi^{3+} ions increase the efficacy of dipolar interactions and lead to a better dielectric relaxation [19].

Taken together, the dielectric behavior of the BBPV glassy samples shows better dielectric performance at higher temperatures, particularly in the low-frequency region. Such an improvement can be mostly attributed to polarization and relaxation of charge carriers, which is enabled by Bi^{3+} ions. The set of these effects implies that such glass-ceramic compositions may become prospective materials in terms of high dielectric permittivity and energy storage with high efficiency over a wide range. The results can be used as instructive ways of glass-based material designs and optimization to be used in the electronic parts and the energy storage gadgets of the upcoming generation [2, 4].

5.3.3. Investigation of the Electrical Modulus

Fig. 5.11(a–b) presents M' and M'' as functions of angular frequency ($log_{10}\omega$) and temperature for various glass samples. The peak value, denoted as M''_{max}, occurs at a characteristic angular frequency ω_{max}. There is a good correspondence of the experimental data to the Bergman equation, which is indicated by the solid black curves in **Fig. 5.11(b)**.

The complex electrical modulus notation (M^*) is convenient in the sense that it is, to a greater extent, able to decouple the contribution of interfacial polarization and dipolar relaxation relative to the contributions of bulk conductivity or dielectric relaxation. In this work, M' and M'' will be measured at different temperatures. **Fig. 5.11(a -b)** shows frequency dependence of M' and M'' in a sorted sample with x = 0.25 over the temperature range 393 to 493 K. When

frequencies are low, the M' tends to "0", and this indicates that there is little interfacial polarization or electrode effect. With higher frequency, M' decreases, and sample stiffness and dispersion increase, with a visibly temperature-dependent relaxation peak [20].

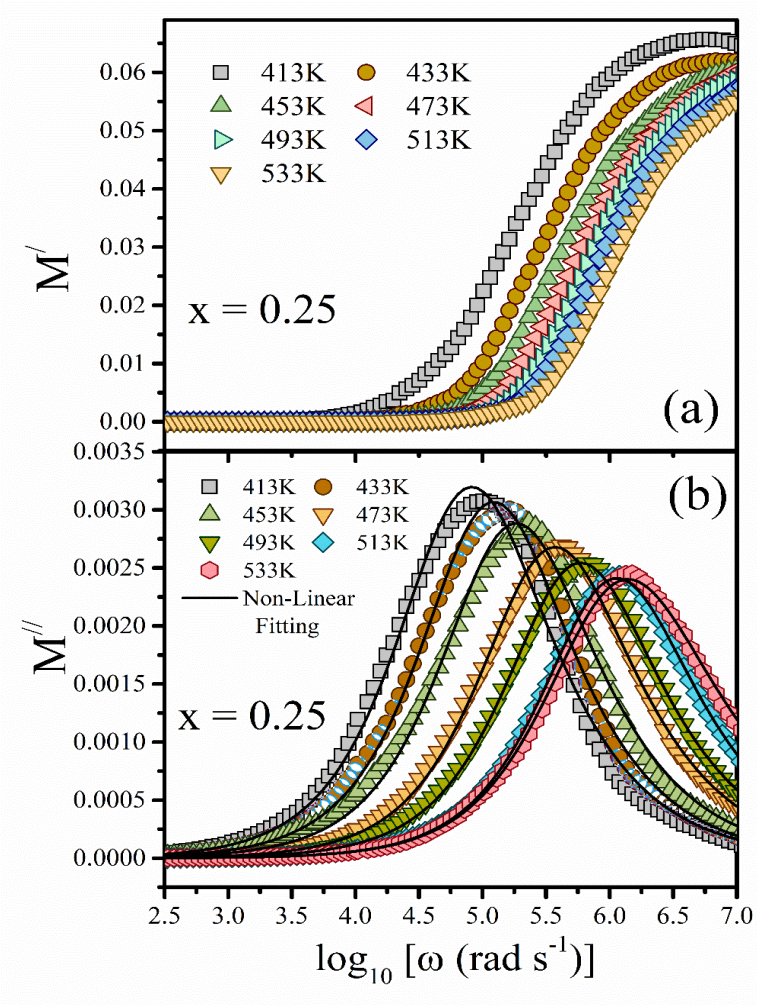

Fig. 5.11 (a-b). Frequency-dependent real (M') and imaginary (M'') parts of the electric modulus for the glass sample with composition x = 0.20

Fig. 5.11(a-b) shows an in-depth analysis of the real (M') and imaginary (M'') parts of the electrical modulus on the (x = 0.25) BBPV glass sample plotted as dependent on angular frequency ($log10\omega$) in the temperature range 393-493 K. At low frequencies, M' approaches to zero indicating that the mobile ions are not affected by restoring forces and they rather move freely through the glass network as it is common with long-range ionic conduction at low frequency [21]. M' also has quite a bit of dispersion with the increase in frequency, which signals that there is a large distribution of relaxation times. The M' peak can be observed at lower frequencies, and its value reduces as the temperature increases. This lowering in peak height implies that at high temperatures, there is a high mobility of ions in the short range,

thereby increasing the conductivity of the glass system. Further, the consistency of M' and M'' profiles so far as temperatures are concerned suggests an equivalent dynamic of relaxation in the samples [22].

Fig. 5.11(b) indicates that M'' is the amount of energy dissipated by dielectric relaxation produced by an applied electric field. At low frequencies, the M' and M'' will be suppressed because of the charge deposition at the interfacial (glass-electrode), which is a direct effect of the electrode polarization and the high interfacial capacitance. As the temperature is raised, the M'' peaks shift systematically to higher frequencies, meaning that the relaxation process is thermally activated [23]. The increased thermal energy allows an ionic movement; hence, it lowers the relaxation time. This can be seen in the M'' increase in frequency shifting of the peak on increasing temperature. A thermally activated process taking place as a result of relaxation in the form of the ionic species in the glass structure by increasing temperature can be confirmed by such peak displacement [24]. The systematic tendency of M''[19,21] to move to high frequencies is an additional support of strong temperature dependence of the relaxation dynamics, as well as emphasizes the enhanced supply of thermal energy dependence of carrier mobility[25].

In addition, the growth in the full width at half maximum (FWHM) of the M'' fell by maximum peak with increasing temperature reveals that the relaxation times are broadly distributed, which is explained by the structural disorder of the amorphous glass network. This dispersion symbolizes the inconsistency of local surroundings and the bonds that the configuration changes in the glass matrix. The scatter plot of M'' against $log10\omega$ further corroborates the presence of multiple overlapping relaxation processes that collectively shape the dielectric response of the material. The wide peak in relaxation gives us information about the changing mechanisms of conduction: with the low frequencies, the conduction process is controlled by the small polaron hopping processes, whereas in the high frequencies, the conduction is more localized [24]. This crossover points to the frequency and temperature-dependent characteristic of ionic transport in disordered glassy installation.

The electrical modulus M^* can be further characterized by the Fourier transform of the relaxation function φ(t)using **Eq. 5.4** [15]. New findings suggest that the relaxations demonstrated here are fairly complex. An important parameter to be used in quantifying deviations away from ideal Debye-type relaxation behavior (β = 1) is the Kohlrausch-Williams-

Watts (KWW) stretching exponent, β(**Eq.5.5**). Values of β < 1 are commonly found in disordered glassy systems, corresponding to stretched exponential relaxation arising because of structural heterogeneity, and a range of relaxation times or relaxation time distributions. Such behavior is due to the non-uniform behavior of the ion transport dynamics within the disordered network. Smaller β values are associated with wider relaxation energy spectra, indicating that charge carriers are exposed to varying local conditions and possible barriers. Conversely, β > 1 is linked with depressed exponential relaxation that is sometimes ascribed to fast, cooperative structural rearrangements [15]. Bergman's theory can be summarised in the form of **Eq.5.6** to calculate $M^{//}$ [27].

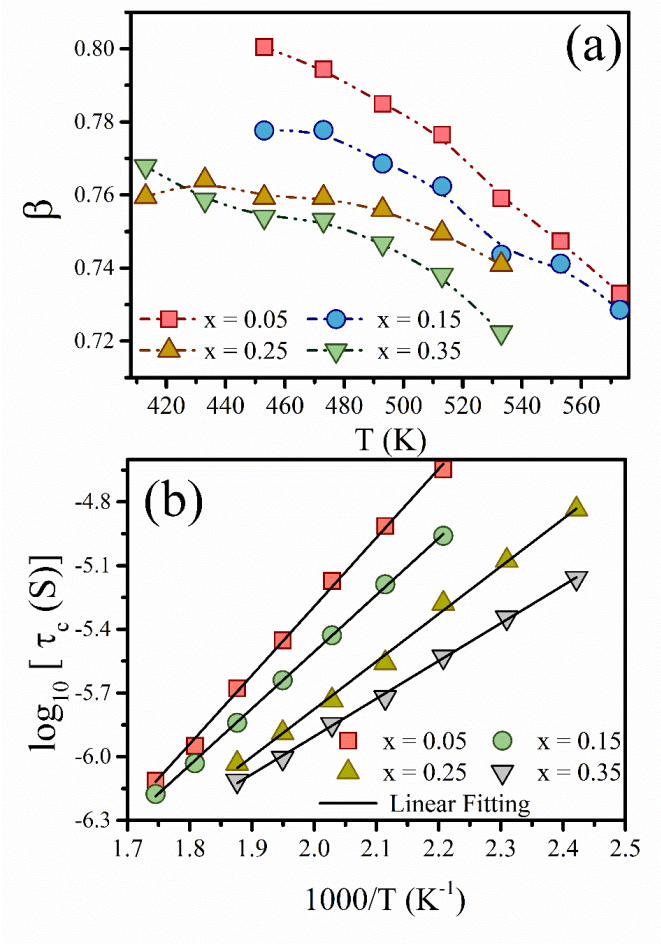

Fig. 5.12(a) Kohlrausch–Williams–Watts (KWW) stretched exponent (β) and (b) conductivity relaxation time (τ_c) plotted as a function of the reciprocal of temperature.

Fig. 5.12(a) shows the temperature dependence of the stretching parameter β of Kohlrausch-Williams-Watts (KWW) describing the distribution of relaxation times within the glassy matrix, and shows a clear downward trend of parameter β with heating through all compositions. The corresponding β values are between 0.78 (around 420 K) and ~ 0.72 (around

560 K), illustrating that the relaxation time distribution becomes narrower with an increase in thermal energy. The occurrence of this trend constitutes a shift against ideal Debye-type behavior (in which β = 1), meaning that the relaxation processes tend to be more locally localised and less broadly dispersed as the increase in temperature occurs. In the case of compositions with a low Bi_2O_3 amount (e.g., x = 0.05), the β value starts at 0.79 at 420 K and falls to ~0.74 at 520 K - an estimated decrease of about 6.3 %, which is indicative of relaxation dynamics being affected by the concentration of bismuth [15]. Variation of Hadriliak Negami (HN) parameters α and β, respectively, of unity in the glass system of Bi_2O_3–BaO–P_2O_5–V_2O_5 also justify the existence of such non-Debye present behavior. This in deviation indicates the order of structural disorder, a non-equivalent ion dynamic, and the interactions of mixed network formers and modifiers in charge carrier mobility and distribution.

In **Fig. 5.12(b)**, the variation of the characteristic relaxation time (τ_c) with temperature is analyzed by plotting $log_{10}^{\tau_c}$ versus the inverse temperature (1000/T) for various Bi_2O_3 concentrations. The evident linearity in all compositions proves the Arrhenius-type behavior, which is an indication that the process of relaxation is thermally activated. In the composition of x = 0.05, the $log_{10}^{\tau_c}$ values are negative, i.e. $log_{10}^{\tau_c}$ decreases towards a value of about -5.5 and -6.0 across the temperatures between lower and high temperature at about 1.9 (1000/T). However, the x = 0.25 composition shows rather long relaxation times, with $log_{10}^{\tau_c}$ greater than -5.1 and greater than -5.6 at the same temperature range. This transition reflects a notable shift from the lower Bi_2O_3 content (~–5.3), suggesting a ~9.4% reduction in τ_c across this compositional range. These findings highlight the usefulness of the elevation of Bi_2O_3 concentration on the dielectric relaxation process. In particular, the greater structural disorder and network complexity provided by Bi_2O_3 act as a hindrance to ion mobility in the glass, further delaying the relaxation process. This slowing down in charge motion expresses the preponderant influence of modifier oxide concentration in the control of relaxing action in disordered glass networks.Turning to **Fig. 5.13(a)**, it shows the normalized imaginary electric modulus spectra (M''/M''_{max}) of the x = 0.25 glass sample, measured between 393 and 513 K. The frequencies in each spectrum are scaled by their maximum so that the relaxation behaviour can be compared directly at different temperatures. Notably, the normalized curves collapse into a single master curve, indicating that the shape of the relaxation spectra remains unchanged with temperature. This superposition exemplifies the time-temperature superposition principle, suggesting that the relaxation mechanism of conductivity in the material is temperature-independent at this composition. The behavior of the master curve also implies that the ion

hopping mechanism describing the dielectric relaxation of the glass is independent of the composition as well as the temperature in the case of x = 0.25. This can be typical of non-Debye-type relaxation, which occurs frequently in structurally disordered glass systems where a general broad form of distribution of relaxation times exists. The scaling is in agreement with the resilience of the relaxation mechanism to thermal fluctuations, and a manifestation of the stability of the ionic conductive pathway to rise in bismuth concentration.

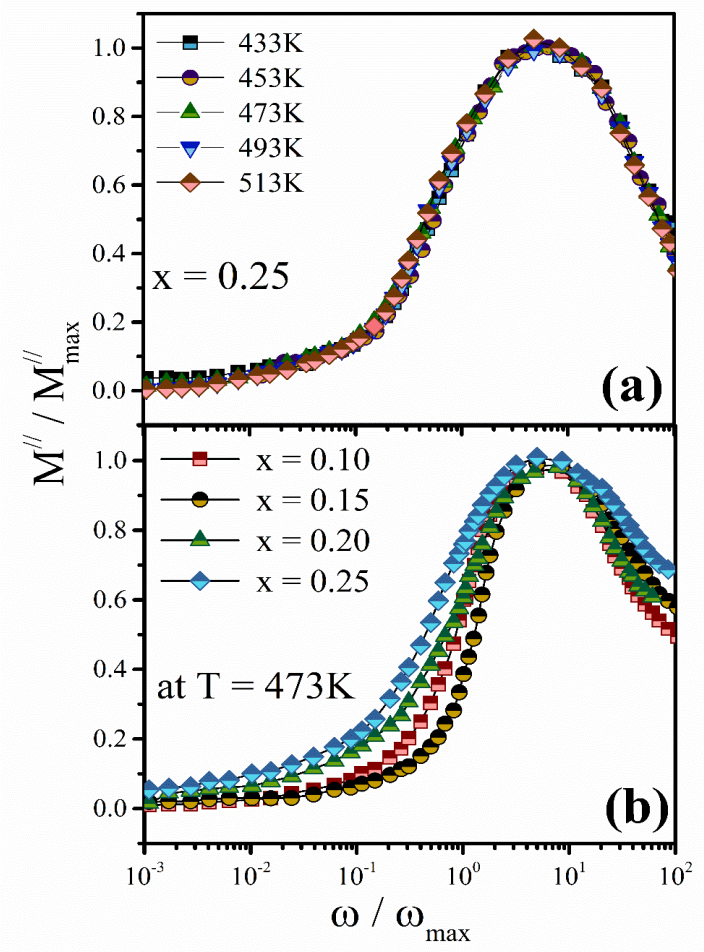

Figs. 5.13(a) Electric modulus scaling spectra of the glass sample with composition x = 0.25 at various temperatures, and (b) compositional modulus scaling spectra of all glass samples measured at 473 K.

Finally, **Fig. 5.13(b)** presents the scaled imaginary modulus ($M^{//}/M^{//}_{max}$) spectra for various glass compositions at a constant temperature of 473 K, offering a comparative perspective on the influence of composition on conductivity relaxation dynamics. These spectra of the x = 0.10 and x = 0.15 compositions show a great degree of overlapping, implying that their local

structural arrangements and ionic mobility channels are rather similar to each other at the given temperature. Conversely, the non-overlapping character of the spectra at the greater concentration of Bi_2O_3 (x = 0.25) indicates a significant imbalance in the relaxation behavior. Such deviations are indicative of the significant structural changes that are incorporated with the virtue of bismuth inclusion, including its aptitude to disrupt networks, its augmented polarizability, and its tendencies to localize the charge carriers.

5.4. Quaternary Bi_2O_3 -Fe_2O_3 -V_2O_5 -P_2O_5 glass system

5.4.1. Investigation of Frequency-Dependent Complex Dielectric Permittivity

In the vanadium–phosphate glass system doped with Bi_2O_3 and Fe_2O_3, both ε' and ε'' have been quantitatively analysed over a wide frequency range and at varying temperatures to assess their dielectric response and energy dissipation behaviour.

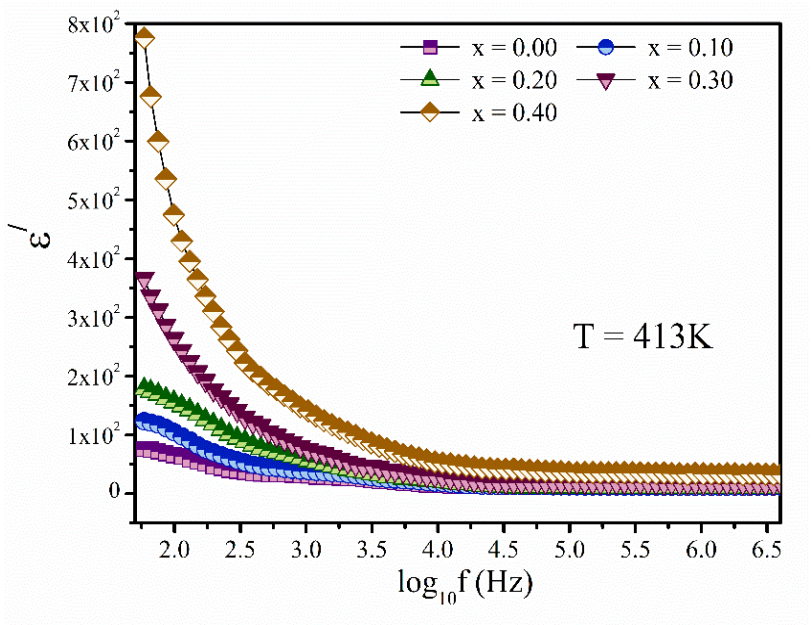

Fig. 5.14 Compositional dependency of dielectric-constant (ε') of glassy samples at 413K

Fig. 5.14 illustrates the compositional dependence of the dielectric constant (ε') in BFPV glasses. Across all compositions, a characteristic trend is observed: an initial sharp decline in ε' with increasing frequency is followed by a gradual levelling off into a plateau. The initial rise in the dielectric constant with increasing Bi_2O_3 content is attributed to the high polarizability of Bi^{3+} ions and their role as network modifiers. The incorporation of Bi^{3+}, with its large ionic radius, enhances dipolar alignment under an external field, thereby increasing ε'.

Furthermore, Bi^{3+} disrupts the phosphate glass network, generating non-bridging oxygens (NBOs) that contribute to increased polarizability and charge storage. The formation of Bi–O bonds also promotes electronic polarization. However, beyond a certain concentration threshold, excess Bi^{3+} may lead to ion clustering, which hinders effective polarization and may result in the saturation or decline of the dielectric constant.

The frequency-dependent complex dielectric permittivity of BFPV glass ceramics exhibits a significant dependence on composition, as illustrated in **Fig. 5.15(a–b)**. Significant fluctuations in both ε' and ε'' are observed at frequencies below 42.5 kHz, particularly at higher Bi_2O_3 contents. These fluctuations are primarily due to the hopping motion of mobile charge carriers within the glass matrix [28]. At higher frequencies, the time available for such hopping decreases, leading to reduced carrier contribution and thus stabilizing the values of ε' and ε''. This transition reflects the decreasing influence of interfacial and space charge polarization at elevated frequencies and confirms the critical role of charge carrier dynamics in governing dielectric behavior.

Fig. 5.16 further explores the compositional impact by showing the variation of ε' and ε'' with different Bi_2O_3 concentrations at a fixed frequency of 42.5 kHz and temperature of 453 K. The data suggest that increasing Bi_2O_3 content enhances both polarization and localized charge carrier hopping. At these frequencies, carriers can effectively move between localized states, resulting in a stronger polarization and dielectric response. These findings underscore the close interdependence between glass composition, polarization mechanisms, and frequency-dependent electrical behavior in BFPV glass systems.

Fig.5.15(a) shows the trend of the real part of permittivity (ε') on the frequency dependency at different temperatures in the BFPV glassy sample with x = 0.30. A sharp downward change in the ε' is experienced as the temperature ranges continue to increase in frequency trend indicates that at lower frequencies, dipolar entities within the glass matrix have sufficient time to align with the applied electric field, resulting in higher permittivity. At higher frequencies, extremely quick alternations of the field do not allow re-orientation of the dipole, and ε' changes since polarization is lower. Additionally, increasing the temperature shifts the ε' curves upward, indicating that thermal energy promotes dipole mobility, thereby improving their alignment with the field and increasing the permittivity at corresponding frequencies.

The imaginary component of the permittivity (ε'') is shown in **Fig.5.15**(b) as a function of the same composition. In this case, the ε'' is monotonically decreasing with frequencies as dielectric losses are lower at the higher frequencies, as the dipolar relaxation no longer keeps pace with the electric field. At low frequencies, the larger the values of ε'' so, the larger the energy dissipation, most of this being due to interfacial polarization and late dipole relaxation. When the temperature is higher, the values of ε'' increase with the spectral value, an indication that thermal stimulation facilitates the mobility of the dipoles, hence, increased dielectric loss. This increase of ε'' with temperature proves both the thermo-activated character of dipolar relaxation and the increasing role of conductive losses processes at higher temperatures.

Such experimental findings prove the fact that frequency and temperature have strong influential roles on the dielectric behavior of BFPV glass ceramics. With more and more Bi_2O_3 and higher temperature, the permittivity and the dielectric loss tend to increase and this can be attributed to the better dipole alignment and the increasing energy dissipation. The broad and asymmetric data in relaxation spectrum with a high frequency dispersion also show the involvement of non-Debye type of relaxation and low activation energy due to ionic hopping accompanied by more localized conduction.

To better explain the complicated dielectric behavior, particularly conduction loss and interfacial polarization, Havriliak-Negami (HN) model is specifically beneficial. This model is an extension of the classical Debye formalism that includes symmetric and asymmetric broadening parameters, allowing a more realistic description of dielectric relaxation within disordered systems (**Eq.5.1**). It offers a solid mathematical approach to use in the fitting of experimental information and understanding how the performance of the dielectric behaves with changes in structural and composition [6]. τ_{HN}, α_{HN}, and γ_{HN} parameters define the relaxation time, the offset of the phase angle and the level of non-linearity at the higher frequencies, respectively. Moreover, the shape parameters are labeled to be α_{HN} and γ_{HN}, and it is within the constraints of their existence, namely the conditions $0 \leq \gamma_{HN} \leq 1$ and $0 \leq \alpha_{HN} \leq 1$[6]. The real, imaginary parts of permittivity are given by $\varepsilon'(2\pi f)$ and imaginary permittivity $\varepsilon''(2\pi f)$ using the Havriliak Negami formalism [6]:

$$\varepsilon'(2\pi f) = \varepsilon_\infty(\varepsilon_s - \varepsilon_\infty)\mathrm{Re}\left[\frac{1}{[1 + (i2\pi f\tau_{HN})^{\alpha_{HN}}]^{\gamma_{HN}}}\right] \quad (5.11)$$

and

$$\varepsilon^{//}(2\pi f) = \varepsilon_{\infty}(\varepsilon_{s} - \varepsilon_{\infty})\mathrm{Im}\left[\frac{1}{[1 + (i2\pi f\tau_{HN})^{\alpha HN}]^{\gamma HN}}\right] + \frac{\check{s}}{(2\pi f)^{p}} \quad (5.12)$$

In the present discourse, the symbol *š* represents the frequency-independent conductivity(σ_{dc}). Meanwhile, the symbol p represents the frequency exponent linked to this conductivity.

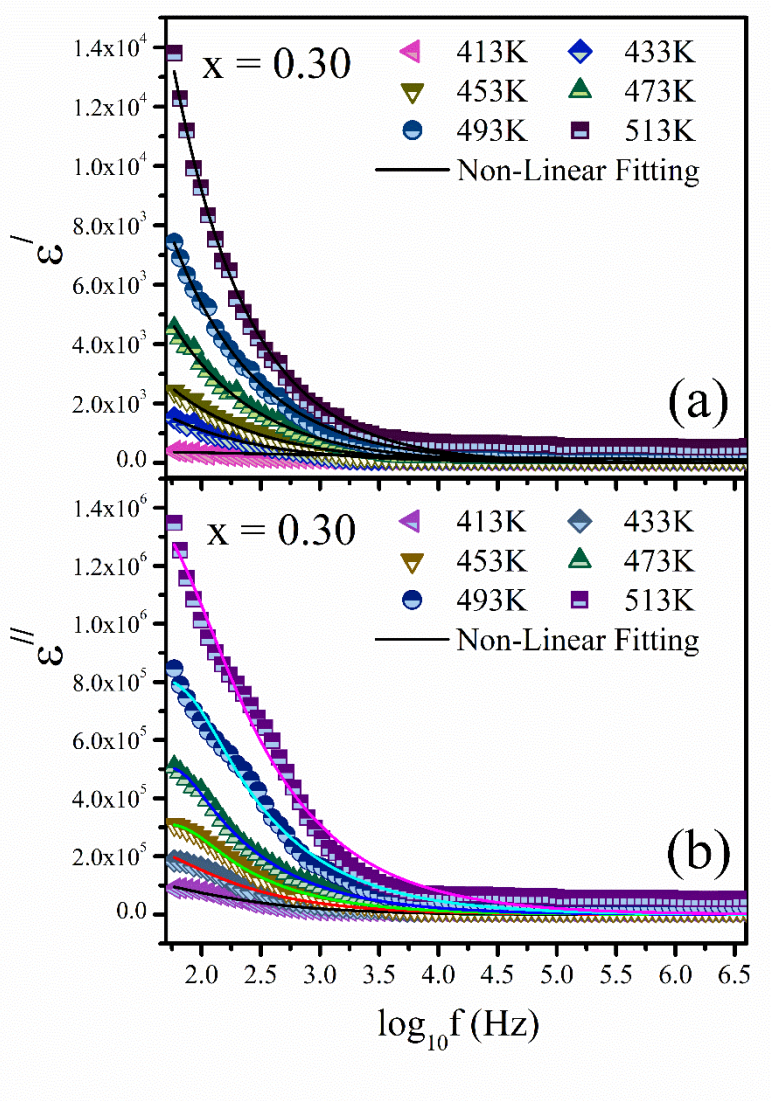

Figs.5.15(a-b). The frequency-dependent dielectric constant($\varepsilon^{/}$) and dielectric loss ($\varepsilon^{//}$) of glass sample x = 0.30 at different temperatures.

The solid black lines in **Figs. 5.15(a–b)** represent the nonlinear best-fit curves applied to the experimental data, based on the Havriliak–Negami (HN) formalism as described in **Eq. (5.17)**, **(5.18)**, and **(5.19)**. The extracted fitting parameters, summarized in **Table 5.3**, provide insights into the complex dielectric relaxation processes occurring in the BFPV glass system. Notably, both γ_{HN} and α_{HN} values are found to be less than unity, indicating a significant deviation from ideal Debye behavior. Additionally, the non-unity values of the frequency exponent p further confirm the non-Ohmic and non-Debye-type relaxation dynamics [6,29].

One of the key observations is the systematic increase in relaxation time (τ_c) with rising Bi_2O_3 concentration. Specifically, τ_c increases from 0.00012 s at x = 0.0 to 0.00071 s at x = 0.40, indicating a clear compositional influence on the dielectric relaxation kinetics. This behavior is attributed to the structural modifications induced by Bi_2O_3, which acts as a network former and a modifier, introducing more rigid and polarizable structural units. These changes restrict the mobility of charge carriers while promoting stronger dipolar interactions, thereby prolonging the relaxation Furthermore, the dielectric strength ($\Delta\varepsilon$), defined as the difference between static permittivity (ε_s) and high-frequency permittivity (ε_∞) in terms of the dielectric constant (ε'), also reflects this compositional dependence. An increase in $\Delta\varepsilon$ implies enhanced polarization capacity and dipolar responsiveness within the low-frequency regime.

The shape parameters of the HN model, namely α_{HN} (broadening parameter) and γ_{HN} (symmetry factor), both exhibit an increasing trend with Bi_2O_3 content. These parameters signify a broader and more asymmetric distribution of relaxation times, confirming that dielectric relaxation becomes increasingly complex with Bi_2O_3 incorporation.

This complexity is likely rooted in the local structural heterogeneity introduced by higher Bi_2O_3content. As Bi^{3+} ions integrate into the phosphate–vanadate matrix, they generate disordered coordination environments, which in turn create multiple relaxation pathways. This structural disorder leads to a broader spectrum of relaxation times and alters the underlying relaxation mechanisms. Ultimately, the results substantiate that Bi_2O_3 plays a pivotal role in modulating the dielectric response of the glass matrix through both structural and dynamic contributions.

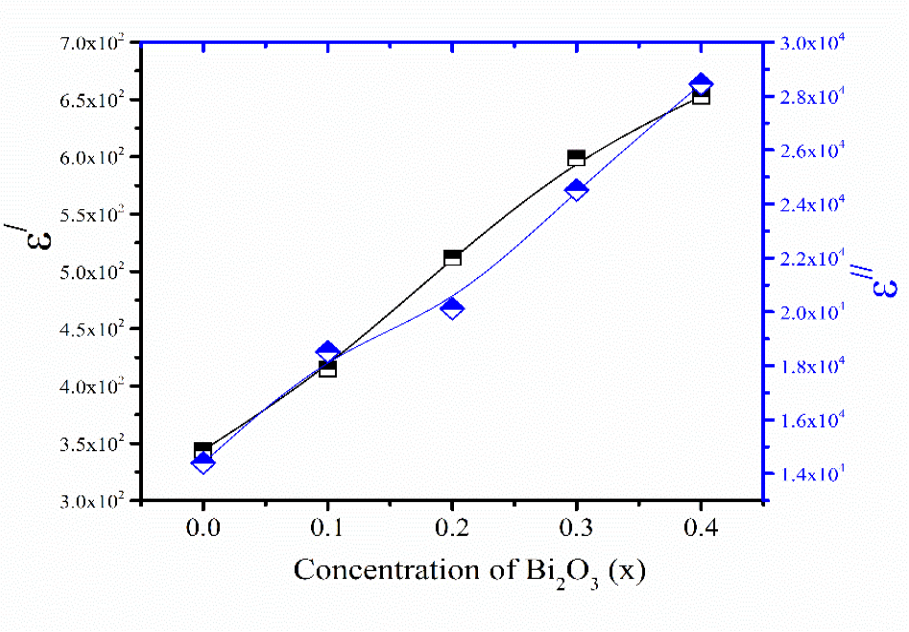

Fig.5.16. The variation of the real ($\varepsilon^{/}$) and imaginary ($\varepsilon^{//}$) parts of the dielectric permitivity with rising Bi_2O_3 content at 42.5 kHz and 453 K.

The power-law exponent (P), which characterizes the frequency-dependent dielectric response, exhibits a significant increase from 0.112 to 0.198 as the Bi_2O_3 concentration rises. This enhancement in P is of greater dependence on dielectric permittivity with frequency and highlights the enhanced dynamic polarization tendency of the glass system due to the composition change. Its increased sensitivity to frequency is an indication of increased dipolar mobility and more sensitive relaxation in the glassy network modification. Specifically, the addition of Bi_2O_3 enhances the flexibility of the structure and polarisisability of the matrix and hence enhances the dielectric behaviour to a wide frequency range.

At the same time, the activation energy ($E\tau$) relating to dielectric relaxation has been shown to reduce with the increment of Bi_2O_3 content, and it decreases between 0.67 and 0.49eV. Such a decrease indicates a decrease in energy needed to rotate a dipole, which causes a more efficient polarization during the application of an electric field. The decrease in activation energy

indicates an improvement in the ease of orientation of the ions or dipoles and results in an increase in dielectric performance.

The attribution of this behavior is mainly because the ionic radius of Bi^{3+} ions is larger in comparison with Fe^{3+} ions. The replacement of Fe^{3+} by Bi^{3+} into more free volume and structural openness in the glass network, thereby facilitating the movement of dipoles and rearrangement. These structural changes can enhance the relaxation dynamics, since they reduce the steric hindrance, thereby allowing a more rapid dipolar response and little energy utilization in reorientation.

The addition of Bi_2O_3 to the glassy mixture is important in improving the dielectric properties of the nanocomposite. The improvements observed, such as enhanced frequency sensitivity, low activation energies, and enhanced dipolar responsiveness, are very remarkable and have made the materials very promising for applications in areas that need high values of dielectric constants, like capacitors, energy storage devices, as well as advanced microelectronic components.

Table 5.3. Evaluated magnitudes of dielectric parameters from Havriliak-Negami fitting at T= 473 K, and E_τ of xBi_2O_3-(0.40-x) Fe_2O_3-0.25P_2O_5-0.35V_2O_5 glassy samples.

x (% mol)	$\Delta\varepsilon$ (± 5.0)	α_{HN} (± 0.01)	γ_{HN} (± 0.01)	τ_{HN} (± 0.0001)	P (± 0.008)	E_τ (eV) (±0.03)
0.00	223.5	0.54	0.75	0.00012	0.22	0.56
0.10	432.5	0.65	0.77	0.00021	0.29	0.51
0.20	655.2	0.69	0.83	0.00052	0.34	0.45
0.30	722.1	0.76	0.87	0.00063	0.44	0.41
0.40	843.4	0.81	0.92	0.00071	0.54	0.35

5.4.2. Investigation of Temperature-Dependent Complex Dielectric Permittivity

The discussion on the temperature dependence of the complex dielectric permittivity of BFPV glassy samples (x=0.30) is highly informative to the functionality of the material in a large frequency and temperature range. The investigations are essential in determining the appropriateness of the glass system under various uses in different environmental situations.

As depicted in the **Figs. 5.17(a-b)**, the real (ε') and imaginary (ε'') values of permittivity rise steadily as temperature rises at all frequency values. As the temperature increases, the increases in the dielectric constant (ε') are more significant at lower frequencies (e.g., 50 kHz, 100 kHz, 500 kHz). This tendency is very indicative of the fact that in these low-frequency ranges, thermally activated dipolar and interfacial polarization mechanisms are predominant in the dielectric response [50]. Such polarization processes are dependent on thermal motion, so that with more thermal energy, there is more realignment of dipoles and more charge to collect at the interfaces.

Conversely, at higher frequencies (1 MHz, 2 MHz, and 5 MHz), the dielectric constant shows a low sensitivity to the changes in temperature. The implication here is that in a case where the field oscillations are too fast, the dipoles are not able to realign fast, and hence the thermal energy influence is insignificant, and only the intrinsic material properties can have a significant impact on the permittivity.

Similar behaviour is also observed in dielectric loss (ε''). At low frequencies, ε'' increases sharply with temperature, which is attributed to enhanced ionic and dipolar mobility at elevated temperatures. This mobility facilitates greater energy dissipation in the form of heat, due to lagging polarization. However, as the frequency increases, the temperature dependence of ε'' diminishes. The occurrence of such attenuation can be attributed to the fact that the time window to execute the dipolar reorientation is short, thus yielding little interaction with the thermal effects. The behavior suggests that the dielectric loss at the higher frequencies is dominated by fast dipolar relaxation processes that are least affected by the thermal fluctuations [30].

These tendencies are also corroborated by the presence of bismuth ions (Bi^{3+}) in the glass matrix. Bi^{3+}ions are sufficiently large in their ionic radius with a large polarizability at a time, making them contribute highly to the dipole interaction to further encourage higher polarization due to the thermal excitation process [19]. These ions are helpful in structural changes that help to provide greater flexibility and responsiveness of the dielectric matrix to changes in temperature and the change in frequency.

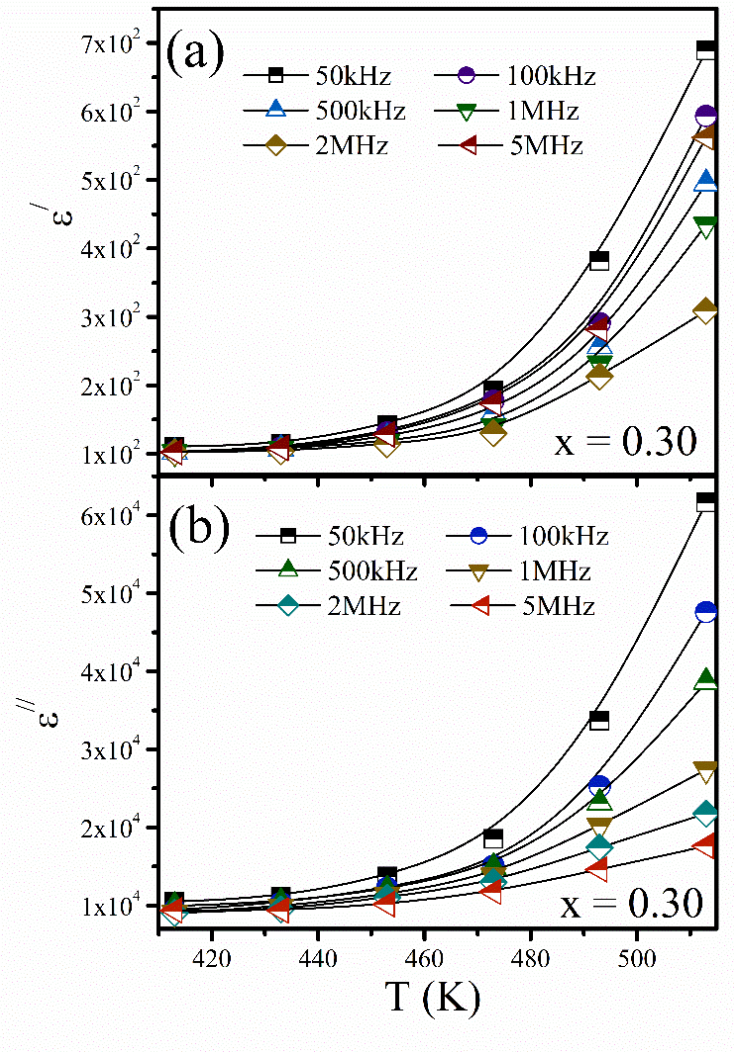

Figs. 5.17(a-b). Temperature-dependent dielectric loss (ε') and dielectric loss (ε'') of glass samples x = 0.30.

Finally, the dielectric properties of the BFPV glassy samples near the glasses at different temperatures are temperature-dependent. This shows that higher temperatures increase both the dielectric constant and dielectric loss, especially at lower frequencies. In the sample with a higher composition of Bi_2O_3 (x = 0.30), there is improved dielectric behaviour. This supports the idea that Bi^{3+} ions significantly contribute to stimulating polarisation and facilitating relaxation. The findings are very useful for determining the suitability of this material in applications that require high dielectric permittivity across a broad range of frequencies and temperatures.

5.4.3. Study of Electrical modulus

In **Fig. 5 .18 (a)**, changes in M' particular and M'' as a result of temperature and frequency at various compositions have been plotted. Complex electrical modulus (M^*) formulation is a successful procedure for differentiating interfacial polarizations and dipolar relaxation, along with bringing lucidity to the relaxation behavior connected with conductivity. Over a range of temperatures, the samples are tested to provide M' and M''. To the composition of x = 0.40, the frequency dependence of M' and M'' between 393 K and 493 K is presented in **Fig. 5 .18 (a-b)**. At low frequencies, M (**Fig. 5.18(a))** tends to "0", which means that the influence of electrode polarization processes is insignificant. With an increase in frequency, there is a marked increase in M', as it is more rigid and interfacial effects are minimized. This is coupled with dispersion tendency as well as temperature-dependent peak in M'' spectrum [31]. **Fig. 5 .18 (a-b)** provides an overview of the behaviour of M' and M'' within the x = 0.40 glass across angular frequencies ($\log_{10}^{f}$) and in between 393 K and 493 K. The value of modulus M' nears zero at lower frequencies would imply that the mobile ions in the matrix have minimal restoring forces, and so there can be free migration of the ions. The property means free ionic movement with low frequencies [32]. With increased frequency M' increases as a result of a wide distribution of relaxation. At higher frequencies, M' exhibits a maximum which declines with increasing temperature. The temperature dependence of the maximum M' (M'_{max}) shows a monotonic decrease that implies that the short range ionic movement plays a significant role in the conductance behavior of the system. Moreover, the details of the similarity in the presentation of the M' spectrum at the various compositions are that there is a similar mechanism of relaxation in the sample[15,33]. By examining both the real (M') and imaginary (M'') components of M^*, the electrical and relaxation dynamics of BFPV glasses can be understood more thoroughly. **Fig. 5 .18 (a-b)** shows how M' and M'' vary with frequency for the x = 0.40 glass composition over a temperature range of 393 K to 493 K. **Fig. 5.18 (a)**, the value of M' approaches "0" at lower frequencies, suggesting minimal influence from interfacial polarization or electrode effects. This behavior implies that the mobile ions in the glassy matrix are not subject to restoring forces and can migrate freely, characteristic of low-frequency regions where ion mobility is unimpeded [53]. As frequency increases, M' rises significantly, reflecting increased rigidity in the glass structure. This is accompanied by a clear dispersion pattern and a peak in M'' that shifts with temperature. The frequency-dependent dispersion is linked to a broad relaxation process, while the decreasing maximum value of $M'(M'_{\max})$ with

increasing temperature suggests that thermally activated short-range ionic motion facilitates electrical conductivity.

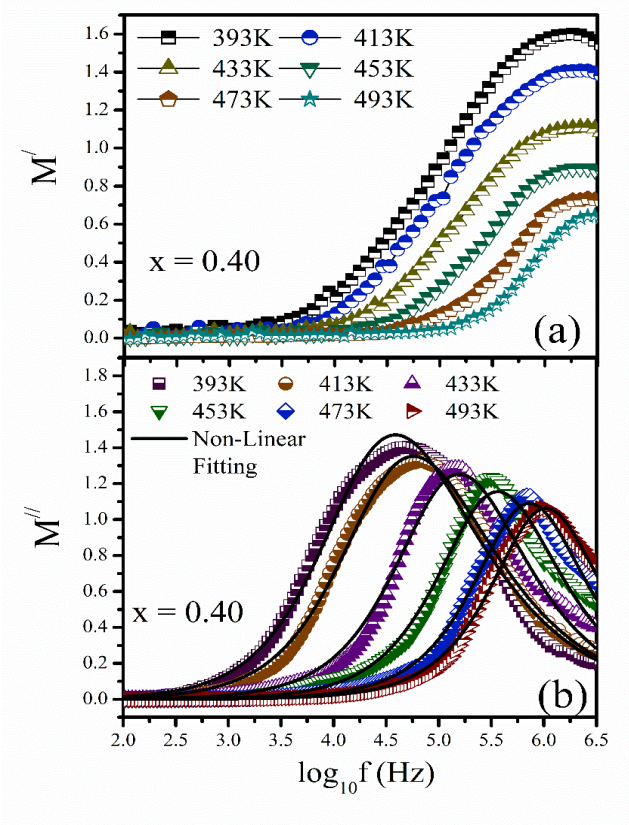

Figs.5.18(a-b). Frequency-dependent real ($M^{/}$) and imaginary ($M^{//}$) parts of the electric modulus for the glassy specimen with composition x = 0.40.

The nearly identical shape of the $M^{/}$ spectra across temperatures further indicates consistent relaxation dynamics across all measured specimens [34].

Fig. 5.18 (b) presents the behavior of $M^{//}$, representing the dielectric energy loss under the influence of an external electric field. At lower frequencies, $M^{//}$ decreases markedly, which is attributed to the accumulation of charge carriers at the electrode-glass interface. This is due to electrode polarization effects and increased interfacial capacitance. As the temperature rises, the $M^{//}$ peak shifts toward higher frequencies, indicating thermally activated relaxation behavior [35]. The thermal energy imparted to charge carriers enhances their mobility, accelerating relaxation processes and shifting the relaxation frequency higher. This trend confirms that relaxation is temperature-sensitive and governed by ion mobility within the disordered glass matrix [25,26].

Moreover, the increase in the full width at half maximum (FWHM) of the M'' peaks with temperature supports the presence of a broad distribution of relaxation times, a hallmark of the structural randomness inherent in glassy materials. The variation in local bonding environments and structural heterogeneities across the matrix contributes to these differences in relaxation behavior. The scatter plots of M'' versus $\log_{10}$f further reveal the coexistence of multiple relaxation mechanisms that govern the dielectric response. The position and behavior of the relaxation peak also reflect a transition in conduction mechanisms—from polaron hopping at lower frequencies to localized conduction at higher frequencies [25].

Additionally, M^* can be described through the Fourier transform of the time-dependent relaxation function φ(t), which accounts for the complex and tensioned relaxation dynamics of the glass network. Recent studies confirm that the relaxation behavior exhibited by these glasses is intricate, influenced by both thermal and structural factors [25].

$$\mathrm{M}^* = M_\infty \left[1 - \int_0^\infty \exp\left(-2\pi f t\right)\left(\frac{d\varphi}{dt}\right) dt\right] \tag{5.12}$$

In this context, M_∞ is the modulus at high frequency and $\varphi(t)$ represents the Kohlrausch-Williams-Watts (KWW) function, which characterizes the time-dependent evolution of the electric field in the glassy matrix [15] as depicted in **Eq.5.5.** Bergman's adjusted KWW function provides additional insight into the behaviour of M''. As per Bergman's theory, the mathematical formula for M'' is as follows [15]:

$$M'' = \frac{M''_{max}}{(1-\beta)+\frac{\beta}{1+\beta}\left[\beta\frac{2\pi f_{max}}{2\pi f}+\left(\frac{2\pi f}{2\pi f_{max}}\right)^{\beta}\right]} \tag{5.13}$$

In this case, the maximum value of M'' is labelled as M''_{max}, and the frequency at this maximum is denoted as f_{max}. The experimental data aligns well with Bergman's equation, as depicted by the continuous black curves in **Fig. 5.18(b)**.

Figs.5.19(a) presents a plot of the Kohlrausch–Williams–Watts (KWW) stretching exponent β as a function of temperature (T), offering insight into the distribution of relaxation times within the glassy samples. Across all compositions, β exhibits a decreasing trend with increasing temperature, suggesting a narrowing of the relaxation time distribution at elevated temperatures. Lower β values reflect a deviation from ideal Debye relaxation (β = 1), signifying broader and more heterogeneous relaxation dynamics [15].

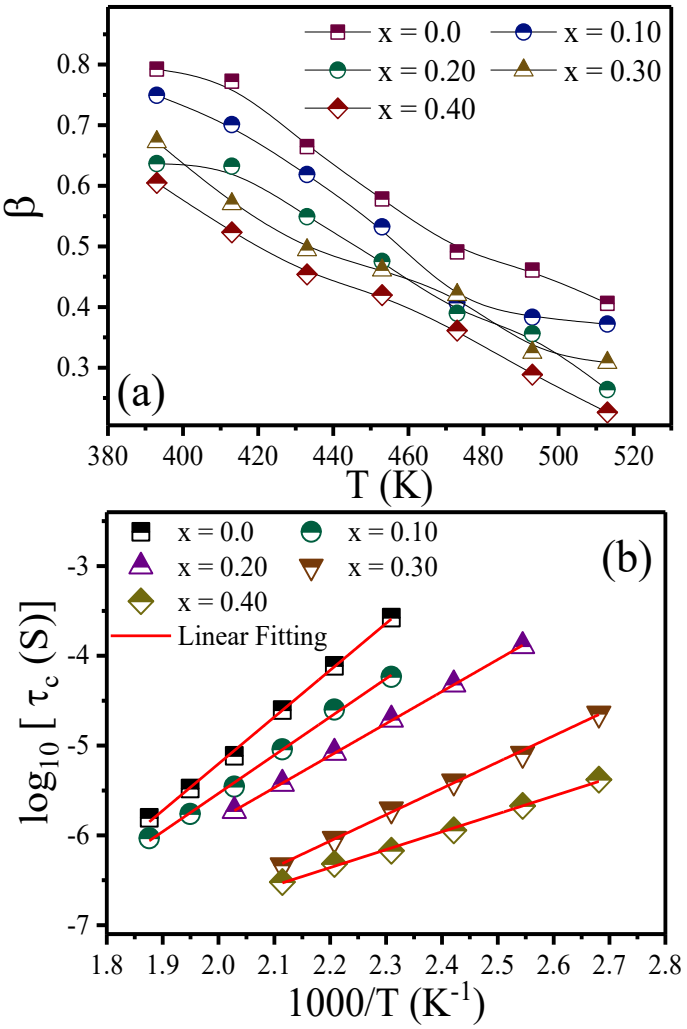

Figs.5.19 (a-b) KWW stretched coefficient (β) and **(b)** conductivity relaxation time (τ_c) against the reciprocal of temperature.

Interestingly, samples with higher bismuth content, particularly at x = 0.40, exhibit relatively higher β values at lower temperatures, indicating a broader distribution of relaxation times. This implies that at reduced temperatures, increased Bi_2O_3 concentrations introduce greater complexity in the dielectric relaxation spectrum, likely due to the variation in local structural environments affecting ion mobility within the disordered glass matrix.

Figs.5.19(b) illustrates the variation of the logarithm of the characteristic relaxation time ($log_{10}^{\tau_c}$) as a function of inverse temperature (1000/T) for various compositions. The values of τ_c (where $f_{max}=1/\tau_c$) were obtained by fitting the M'' spectra using **Eq. (5.13)**. The observed linearity in this plot is characteristic of Arrhenius-type behavior, confirming that the relaxation processes are thermally activated. As temperature increases, relaxation times decrease,

reflecting enhanced mobility of dipoles or Bi^{3+} ions within the matrix. Notably, glasses with higher Bi_2O_3 content (x = 0.30) exhibit longer relaxation times (i.e., higher $log_{10}^{\tau_c}$ values), indicating slower relaxation dynamics. This behavior can be attributed to increased structural disorder and the presence of more complex local bonding environments introduced by higher bismuth concentrations.

To investigate the universality of the dielectric relaxation behavior, each M'' spectrum was normalized by dividing by its maximum value (M''_{max}), and the corresponding frequency axis was rescaled using the ratio $\frac{f}{f_{max}}$. **Fig.5.20 (a)** presents the scaled M'' spectra for the x = 0.20 glass sample across the temperature range of 393–493 K. The convergence of the spectra onto a single master curve indicates that the conductivity relaxation process is thermally independent and governed by a common mechanism. In contrast, **Figs. 5.20 (b)** displays the scaled spectra of different glass compositions measured at a fixed temperature of 433 K. The absence of spectral overlap in this case highlights the influence of glass composition on the relaxation behavior, indicating that the dielectric response is significantly dependent on the structural and compositional variations within the glass matrix.

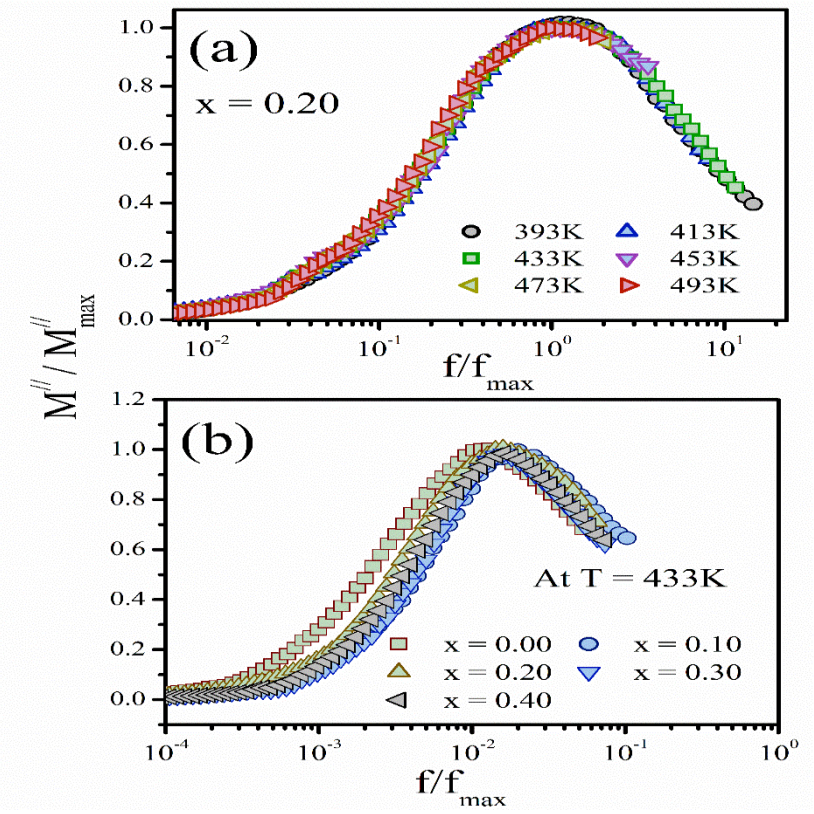

Figs. 5.20 (a) Electric modulus scaling spectra of glassy sample x = 0.20 at various temperatures and **(b)** Compositional modulus scaling spectra of all glassy samples at 433K.

5.5. Summary

The comprehensive dielectric analysis of the VNZP, BBVP, and BFVP glass nanocomposite systems reveals significant insights into the frequency- and temperature-dependent electrical behavior driven by compositional modifications. The findings underscore the crucial role of oxide constituents, particularly the incorporation of transition metal oxides such as V_2O_5, Bi_2O_3, and Fe_2O_3, in shaping the dielectric response of the glass network. These oxides influence the dielectric constant ($\varepsilon^{/}$), dielectric loss ($\varepsilon^{//}$), and electric modulus ($M^{/}$ and $M^{//}$) through mechanisms including polaron hopping, interfacial polarization, and dipolar relaxation, each sensitive to both the structural order and the ionic mobility of the constituent ions.

The observed increase in dielectric dispersion and loss in certain compositions is attributed to the presence of mixed valence states (e.g., V^{5+}/V^{4+}), lone-pair electron activity (Bi^{3+}), and redox centres (Fe^{3+}/Fe^{2+}), all of which facilitate localized charge hopping and inter-site polarization. Additionally, the contributions of ZnO and BaO in modifying the oxygen coordination and enhancing non-bridging oxygen content further influence ion transport and relaxation processes. The implementation of the electric modulus formalism proved effective in eliminating electrode polarization artefacts, thereby isolating bulk relaxation phenomena and elucidating the intrinsic conductivity and relaxation behavior within the glassy systems.

Variations in the dielectric behavior across the three glass systems emphasize the composition-sensitive nature of polarization dynamics and conduction mechanisms. The shifting of relaxation peaks with temperature and frequency points to a range of localized and long-range conduction processes, each modulated by the glass network's structural flexibility and field strength of the incorporated cations.

In conclusion, this chapter affirms that systematic tuning of the glass composition enables controlled tailoring of dielectric properties. Among the studied systems, specific compositions exhibit promising potential for use in advanced dielectric applications such as frequency-stable capacitors, energy storage elements, and optoelectronic devices. These insights contribute meaningfully to the fundamental understanding of structure-property relationships in glassy dielectrics and highlight the path forward in engineering high-performance glass-based electronic materials.

5.6. References

1. Atef, N., El Damrawi, G., Hassan, A., & El-Deen, L. S. (2020). Dielectric studies on $CuO–Na_2O–B_2O_3$ glasses. New Journal of Glass and Ceramics, 10(4), 45–56. https://doi.org/10.4236/njgc.2020.104004
2. Das, A. S., & Biswas, D. (2019). Investigation of AC conductivity mechanism and dielectric relaxation of semiconducting neodymium–vanadate nanocomposites: Temperature and frequency dependency. Materials Research Express, 6(7), 075206. https://doi.org/10.1088/2053-1591/ab13ee
3. Singh, Y. B., Chatterjee, P., Ningthemcha, R. K. N., Adhikary, S., Mondal, R., Das, A. S., Kabi, S., Singh, L. S., & Biswas, D. (2021). Compositional dependence of structural, physical, and, in particular, optical parameters of $Se_{50}–xTe_{30}Sn_{20}Sb_x$ chalcogenide glassy systems. Materials Chemistry and Physics, 274, 125153. https://doi.org/10.1016/j.matchemphys.2021.125153
4. Mahani, R. M., & Marzouk, S. Y. (2013). AC conductivity and dielectric properties of $SiO_2–Na_2O–B_2O_3–Gd_2O_3$ glasses. Journal of Alloys and Compounds, 579, 394–400. https://doi.org/10.1016/j.jallcom.2013.05.173
5. Ningthemcha, R. K. N., Biswas, D., Mondal, R., Das, A. S., Kabi, S., Ghosh, D., Singh, L. S., & Deb, B. (2022). Study of mixed modifier effect on dielectric and optical properties of zinc–phosphate based ternary and quaternary nanocomposite systems. Journal of Non-Crystalline Solids, 591, 121701. https://doi.org/10.1016/j.jnoncrysol.2022.121701
6. Havriliak, S., & Negami, S. (1967). A complex plane representation of dielectric and mechanical relaxation processes in some polymers. Polymer, 8(4), 161–210. https://doi.org/10.1016/0032-3861(67)90021-3
7. Biswas, D., Singh, Y. B., Das, A. S., Mondal, R., Roy, D., Adhikari, S., & Singh, L. S. (2019). Investigation of microstructure and temperature- and frequency-dependent dielectric relaxation of molybdenum–zinc–selenite glass nanocomposite systems. Materials Research Express, 6(11), 115205. https://doi.org/10.1088/2053-1591/ab4615
8. Macedo, P. B., Moynihan, C. T., & Bose, R. (1972). The role of ionic diffusion in polarization in vitreous ionic conductors. Physics and Chemistry of Glasses, 13(6), 171–179.

9. Brow, R. K., Tallant, D. R., Myers, S. T., & Phifer, C. C. (1995). The short-range structure of zinc polyphosphate glass. Journal of Non-Crystalline Solids, 191(1–2), 45–55. https://doi.org/10.1016/0022-3093(95)00289-8
10. Patro, L. N., & Hariharan, K. (2009). AC conductivity and scaling studies of polycrystalline SnF_2. Materials Chemistry and Physics, 116(1), 81–87. https://doi.org/10.1016/j.matchemphys.2009.02.056
11. Vaish, R., & Varma, K. B. R. (2009). Dielectric properties of $Li_2O–3B_2O_3$ glasses. Journal of Applied Physics, 106(6), 064106. https://doi.org/10.1063/1.3225583
12. Moynihan, C. T. (1996). Analysis of electrical relaxation in ionically conducting glasses and melts. Journal of Non-Crystalline Solids, 203, 359–363. https://doi.org/10.1016/0022-3093(96)00501-7
13. Bergman, R. (2000). General susceptibility functions for relaxations in disordered systems. Journal of Applied Physics, 88(3), 1356–1365. https://doi.org/10.1063/1.373824
14. Aziz, S. B., Brza, M. A., Kadir, M. F. Z., Hamsan, M. H., Abidin, Z. H. Z., Tahir, D. A., & Abdullah, O. G. (2019). Investigation on degradation and viscoelastic relaxation of Li ion in chitosan-based solid electrolyte. International Journal of Electrochemical Science, 14(6), 5521–5534. https://doi.org/10.20964/2019.06.13
15. Rabiei, N., Amirshahi, S. H., & Haghighat Kish, M. (2019). Description of physical aging kinetics of glassy polymers by interpretation of parameters of the Kohlrausch–Williams–Watts relaxation function via simulation. Physical Review E, 99(3), 032502. https://doi.org/10.1103/PhysRevE.99.032502
16. Davidson, D. W., & Cole, R. H. (1951). Dielectric relaxation in glycerol, propylene glycol, and n-propanol. The Journal of Chemical Physics, 19(12), 1484–1490. https://doi.org/10.1063/1.1748105
17. Deb, B., & Ghosh, A. (2010). Dielectric and conductivity relaxation in AgI-doped silver selenite superionic glasses. Journal of Applied Physics, 108(7), 074104. https://doi.org/10.1063/1.3491045
18. Jang, J. S. C., Jian, S. R., Chang, C. F., Chang, L. J., Huang, Y. C., Li, T. H., Huang, J. C., & Liu, C. T. (2009). Thermal and mechanical properties of the $Zr_{53}Cu_{30}Ni_9Al_8$-based bulk metallic glass microalloyed with silicon. Journal of Alloys and Compounds, 478(1–2), 215–219. https://doi.org/10.1016/j.jallcom.2008.11.135
19. Chen, Y., Chen, D., Meng, L., Wan, L., Yao, H., Zhai, J., Yuan, C., Talwar, D. N., & Feng, Z. C. (2020). Dielectric and energy storage properties of $Bi_2O_3–B_2O_3–SiO_2$-doped

$Ba_{0.85}Ca_{0.15}Zr_{0.1}Ti_{0.9}O_3$ lead-free glass–ceramics. Royal Society Open Science, 7(2), 191822. https://doi.org/10.1098/rsos.191822

20. Shaheen, A., Maghrabi, M., Salman, F., & Khattari, Z. (2017). Effects of temperature and frequency on the dielectric properties of $AgPO_3$ glass. Applied Physics A, 124(1), 54. https://doi.org/10.1007/s00339-017-1484-2
21. Rao, B. H. (1962). Dielectric properties of glasses in the systems Bi_2O_3–CdO–SiO_2, Bi_2O_3–CdO–B_2O_3, and Bi_2O_3–CdO–GeO_2 and their relation to the structure of glass. Journal of the American Ceramic Society, 45(12), 555–563. https://doi.org/10.1111/j.1151-2916.1962.tb11056.x
22. Biswas, D., Patra, D., Hota, S. B., Das, A., Modak, N., & Mondal, R. (2025). Influence of bismuth content on the properties of glass–ceramics with composition xBi_2O_3–(0.40–x)B_2O_3–0.15ZnO–0.45P_2O_5: Synthesis, structural, thermal analysis, and dielectric relaxation process. Physica B: Condensed Matter, 697, 416728. https://doi.org/10.1016/j.physb.2024.416728
23. Shapaan, M., El-Badry, S. A., Mostafa, A. G., Hassaan, M. Y., & Hazzaa, M. H. (2012). Structural and electric–dielectric properties of some bismuth–phosphate glasses. Journal of Physics and Chemistry of Solids, 73(3), 407–417. https://doi.org/10.1016/j.jpcs.2011.11.007
24. Kumar, A., Dwivedi, R. K., & Pal, V. (2012). Dielectric behavior and impedance spectroscopy of $Ba_{1-x}Bi_xTi_{1-x}Fe_xO_3$ system. Advanced Materials Research, 585, 190–194. https://doi.org/10.4028/www.scientific.net/AMR.585.190
25. Sridharpanday, M., Brindha, R., Vinoth, M., Narthana, K., & Rajendran, V. (2021). Investigation on temperature-dependent structural, dielectric and impedance characteristics of Cu-doped $CaFe_xTi_{1-x}O_3$–δ nanotitanates. Journal of Materials Science: Materials in Electronics, 32(28), 22076–22092. https://doi.org/10.1007/s10854-021-06677-w
26. Ashwini, K., Poorva, S., Qiu, F., Hu, J., & Cui, J. (2024). Electrical resistivity behavior and small polaron conduction transport mechanism in semiconducting $RMnO_3$ manganites. Advances in Materials, 13(1), 16–19. https://doi.org/10.11648/j.am.20241301.13
27. Alvarez, F., Alegría, A., & Colmenero, J. (1991). Relationship between the time-domain Kohlrausch–Williams–Watts and frequency-domain Havriliak–Negami relaxation functions. Physical Review B, 44(12), 7306–7312. https://doi.org/10.1103/PhysRevB.44.7306

28. Wu, Z. W., Kob, W., Wang, W.-H., & Xu, L. (2018). Stretched and compressed exponentials in the relaxation dynamics of a metallic glass-forming melt. Nature Communications, 9, 5334. https://doi.org/10.1038/s41467-018-07759-w
29. Hodge, I. M. (2019). Conductivity relaxation. In I. M. Hodge (Ed.), Classical relaxation phenomenology (pp. 153–158). Springer. https://doi.org/10.1007/978-3-030-02458-1
30. Hota, S. B., Roy, D., Ghosh, B. K., Das, A. S., Mondal, R., Kabi, S., Chakrabarti, C., & Biswas, D. (2023). Effect of transition metal and alkali oxides on structural, optical and dielectric properties in zinc–phosphate amorphous glassy systems. Journal of Non-Crystalline Solids, 609, 122235. https://doi.org/10.1016/j.jnoncrysol.2023.122235
31. Das, A. S., & Biswas, D. (2019). Investigation of AC conductivity mechanism and dielectric relaxation of semiconducting neodymium–vanadate nanocomposites: Temperature and frequency dependency. Materials Research Express, 6(7), 075206. https://doi.org/10.1088/2053-1591/ab13ee
32. Biswas, D., Das, A. S., Kabi, S., Singh, L. S., Ahmed, M., Mukherjee, S., & Nambissan, P. M. G. (2021). Positron annihilation and correlated dielectric property studies of a transition metal oxide-modified quaternary nanocomposite $0.1P_2O_5$–$0.4ZnO$–$0.5(xV_2O_5$–$(1–x)MoO_3)$. Journal of Alloys and Compounds, 864, 158395. https://doi.org/10.1016/j.jallcom.2020.158395
33. Shapaan, M., El-Badry, S. A., Mostafa, A. G., Hassaan, M. Y., & Hazzaa, M. H. (2012). Structural and electric–dielectric properties of some bismuth–phosphate glasses. Journal of Physics and Chemistry of Solids, 73(3), 407–417. https://doi.org/10.1016/j.jpcs.2011.11.007
34. Kumar, A., Dwivedi, R., & Pal, V. (2012). Dielectric behavior and impedance spectroscopy of $Ba_{1-x}Bi_xTi_{1-x}Fe_xO_3$ system. Advanced Materials Research, 585, 190–194. https://doi.org/10.4028/www.scientific.net/AMR.585.190
35. Biswas, D., Rakshit, A., Hota, S. B., Kabi, S., Kuiri, B., Roy, D., & Mondal, R. (2024). Thermal, electrical, and dielectric properties of xNa_2O–$(0.4–x)$ B_2O_3–$0.4SiO_2$–$0.2P_2O_5$ glassy systems for advanced material applications. Journal of Alloys and Compounds, 1010, 177878. https://doi.org/10.1016/j.jallcom.2024.177878

Chapter 6

Analysis of Electrical Conductivity of Glass Nanocomposite Systems

6.1. Introduction

The electrical conductivity behavior of glassy materials, particularly in disordered systems containing transition metal oxides, is a vital parameter in determining their suitability for various electronic and electrochemical applications. In this chapter, an in-depth study has been carried out on the AC and DC electrical conduction mechanisms in three series of nanocomposite phosphate-based glasses—namely V_2O_5–Na_2O–ZnO–P_2O_5, Bi_2O_3–BaO–V_2O_5–P_2O_5, Bi_2O_3–Fe_2O_3–V_2O_5–P_2O_5 and systems—each doped with varying molar fractions of Bi_2O_3 or V_2O_5.

The chapter begins by analyzing the frequency- and temperature-dependent total conductivity (σ_{total}) spectra, followed by deconvolution into DC conductivity (σ_{dc}) and AC conductivity (σ_{ac}) components. The Almond-West formalism is applied to evaluate conductivity spectra, and various conduction mechanisms are interpreted through established models such as Mott's Variable Range Hopping (VRH) model, Greaves's VRH model, and the Correlated Barrier Hopping (CBH) theory.

To identify the dominant charge transport phenomena, experimental σ_{ac} data are interpreted using Jonscher's universal power law, which further aids in calculating the frequency exponent s. The behavior of s with temperature allows the identification of appropriate models—either CBH or modified CBH—as fitting representations of the conduction mechanism in these disordered glass systems. Additionally, key electrical parameters such as hopping distance (R_{Hop}), hopping energy (W_{Hop}), activation energy (E_{ac}, E_H), and density of localized states $N(E_F)$ are extracted from curve fittings, giving insight into polaron dynamics and the influence of structural disorder.

This chapter also explores the scaling behavior of AC conductivity using the Pan and Ghosh model to assess the validity of time–temperature superposition (TTS). Furthermore, the relationship between compositional changes (specifically Bi_2O_3 content), conduction pathways, defect states, and dielectric behavior is critically analyzed. The aim is to develop a thorough understanding of how these nanocomposite glass systems manage charge transport under different thermal and structural conditions.

6.2. Quaternary V_2O_5–Na_2O–ZnO–P_2O_5 glass system

6.2.1. Study of electrical conductivity

The total electrical conductivity (σ_{total}) was represented in **Fig. 6.1(a)** and **(b)** with a composition of x= 0.05 and x= 0.25, respectively. In all the remaining samples of the series, similar trends can be observed. There is a nonlinear rise in the σ_{total} values of the composition at every 50 °C and that itself points towards semiconducting behavior.

In both of the isothermal plots, two features will be apparent. The former is a frequency-independent, plateau, at low frequencies, corresponding to the direct current (dc) conductivity (σ_{dc}), which is mostly ascribed to the long-range translational diffusion of charge carriers through the glass media. The second characteristic is that at higher frequencies, there is a frequency-dependent region, which is increasing in nature and frequently called alternating current (AC) conductivity (σ_{ac}). It is due to localized and short-range hopping, or orientation of charge carriers, and occurs in the higher frequency ranges at elevated temperatures.

The conductivity dispersion region will decrease in temperature at high temperatures. This is mainly attributed to the effects of electrode polarization whereby mobile ions are driven to the interfaces of the electrodes, thereby plugging the transport of ions further. Consequently, apparent conductivity decreases in this area with a decrease in frequency.

This effect indicates ionic transport, and the presence of it in the conductivity spectrum implies the higher mobility of Na ions. The σ_{total} plots reveal that σ_{total} is the sum of both dc conductivity (σ_{dc}) and ac conductivity ($\sigma_{ac}(\omega)$). By using the following Almond-West formalism, the σ_{total} can be investigated [1, 2]:

$$\sigma_{total} = \sigma_{dc}\left[1 + \frac{\omega}{\omega_H}\right]^n \qquad (6.1)$$

The crossover frequency, or hopping frequency, ω_H is an important parameter, in the sense that it is the point where a low frequency dc conductivity region changes to a high-frequency dispersive ac conductivity. It is this frequency that is the characteristic of the charge carriers that are generally small polarons, which corresponds to electrical conduction.Analysis of experimental sigma total data was done under the Almond West model (**Eq. 6.1**), with the optimum non-linear inset curves in **Fig. 6.1** represented by solid black lines. Based on these fits, good parameters were obtained (e.g.), σ_{dc}, n, and ω_H.

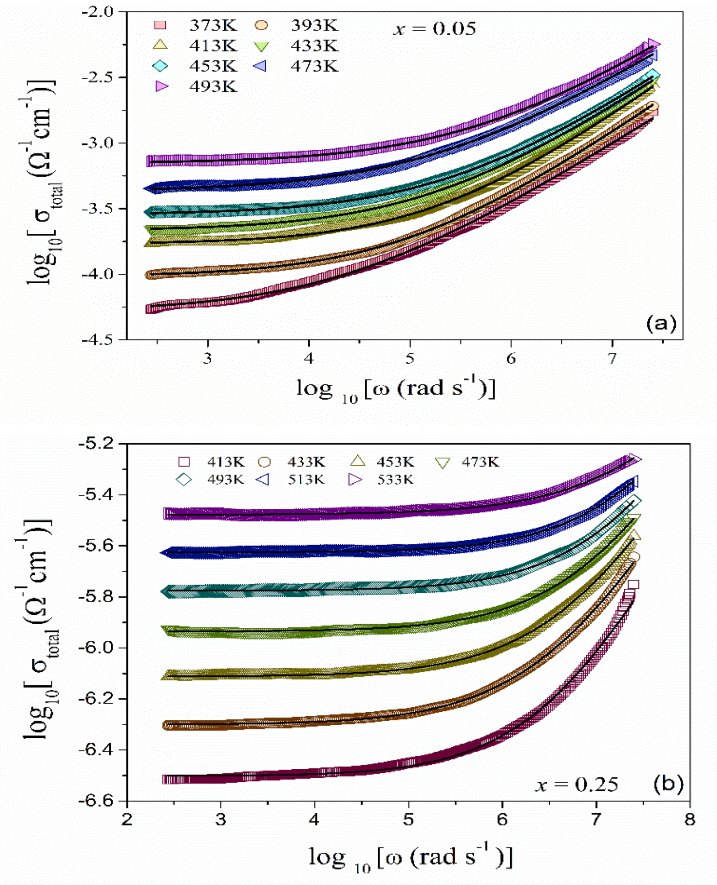

Fig. 6.1 Total conductivity (σ_{total}) spectra of the (a) $x = 0.05$ and (b) $x = 0.25$ system at various temperatures.

Conversely, n is a subscript which is fractional and is critical to determining the dominant conduction mechanism. Whether the conduction pathways are ionic or non-ionic can be differentiated by their means and gives an idea about the dimensionality of the conduction pathways [3]. It is interesting to note that values of n depend on more than just inherent material factors and the temperature profile of the surroundings [1,3].

Values of the ac conductivity (σ_{ac}) have been obtained by previously obtaining the dc conductivity (σ_{dc}), with the following relationship: $\sigma_{ac} = \sigma_{total} - \sigma_{dc}$

AC conductivity is highly sensitive in bulk amorphous or polycrystalline materials in terms of structural symmetry, grain distribution, and grain-size or crystallite-size embedded inside the glass network [4]. Localised charge transport is considered a major contribution to the

conduction mechanism of this regime and can be attributed to oxygen vacancies, short hopping of charge carriers, small polaron motion, or a combination of these factors [3].

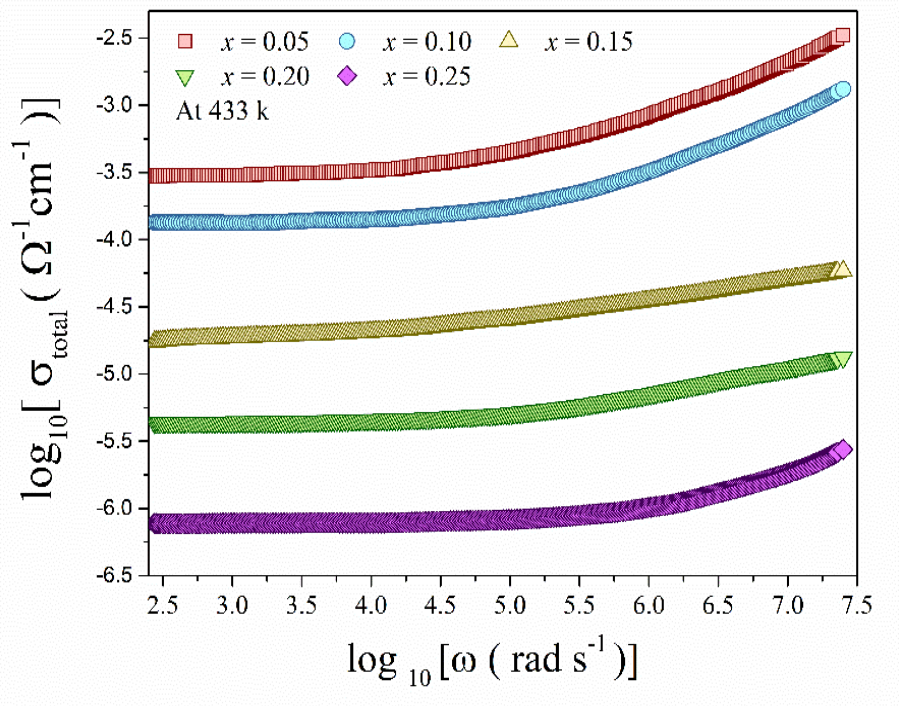

Fig. 6.2 Total conductivity (σ_{total}) spectra of all the nanocomposites at 433 K.

Fig.6.3 presents the variation of σ_{ac} for all glass samples at a temperature of 453 K. The results mirror those observed for σ_{total}, showing that σ_{ac} decreases as the V_2O_5 content increases. This tendency strengthens the idea that the increment of V_2O_5 changes the dynamics of the conduction, and this transformation may be in terms of the mobile charge counts or structural conduction channels.

Also, the value of sigma ac is increasing with the increase of the frequency. It is a usual behavior because an increase in frequency increases the possibility of release of space charges trapped in the disordered matrix, which makes the charge carriers mobile.

Overall, any ac conduction on disorderly materials is controlled by the level of atoms and the composition disorder. Such disorder may create localized electronic states or clusters, and these states greatly affect the conduction process. The Jonscher universal power law is largely applied to effectively quantitatively explain the phenomenon of σ_{ac} being a frequency-dependent phenomenon. This empirical model is like this [5]:

$$\sigma(\omega) = \sigma_{dc} + A\,\omega^{S} \qquad (6.2)$$

In this equation, σ_{dc} is the conductivity under direct current (DC), and A is a pre-exponential constant that in some materials is temperature-dependent and in others it is temperature-independent. The parameter *S* is the power law exponent, and it gives us information about the nature and the strength of the interaction between charge carriers, e.g. small polarons or electrons and the disordered glass network the carriers move in.

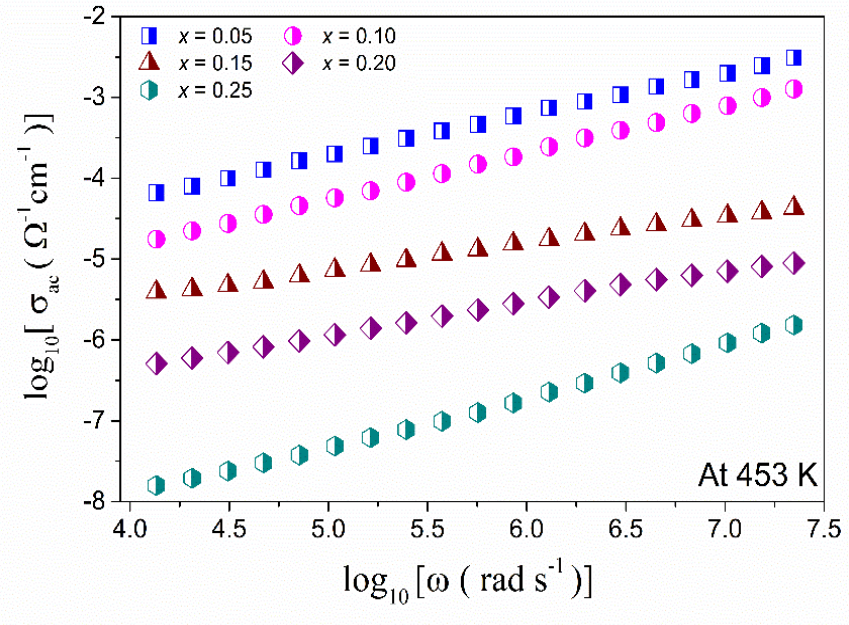

Fig. 6.3. AC conductivity (σ_{ac}) of all the samples at 453 K.

The values of the power-law (*S*) exponent were obtained on the basis of linear least-squares fit of the dispersive region of the This region covered a regime where the ac conductivity has its low-frequency response. These values can be great hints to the driving underlying mechanism of conduction, and their temperature-dependent behavior can aid in determining the prevailing model. Depending on the observed behavior (experimentally) [7], the number of basically different *S* vs. temperature trends is related to different mechanisms of ac conduction processes.

As it is shown in **Fig. 6.4**., the *S* value diminishes with the temperature, which means that the most appropriate model that describes the ac conductivity behavior in the research system under consideration is the Correlated Barrier Hopping (CBH). The introduction of the CBH model by Pike [7] and its subsequent development by Elliott [8] has found wide usage as a highly convenient description of frequency-dependent conductivity in structurally disordered materials.

CBH mechanism is done on some basic assumptions. It is assumed that charge carriers (usually small polarons) can hop between localized states with an energy barrier being overcome in the process. These hopping processes are thermally activated and the relatively high barriers encountered therefore necessitate the aid of a good number of phonons. This model is the model of charge carriers that are supposed to be non-interacting and are situated in the lattice where they have an opportunity to make only nearest-neighbour jumps. The rate of hopping, the hopping Occurrence rate, or the probability of hopping by a particle in a unit time has been assumed to be symmetrical in each of the directions.

Notably, in contrast to quantum tunnelling processes, the CBH model considers jumps over potential barriers, as opposed to the quantum tunnelling process across the barrier. That is why it is especially applicable at higher temperatures, as thermal energy has enough strength to help carriers overcome the energy barriers. Therefore, the theoretical estimations provided by the model of CBH are accurate in explaining the experimental results of the observed decline in S at an increase in temperature, thus justifying the application of the said model to the glass samples under study.

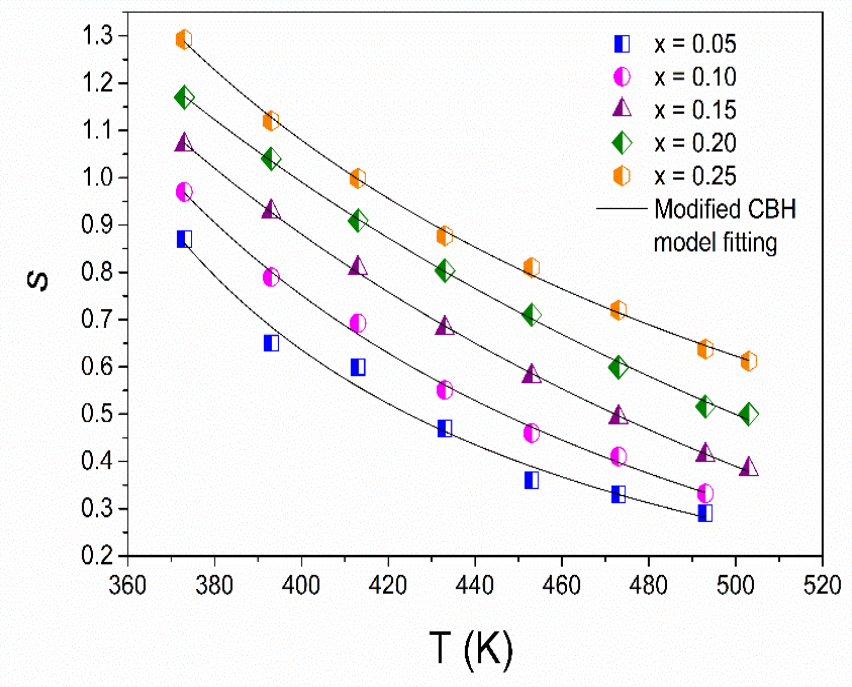

Fig. 6.4. The power-law exponent (s) against temperature (T) plot fitted with modified CBH model (solid black lines) of all the samples.

When it comes to ac conduction, presence of defined defect states in the material becomes very important. The defect states have a high mutual interaction which allows these states to cause

a widening of the energy barriers which separate the localized sites. This variation in barrier heights directly influences the hopping behavior of charge carriers and is a key feature of the Correlated Barrier Hopping (CBH) model [7]

In this context, the power-law exponent (*S*) that defines the dependence of frequency dependence of ac conductivity can be rescued quantitatively as a function of temperature (T) as follows [7,8]:

$$S = 1 - \frac{6\,K_B\,T}{W_M + K_B T * \ln(\omega \tau_0)} \tag{6.3}$$

The Debye relaxation time is defined as τ_0 in the above equation; hopping barrier potential; W_M is often thought of as the polaron binding energy; K_B is the Boltzmann constant. The S value which was found using experiments is more than 0.75 on all the analyzed samples as illustrated in **Fig. 6.4**. As it is confirmed by one of the previously established literatures [9,10], the conventional CBH model is inappropriate to apply to the materials when S exceeds 0.75 because the values above this predictive range are beyond its capabilities.

To overcome this shortcoming, we have used the modified CBH model [9,10], where long-range interactions are taken into consideration as well as complicated barrier distributions. The behavior of disordered systems with much higher S values is closer to this model. As can be seen in solid black fitting curves in **Fig. 6.4**, the modified CBH model has a high performance when applied to the experimental data, which demonstrates its usefulness in this study. The theoretical implementation becomes mathematically defined as given below [9,10]

$$S = 1 - \frac{6\,K_B\,(T - T_0)}{W_M + K_B\,(T - T_0)\,\ln(\omega \tau_0)} \tag{6.4}$$

T_0 is an ideal thermodynamic glass transition temperature in the context of the modified CBH model. The parameter is deducted to fine-tune the applicability of the parameter to disorderly glass systems, as calculated by the model, by the actual operating temperature (T). In theory, by including T_0 in the model, the behavior of the glass transition can be better estimated with electrical stimulation in the model.

The most important fitting parameters of the modified CBH model, that is, W_M (hopping barrier energy or polaron binding energy), T_0 (ideal glass transition temperature) and T0 (Debye relaxation time), were then extracted from the best fits with the experimental conductivity data. This is summarized in **Table 6.1**.

In **Table 6.1**, that indicates that, the lowest values of W_M, τ_0 and T_0 and the maximum value of conductivity are observed in the sample with x = 0.05, and this is consistent with the higher conductivity already demonstrated in **Fig. 6.2**. This tendency proves the negative correlation between these parameters and electrical conductivity. The increases in W_M, τ_0 and T_0 have clearly been seen as the content of V_2O_5 (x) becomes higher and as a result, conductivity decreases in total. The above behavior complies with the fact that a higher polaron binding energy and relaxation time place more constraints on carrier mobility, thus discouraging conduction.

Table 6.1. All values of modified CBH model fitting parameters for all the specimens.

x **(mol %)**	Modified CBH model		
	τ_0 (sec)	W_M (eV)	T_0 (K)
0.05	2.34×10^{-2}	0.038	361
0.10	9.41×10^{-3}	0.052	369
0.15	2.71×10^{-3}	0.071	382
0.20	2.07×10^{-3}	0.082	398
0.25	1.41×10^{-3}	0.086	412

The crossover (or hopping) frequency (ω_H) associated with the charge carriers or small polarons varies in an Arrhenius like manner as evident in **Fig. 6.5(a)** as a function of the inverse of temperature (1/T). This thermally activated profile states that the hopping frequency augments with temperature resembling prior to same condition in disordered materials in transporting localized charges.

To measure this behavior, the activation energy (E_H) corresponding to ω_H was calculated by fitting the experimental data linearly (by least squares) with ω_H. **Fig. 6.5(a)** shows the solid black lines that represent the fitting. They adopt the standard Arrhenius equation to the analysis, and it is written as [11]:

$$\omega_H = \omega_e \exp\left(\frac{-E_H}{K_B T}\right) \tag{6.5}$$

In the expression given above, the term ω_e is called the effective attempt frequency, it is the frequency of hopping by the charge carriers or small polarons to hop between localized sites.

Absolute temperature is T, and activation energy E_H represents the energy needed by these carriers to pull them out of the potential barrier of defect or localized states.

The physical association of E_H represents the least amount of energy required to enable the charge carriers to jump or tunnel through the energy barriers constructed by structural disorder or defect states in the glass matrix.

Interestingly, and as depicted in **Fig. 6.5(b)**, a very evident inverse relationship is witnessed: larger values of E_H are found when lower values of σ_{ac} or σ_{total} are used. This means that the systems having greater electrical conductivity demand less energy in triggering carrier hopping thus suggesting more efficient process of charge transport.
The greater the temperature, the less energy charge carriers or small polarons need, the greater the movement. At high temperatures, these carriers will start to oscillate more strongly and are thus able to more easily tunnel through or jump between localized or defect states in the glass matrix. The nature of the materials also determines this thermally activated process, further by the structural characteristics of the material. Specifically, the presence of both V^{4+} and V^{5+} ions in nanocrystallites also provides a source of variation in the atomic potential of the generation of electron trapping sites. These localized states also enable hopping conductivity whereby the electrons or the small polarons hop between various valence states of the same transition metal ions (TMIs), which is a typical process in disordered transition metal oxide systems.

The electrical conductivity as well as the activation energy of the ionic transport in glassy systems can be largely dominated by two factors, as per the Anderson-Stuart model of the glassy systems:

i) electrostatic binding energy (E_B), the energy that must be added to release the charge carriers out of their binding sites,

ii) the energy of strain, (E_s), which sometimes assumes the strain energy of deformation of the glass matrix around the ion movement [12].

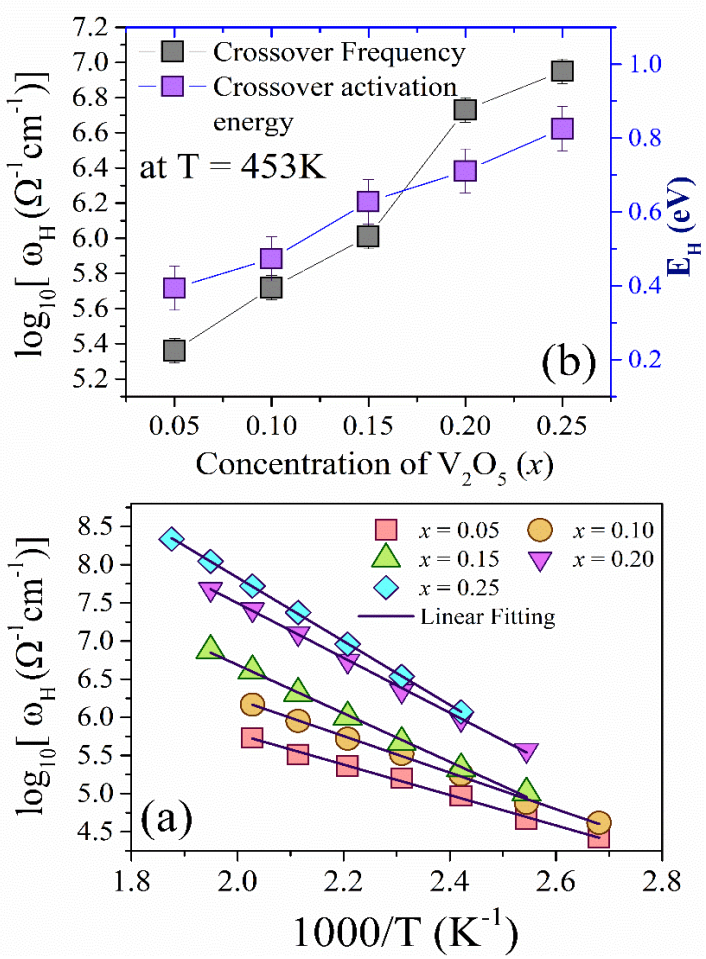

Fig. 6.5 (a) The small polaron hopping frequency (ω_H) values at a fixed temperature (453 K) and the activation energy (E_H) values with different values of *x,* and **(b)** the values of ω_H against the reciprocal temperature of all the composites.

In the current study, there are sodium ions (Na^+) and also multivalent vanadium ion that contributes to the overall electrical conductivity. It is, however, hypothetically dominant that Na^+ ions serve as carriers of charge, especially where the concentration of V_2O_5 is low (x). An obvious method of conductivity improvements is thus the way whereby more mobile charge carriers (n) have been augmented without loss to their mobility (μ) . Alternately, a relative ratio adjustment of the components of the glasses may be able to maximize both E_B and E_S, thus maximally increase conductivity.

Based on the analysis of the Almond-West model, one can say that the temperature dependence of σ_{dc} is high, and a plot of σ_{dc} versus 1/T shows a linear Arrhenius dependence as illustrated in **Fig.6.6(a)**. The data show that as the temperature rises, σ_{dc} rises and with increase in

concentration of V_2O_5 (x), its value falls. This reverse trend is mainly explained by the fact that Na_2O goes down as x increases, as is borne out in **Table 3.1** of **Chapter 3**. When x is low, the increased level of sodium ions increases the ionic conductivity in the mixture and improves the value of σ_{dc}.

This indicates that the ionic transport that involves the movements of Na^+ ions is more dominant in the total conductivity as compared to the means of electronic transport, which involves changing the valences that are involved across the atom of the vanadium ion. As the melt-quenching process takes place, the glass matrix changes in a way that the mobility of the Na ions increases. There is an explanation of this by alterations in local bond polarizability, chemical ordering and network firmness.

When inserted into the phosphate-based glass, Na_2O modifies the network of the phosphate-based glass through the breaking of the P-O-P bonding in the glass network. This reaction leads to the formation of NBOs, or more simply, P–O–Na^+ bonds [13]. These NBOs promote the ionic strength of the glass network, which allows the glass to have a higher conductivity owing to the ionic nature of the bonding of sodium with the matrix. Therefore, the increment of Na^+ quantity and NBO proportion results in the enhancement of the electrical conductivity.
A polycrystalline or amorphous solid has its overall ionic conductivity (sigma or written as sigma) represented by the following equation:

$$\sigma = nq\mu \qquad (6.6)$$

where n is the concentration of mobile charge carriers, q is the charge of a single carrier and mu the mobility of the carriers [14]. Lastly, the ionic conductivity is usually temperature dependent, where thermally-activated ionic migration can be summarized in an Arrhenius-type relation in disordered glass [14]:

$$\sigma_{dc}T = \sigma_0 \exp^{\left(-\frac{Q_C}{RT}\right)} = \left(\frac{n\,\lambda^2 q^2 \gamma \nu}{K}\right) \exp^{\left(-\frac{Q_C}{RT}\right)} \qquad (6.7)$$

In the above expression, the λ represents the distance between hopping sites on average, i.e. the inter-site spacing, whereas the ν represents the rate of attempts to hop between sites, also known as jump frequency. The symbol γ is the geometric constant between the sites where the hopping occurs. Q_c is the activation energy of mobility, which includes both the energy to

produce mobile defects and the energy of movement. The constants K and R refer at the Boltzmann constant and the universal gas constant, respectively.

The values of Q_C were determined based on the linear fits of the data of the experiment: the solid black lines in **Fig.6.6(a)**. The trend is evident in **Fig.6.6(b)**, whereby, as the values of the σ_{dc} increase, the values of Q_C decrease. The inverse relationship is what the theoretical vision on the basis of the mobility equation indicates the greater the ionic conductivity then the lesser the activation energy, because those energy barriers to ion transport are simply reduced. This tendency is an additional effect indicating that the rise in the ionic mobility, which is facilitated by the presence of Na^+ ions in this glass system, is the decisive factor contributing to the electrical conductivity.

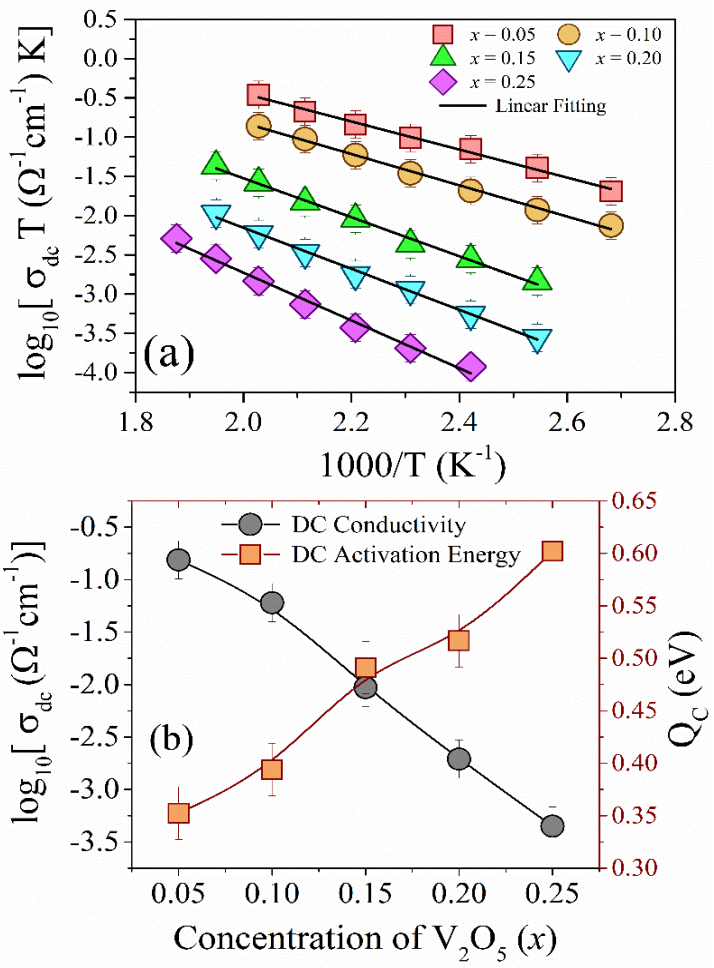

Fig. 6.6. (a) Temperature-dependent σ_{dc} T value of all the composites, the solid lines are best-fitted linear fit data and **(b)** σ_{dc} value and activation energy against *x*.

In view of understanding the isothermal conductivity behaviour of the present glass system, it can be seen to behold a situation similar to that of the ion-ion interactions, as in the mixed alkali effect, but with ion-polaron interactions to take place here [15]. A second perspective takes the ionic and electronic processes of conduction as separate and independent, and they traverse the disordered network of glass in different ways.

With this model, the space between the network is occupied by the V^{4+} and V^{5+} cations and the electronic conductivity is achieved through the movement of the electrons between the ions themselves. Using this redox pair, the dynamic redox changes can be used to transfer charges in a chain-reaction-like fashion, as an endless illuminated wire.

On the contrary, the ionic conduction is caused by the presence of structural disturbances induced by non-bridging oxygen atoms (NBOs). The formation of these NBOs, due to the cleavage of the P-O-P bonds on the addition of the Na_2O, makes open channels, into which the Na^+ ions migrate. The NBOs are efficient in setting up ion-conducting pathways, and the displacement of mobile ions is facilitated by the former phosphate chains.

With further increase in V_2O_5 concentration, the V^{4+}/V^{5+} chains of conduction paths are less likely to form continuous chains and efficiency of electronic paths becomes impaired. Such change is relevant to reducing the electronic conductivity, with such contribution as ionic transport becoming more eminent, particularly with the elevated structural disorder, and higher NBO.

Therefore, the electric performance of this system signifies a mixed mechanism wherein a synergy between electronic and ionic conduction is present. The prevalence of one influences heavily on the relative composition, especially the balance between Na_2O and V_2O_5 that determines the availability of charge carriers and relative connectivity of their respective conduction pathway.

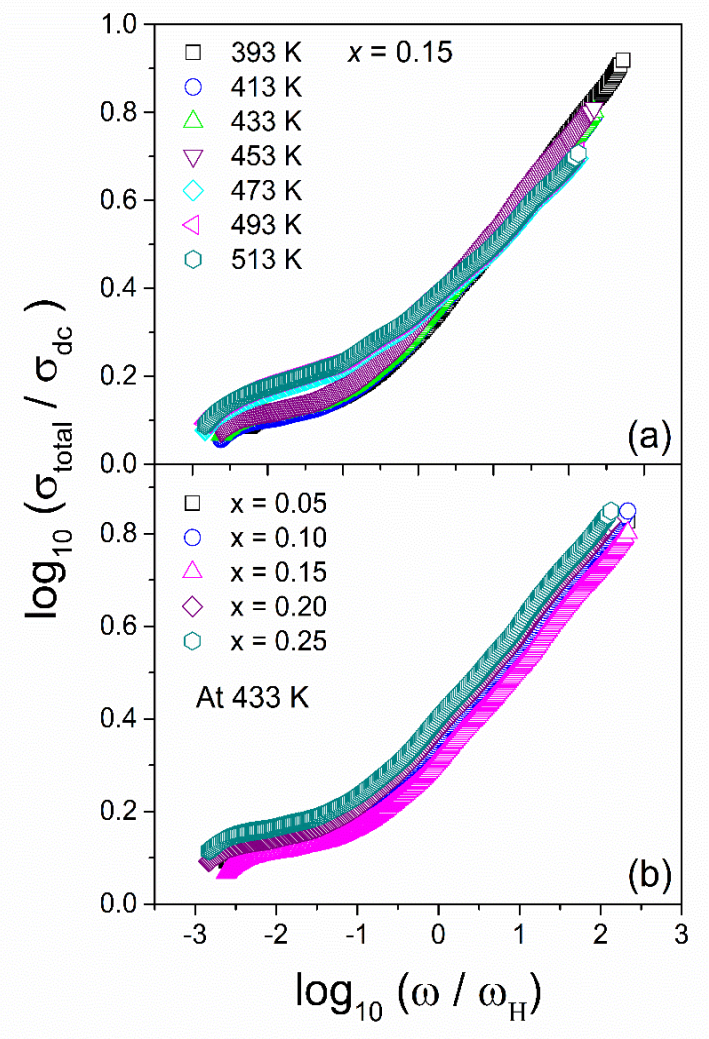

Fig. 6.7. (a) AC conductivity temperature scaling spectra of $x = 0.15$ sample at different temperatures and (b) AC conductivity composition scaling spectra at 423 K.

It is possible to analyse the effect of temperature and composition on the dynamics of conductivity relaxation meaningfully with the help of the scaling behavior of sigma total, which is usually determined by the time, temperature superposition (TTS) principle [16]. Within this context, the sigma-total spectra are then normalized, where the frequency axis is divided by crossover frequency (ω_H), and the conductivity axis by the dc conductivity (σ_{dc}).

This scaling technique was done in two approaches:

- Temperature scaling, with spectra of the x = 0.15 sample being measured at different temperatures (**Fig. 6.7(a)**),

- Scaling of composition, in which all of the spectra were acquired over one constant temperature (**Fig.6.7(b)**). At the example of the temperature scaling (**Fig.6.7(a)**), the scaled curves are not collapsed on a single master curve, which means that the relaxation dynamics do depend on temperature; hence, the TTS principle is not fulfilled at this composition. Other compositions that were studied have been found to have had similar TTS violations as well.

The fact that TTS principle fails implies that the system fails to satisfy the BNN relation, which is normally associated with TTS validity [16]. In this regard, the fact that the BNN relation is not followed is probably the main cause of the TTS violation observed. Nevertheless, some other factors can also lead to this kind of behavior. It is possible that in such glassy systems, the short-range dynamics of Na^+ ions are not linked to long-range ionic transport channels [17]. Besides, the effects of incorporating nanocrystallites into the glass digressive engine Na^+ ion mobility on various length scales added another constraint to homogenous relaxation [18].

Another possible cause is the significant variation in the dimensionality of conduction pathways, coupled with the coexistence of both ionic and polaronic conduction mechanisms. These mixed transport processes complicate the relaxation dynamics, leading to further deviation from ideal scaling behavior.

6.3. Quaternary Bi_2O_3-BaO-V_2O_5-P_2O_5 glass system

6.3.1. Study of electrical conductivity

This section reports the study of the electrical conduction properties of the investigated system of glass over different temperatures in detail. **Fig. 6.8(b)** shows the frequency-dependent composite conductivity spectra (σ_{total}) as a composition x = 0.15 was measured between 523 K and 673 K. It can be noticed that the values of 0.48 have increased significantly with the increase in temperature, which confirms the presence of semiconducting nature of the material. Each of the sigma total spectra shows two clear zones. At low frequencies, the conductivity is approximately equal and does not depend on frequency, which is the conductivity at DC (σ_{dc}). With an increase in temperature, the span of this flat region widens, signifying an improvement in the mobility of the charge carriers. The high-frequency range, on

the other hand, exhibits a frequency dispersive effect with conductivity rising almost linearly with frequency--a feature characteristic of ac conductivity controlled by processes of hopping or tunnelling. Temperature-dependent measurement shows that the clarity between the flat and dispersive regions increases with increase in temperature therefore indicating increased dynamics of the charge carriers. This transition is contributed by the combined effect of ionic as well as polaronic (electronic) conduction mechanisms that increase in activity at higher temperatures. The dispersion of dissimilar regions, therefore, starts to interfere more with each other, indicating a more substantial ionic-electronic spectrum fusion at the high-frequency levels.

As seen in **Fig. 6.8(b),** the σ_{total} spectra of all glass samples at the same temperature, ie, 598 K, were compared. As can be seen in the graph, the overall conductivity decreases with an increase in Bi_2O_3 concentration (x). This drop can be related to the structure changes caused by Bi_2O_3, which potentially interferes with the formation of greater conduction pathways, which are made firmer or in which connectivity is disturbed with the glass network.

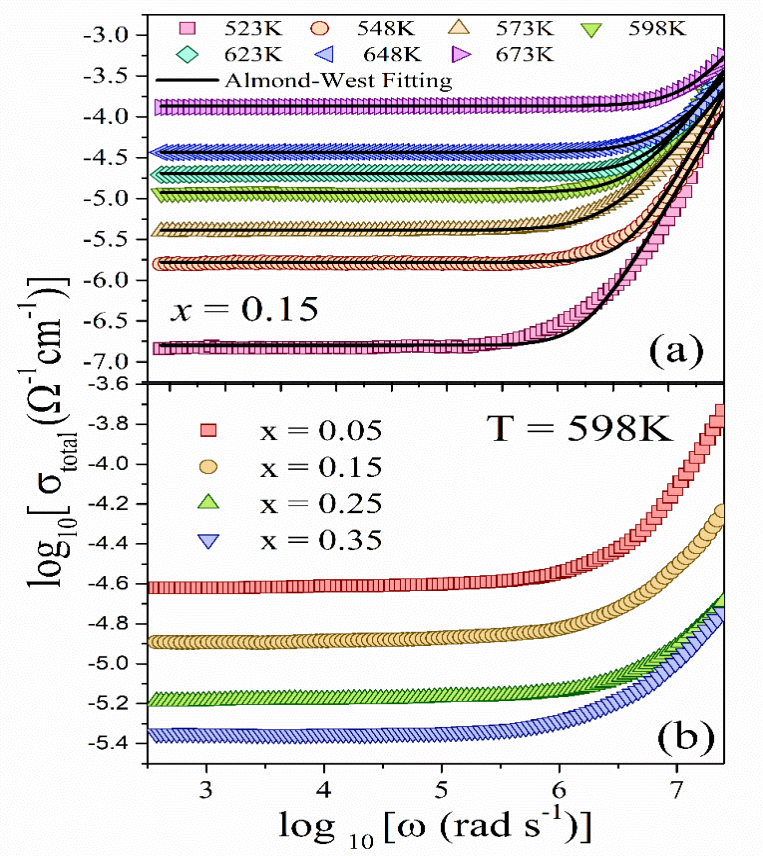

Fig. 6.8 Frequency-dependent overall conductivity of **(a)** glass sample of $x = 0.15$ and **(b)** all the glass samples at 598K.

The dispersion effect that is frequency-dependent and apparent in the conductivity spectra in glassy materials occurs through a number of mechanisms. Primarily, it is due to the motions of mobile ions in the amorphous glassy matrix, and to hopping or tunnelling motion of localized charge carriers or small polarons across defect states inside the band gap [1,2]. Of these, the tunnelling of the small polarons feature is of leading order in contributing to giving rise to the observed dispersion in the full frequency regime.

The frequency dependence of activation energy is also observed, and with increasing frequency, the activation energy for conduction decreases gradually, which can be explained by the fact that the charge carriers, which are mainly small polarons, exhibit a localized hopping between adjacent defect states. Processes involving lower-energy carriers, over distances which are relatively small, and where not so high potential barriers have to be overcome, are generally also less energy-consuming than the optical activation energy (E_{opt}) [5].

The general profile of conductivity spectra of all these disordered glass systems is in good agreement with Jonscher's universal power law, which is an empirical relation to describe the nature of ac conductivity of amorphous materials. Also, the data are interpretable in the Almond West formalism, and the two are well-known models of conduction mechanisms in ion-conducting and semiconducting glasses. The relevant mathematical form of Jonscher's universal power law is given in **Eq. (6.2)** [6], which indicates that the frequency dependency of ac conductivity is a power dependence. The power-law exponent and pre-factor in **Eq. (6.2)** are denoted by s and A, respectively. Almond-West formalism also explains the σ_{total}, which is given in **Eq. (6.1)**. The fractional exponent (n) provides essential insights into the nature of the conduction mechanism—specifically indicating the ionic or non-ionic nature, the dimensionality of the conduction pathways, and the dominant charge transport mechanism involved. Additionally, ω_H represents the hopping frequency (or crossover frequency) of mobile charge carriers such as small polarons. This parameter marks the critical transition point ($\omega = \omega_H$) that separates the frequency-independent dc conduction region from the frequency-dependent ac dispersive region in the conductivity spectra [6].

Fig. 6.9(a) presents the variation of the hopping frequency with the inverse of temperature, following an Arrhenius-type behaviour. This temperature dependence of ω_H implies a thermally activated hopping process. The activation energy for hopping (E_H) can be extracted by fitting the experimental data using the Arrhenius relation as described in **Eq. (6.5)**. The fitting, carried

out using the least-squares method, is shown by the solid black lines in **Fig. 6.9(a)**, providing a reliable estimate of E_H for the glass system under investigation. Here, T is the absolute temperature in Kelvin, and ω_e is the attempted frequency of hopping of the charge carrier that is mostly effective. The parameter $E_{H,}$ frequently called the energy threshold, represents an absolute lower limit of energy necessary to have small polarons be able to surmount any potential barriers - to be able to hop, tunnel or move across the localized or defect states in the disordered glass matrix. Interestingly, E_H is low when the overall conductivity of the glass system is also low, and this shows that carrier mobility is lower in more resistive circumstances.

This effect can be assigned to the emergence of nanocrystallites with an enrichment of the V^{4+}/V^{5+} ionic pair, with the different atomic potentials. These transition metal ions are used as electron traps, and they create localized energy levels that lead to electron hopping between various valence states of adjacent transition metal ions (TMIs). These local conducting channels take the lead in the transportation of charge in such disordered glass materials. The frequency of hopping (ω_H) was observed to be affected by increasing concentration of Bi_2O_3 (**Fig. 6.9(b)**), which points to the hindrance of hopping activity. The observed trend can be linked to the negative correlation between ω_H and E_H, and this is across the system, which indicates that the higher the activation barriers are, the lower the frequencies of hopping will be across the system.

In the above equation, T is the absolute temperature in Kelvin, and ω_e is the effective attempt hopping frequency. The E_H, also known as the energy threshold, is the lowest energy needed for small polarons to hop, tunnel, or pass through localized or defect sites that are spaced apart by a potential barrier. The E_H value increases as the overall conductivity of the glass decreases. Nanocrystallites include V^{4+}/V^{5+} ions with various atomic potentials, which trap electrons, create localized sites, and allow electrons or tiny polarons to hop between distinct valence states of associated transition metal ions (TMIs). The values of are seen to decrease with the addition of Bi_2O_3, while ω_H and E_H exhibit an inverse relationship in **Fig. 6.9(b)**.

DC conductivity (σ_{dc}), derived from the Almond-West formalism, is also dependent on temperature. The nonlinearity of the σ_{dc} data arises from the involvement of multiple conduction mechanisms. In **Fig. 6.10(a)**, the σ_{dc} plot against reciprocal temperature is displayed, and σ_{dc} can be described by the following Arrhenius equation [19, 20].

$$\sigma_{dc} = \sigma_{High} \exp\left(-\frac{E_{High}}{K_B T}\right) + \sigma_{Low} \exp\left(-\frac{E_{Low}}{K_B T}\right) \quad (6.8)$$

Fig. 6.10(a) shows the plot of DC conductivity (σ_{dc}) versus the reciprocal temperature (1/T), in the studied glass systems. The trend in the spectra is nonlinear which confirms the semiconductive nature of the materials. The behavior of the DC conductivity is explained in terms of two regimes of thermal behavior, as mentioned in the first term of **Eq. (6.8)**.

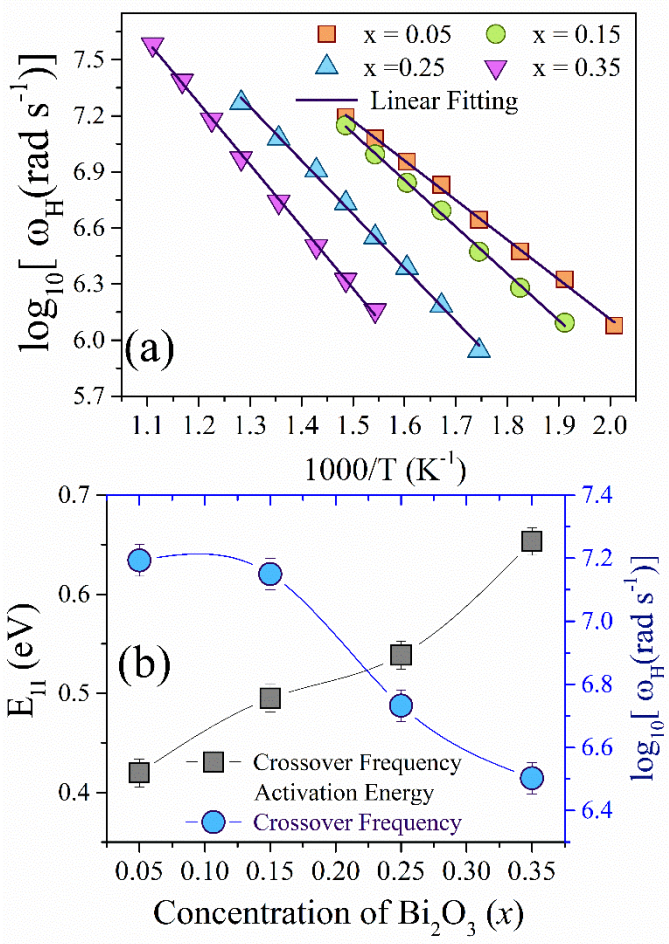

Fig. 6.9 Variations of **(a)** crossover frequency with reciprocal of temperature and **(b)** estimated values of crossover activation energies and crossover frequency at 573K with the variation of concentration of Bi_2O_3

In the high-temperature range, σ_{dc} is dominated by thermally activated transportation and is known as σ_{High}. Conversely, the low-temperature conductivity (σ_{Low}) is due to quantum mechanical tunnelling between empty nearest neighbour sites or due to small polaronic hopping between localized states having energetic disorder or defect-associated localized states. Both σ_{High} and σ_{Low} are pre-exponential factors that are dependent on composition and

are related to the effects of structural changes on charge transport properties [19,20]. The linear regions of the σ_{dc} plots in each temperature domain were used to extract activation energies corresponding to high- and low-temperature conduction processes, denoted as E_{High} and E_{Low}, respectively. These values were acquired based on the tendency of least-squares linear regression fitting of the experimental data, as depicted in **Fig. 6.10(a)**.

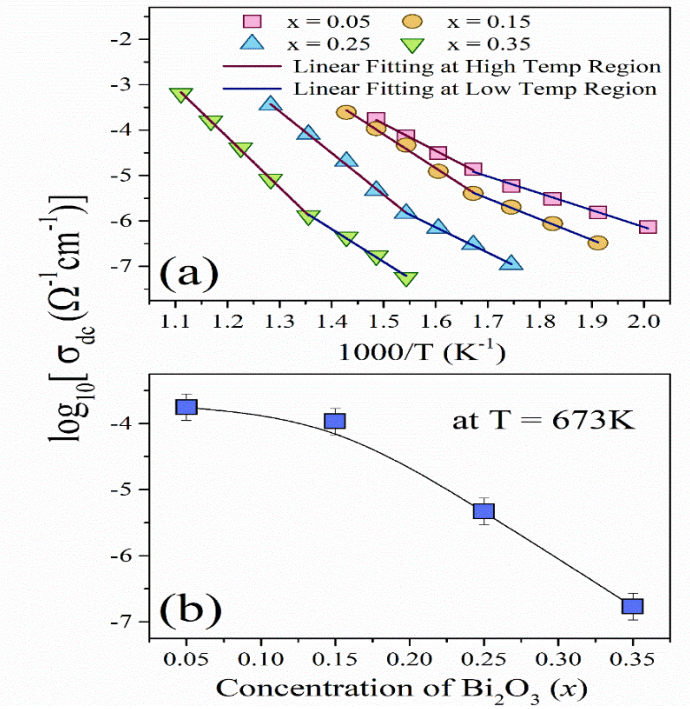

Fig. 6.10(a) Temperature-dependent DC conductivity and **(b)** comparison of DC conductivity at 673K of all the glass samples

Table 6.2 includes a summary of the calculated values for E_{High} and E_{Low}. The decrement in σ_{dc} of glass samples with higher Bi_2O_3 concentration is authenticated by the increasing trends of E_{High} and E_{Low}.

At low temperatures, charge carriers or small polarons frequently migrate by hopping between localized energy states, a process well-explained by Mott's Variable Range Hopping (VRH) model [21, 22]. This conduction mechanism is dominant within the mobility gap or optical bandgap, where thermal energy is insufficient to activate carriers into extended states. The applicability of Mott's VRH model arises when localized states exist near the Fermi level, and the density of states (DOS) at this energy is finite. Under these specific conditions, the hopping conduction becomes temperature-dependent and follows a characteristic behavior described by the VRH expression, given by the following equation.

$$\sigma_{dc} = B \exp\left[-\left(\frac{T_0}{T} \right)^{1/4} \right] \tag{6.9}$$

and,

$$T_0 = \frac{16\alpha^3}{K_B N(E_{FM})} \tag{6.10}$$

Here, $N(E_{FM})$ is the density of states at the Fermi Level, T_0 is the characteristic temperature of the hopping process, and α^{-1} is the localization length of the small polaron wave function [22]. **Fig. 6.11(a)** gives the plot of σ_{dc} against $T^{-0.25,}$ and both the experimental and theoretical correlations based on **Eq. (6.10)** are in great agreement. Taking into account the slope of the data that were plotted in **Fig. 6.11(a)** by using the linear fit and assuming that the localization length is always constant (i.e., 10 Å), the values of $N(E_{FM})$ were extracted [21, 22]. Moreover, mean hopping distance (R_{hop}) and hopping energy (W_{hop}) are critical temperature-dependent hopping parameters. It was by applying the following relations that they were calculated [23].

$$R_{hop} = \left(\frac{9}{8\pi N(E_{FM})\alpha K_B T} \right)^{1/4} \tag{6.11}$$

and,

$$W_{hop} = \frac{3}{4\pi \left(R_{hop} \right)^3 N\left(E_{FM} \right)} \tag{6.12}$$

At constant temperature, e.g. at 573 K, the parameters R_{hop} and W_{hop} were calculated using **Eqs. (6.11)** and **(6.12),** and data on these values are assembled in **Table 6.2**. To ensure that the model of Mott Variable Range Hopping (VRH) is still applicable, there are two key requirements to be met: $R_{hop}\alpha \geq 1$ and $W_{hop} > K_B T$ for all the glass mixtures under study. These conditions are completely met; it substantiates the adequacy of the VRH model in this temperature range. Most significantly, Bi_2O_3 inclusion causes the rise in R_{hop} and W_{hop} (as appears in **Table 6.2**), which refers to a reduced rate of conduction. This trend can be attributed to the increased spatial and energetic barriers encountered by polarons as they migrate between adjacent localized states.

Nevertheless, it should be mentioned that the VRH model developed by Mott becomes inadequate when the temperature dependence of σ_{dc} spectra is above half the Debye temperature ($\theta_D/2$). Greaves has put forward a different model to overcome this disadvantage,

which better describes how the DC conduction in disordered systems is conducted at higher temperatures, i.e., > $\theta_D/2$ [25].

$$\sigma_{dc}T^{1/2} = A' \exp\left[-\left(\frac{T_0'}{T}\right)^{1/4}\right] \tag{6.13}$$

and,

$$T_0' = \frac{19.4\alpha^3}{K_B N(E_{FG})} \tag{6.14}$$

Greaves's VRH model has been used to fit the experimental σ_{dc} spectra of all glassy systems at higher temperatures.

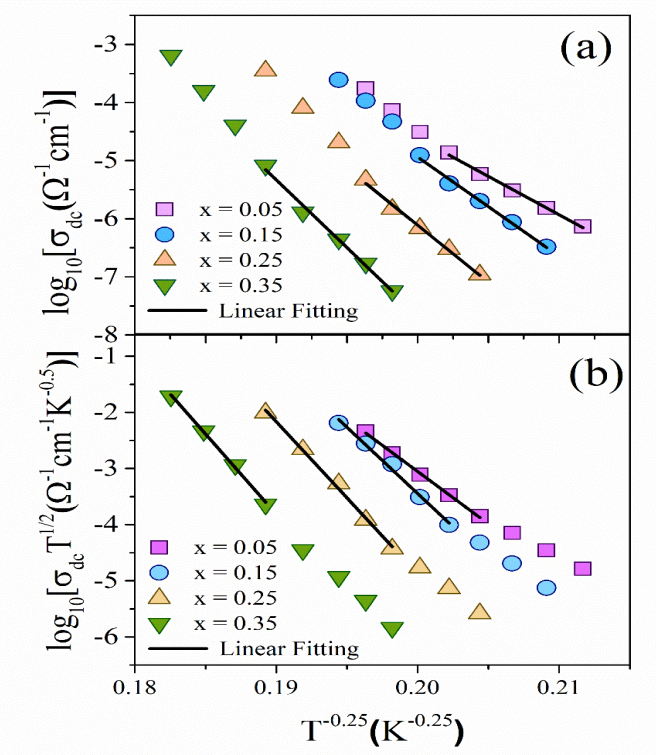

Fig. 6.11 (a-b) Mott's and Greaves's Model representation of DC conductivity spectra.

Fig. 6.11(b) shows the slope of the linear fit of the experimental data by means of Greaves Variable Range Hopping (VRH) modelling at high temperatures. As evident in **Table 6.2**, $N(E_{FM})$ and $N(E_{FG})$ values decreased with a rise in the concentration of Bi_2O_3 (x). Such organised depletion of the localized states density causes a decrease in the quantity of possible hopping sites of charge carriers, directly causing a reduction of σ_{dc} in all glass compositions. In this way, the reduction of $N(E_{FM})$ and $N(E_{FG})$ is the effective reason for decreasing the electrical conductivity of the compositions under study.

Jonscher's universal power law [**Eq. (6.2)**] gives an adequate account thereof, through the dependence of the AC conductivity on frequency and temperature. The critical value in this model is the exponent of the power law (s), which can provide information about the dynamics of active interaction between the moving charge carrier (e.g., polarons) and their environment of the nanocrystalline or amorphous phase.

Table 6.2 Several activation energy values, the density of states value of the Mott and Greaves model, and the values of hopping distance (R_{hop}) and average hopping energy (W_{hop})

x (mol %)	E_{Low} (Low T) (eV) (±0.01)	E_{High} (High T) (eV) (±0.01)	E_H (eV) (±0.01)	E_{ac} (eV) (±0.01)	$N(E_{FM})$ ($\times 10^{27}$ $eV^{-1}cm^{-3}$) (±0.10)	$N(E_{FG})$ ($\times 10^{27}$ $eV^{-1}cm^{-3}$) (±0.10)	R_{Hop} (at 573K) (nm) (±0.15)	W_{Hop} (at 573K) (meV) (±0.15)
0.05	0.73	1.17	0.42	0.14	13.02	3.96	2.86	0.77
0.15	0.90	1.47	0.49	0.22	04.71	1.54	3.69	1.02
0.25	1.31	1.81	0.53	0.34	02.61	0.89	4.27	1.16
0.35	1.42	2.13	0.65	0.47	01.37	0.76	5.06	1.36

The value of s can be used to deduce the nature of the conduction mechanism, that is, when the value of s is less than 1, it usually implies that there is thermally activated hopping or translation of carriers between neighbouring localized states across potential barriers [26]. On the other hand, as Gilroy et al. state, values of s > 1 can be attributed to charge being transported through asymmetric double-well potentials based on quantum mechanical tunnelling between localized defect sites (s > 1) [27].

The frequency-dependent spectra of x=0.05, quaternary glass systems are given in **Fig. 6.12(a)**. There is a definite linear increase in sigma ac with frequency, which fits the hopping type of conduction. **Fig. 6.12(b)** gives the temperature-dependent 0. In this case, all the nanocomposite systems are plotted at a constant frequency, where 1 MHz was used. The data are quite common to the thermally activated AC conduction trend. With the aid of linear fits (solid black line of **Fig. 6.12(b)**), the values of the activation energies (E_{ac}) were obtained at each composition, and the respective values are captured in **Table 6.2**.

It is interesting to note that the addition of Bi_2O_3, a heavy metal oxide, is associated with a progressive accentuation of E_{ac} across all the glass samples. This means that systems to facilitate the AC conduction, greater thermal energy to acquire, which eventually leads to loss of AC conductivity. The parameter E_{ac} is the lower limit of energy which charge carriers must

go through to participate in the conduction process in these disordered glassy semiconductors [28].

The high-frequency linear regression of σ_{ac} offers key insights into the temperature dependence of ac conductivity as per **Fig. 6.12 (a)**. The power-law exponent (s) temperature variation is one of the key pointers in determining the most appropriate AC conduction mechanism [29].

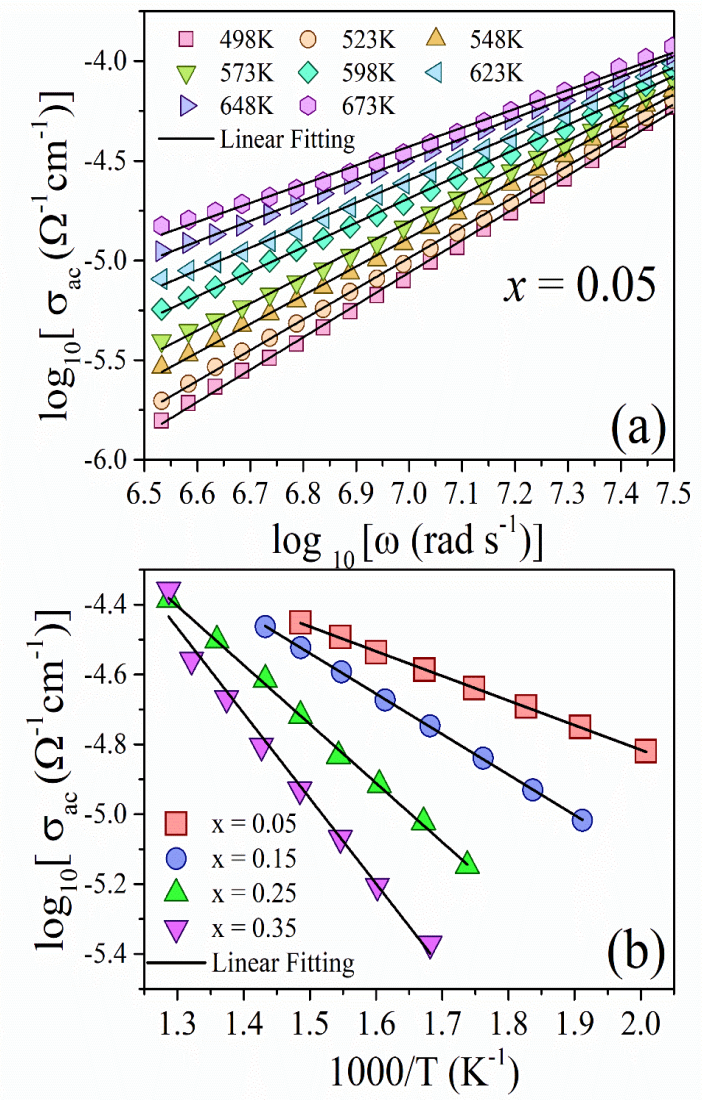

Fig. 6.12 (a) AC conductivity of $x = 0.05$ glass system with frequency and **(b)** AC conductivity at f = 1MHz of all glasses with temperature.

The estimated values of "s" in **Fig. 6.13** consistently decline with rising temperature. This tendency firmly confirms that the Correlated Barrier Hopping (CBH) is realistic in the vast majority of cases, first introduced by Pike and Elliott [30,31] to explain the process of conducting alternating current in disordered or amorphous systems of semiconductors.

In the CBH model, AC conduction is attributed to a thermally activated hopping process involving small polarons or charge carriers that jump over potential barriers separating localized states. The existence of these energy barriers is not random, and they are, instead, associated with the distance between sites as a result of Coulombic forces. Critically, the CBH model also limits hopping between only nearest-neighbour sites, and the charge carriers are usually localized into potential wells of the disordered lattice. The model presupposes a hopping rate symmetry, i.e. the rate of the hopping process of a charge carrier between two localized sites with forward and backwards steps is the same. Such symmetric hopping is particularly pronounced at high temperatures due to the fact that at such temperatures, the carriers have enough thermal energy to surmount the correlated energy barriers successfully.

In contrast to the tunnelling-based mechanisms, the CBH model is based on the concept of hopping conduction, which presupposes a significant role of defect states in the glass matrix in the process of carrier transfer. Such defect states will lead to broader distributions of barrier heights and thus affect the frequency and temperature dependence of the AC conductivity. Consequently, the CBH model can be deemed successful in an effort to describe the intricate nature of conduction in amorphous semiconductors and glassy semiconductors. The mathematical expression that holds the relationship between power-law exponent (s) and temperature (T) in the CBH model is given in **Eq. (6.3)** [30]. Based on **Fig. 6.13,** it can thus be concluded that the computed values of the frequency exponent s are greater than 0.80 in all the glass composites that were studied. Such large s-values, however, are beyond the limits of the classical Correlated Barrier Hopping (CBH) theory that is usually limited to the single values of $s < 0.80$ [10, 5]. Thus, in a bid to be more precise in the description of the observed conduction behavior, a modified CBH model, as described earlier in the literature [10], was borrowed and used in the further analysis.

It is a more refined model, which considers situations in which the enhanced interactions, or more intricate localized defect environments, occur--situations in which the original CBH hypotheses cease to be valid. As shown by the solid black lines in **Fig. 6.13**, the experimental data exhibit a strong agreement with the modified CBH model, indicating its superior applicability in these high “s” regimes. The simplified CBH model has the improved frequency-exponent temperature dependence, and mathematically it looks as provided in **Eq. (6.4)** [10]. The concept used to describe the Vogel-Tammann-Fulcher (VTF) type of behaviour can also be used to assess the effective temperature applied to a glass sample by subtracting T_0 from the operating temperature [31]. By incorporating T_0 as a variable in the fitting of the

modified CBH model, the theoretical value of T_0 can be determined. **Fig.6.13** depicts the fitting of experimental data by using **Eq. (6.20)**. The obtained values of fitting parameters are tabulated in **Table 6.3**. It is found that the values of W_m, τ_0, and T_0 increase with rising Bi_2O_3 content (x), and conductivity decreases.

According to the CBH model, σ_{ac} for these glass systems can also be written as [32]:

$$\sigma_{ac} = \frac{\eta\pi^3 \left[N(E_F)\right]^2 \varepsilon\varepsilon_0 \omega R_{H\omega}^2}{24} \tag{6.15}$$

The relationship shown below is employed for determining the hopping distance ($R_{H\omega}$) of polarons at constant frequencies and the concentration of defect pair states ($N(E_F)$) [32].

$$R_{H\omega} = \frac{me^2}{\pi\varepsilon\varepsilon_0 \left[W_m + K_B T \ln(\omega\tau_0)\right]} \tag{6.16}$$

At different temperatures, $R_{H\omega}$, $N(E_F)$, and ε can be obtained by using the formula (**Eq. 6.21**). **Table 6.3** gives all the estimated values at T = 523 K. As it is noted, σ_{ac} has an inverse correlation with $R_{H\omega}$ and decreases with decreasing value of $N(E_F)$ [32]. This implies that a decreasing trend of σ_{ac} could be a result of a decrease in $N(E_F)$, which would probably be a result of localized or defect states that influence the mobility gap. **Table 6.3** also demonstrates that the ε values reduce with the decreasing σ_{ac}, which implies that the number of dipoles is less due to differing polarization effects [33].

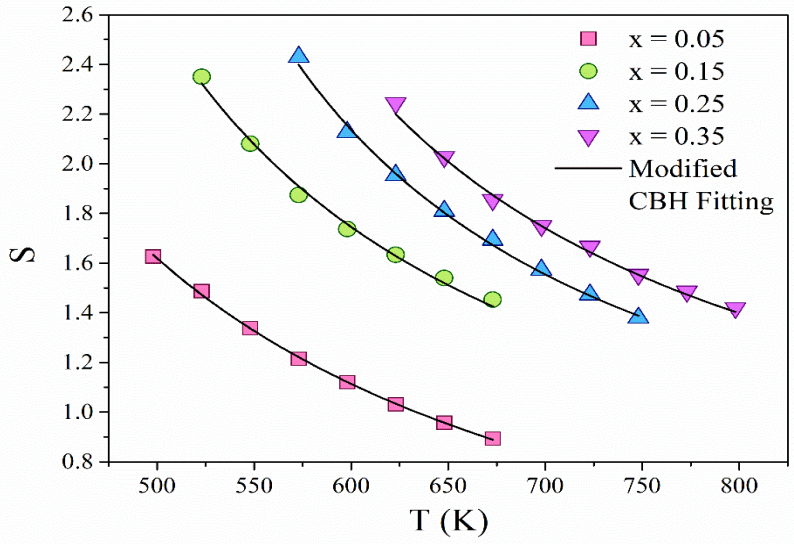

Fig.6.13. The s versus T plot and solid lines show the fitting of the modified CBH model

Table 6.3: Some estimated parameters associated with the AC conduction mechanism.

x (mol %)	W_M (eV) (± 0.02)	τ_0 (sec) (± 0.02)	T_0 (K) (± 3.5)	$R_{H\omega}$ (Å) (± 0.04)	$N(E_F)$ (× 10^{27} $eV^{-1}cm^{-3}$) (± 0.05)	ε (± 0.05)
0.05	0.16	0.019	633	2.33	4.17	41.76
0.15	0.33	0.208	856	2.91	3.87	39.87
0.25	0.40	0.706	946	3.12	3.55	29.65
0.35	0.49	0.967	1041	4.32	2.95	15.94

6.4. Bi_2O_3-Fe_2O_3-V_2O_5-P_2O_5 glass

6.4.1.Study of Electrical Conductivity

Within this section, the electrical conduction mechanisms over a given temperature range are elaborately discussed using traditional methods of science. The frequency-dependent total conductivity (σ_{total}) spectra of all the glass samples whose compositions had the value of x = 0.0 and 0.30, were all measured at the temperatures between 413 K and 533 K as illustrated in **Fig. 6.14.** The progressive increase in σ_{total} with rising temperature, as seen in **Fig. 6.14**, validates the semiconductor properties of the materials.

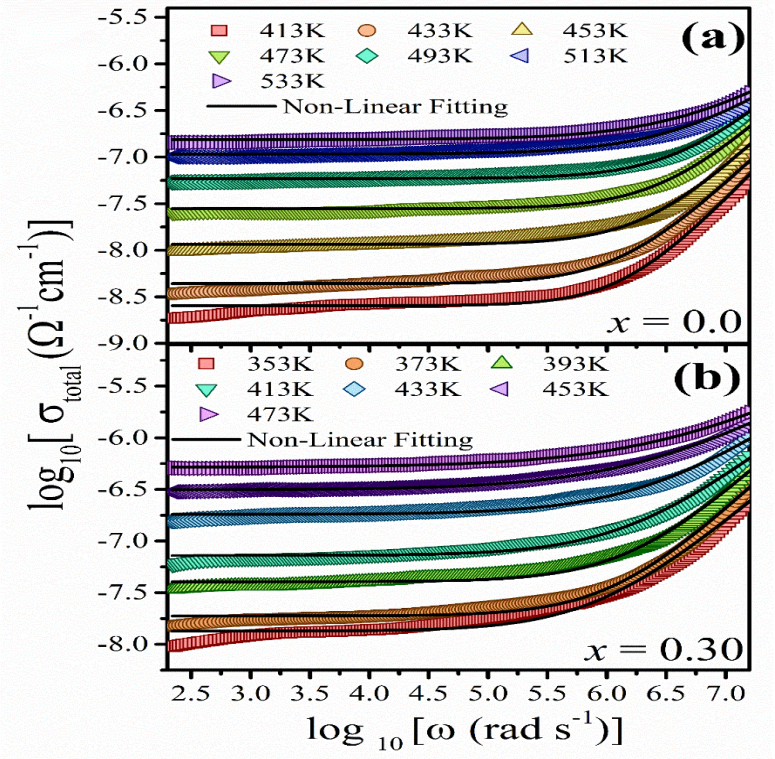

Fig. 6.14 (a-b). Spectra of total conductivity of x = 0.0 and x=0.30 glass samples at different temperatures

The σ_{total} spectra at all the temperatures studied have two well-defined regions. At low frequencies, the conductivity is almost constant at what is referred to as DC conductivity. This plateau area expands with temperature increase, and it shows an increase in the mobility of charge carriers. Conversely, the high-frequency data has a dispersive behaviour with increasing conductivity with increasing frequency and leading to a linear behaviour typical of hopping or localized carrier motion.

Having ascended to a higher temperature initially, there is a gradual shift of the frequency-independent DC region towards higher frequencies due to the faster dynamics of ions. At the same time, the ionic and electronic modes in the conduction begin to overlap, making the dispersive areas merge at elevated frequencies.

Fig. 6.15 is a plot of the 433 K σ_{total} spectra of all the glass samples, where it is observed that 4total is increasing with the increased content of Bi_2O_3 (x). This finding supports the importance of Bi_2O_3 as a network modifier, thus changing the structural arrangement and giving rise to additional non-bridging oxygens, causing the enhanced charge transport. On balance, the analysis highlights the intricate associative nature of temperature, composition and conduction phenomenon on the glass system.

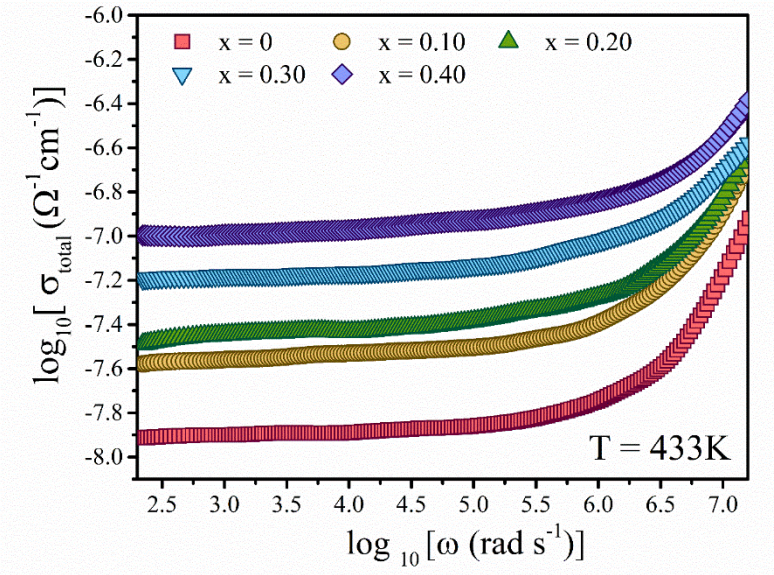

Fig.6.15 Comparison study of total conductivity at T = 433K

More complex processes that contribute to the frequency-dependent variation in conductivity include the migration of ions within the amorphous glass network, the hopping or tunnelling of charge carriers or polarons between various localized (or defect) states lying within the optical bandgap (E_{opt}) [34, 2]. The resulting total dispersion is the result of forward and backwards hopping or tunnelling of the small polarons. Because these transitions are normally between localized states nearby, they necessitate reduced energy in comparison to $E_{opt,}$ leading to a decrease of activation energy with the increase of frequency [10].

The conductivity spectra of such glass nanocomposites display a corresponding well that follows the Jonscher universal power law and the Almond-West formalism. The Jonscher power law used to describe the frequency dependence of the AC conductivity of amorphous materials is mathematically expressed as given in **Eq. (6.2).**

Additionally, the Almond-West formalism defines the σ_{total}, expressed as shown in **Eq. (6.1)**:

The factor k fractional exponent in **Eq. (6.1)** is also an indicator that distinguishes between non-ionic and ionic transport, the degree of conduction, and the charge transfer mechanism. The parameter ω_H represents the hopping or crossover frequency for polarons, marking the transition from the dispersive AC region to the DC conduction region at $\omega = \omega_H$ [42]. When the value of k is less than one, it verifies that charge carriers or small polarons have gone through the hopping or tunnelling process. Non-linear curve fitting of **Eq. (6.1)** to the σ_{total} spectra in **Fig. 6.14** enables extraction of σ_{dc}, ω_H, and k.

According to XRD data in **Fig. 3.11** (**Chapter 3**), as the content of Bi_2O_3 (x) increases, the number of nanophases increases and crystallinity increases, resulting in a corresponding increase in total conductivity (σ_{total}). Also, a negative correlation is found between the optical bandgap and total conductivity (σ_{total}).

Fig. 6.16(a) depicts the Arrhenius type of dependence of the hopping frequency, whereby ω_H increases with temperature (see also **Fig. 6.14(a)**). To obtain the activation energy E_H, linked to the hopping process, the data are fitted in **Fig. 6.16(a)** with **Eq. (6.5)** by a least-squares linear procedure, and the solid black lines are taken as the best fits to the data. The threshold energy E_H is a parameter that represents the minimum energy required to allow a small polaron to hop, tunnel, or migrate between localized states, through states of localization, that are separated by potential barriers. Remarkably, at a higher overall conductivity of the glass system, the value of E_H decreases.

As the amount of Bi_2O_3 is incremented, more of the measured values of ω_H. Moreover, Fig. **6.16(b)** indicates an evident negative relationship between ω_H and E_H.

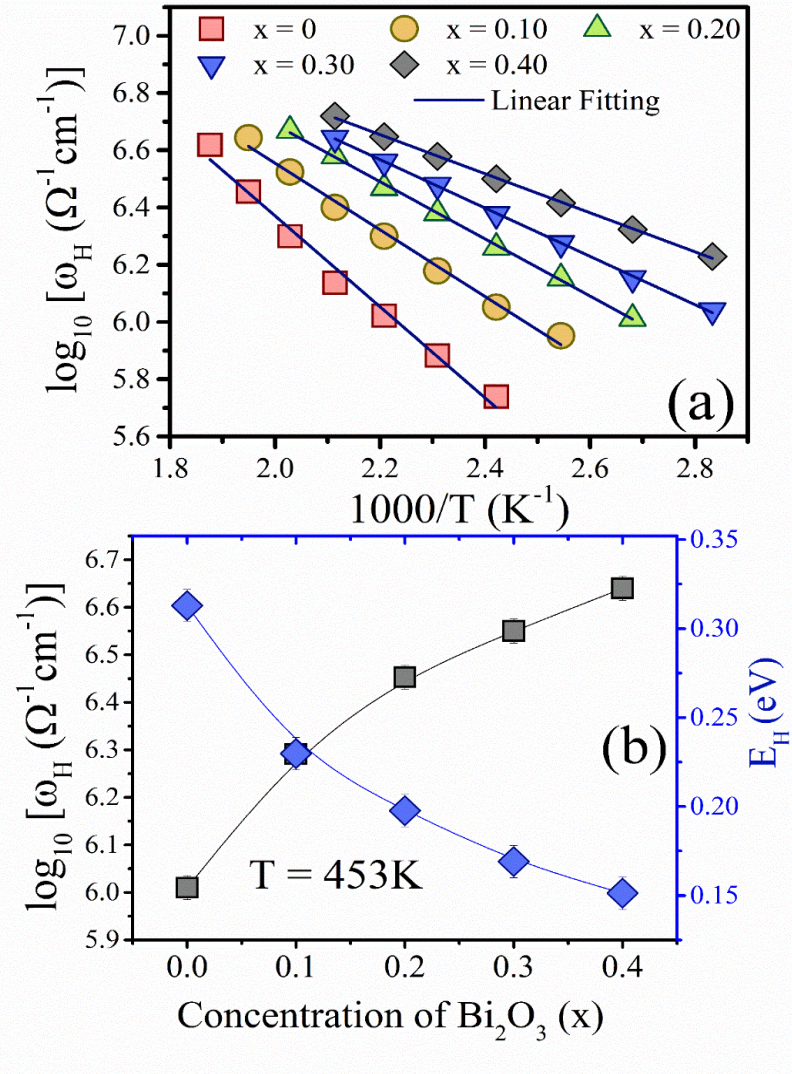

Fig.6.16(a) Estimated values of ω_H plotted against the reciprocal of temperature for all glassy systems. **(b)** Deviation of ω_H at T = 453K and E_H against the concentration of Bi_2O_3 (x).

6.4.2. Study of DC conductivity

The Almond-West formulation reveals information about the direct current conductivity (σ_{dc}), which is sensitive to the temperature. The non-linear behaviour of σ_{dc} can be attributed to the simultaneous presence of various conduction mechanisms. **Fig. 6.17** shows σ_{dc} plotted versus the inverse temperature, and its behavior can be seen to be as described by **Eq. (6.8)** [35, 37].**Fig. 6.17** presents the σ_{dc} spectra as a function of inverse temperature, revealing two distinct temperature-dependent regions in σ_{dc}. The nonlinear trend and the rise of σ_{dc} with

temperature across all glass compositions confirm their semiconducting nature. This behavior aligns with typical temperature-dependent conductivity patterns observed in semiconductors. The high-temperature region (σ_{High}), represented by the first term in **Eq. (6.8)**, corresponds to band conduction via extended states that form within the mobility gap due to the disordered glass structure. Conversely, the low-temperature region (σ_{Low}) is attributed to tunnelling or hopping of charge carriers, such as small polarons or electrons, between localized or defect states. The pre-exponential terms σ_{High} and σ_{Low} vary with composition [21,22].

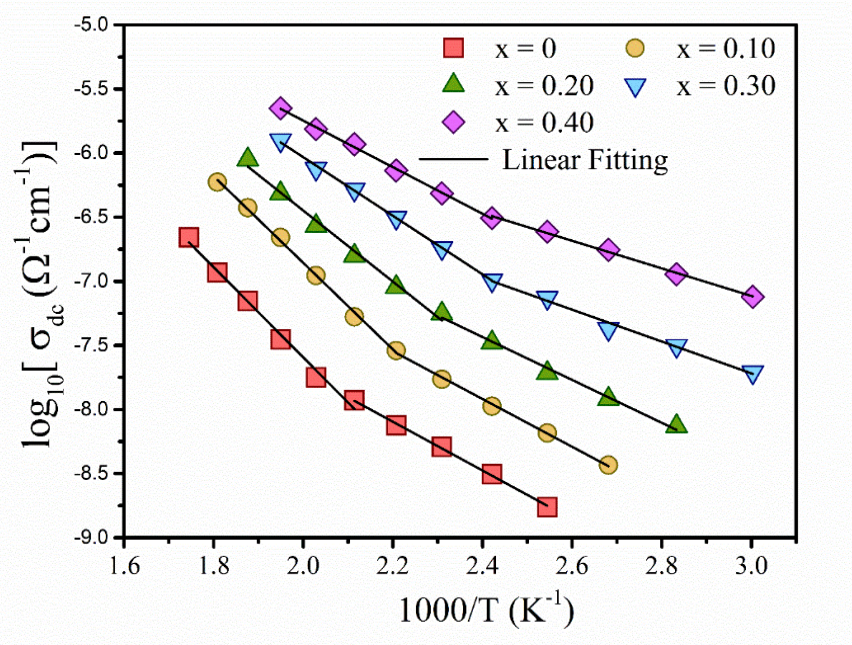

Fig.6.17 . Plot illustrating the dependence of dc conductivity (σ_{dc}) on the reciprocal of temperature.

Fig. 6.17 shows that using linear regression fitting of the data leads to the result that the activation energy of σ_{dc} in the region of high temperature (E_{High}) and low temperature (E_{Low}). All the calculated values are presented in **Table 6.4**. The observed increase in σ_{dc} with rising Bi_2O_3 concentration (x) corresponds to a progressive decrease in both E_{High} and E_{Low} Conduction at low temperatures in the mobility gap or optical gap is by hopping of the small polarons or charge carriers between localized states, as consistent with the variable range hopping (VRH) model of Mott [1]. The VRH model is used in the case of a finite density of localized states near the Fermi level, and the expression of VRH conductivity is depicted in **Eq.(6.9)** and **(6.10)** [38, 32].

The σ_{dc} plotted against $T^{-0.25}$, in **Fig. 6.18(a)**, agrees well with the experimental data obtained and the theoretical curve of **Eq. (6.9)**. The value of $N(E_{FM})$ is extracted using **Eq. (6.10)**, based

on the slope of the linear fit observed in **Fig. 6.18(a)**, assuming a localization length (α^{-1}) of 10 Å for the relevant localized states [1] To analyse the basis of temperature-dependent characteristics of small polaron transport, i.e. hopping distance (R_{hop}) and average hopping energy (W_{hop}) the mathematical expression can be used as stated in **Eq.(6.11)** and **(6.12)** [32]. At a fixed temperature of 453 K, values of R_{hop} and W_{hop} were computed with the help of **Eq. (6.11)** and **Eq. (6.12)**, and the results have been summarised as shown in **Table 6.4**. These three conditions of the applicability of the Variable Range Hopping (VRH) model of Mott, i.e., $R_{hop}\alpha \geq 1$ and $W_{hop} > K_BT$, are continuously satisfied for all the glass compositions under study [38]. As **Table 6.4** indicates, a definite trend has been achieved, whereby values of R_{hop} and W_{hop} reduce with respect to Bi_2O_3 content (x) as the DC conductivity improves. This means that movement of charge gets enhanced, because electrons need less energy and wider ranges to jump between neighbouring localized sites.

Nonetheless, it is important to note that Mott's VRH model falls short in accurately describing the temperature dependence of the σ_{dc} spectrum at temperatures above half of the Debye temperature ($\theta_D/2$). To overcome this shortcoming, Greaves has offered an alternative formulation which clarifies conduction behavior in the high-temperature regime ($T > \theta_D/2$) as given in **Eq. (6.13)** and **(6.14)**. The model of variable range hopping (VRH) developed by Greaves has been successfully used to explain experimental behaviour of dc conductivity (σ_{dc}) in all the nanometer composite glass systems, especially at higher temperature regions. The model fits well with experimental data and has the necessary transport features in the case of the essential transport characteristics. To evaluate the density of states (DOS) at the Fermi level, referred to as $N(E_{FG})$, Greaves's model is applied by utilising the slope derived from the linear region of the high-temperature σdc data, as represented by the solid lines in Fig. **6.18(b)**. This amount was calculated using the equation, **Eq. (6.13)**, which connects this slope to DOS. The values of $N(E_{FM})$ and $N(E_{FG})$ are increasing consistently with the content of Bi_2O_3 (x), it is seen in **Table 6.4**. Such an increase in the density of states is directly related to the trend in the improvement of σ_{dc} values in all the glass compositions, which shows that the presence of localized states around the Fermi level is instrumental in the ease of charge transport in these materials.

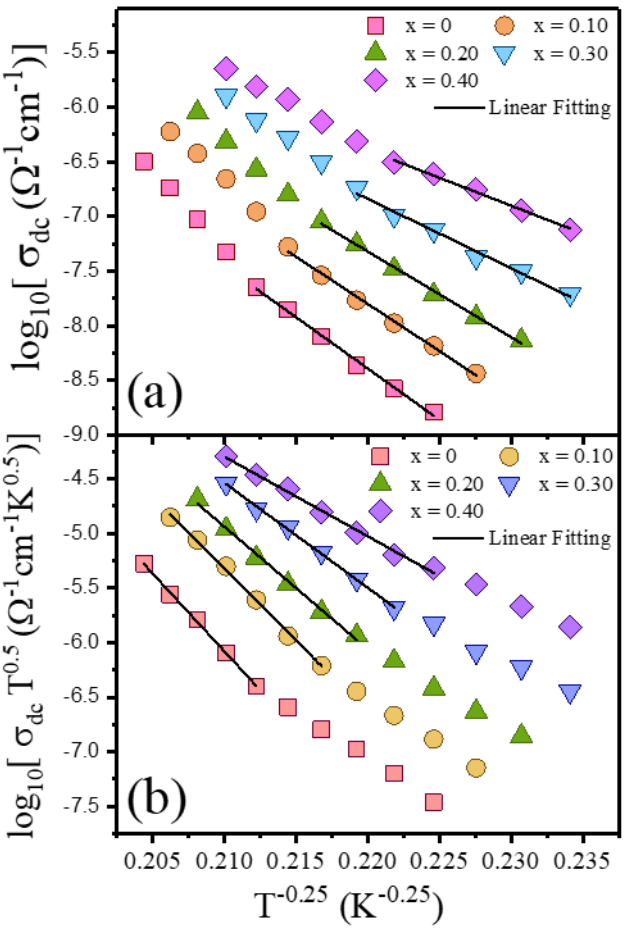

Fig.6.18 (a) Changes in σdc for temperature based on Mott's model. (b) Fluctuations of $\sigma_{dc}T^{0.5}$ with temperature following Greaves's model.

Table 6.4 The parameters are estimated from Mott's and Greaves's VRH model.

x	$N(E_{FM})$ ($\times 10^{28}$ $eV^{-1}cm^{-3}$)	$N(E_{FG})$ ($\times 10^{28}$ $eV^{-1}cm^{-3}$)	R_{hop} (nm)	W_{hop} (meV)
0.00	5.13	1.17	2.97	1.75
0.10	7.19	1.62	3.87	1.34
0.20	10.5	3.02	5.43	1.02
0.30	24.5	5.14	8.13	0.91
0.40	58.8	7.77	9.97	0.72

Jonscher's universal power law [**Eq. (6.2)**] is efficient in explaining the AC conduction behavior of the studied glass systems, which emphasizes the effect of both the frequency and temperature on the conductivity. Another important parameter in the case of this model is the frequency exponent (s) that helps in providing information on the underlying charge transport processes. The significance of "s" indicates the carrier dynamics type in glass, which is lower than one, and it is usually an indication of charging carriers experiencing hopping between concentrated locations in the glass and surmounting potential energy barriers [39]. On the

contrary, Gilroy et al. [27] have stated that s > 1 may reflect the case of quantum mechanical tunnelling when the carriers traverse an unsymmetrical double-well potential to arrive at a defect or localised sites.The conduction characteristics of alternating current (AC) are analyzed by taking a difference between the total conductivity (σ_{total}) and the DC conductivity (σ_{dc}); the result is the AC conductivity (σ_{ac}). The frequency-dependent spectrum of the binary (x = 0.0) and quaternary (x = 0.20) glass samples is shown in the **Figs. 6.19(a)** and **6.19(b),** respectively. These data are very evident when the linear variation of the σ_{ac} with frequency is considered to be the universal reaction of the disordered materials.Additional information is revealed in **Fig. 6.20**, which shows the values of 1 MHz frequency dependence of σ_{ac} against the temperature of all the nanocomposite glasses. The thermally activated conduction process is also evident in the plot due to the positive variation of σ_{ac} with temperature. Based on linear fittings of these results, where the continuous black curves are in **Fig. 6.20**, the AC activation energy (E_{ac}) of each composition is obtained. The associated values are tabulated in **Table 6.5**[28].

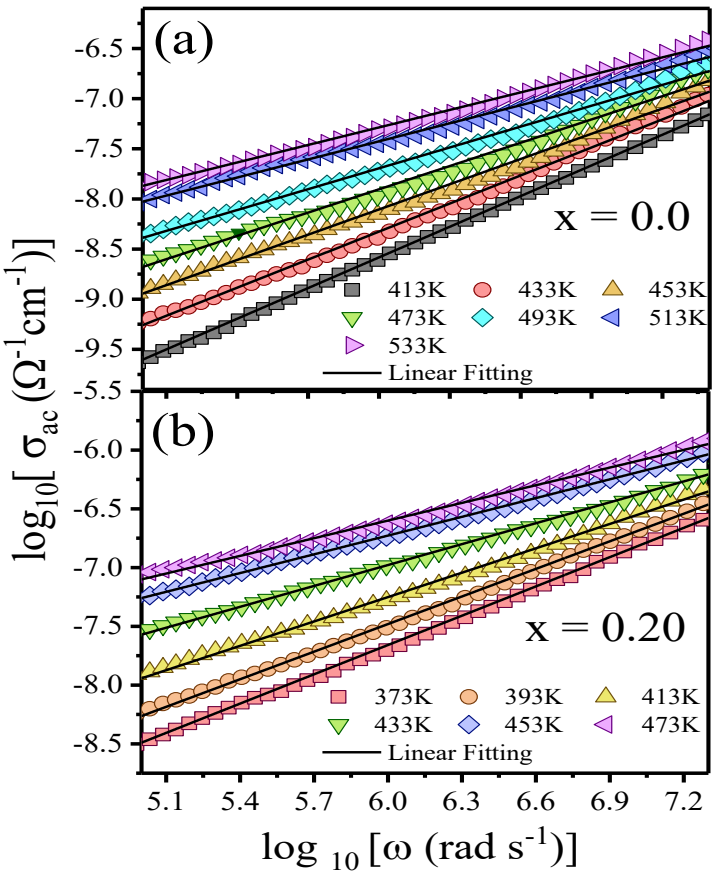

Fig.6.19 (a) Frequency dependency of AC conductivity of *x* = 0.0 and **(b)**0.20 glass systems

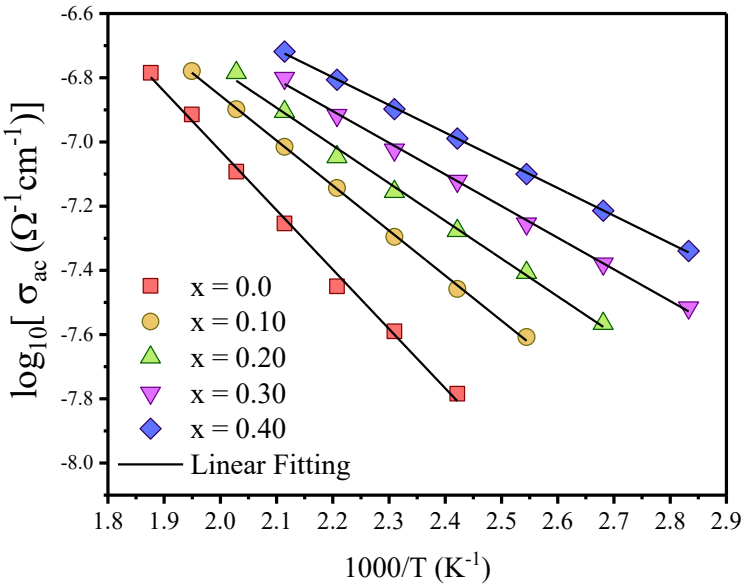

Fig. 6.20. Temperature dependency of AC conductivity at f = 1MHz

As shown in **Fig. 6.19(a)** and **6.19(b)**, the linear fitting of σ_{ac} data at higher frequencies provides a pathway to extract the temperature-dependent power-law exponent, "s". This exponent plays a key role in the diagnosis of the underlying AC conduction mechanism in different thermal environments [29]. The dependence of "s" on temperature provides good insight, and as illustrated in **Fig. 6.21**, the values of "s" exhibit a negative trend with the increase of temperature, which implies a different conduction trend which is characteristic of the material.

This is consistent with the Correlated Barrier Hopping (CBH) model that was first proposed by Pike and Elliott [29,30], which provides a rather comprehensive model to describe the AC conduction in disordered systems, including the glass or amorphous semiconductors. Under this model, hopping of the localized charge carriers or small polarons is seen to deliver the charge transport via overcoming potential barriers. The energy barrier is proportional to the inter-site spacing through Coulombic interaction. In the CBH model, nearest neighbour hopping only is allowed, and the prevalence of charge carriers or small polarons is within a lattice potential well. The hopping rates expected are symmetrical, which means that a transition of charge carriers or small polarons between two localized states is the same forward and reverse. As a result, the mechanism is generally seen under high temperatures.

Nearest-neighbour hopping is the hopping that is most likely to occur in the mechanism of CBH, which makes the perturbation of charge carriers localised inside the potential wells that are produced by the disordered lattice. The hopping process is thermally assisted, and the model supposes symmetrical hopping rates, i.e. the possibility of a jump of the two localized states forward and backwards is close to the same. This symmetry is more pronounced at elevated temperatures when the charge carriers are more likely to satisfy the potential barriers by having the thermal energy to facilitate this action

In contrast to quantum-tunnelling mechanisms, the CBH model is a classical (thermally-assisted) hopping study with the carriers not tunnelling but, rather, hopping above the energy barriers. An especially important role in the process is played by defect states. These states, which are frequently added by the structural defects or the existence of heavy metal oxides such as Bi_2O_3, are used to enlarge the distribution of the energy barriers, and they affect the dynamics of hopping. The thickening of the barrier heights in virtue of these defects further confirms the appropriateness of the CBH mechanism to such glasses.

To determine the temperature dependence in the exponent s in the CBH model, **Eq. (6.3)** can be used [30], which gives the connection between s, thermal energy and the nature of barriers [30].The parameters in the given equation are K_B, the Boltzmann constant, W_m, the hopping barrier potential or the polaron binding energy and τ_0, the Debye relaxation time, which shows the characteristic relaxation time of the charge carriers. Notice that all glass compositions, as shown in **Fig. 6.21**, have "s" values above 0.80. As in the earlier accounts [10], the traditional CBH model does not merge well with systems as $s > 0.70$. Hence, the modified model of CBH [30] was taken. It was seen in **Fig. 6.18** that the model fits perfectly to the experimental result through constant black lines, thus showing its applicability. The modified CBH model is delineated by **Eq. (6.4)** [10]. The fitting of the experimental data is then carried out in a nonlinear manner with the use of the modified version of the CBH model, as presented in **Eq. (6.15)**. The three associated fitting parameters, W_m (hopping barrier potential), τ_0 (Debye relaxation time), and T_0, increase as the content of Bi_2O_3(x) rises (as shown in **Table 6.5**). This points to the fact that with the augmented amount of Bi_2O_3 in the network of the glass, there is an increment in the energy barriers and strictness of the structure, which consequently declines the total AC conductivity. The same has been observed in as much as the modified CBH model can predict, then in a more refined form, about the AC conductivity (σ_{ac}) of the current glass

systems [32]. Using **Eq. (6.16)**, the values of key parameters—namely the hopping distance ($R_{H\omega}$), the density of states at the Fermi level ($N(E_F)$), and the dielectric constant (ε)—were calculated at various temperatures. The findings acquired at a particular temperature of 433 K have been summarized in **Table 6.5**. An inverse correlation is observed between AC conductivity (σ_{ac}) and $R_{H\omega}$, implying that as the hopping distance increases, σ_{ac} tends to decrease. This is in line with the observation that the shorter the rate of hopping, the more efficient the charge transport becomes. On the other hand, the correlation between σ_{ac} and $N(E_F)$ reveals a linear relationship against direct proportionality, indicating that the higher the concentration of defect pair states near the Fermi level higher be AC conduction process [32]. This is done because of the characteristics of localized or defect states in reducing the mobility gap, hence facilitating charge hopping.It is also observed in **Table 6.5** that there is a tendency, as σ_{ac} increases, for the dielectric constant to rise as well. This may be associated with fewer available dipoles as a result of other competing processes of polarization in the disordered structure. It is found that the relationship between defect density and hopping dynamics, with polarization effects, plays a major role in determining the conductivity and dielectric properties of the glass system [33].

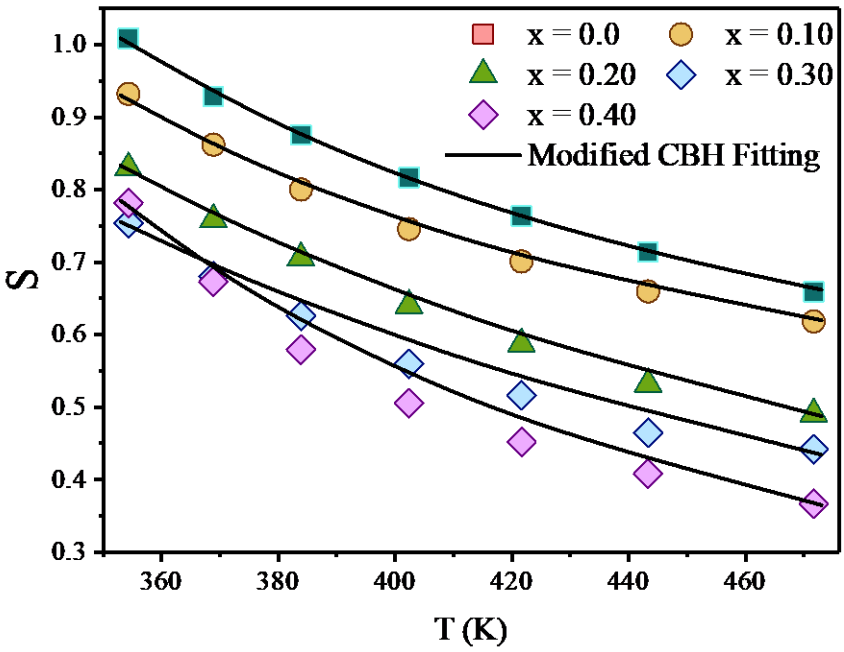

Fig.6.21 The power-law exponent (s) versus Absolute Temperature (T) plot and continous lines show the fitting of the modified CBH model

Table 6.5 Various calculated electrical conductivity parameters

x	E_H	E_{ac}	DC Activation Energy		W_M	τ_0	T_0	$R_{H\omega}$	$N(E_F)$	ε
	(eV) (± 0.02)	(eV) (± 0.02)	At low-temperature (eV) (± 0.03)	At high-temperature (eV) (± 0.03)	(eV) (± 0.06)	(sec) (± 0.02)	(K) (± 2)			(± 0.2)
0.0	0.312	0.370	0.392	0.694	0.354	0.089	712	11.23	6.32	56.6
0.1	0.229	0.277	0.368	0.667	0.312	0.081	702	09.43	8.12	62.1
0.2	0.197	0.232	0.330	0.548	0.278	0.078	696	07.65	8.87	67.3
0.3	0.169	0.195	0.261	0.451	0.254	0.062	687	07.11	10.12	87.2
0.4	0.151	0.171	0.233	0.392	0.223	0.059	677	05.21	17.22	91.2

The Pan and Ghosh model has also been employed in investigations as to whether the type of relaxation that occurs in electrical conduction between the glass systems studied is dependent on temperature or composition difference [16]. To test this, both the frequency axis (X-axis) and conductivity axis (Y-axis) were normalised by their respective characteristic frequency (ω_h) and DC conductivity (σ_{dc}) values. The resulting normalized conductivity spectra are presented in **Fig. 6.22(a)** and **6.22(b)**, which help visualize the extent to which conductivity relaxation follows universal scaling laws. In **Fig. 6.22(a)**, the temperature-scaled AC conductivity spectra for the x = 0.10 glass composition display an excellent overlap across all measured temperatures, forming a single master curve. Such behavior makes the time temperature superposition principle [16] hold, having a picture of the conduction dynamics being thermally activated, but displaying a universal relaxation process with variations in temperatures. In contrast, **Fig. 6.22(b)** illustrates the composition-scaled spectra for all glass samples at a constant temperature of T = 413 K. Unlike the temperature-scaled case, the data from different compositions fail to merge into a single master curve, indicating that composition plays a more dominant role than temperature in determining the relaxation dynamics of the system. Collectively, all these results indicate that even though a change in temperature does not considerably influence the relaxation mechanism of charge carriers, which are primarily small polarons, the compositional structure, particularly the Bi_2O_3 content, is of crucial cadre in determining the conduction pattern. This composition-controlled deactivation indicates that the type of structure of the glass matrix determines hopping behavior, regardless of a change in temperature. Importantly, this compositional stability suggests that the investigated Bi_2O_3-doped glass systems could serve as promising candidates for high-temperature electronic applications, maintaining reliable performance without significant degradation in electrical functionality [32].

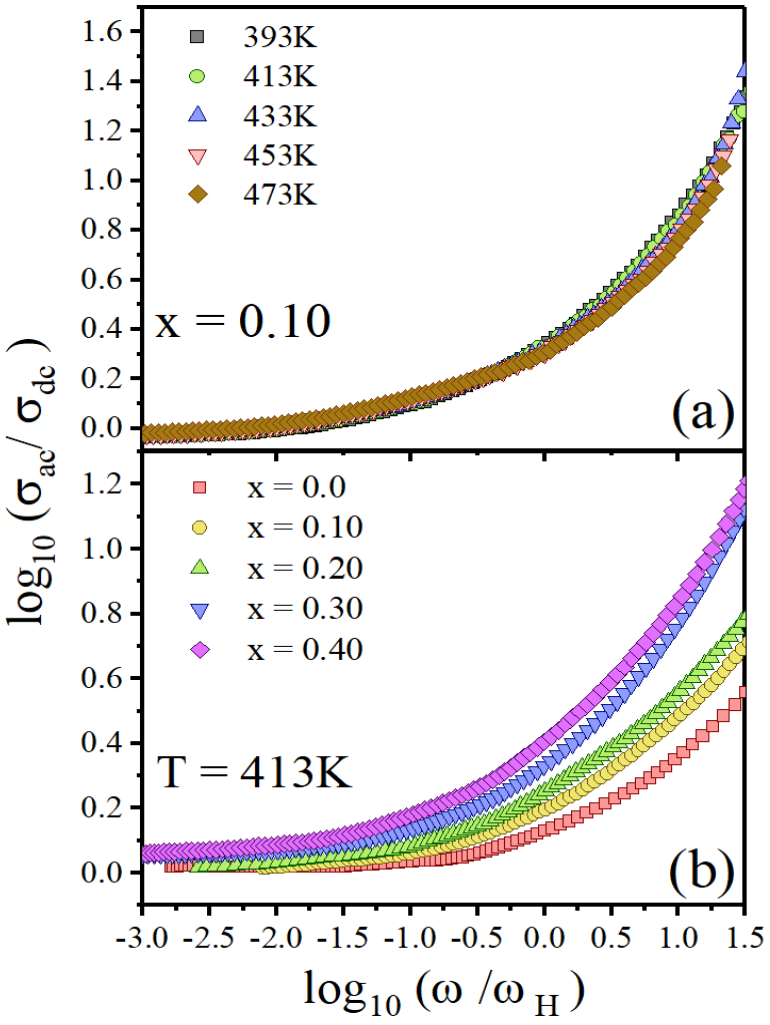

Fig. 6.22 (a) Temperature scaling of AC conductivity spectra of x = 0.10 specimen at various temperatures and **(b)** composition scaling of AC conductivity spectra at 413 K.

6.5. Summary

In conclusion, the electrical conductivity behavior of the investigated nanocomposite glass systems—VNZP, BBVP, and BFVP—is strongly governed by the combined effects of vanadium inclusion and the progressive modification of the phosphate glass network by Bi_2O_3 and other metal oxides. The incorporation of vanadium (V_2O_5) plays a central role across all systems by introducing multivalent V^{4+}/V^{5+} redox pairs, which enable small polaron hopping and contribute significantly to electronic conductivity, particularly at lower V_2O_5 concentrations. In the VNZP system, higher Na_2O content enhances ionic conduction via mobile Na^+ ions, whereas increasing V_2O_5 results in decreased conductivity due to reduced ionic mobility and structural densification. In the BBVP and BFVP systems, the addition of heavy metal oxides like Bi_2O_3 and BaO or Fe_2O_3 further alters the glass network by increasing

structural rigidity and introducing more localized defect states, thereby affecting both AC and DC conduction mechanisms. The electrical transport across all systems exhibits semiconducting behavior, with conductivity increasing with temperature. DC conductivity **(**σ_{dc}**)** follows an Arrhenius-type trend, well-described by Mott's VRH model at lower temperatures and Greaves's model at higher temperatures. AC conductivity **(**σ_{ac}**)** adheres to Jonscher's universal power law, with the power-law exponent (s) decreasing with temperature, confirming the dominance of thermally activated hopping mechanisms. For compositions where s exceeds 0.80, the modified CBH model provided an accurate representation of the conduction behavior, validated by excellent fitting across all glass series. Key electrical parameters such as activation energy (E_{ac}, E_H), density of states ($N(E_F)$), hopping distance ($R_{H\omega}$), Debye relaxation time (τ_0), and barrier energy (Wm) show strong correlations with Bi_2O_3 and V_2O_5 content, reflecting how structural and electronic modifications impact carrier mobility. Furthermore, scaling analysis using the Pan and Ghosh model indicated that while temperature has minimal effect on conductivity relaxation dynamics, glass composition—particularly Bi_2O_3 content—plays a decisive role. Overall, the conduction in these glasses is governed by a mixed ionic–electronic transport mechanism, which can be finely tuned through compositional engineering. This makes the VNZP, BBVP, and BFVP glass systems promising candidates for high-temperature and solid-state electronic applications where reliable performance and compositional adaptability are essential.

6.6 References

1. Almond, D. P., & West, A. R. (1983). Anomalous conductivity pre-factors in fast ion conductors. Nature, 306(5941), 456–467. https://doi.org/10.1038/306456a0
2. Almond, D. P., Duncan, G. K., & West, A. R. (1983). The determination of hopping rates and carrier concentrations in ionic conductors by a new analysis of ac conductivity. Solid State Ionics, 8(2), 159–164. https://doi.org/10.1016/0167-2738(83)90079-6
3. Jonscher, A. K. (1983). Dielectric relaxation in solids (pp. 10–152). Chelsea Dielectrics.
4. Cizman, A., Rysiakiewicz-Pasek, E., Krupiński, M., Konon, M., Antropova, T., & Marszałek, M. (2017). The effect of Fe on the structure and electrical conductivity of sodium borosilicate glasses. Physical Chemistry Chemical Physics, 19(34), 23318–23324. https://doi.org/10.1039/C7CP02042B
5. Jonscher, A. K. (1977). The 'universal' dielectric response. Nature, 267(5613), 673–679. https://doi.org/10.1038/267673a0
6. Elliott, S. R. (1978). Temperature dependence of AC conductivity of chalcogenide glasses. Philosophical Magazine, 36(6), 1291–1304. https://doi.org/10.1080/01418637808226448
7. Pike, G. E. (1972). AC conductivity of scandium oxide and a new hopping model for conductivity. Physical Review B, 6(4), 1572–1580. https://doi.org/10.1103/PhysRevB.6.1572
8. Elliott, S. R. (1987). A.c. conduction in amorphous chalcogenide and pnictide semiconductors. Advances in Physics, 36(2), 135–217. https://doi.org/10.1080/00018738700101971
9. Das, A. S., Roy, M., Biswas, D., Kundu, R., Acharya, A., Roy, D., & Bhattacharya, S. (2018). AC conductivity of transition metal oxide doped glassy nanocomposite systems: Temperature and frequency dependency. Materials Research Express, 5(9), 095201. https://orcid.org/0000-0002-2974-2900
10. Biswas, D., Das, A. S., Mondal, R., Banerjee, A., Dutta, A., Kabi, S., Roy, D., & Singh, L. S. (2020). Structural properties and electrical conductivity mechanisms of semiconducting quaternary nanocomposites: Effect of two transition metal oxides. Journal of Physics and Chemistry of Solids, 144, 109505. https://doi.org/10.1016/j.jpcs.2020.109505

11. Das, A. S., & Biswas, D. (2019). Investigation of AC conductivity mechanism and dielectric relaxation of semiconducting neodymium-vanadate nanocomposites: Temperature and frequency dependency. Materials Research Express, 6(7), 075206. https://orcid.org/0000-0002-3129-5951
12. Anderson, O. L., & Stuart, D. A. (1954). Calculation of activation energy of ionic conductivity in silica glasses by classical methods. Journal of the American Ceramic Society, 37(12), 573–580. https://doi.org/10.1111/j.1151-2916.1954.tb13991.x
13. Le, Q. H., Calahoo, C., Xia, Y., Buchheim, J., Bragatto, C. B., & Wondraczek, L. (2020). Optimization of electrical conductivity in the $Na_2O–P_2O_5–AlF_3–SO_3$ glass system. Journal of the American Ceramic Society, 103(8), 4939–4956. https://doi.org/10.1111/jace.17150
14. Gundusharma, U. M., & Secco, E. A. (1990). Fast Na^+ ion conductivity in glass, intermediate and crystalline phases of $Na_4UO_2(SO_4)_3$. Applied Physics A, 51(1), 7–12. https://doi.org/10.1007/BF00324458
15. Jayasinghe, G. D. L. K., Dissanayake, M. A. K. L., Careem, M. A., & Souquet, J. L. (1997). Electronic to ionic conductivity of glasses in the $Na_2O–V_2O_5–TeO_2$ system. Solid State Ionics, 93(3-4), 291–295. https://doi.org/10.1016/S0167-2738(96)00494-8
16. Ghosh, A., & Pan, A. (2000). Scaling of the conductivity spectra in ionic glasses: Dependence on the structure. Physical Review Letters, 84(10), 2188–2190. https://doi.org/10.1103/PhysRevLett.84.2188
17. Singh, P., Banhatti, R. D., & Funke, K. (2005). Correlation between viscosity and ion dynamics in a fragile ionic melt. Physics and Chemistry of Glasses, 46(3), 241–244.
18. Sidebottom, D. L., Green, P. F., & Brow, R. K. (1996). Scaling behavior in the conductivity of alkali oxide glasses, polymers, and doped crystals. Journal of Non-Crystalline Solids, 203(3), 300–305. https://doi.org/10.1016/0022-3093(96)00362-6
19. Mott, N. F., & Davis, E. A. (1977). Electronic processes in non-crystalline materials (pp. 3–152). Clarendon Press.
20. Hassanien, A. S., & Akl, A. A. (2016). Electrical transport properties and Mott's parameters of chalcogenide cadmium sulphoselenide bulk glasses. Journal of Non-Crystalline Solids, 432, 471–479. https://doi.org/10.1016/j.jnoncrysol.2015.11.007
21. Banday, J. A., Mir, F. A., Farooq, S., Qurishi, M. A., Koul, S., & Razdan, T. K. (2012). Structural, thermal and optical studies of oxypeucedanin hydrate monoacetate micro-crystals from Prangos pabularia. American Journal of Analytical Chemistry, 3(3), 204–209. https://doi.org/10.4236/ajac.2012.33029

22. Mott, N. F. (1969). Conduction in non-crystalline materials. Philosophical Magazine, 19(160), 835–852. https://doi.org/10.1080/14786436908216338
23. Biswas, D., Singh, L. S., & Das, A. S. (2019). An investigation of S–Se–Te semiconducting glassy alloys: Structural characterization and electrical conductivity. Journal of Non-Crystalline Solids, 510, 101–111. https://doi.org/10.1016/j.jnoncrysol.2019.01.013
24. Reis, S., Karabulut, M., & Day, D. (2001). Chemical durability and structure of zinc–iron phosphate glasses. Journal of Non-Crystalline Solids, 292(1-3), 150–157. https://doi.org/10.1016/S0022-3093(01)00880-8
25. Elliott, S. R. (1994). Frequency-dependent conductivity in ionically and electronically conducting amorphous solids. Solid State Ionics, 70–71, 27–40. https://doi.org/10.1016/0167-2738(94)90284-4
26. Vedeanu, N., Stanescu, R., Filip, S., Ardelean, I., & Cozar, O. (2012). IR and ESR investigations on V_2O_5–P_2O_5–BaO glass system with opto-electronic potential. Journal of Non-Crystalline Solids, 358(14), 1881–1885. https://doi.org/10.1016/j.jnoncrysol.2012.05.010
27. Gilroy, K. S., & Phillips, W. A. (1981). An asymmetric double-well potential model for structural relaxation processes in amorphous materials. Philosophical Magazine B, 43(5), 735–746. https://doi.org/10.1080/01418638108222343
28. Dhahri, A., Dhahri, E., & Hlil, E. K. (2018). Electrical conductivity and dielectric behaviour of nanocrystalline $La_{0.6}Gd_{0.1}Sr_{0.3}Mn_{0.75}Si_{0.25}O_3$. RSC Advances, 8(17), 9103–9111. https://doi.org/10.1039/C8RA00037A
29. Elliott, R. (1977). A theory of a.c. conduction in chalcogenide glasses. Philosophical Magazine A, 36(6), 1291–1304. https://doi.org/10.1080/14786437708238517
30. Pike, G. E. (1972). AC conductivity of scandium oxide and a new hopping model for conductivity. Physical Review B, 6(4), 1572–1580. https://doi.org/10.1103/PhysRevB.6.1572
31. Biswas, D., Das, A. S., Mondal, R., Banerjee, A., Deb, D., Dutta, A., Bhattacharya, S., Kabi, S., & Singh, L. S. (2020). Study of microstructure and electrical conduction mechanisms of quaternary semiconducting glassy systems: Effect of mixed modifiers. Journal of Non-Crystalline Solids, 542, 120104. https://doi.org/10.1016/j.jnoncrysol.2020.120104
32. Biswas, D., Singh, L. S., & Das, A. S. (2020). An investigation of S–Se–Te semiconducting glassy alloys: Structural characterization and electrical conductivity.

Journal of Non-Crystalline Solids, 510, 101–111. https://doi.org/10.1016/j.jnoncrysol.2019.01.013

33. Biswas, D., Singh, Y. B., Das, A. S., Mondal, R., Roy, D., Adhikari, S., & Singh, L. S. (2019). Investigation of microstructure and temperature and frequency dependent dielectric relaxation of molybdenum–zinc–selenite glass nanocomposite systems. Materials Research Express, 6(11), 115205. https://doi.org/10.1088/2053-1591/ab4615

Chapter 7

Analysis of Mechanical and Thermal Properties of Glass Nanocomposites

7.1. Introduction

Mechanical strength and thermal stability of glass nanocomposites are among the main properties that make them suitable for structural, optical, and energy storage devices[1,2]. It is not just the resistance to deformation, cracking or thermal shock that these properties can dictate, but also the compactness and strength of the glass network beneath. This chapter will look into the mechanical and thermal characteristics of the synthesized vanadium phosphate-based systems of glass nanocomposites, i.e., V_2O_5-NaO-ZnO-P_2O_5 (VNZP), Bi_2O_3 -BaO – V_2O_5 -P_2O_5 (BBVP), and Bi_2O_3 –Fe_2O_3 –V_2O_5 –P_2O_5 (BFVP).

To investigate mechanical performance, a range of methods was employed. The surface hardness was assessed through Vickers microhardness test which determines the material resistance to plastic deformation on a static load[3-6]. To complement this, nanoindentation methods gave information into local hardness and elastic modulus, at nanometer resolution, on how atomic structure and bonding behave lattice under very confined stress[7,8]. Furthermore, the longitudinal and shear wave velocity were measured using the ultrasonic pulse-echo technique and the essential elastic coefficients calculated as well using shear and longitudinal velocity determinations; namely, Young modulus, bulk modulus, and shear modulus. These mechanical constants provide is an extensive picture of the internal strength and tension of the glass matrices[9-14].One of the most important components of the composition in this work is bismuth oxide (Bi_2O_3). The quality of mechanical reinforcement and structural compactness of glasses was seen to vary largely with increasing content of Bi_2O_3. The increasing concentrations of Bi_2O_3 increase the density of the bonding and the compactness of the coordination, which present the glass networks as harder and elastic. This tendency is in line with the previous results on the case of sputtered thin films, in which Bi_2O_3 has been said to contribute to densification of the network. The micro-/nanohardness values indicate and support the mechanical improvement[3,7] whereas the increase in ultrasonic velocities and elastic moduli[10,11] have been observed with the enrichment of Bi_2O_3.Theoretically, on the thermal side, the differential scanning calorimetry (DSC) data unambiguously indicate the stabilizing effect of Bi_2O_3 in systems based on phosphates[15,16]. Bi_2O_3 is used as an additive to stabilise the glass structure, raising the temperature transition (T_g) and enhancing the thermal stability of the material[16]. To give an example, a progressive addition of Bi_2O_3 with the concentration up to 35 mol% caused the increase of Tg by 34%, which proves its efficiency

in improving the thermal stability and postponing the time of structural rearrangement. This enhancement supports the paramount significance of Bi_2O_3 in the regulation of mechanical strength as well as heating stability of glass nanocomposites.Therefore, the chapter has presented a united study of the two phenomena of mechanical and thermal behaviors in the three systems of glasses and links changes in property and structural modification, as well as composition design. The mechanico-thermal review forms a basis of the determination and development of glass compositions that have optimum performance towards advanced functional applications.

7.2. Quaternary V_2O_5–Na_2O–ZnO–P_2O_5 glass system

7.2.1. Microhardness Analysis

The Vickers microhardness (Hv) measurements for the glass system with the general formula V_2O_5–Na_2O–ZnO–P_2O_5, where x varies from 0.05 to 0.25, are summarised in **Table 7.1**. The data reveal a clear and systematic decrease in hardness with increasing V_2O_5content. Among the studied compositions, the glass containing the lowest vanadium concentration (x = 0.05) exhibited the highest average microhardness value of 490.6 Hv, indicating a more rigid and densely packed glass structure. Conversely, the sample with the highest V_2O_5 concentration (x = 0.25) displayed the lowest average Hv value of 387.2, highlighting a significant reduction in mechanical rigidity as the vanadium content increases as depicted in **Fig.7.1. [3].**

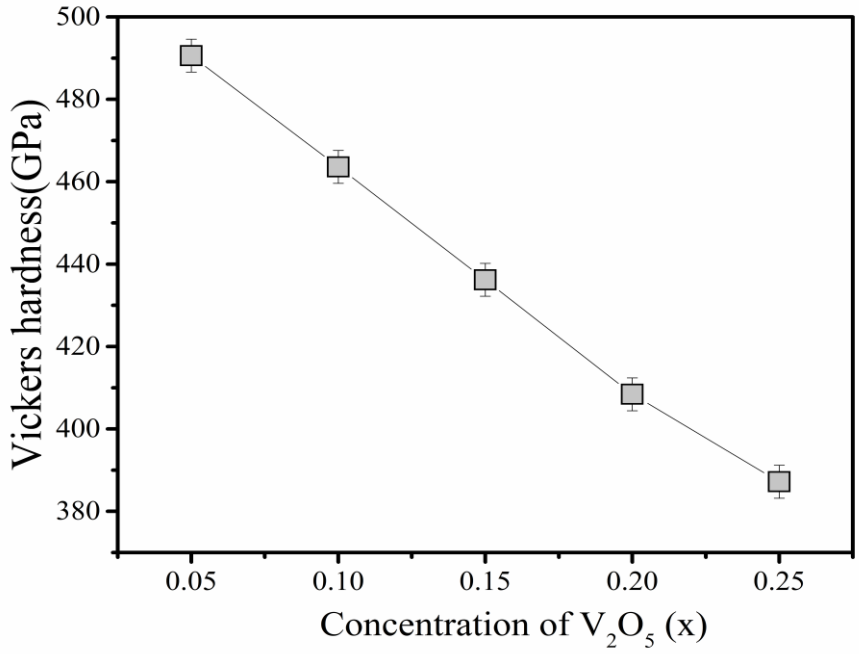

Fig.7.1. Average Micro-hardness data against the concentration(x) of V_2O_5 for glass samples

This decline in hardness with rising V_2O_5 concentration can be attributed to the role of vanadium as a network modifier within the phosphate-based glass matrix. At lower concentrations, the structure is primarily composed of strongly bonded P–O–P and Zn–O linkages, which promote a more polymerized and mechanically robust network. However, as the V_2O_5 content increases, the substitution of Na_2O with V_2O_5 leads to the formation of non-bridging oxygen (NBO) sites. These NBOs reduce the overall connectivity of the phosphate network, resulting in a more open and depolymerized structure that lacks the compactness required to resist indentation, thus lowering the observed Hv values[4].

Furthermore, vanadium, in the form of V^{5+} ions, tends to form VO_4 and VO_5 polyhedra that interact differently with the phosphate framework compared to the Na^+ or Zn^{2+} ions they replace. These vanadate units weaken the rigidity of the network by introducing structural irregularities and promoting ionic rather than covalent interactions within the glass matrix. This behavior aligns with earlier reports on vanadium-containing phosphate glasses, where an increase in V_2O_5 concentration correlates with improved ionic mobility and electrical conductivity, albeit at the expense of mechanical strength.

In the Vickers microhardness testing of V_2O_5–Na_2O–ZnO–P_2O_5 glasses doped with increasing amounts of V_2O_5, two distinct yet interconnected trends emerge. First, hardness systematically decreases with increasing load—a clear manifestation of the indentation size effect (ISE)—where smaller indentations (produced by lower loads) exhibit artificially elevated hardness due to the high strain gradients that generate additional geometrically necessary dislocations (GNDs), reinforcing the material locally(**Fig.7.2**). Second, higher V_2O_5 content consistently boosts the overall hardness of the glass across all loads. This is likely because the addition of vanadium oxide strengthens the glass network, enhancing its rigidity and resistance to deformation. Thus, while the basic ISE behavior—the downward slope of hardness with load—remains intact, each curve shifts upward as V_2O_5 content increases, reflecting a more robust glass structure. The microhardness data not only reflect the intrinsic mechanical strength of the glasses but also offer insights into the structural evolution of the glass network with increasing V_2O_5 content. The continuous decrease in Hv values confirms that higher vanadium loading leads to a softer and less rigid glass, which may be advantageous in applications requiring improved formability but less so for those demanding high mechanical durability [3].

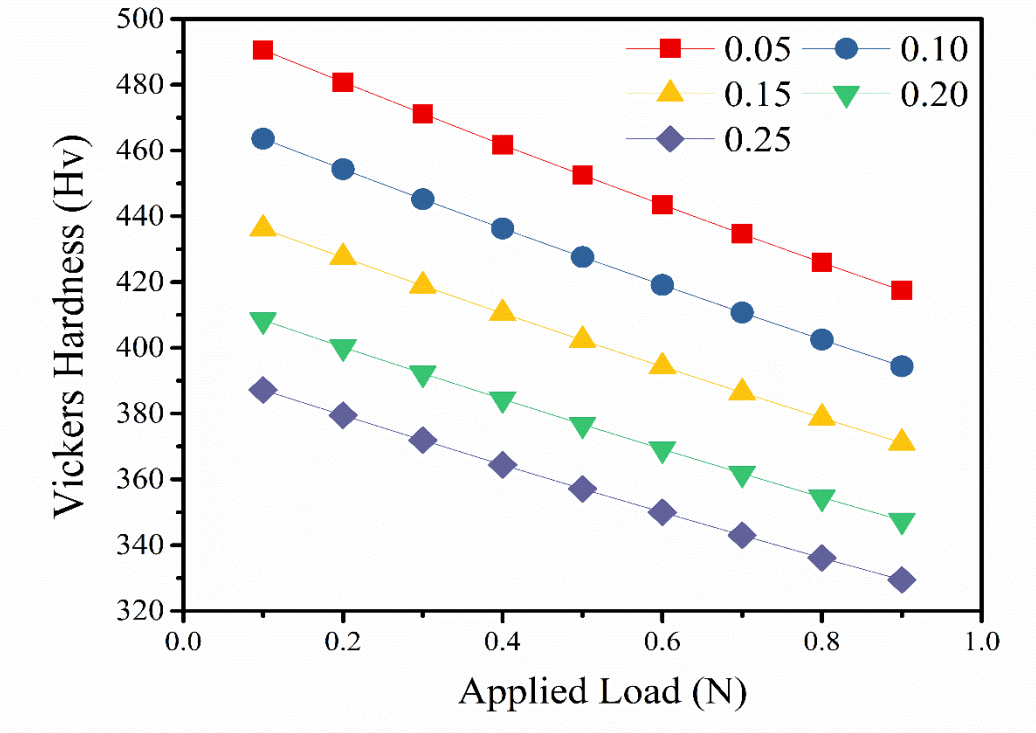

Fig.7.2. Micro-hardness data against the applied load for all glassy specimens

Table 7.1 Vickers microhardness (Hv) values for xV_2O_5–(0.40–x) Na_2O–0.35ZnO–0.25P_2O_5 glass system at varying V_2O_5 concentrations (x = 0.05 to 0.25).

***x*V_2O_5–(0.40-*x*)Na_2O–0.35ZnO–0.25P_2O_5**

Composition (x)	Hv_1	Hv_2	Hv_3	Hv_4	Hv_5	Average Hv
0.05	487	492	489	495	490	490.6
0.1	460	465	462	468	463	463.6
0.15	435	438	432	440	436	436.2
0.2	408	412	410	405	407	408.4
0.25	385	390	388	386	387	387.2

7.2.2 Nano-Indentation Analysis

In the nano-indentation data, each curve—distinguished by varying "x"values (0.05, 0.10, 0.15, 0.20, 0.25)—demonstrates a generally linear increase in force as displacement grows, reflecting the typical elastic-to-plastic transition under the indenter(**Fig.7.3**)[17].All the usefull calculation for nano-indentation related parameters including nano hardness are calculated using **Eq.(2.17)-(2.22)** of **Chapter 2**[18,19]**.** The nearly overlapping slopes at lower displacements indicate that the initial elastic stiffness is fairly similar across all compositions, suggesting that the bulk elastic moduli of the glasses aren't dramatically changed by modest

V_2O_5 additions. As displacement increases beyond the elastic limit, differences begin to emerge: the curves diverge slightly, with glasses having higher vanadium content (e.g., x=0.05 and 0.10) demonstrating somewhat higher resistance to penetration—evidenced by requiring greater force for the same indentation depth compared to those with more V_2O_5.

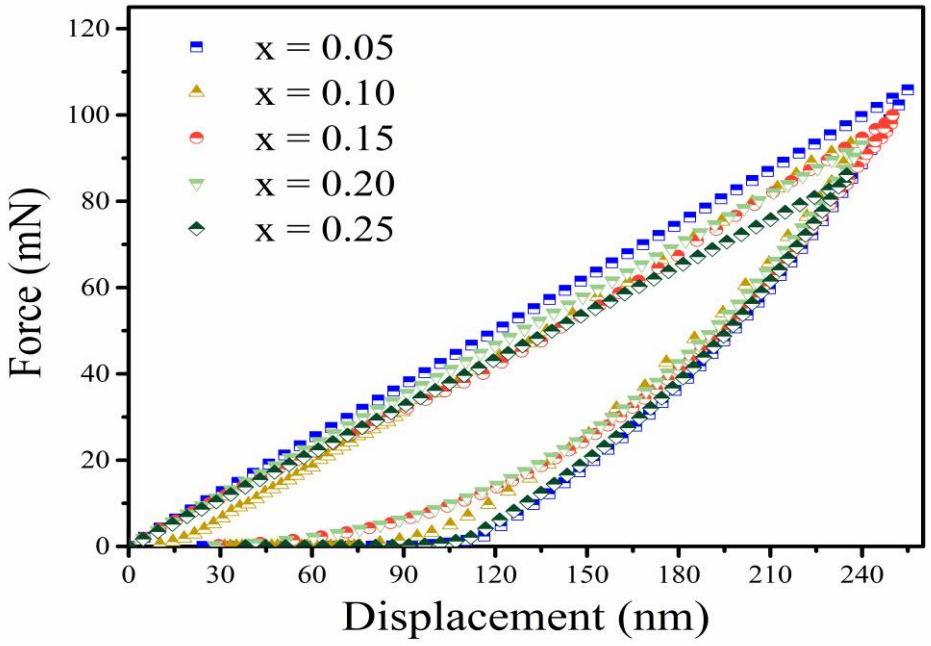

Fig.7.3 Nano-indentation data plots for glassy samples

This behavior implies that adding small amounts of V_2O_5 tends to subtly reinforce the glass matrix, making it slightly tougher against indenter penetration—especially noticeable in the plastic deformation regime. Conversely, at higher V_2O_5 concentrations, the glasses appear to yield more readily under load, suggesting a softening effect in terms of plastic deformation behavior. Overall, the nano-indentation curves reflect an elegant balance: while the elastic stiffness remains broadly consistent, the compositional tweak of vanadium oxide subtly tailors how the glass transitions into the plastic regime[20].

7.3. Quaternary Bi_2O_3-BaO-V_2O_5-P_2O_5 glass system

7.3.1. Microhardness Analysis

All the studied BBVP glass samples show typical indentation size effect (ISE) as seen in the Vickers hardness versus load curves in each composition (**Fig.7.4)**. The characteristic feature of this phenomenon is that an increase in hardness is observed at low loads and a subsequent plateau or slight decrease at high loads. This decreased behavior at high loads is normally linked to plastic straining and the possible formation of microcracks founded under the

indenter. The hardness can be calculated by using **Eq. (2.16)** mentioned in **Chapter 2**[3].

The composition in the glass of highest Bi_2O_3 content (x = 0.35) exhibited the highest value of hardness (Vickers), which is 567.6 GPa, and that of lowest Bi_2O_3 (x = 0.05) gave the lowest value of hardness (Vickers), which is 430.2 GPa. This tendency is also valid through the average hardness vs. Bi_2O_3 concentration graph (**Fig.7.5**), in which it is clear that the microhardness increases almost linearly the whole range of the composition, between x = 0.05 and x = 0.35.

This gradual increase in hardness due to the presence of progressively more Bi_2O_3 can be explained by particular qualities of Bi^{3+} ions. Their ionic radius and the polarizability are big, which leads to densification of the structure, a decrease in molar volume, and the establishment of a stiffer and denser glass structure [3]. Moreover, Bi_2O_3 has a network modifying effect whereby it encourages the presence of strong Bi–O–P linkages and this increases the local crosslinking density and mechanical strength [3].

Moreover, the Bi^{3+} ions constrain deformation near the impression location because they provide a densification effect, which leads to higher resistance to localized mechanical strain and better hardness in general.

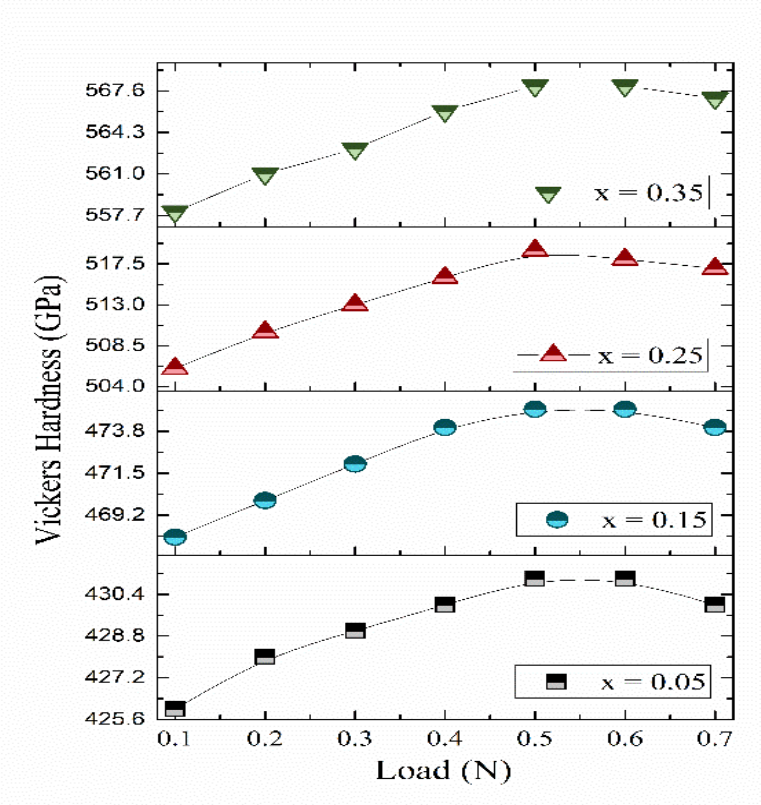

Fig.7.4. Micro-hardness data against the applied load for all glass samples

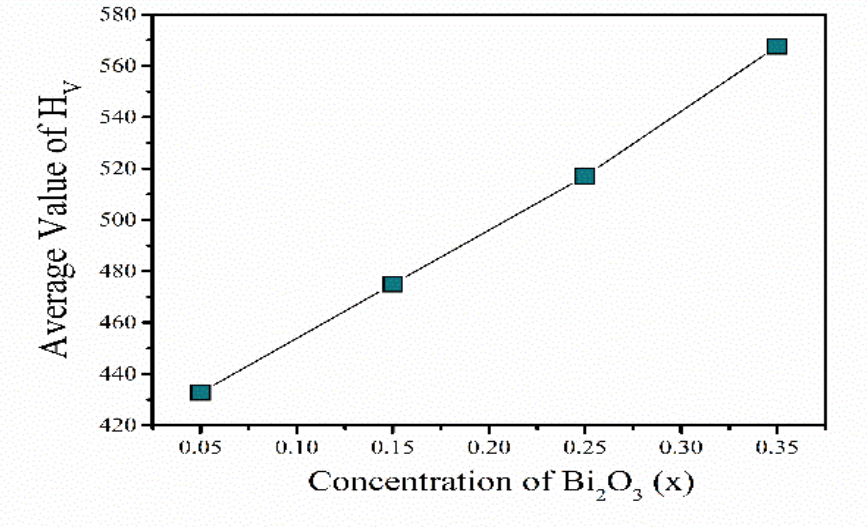

Fig.7.5. Average Micro-hardness data against the concentration(x) of Bismuth(Bi) for glass samples

In addition, the strength of Bi-O bonding enhances the structural unit mobility in compression, which results in an increase in the values of hardness. Thus, the successive addition of Bi_2O_3 at the replacement of BaO increases internal structure strength of the glass, hence improving its resistance to localized plastic deformation, with the higher values of the micro-hardness across the composition alkali line showing such marks.

7.3.2. Investigation of Nano hardness

All the usefull calculation for nano-indentation related parameters including nano hardness are calculated using **Eq.(2.17)-(2.22)** of **Chapter 2**[18,19]. The load displacement curves (**Fig.7.6**) provide vital information on the mechanical behavior of the material under localised loading conditions in the BBVP glass system, in which the modifier concentration (x = 0.05, 0.15, 0.25 and 0.35) are systematically varied. These plots can be considered in terms of the resistance to penetration of the glass network and reflects their useful information into the nature of the elastic and plastic deformation which is dependent on each composition [20].

An observed curvature changes with a change x values especially when directed to the upper levels of the load axis and lower values of the displacement will indicate a progressive improvement of the mechanical rigidity. In the case of sample with x = 0.35, the maximum displacement at the given any load is minimum which means that the given sample is showing maximum resistance to indentation. On the other hand, the sample having the x = 0.05 displays the maximum penetration depth, which means the lowest resistance.

As the modifier content is progressively added the loading segments of the curves increasingly become steeper, that is, most noticeable in comparison of x = 0.05, x = 0.35, showing monotonic increase in hardness. This tendency means that more force will be needed to reach the same indentation depth, which testifies to greater mechanical strength. In line with this, the nano-hardness recorded increases with x such that it is 3.23 GPa at x = 0.05 and 4.43 at x = 0.35.

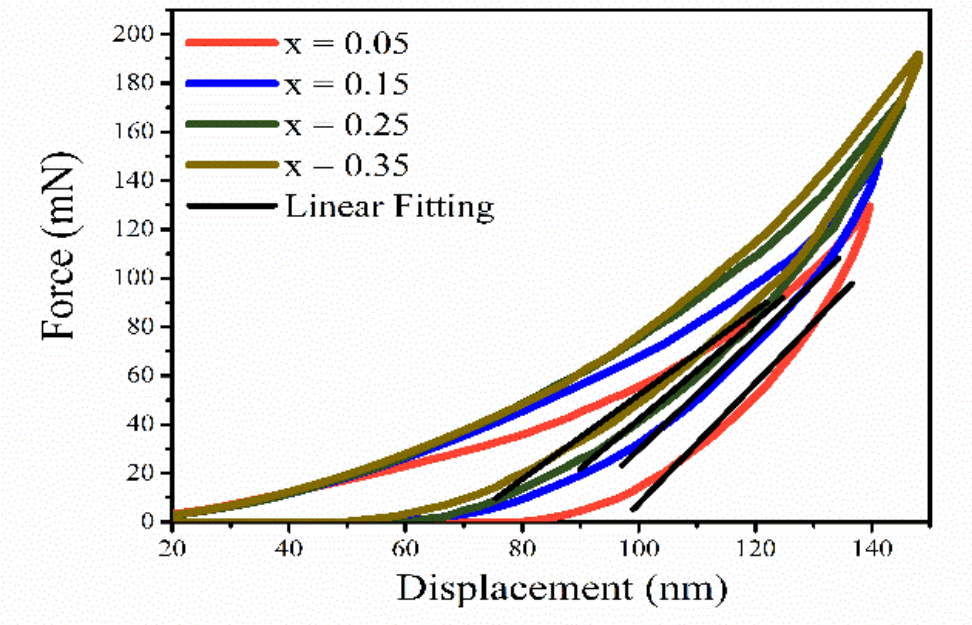

Fig.7.6 Nano-indentation data plots for glass samples

The contact stiffness, calculated from the gradient of the unloading segment using linear fitting (**Fig.7.6**) [17-19], shows a decreasing trend, dropping from 2.47 mN/nm to 1.98 mN/nm as the Bi_2O_3 content increases. Despite the simultaneous rise in nanohardness, elastic modulus, and fracture toughness, this decline likely stems from increased energy dissipation mechanisms such as localized densification and crack-tip blunting [18,19]. Additionally, the transition from a gentler to a steeper loading slope indicates a shift from a softer, more plastically deformable network at low Bi_2O_3 content (x = 0.05) to a stiffer yet more energy-absorbing glass structure at higher concentrations (x = 0.35).

7.3.3. Investigation of Elastic modulus

In the unloading process of nano-indentation, the measurements of all the samples of BBVP glass undergo some degree of elastic recovery. A sloping (less vertical) unloading curve denotes a lower reduced elastic modulus, and denotes greater resistance to permanent

deformation. With Bi_2O_3 modifier content, the unloading portions of the curves are seen to sharpen with an improvement in elastic recovery and the increase in stiffness of the glass network [19].

The increase in lower values of elastic modulus (Er) that show that Er value go up by 18.1 GPa between x = 0.05 and 0.35 is quantitative evidence of this trend. Optimization of these mechanical properties with increasing trends is caused due to change in structural connectivity or by increasing cross-linking volume in glass matrix which has been achieved by changing the composition [19]. The reasonability of this interpretation is also substantiated by the fact that the calculated value of the Young modulus (E) (**Table 7.2**.) calculated with the utilization of **Eq.(2.22)** of **Chapter 2** [19], shows a similar upward trend with the Bi_2O_3 concentration. Namely, modulus rises up to around 77.28 GPa in x = 0.05 to 97.12 GPa in x = 0.35 indicating the presence of Bi_2O_3 in strengthening the glass net.

This is an incremental effect which can be attributed to functions of Bi_2O_3 preceding stronger interatomic bonding and huge amounts of cross-linking in the glass matrix that increases rigidity and deteriorates sensitivity to elastic displacement [17].

Also, the region contained in the load-displacement hysteresis loop provides information on the deformation processes underlying it. Those glass samples that are less loaded with Bi_2O_3 have wider hysterisis loops, meaning that more plastic energy has been dissipated during indentation. On the contrary, compositions that possess increased concentration in Bi_2O_3 show diminished plastic work, which suggests that the material shifts toward brittle behavior leading to further susceptibility to stresses that crack in nature [20].

7.3.4. Investigations of Fracture Toughness

Fracture toughness (K_{IC}) given by **Eq.(2.23)** of **Chapter 2,** [22,23] exhibits a steady enhancement with increment of Bi_2O_3 in the BBVP glass nanocomposites. Particularly, K_{IC} increases at a higher modifier concentration with a significant improvement in terms of crack resistance propagation at x=0.35 to 0.565 MPa 1 5 at x=0.05 (**Table 7.2**). This increase in toughness is directly related to the indentation measured crack lengths (c), which exponentially reduce between the range of x = 0.05 and 0.35 (1.000 - 0.777 m) [7]. The shorter crack lengths

suggest greater fractural resistances, and they substantiate the glass reinforcement role of Bi_2O_3 on the glass matrix.

Also, the stored elastic energy (Ur) or the amount of energy that is absorbed before the failure (**Eq. (2.24)**) depicts an upward relationship; the values range between 0.068 MJ/m until x = 0.05 to 0.103 MJ/m at x = 0.35. This implies that the material gains increasing strength in resisting mechanical stress before the occurrence of cracks and their propagation. The concomitant enhancement of K_{IC} and U_r depicts dual functionality of Bi^{3+} ions: they lead to the compaction of the network and the strengthening of the interatomic bonding, therefore, compensating the flaw sensitivity and adding mechanical resilience [24].

Table 7.2. Mechanical parameters of the studied glassy materials

x	*E(GPa)*	c(μm)	K_{IC}(MPa·m$^{0.5)}$	U_r(MJ/m^3)
0.05	77.28	1	0.565	0.068
0.15	83.89	0.918	0.619	0.077
0.25	90.14	0.85	0.674	0.087
0.35	97.12	0.777	0.742	0.103

7.3.5. Measurement of Mechanical Parameters

A systematic procedure was employed to determine the mechanical properties of the synthesized samples of the glass by measuring their ultrasonic velocity[9-14]. These readings play a paramount role in deducing the fundamental elastic properties, viz., the longitudinal modulus (*L*), shear modulus (*S*), bulk modulus (*K*), and Young modulus (*Y*), that altogether describe the mechanical properties of the material in response to stress and deformations. These moduli also give an indication of how stiff and elastic the glass is, in addition to the nature of the bonding of atoms and compactness. Also, the internal friction parameter, which is frequently defined in terms of Poisson ratio (Pr), is quite important in the interpretation of the behavior of glassy materials under stress, especially focusing on the ability to dissipate energy [38].All the necessary calculations are done with the help of **Eq.(2.25)-(2.30)** of **Chapter 2** [9-14].

To calculate the above-mentioned moduli, ultrasonic longitudinal υ_L and transverse υ_T waves were used in this study to work out the velocities[13]. Also, the velocities of the waves were found to be increasing considerably as the concentration of Bi_2O_3 rose from 3132 m/s to 3274 m/s and from 1796 m/s to 1878 m/s, respectively. It is probably connected with the

reconstruction of the structure, decreasing acoustic impedance, growth of molar volume, and means the densification of the network and growth of the strength of bonds. It has been suggested that structural changes, an increase in the molar volume, and a decrease in the impedance of the glasses under study are the cause of this rise in ultrasonic velocities.

The *L* and *S* values that are calculated using the given **Table 7.3.** show that the values of both *L* and *S* increased when more and more Bi_2O_3 was added to the values that were calculated which were 41.00 GPa and 13.48 GPa, respectively, after adding Bi_2O_3 to the values that had been calculated to 42.66 GPa and 14.03 GPa, respectively. On the same note, *K*, *Y*, and *Pr* portray an upward trend. The bulk modulus is especially an informative measure of the compressibility when pressure is exerted on a substance and a major metric of strength [39]. The increased Young's modulus and bulk modulus mean that the addition of the Bi_2O_3 causes changes in the network, which is most probably through the addition of the number of cross-links, as well as the decrease of the non-bridging oxygen fraction.

This behavior may also be explained through bonding nature and coordination environment. The Bi-O bonds and the creation of P-O-Bi linkages increases the connectivity of the glass network, leading to greater rigidity. Structural stiffness is enhanced, and flexibility decreased by such arrangements of bonds. Field strength of the modifier cations like Bi^{3+} is reputed to affect the bulk modulus through their polarizing effects, which increases network tightness and bond density [13,14].

Due to supporting Raman spectroscopy data, it can be assumed that the internal structural reconfiguration and the preservation of the bonds will occur, accompanied by changes in vibrational modes. Presence of Bi_2O_3 not only modifies the interatomic interactions but it also facilitates their higher deformation resistance due to augmentation of cohesive forces in the compound.

The Poisson's ratio (*Pr*) of 0.252-0.254, as presented in the study, indicates enhanced physical integrity and is acceptable in mechanically perfect glasses. This region can be effectively related to that found in previous studies, for example, in reference [10,13], El-Mallawany et al. found Poisson ratios of 0.227 to 0.256 in Bismuth-Doped tungsten tellurite glasses, and El-Adawy and Moustafa have reported 0.244 and 0.283 in systems based on bismuth and borate [25]. These findings confirm that the slightest additions of Bi_2O_3 may cause significant changes in the mean connectivity and, therefore, the mechanical behavior of glass materials [13].

From an application perspective, the improved elastic moduli will represent improved mechanical longevity, higher resistance to surface deformation, scratch resistance, and susceptibility to high wear factor environments. In addition, such enhancements may lead to low maintenance requirements and high overall performance in further glass technologies [15].

Table 7.3. The mechanical parameters of the studied glasses

X	**υ_L (m/s) (±05)**	**υ_T (m/s) (±05)**	***S*** **(Gpa) (±0.05)**	***L*** **(Gpa) (±0.5)**	***K*** **(Gpa) (±0.5)**	***P_r*** **(Gpa) (±0.02)**	***Y*** **(Gpa) (±0.5)**
0.05	3132	1796	13.48	41.00	23.08	0.257	33.75
0.15	3186	1821	13.59	41.61	23.54	0.256	34.15
0.25	3224	1848	13.86	42.20	23.77	0.254	34.78
0.35	3274	1878	14.03	42.66	24.01	0.253	35.18

7.4. Quaternary Bi_2O_3-Fe_2O_3-V_2O_5-P_2O_5 glass system

7.4.1 Micro Hardness Study

When x = 0.0, the microhardness is relatively low, measured at 182 Hv, which is expected since the glass matrix at this composition comprises only the base glass constituents and lacks any contribution from Bi_2O_3. In this state, the structure is less compact and exhibits weaker interatomic bonding, leading to a softer glass network that is more susceptible to indentation [3].

As Bi_2O_3 is incrementally introduced into the matrix (x = 0.1 and x = 0.2), the microhardness shows a notable increase, reaching 203 Hv and 252 Hv, respectively. This enhancement can be directly attributed to the role of Bi_2O_3 in promoting densification and improving crosslinking within the glass network. The Bi^{3+} ions, possessing high polarizability and larger ionic radii, contribute to stronger and more rigid bonding environments, thereby increasing the resistance of the glass to localized deformation under load.

A more dramatic increase in microhardness is observed for x = 0.3 **(**598 Hv**)** and x = 0.4 (766 Hv). This sharp rise indicates a significant structural transformation occurring at higher Bi_2O_3 concentrations. At these levels, Bi_2O_3 not only continues to enhance the packing efficiency of

the network but may also transition from acting merely as a modifier to partially functioning as a network former. This dual role leads to the formation of Bi–O–P or Bi–O–V linkages, which introduce stiffer, more directionally bonded units into the glass. Additionally, the presence of a high density of Bi^{3+} ions could encourage nanocrystalline phase formation or partial phase separation, resulting in a more rigid and compact structure—features typically associated with increased hardness.

These trends are visually represented in **Fig.7.7**, which plots microhardness as a function of applied load across varying compositions, clearly illustrating the reinforcing effect of Bi_2O_3 incorporation into the glass network.

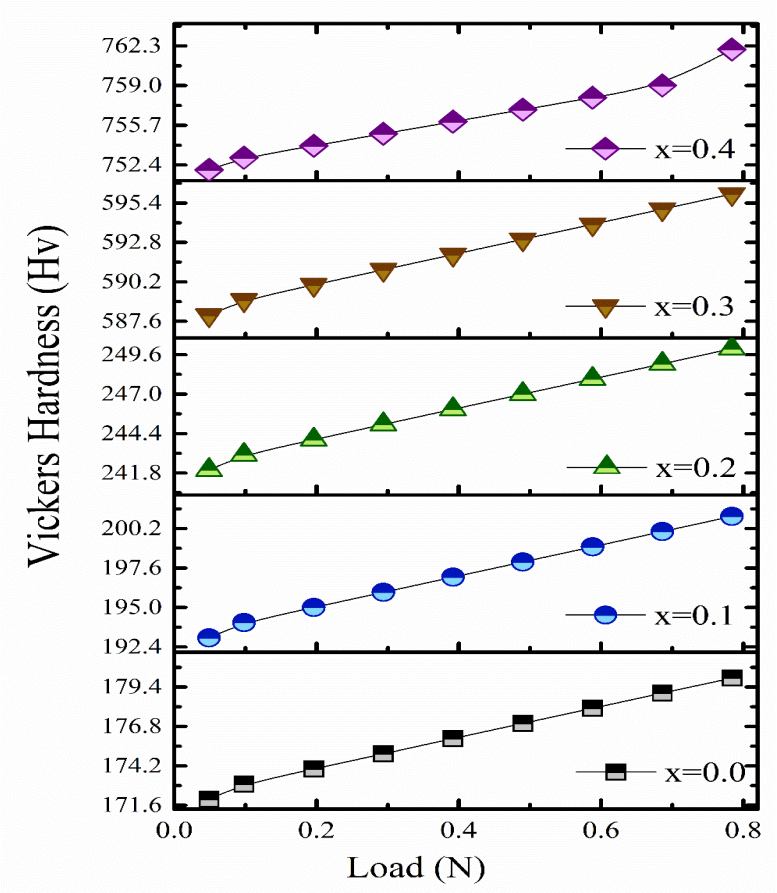

Fig. 7.7. Micro-hardness data for glass samples

7.4.2. Nano Hardness and Elastic Modulus Study

The Oliver–Pharr method, widely recognized for its precision in nanoindentation analysis, is employed here in conjunction with a Continuous Stiffness Measurement (CSM) nanoindenter to evaluate the mechanical properties of the glass samples [18]. This methodology relies on a series of well-established computational steps to extract meaningful physical parameters from

the load-displacement data acquired during the indentation process. All the necessary parameters to be derived in this technique are utilizing the **Eq. (2.17) - (2.22)** of **Chapter 2** [18,19]. Calibration of the Berkovich indenter was rigorously performed using fused silica as the standard reference material. The stiffness of the indenter can be measured against the fused silica, and the stiffness values for different displacements are depicted in the **Table.7.4** This ensures the reliability of stiffness measurements across various depths, and the resulting stiffness–displacement profile was validated against reference data available in the literature [19], further affirming the robustness of the experimental setup.

Overall, the Oliver–Pharr method in conjunction with CSM technology provides a highly accurate and comprehensive insight into the indentation response of the glasses studied. It allows for the extraction of depth-dependent mechanical properties such as hardness, modulus, and their derivative parameters, which are crucial for understanding the structural modifications induced by compositional changes in multicomponent glass systems.

Table 7.4. Stiffness values against various displacement procured while calibrating the prob (Berkovich indenter)

Displacement (nm)	**0**	**500**	**1000**	**1500**	**2000**	**2500**
Stiffness (mN/nm)	0	137.0	287.0	443.0	558.0	676.0

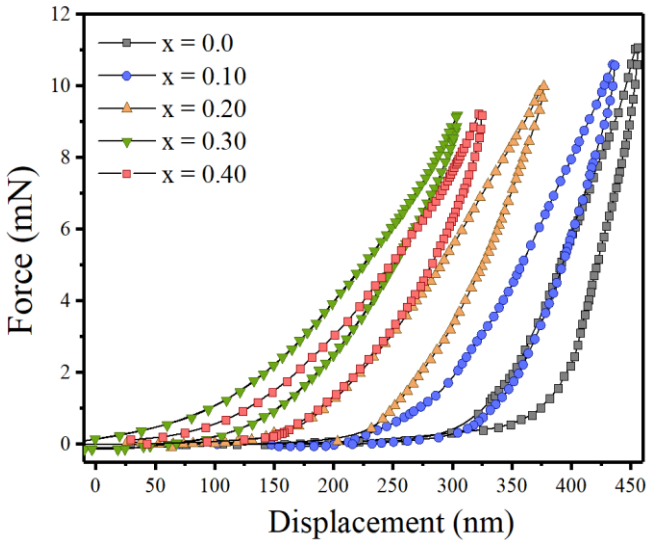

Fig. 7.8. Nano-indentation data plots for glass samples

Fig. 7.8 illustrates the nano-indentation behaviour of the synthesized glass samples with varying compositions of Bi_2O_3, specifically for x = 0.0, 0.1, 0.2, 0.3, and 0.4 in the xBi_2O_3-

$(0.40\text{-}x)Fe_2O_3\text{-}0.25P_2O_5\text{-}0.35V_2O_5$ system. The mechanical response, in terms of nano-hardness and elastic modulus, was evaluated using the well-established Oliver-Pharr method, which is widely regarded for deriving mechanical properties from instrumented indentation data. This method facilitates the extraction of key parameters such as maximum load (F_m), maximum displacement (h_m), contact stiffness (S), contact depth (h_c), residual depth (h_r), plastic depth (h_p), empirical constants like the power-law exponent (m), and projected contact area (A_p), along with the geometry-dependent constant (ε) [18,19]. To ensure accurate and reproducible measurements, each flat glass specimen was precision-polished using silicon carbide paper (5000 grit) and embedded in cold-setting resin to maintain stability during indentation. Due to the limited thickness (1.2 mm) of the samples, the Poisson's ratio was assumed to be 0.30 across all compositions, as lateral measurements via Continuous Stiffness Measurement (CSM) typically require sample thicknesses of 20–30 mm for reliable evaluation [36].

For the undoped glass sample (x = 0.0), the nano-hardness was measured to be 191.52 Hv. The corresponding mechanical parameters included a maximum load (F_m) of 10.07 mN, maximum displacement (h_m) of 450.6 nm, contact stiffness (S) of 0.15 mN/nm, and contact depth (h_c) of 398.7 nm. The residual depth (h_r) was calculated to be 384.7 nm, with a plastic indentation depth (h_p) of 374.3 nm and a projected contact area (A_p) of 4,867,496 nm². The power-law exponent (m) stood at 1.2, while ε was found to be 0.8, indicating moderate elastic recovery and plastic deformation.

Upon increasing the Bi_2O_3 content to x = 0.1, a notable enhancement in nano-hardness to 216.29 Hv was observed. The reduction in h_m to 433.3 nm and the decrease in h_c to 373.6 nm suggest enhanced resistance to indentation, supported by a contact stiffness of 0.12 mN/nm. The residual and plastic depths were 352.1 nm and 298.2 nm, respectively, with a reduced contact area of 4,301,701nm². An increase in the power-law exponent to 1.8 reflects changes in the material's viscoelastic deformation behavior, and ε was calculated as 0.7.

At x = 0.2, the nano-hardness further increased to 278.02 Hv, with a corresponding decrease in maximum displacement to 388.3 nm. The contact stiffness improved to 0.14 mN/nm, and the contact depth was calculated as 332.5 nm. The material exhibited increased elastic recovery, with hr = 313.83 nm and h_p = 265.4 nm, and a smaller projected contact area of 3,350,728 nm². The power-law exponent (m) was 1.5, and ε remained stable at 0.8.

A significant structural shift is evident at x = 0.3, with a sharp rise in nano-hardness to 654.62 Hv, accompanied by a pronounced reduction in h_m to 284.6 nm. The contact stiffness also rose markedly to 0.17 mN/nm. Correspondingly, the contact depth (h_c) was 246.3 nm, while hr and hp were 232.9 nm and 203.7 nm, respectively. The contact area was minimised to 1,423,973 nm², indicating denser and more resistant glass networks. The power-law exponent remained high at 1.6, while ε stayed consistent at 0.7.

At the highest substitution level, x = 0.4, the glass reached its maximum nano-hardness of 828.67 Hv. The force applied (F_m) was 10.03 mN, and the displacement (h_m) decreased further to 272.8 nm, reflecting maximum resistance to deformation. The contact stiffness slightly declined to 0.19 mN/nm, while the contact depth was further reduced to 230.8 nm. The residual depth (hr) was 216.8 nm, and the plastic depth (h_p) reached its minimum at 184.8 nm. The projected contact area also reached its minimum at 1,121,055 nm². The m value remained consistent at 1.5, and ε at 0.8.

Furthermore, the instrumented elastic modulus (EIT), as shown in **Fig. 7.9**, exhibited a consistent upward trend—from 56.97 GPa at x = 0.0 to 150.94 GPa at x = 0.4. This gradual increase in stiffness aligns with the higher content of Bi_2O_3, which enhances network densification, improves bonding, and reduces porosity and microstructural defects [19,20]. The presence of Bi^{3+} ions likely promotes stronger electrostatic interactions, increasing the matrix's rigidity. Since nano-hardness and elastic modulus are both affected by atomic packing and resistance to deformation, their concurrent rise indicates a synergistic reinforcement of the glass network [17]. This relationship supports the idea that mechanical robustness in oxide glass systems can be effectively tailored through controlled compositional modifications.

The presence of Bi_2O_3 distinctly enhances the nano-hardness values of the glass samples, as evidenced by the progressive increase in Vickers hardness from x = 0.0 to x = 0.4. Notably, a significant mechanical reinforcement is observed beginning at x = 0.3, marking a pivotal transition in the mechanical integrity of the glass system. This sharp increase in hardness can be better understood by examining the cross-linking density of the studied compositions. In the current glass matrix, the coordination number of P_2O_5 is four, while that of V_2O_5 is five. Structurally, phosphate glass is unique due to the presence of one double bond per PO_4 tetrahedron, which forms a three-dimensional network with a cross-linking value of two [19,20]. Upon the incorporation of Fe_2O_3 and V_2O_5 into the phosphate glass network, the structure becomes increasingly cross-linked.

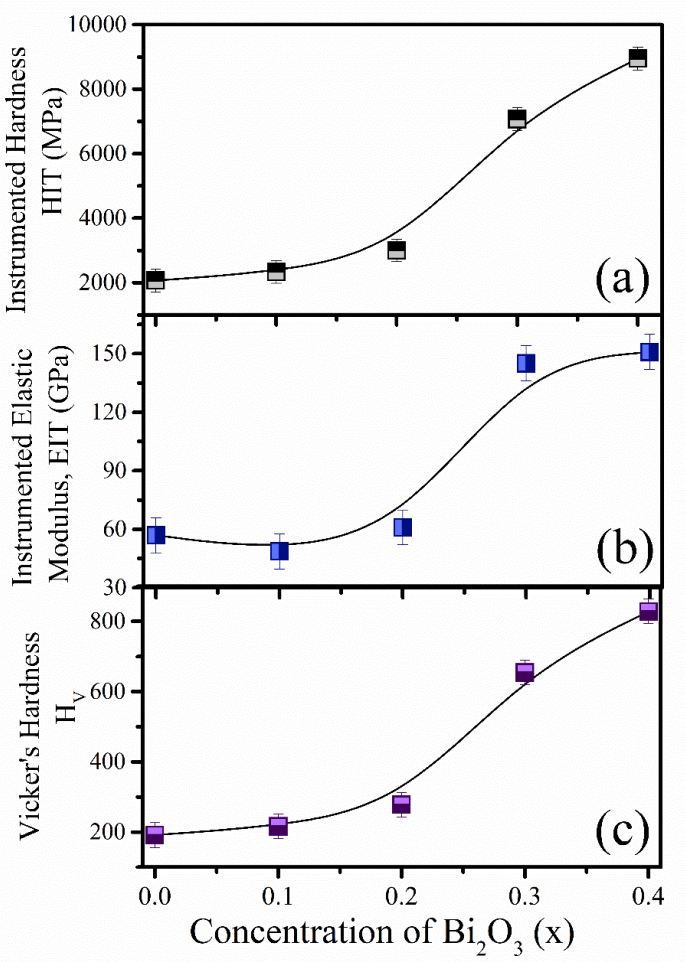

Fig. 7.9 Variation of Instrumented Hardness (HIT), Instrumented Elastic Modulus (EIT) and Vickers Hardness (Hv) with the incremental inclusion of Bi_2O_3(x)

These additional cross-links result in a greater number of network bonds per unit volume, thereby elevating the cross-linking density of the system, as corroborated by earlier research [17,20].

Bismuth oxide doping further amplifies this effect by raising the calculated cross-link density. Specifically, the cross-linking values for x = 0.0, 0.1, and 0.2 were computed as 2.10, 2.33, and 2.53, respectively—demonstrating a steady increment. However, a pronounced increase is observed in samples with x = 0.3 and x = 0.4, where the cross-linking densities sharply rise to 3.00 and 3.50, respectively. This dramatic enhancement in the network connectivity likely contributes to the marked mechanical reinforcement seen at these compositions.

Moreover, the nano-indentation results derived using the Oliver-Pharr method (as summarized in **Table 7.5**) further substantiate that the substitution of Fe_2O_3 with Bi_2O_3 significantly improves the hardness and stiffness of the glass system. This trend implies a more compact and

less deformable glass structure with increasing Bi_2O_3 content. The enhanced mechanical performance can be attributed not only to the increased cross-linking density but also to the role of Bi_2O_3 in promoting densification and reducing microstructural defects such as cracks and porosity—factors that collectively contribute to improved nano-hardness and mechanical stability.

Table 7.5. Evaluated nanoindentation parameters of xBi_2O_3-(0.40-x) Fe_2O_3-$0.35V_2O_5 0.25P_2O_5$ glassy samples.

x (% mol)	F_m (mN)	h_m (nm)	S (mN/nm)	h_c (nm)	h_r (nm)	h_p (nm)	A_p (nm²)	m	ε	Nano-hardness (Hv)
0.0	10.07	450.6	0.15	398.6	384.7	374.3	4,867,496	1.2	0.8	191.52
0.1	10.05	433.3	0.12	373.6	352.1	298.2	4,301,701	1.8	0.7	216.29
0.2	10.06	388.3	0.14	332.5	313.8	265.4	3,350,728	1.5	0.8	278.02
0.3	10.07	284.6	0.17	246.3	232.9	203.7	1,423,974	1.6	0.7	654.62
0.4	10.03	272.8	0.19	230.8	216.8	184.8	1,121,055	1.5	0.8	828.67

7.4.3. Comparison of micro and nano hardness

The observed disparity between nano-hardness and micro-hardness values arises primarily from the difference in indentation scale and the associated material response mechanisms. Nano-indentation operates at extremely shallow depths—typically in the nanometer range—targeting a highly localized region of the material. Consequently, nano-hardness measurements are sensitive to surface phenomena, such as atomic-scale structure, localized densification, and the presence of harder phases near the surface. At such small scales, the strain gradient is significantly higher, which often leads to a more pronounced strain-hardening effect and, therefore, an elevated hardness value.

On the other hand, micro-hardness testing employs larger loads and produces indentations on the micrometer scale. This results in an averaged response over a broader volume of the material, encompassing grain boundaries, compositional heterogeneities, and potentially softer or more compliant regions. The response captured through micro-indentation is, therefore, more representative of the bulk material behavior and often registers lower hardness values compared to nano-indentation.

This scale-dependent mechanical behavior underscores the importance of choosing the appropriate indentation method based on the desired resolution and the structural features of the material under investigation. Nano-indentation, particularly when combined with continuous stiffness measurement (CSM), provides critical insight into depth-dependent properties, while micro-hardness remains valuable for assessing bulk or averaged responses across the material's cross-section.

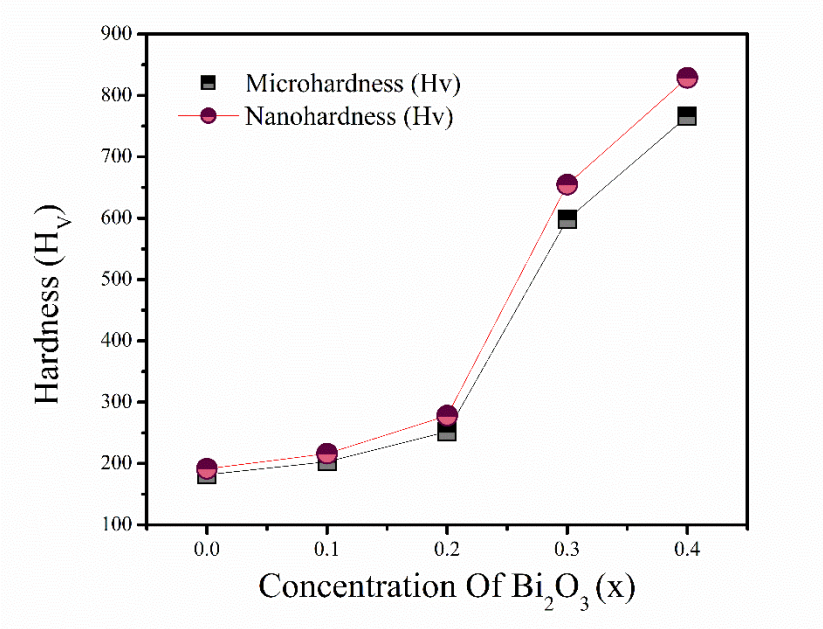

Fig. 7.10 Comparison between micro and nano hardness values (Hv) with the different Bi_2O_3 concentrations (x)

As a result, micro-hardness values are generally lower than nano-hardness values, as they reflect an averaged mechanical response over a broader volume of the material. This includes contributions from both rigid and compliant regions, such as grain boundaries, amorphous zones, or phase-separated structures. The larger contact area during micro-indentation facilitates more extensive plastic deformation, allowing dislocations and structural defects to migrate more easily, thereby reducing the measured hardness.

In contrast, nano-indentation probes a much smaller, localized zone, often avoiding the influence of such microstructural heterogeneities. This leads to higher hardness readings due to localized constraint of plastic flow and the activation of strain gradient hardening mechanisms, where the resistance to deformation increases with decreasing indentation depth.

This distinction is visually presented in **Fig. 7.10**, which illustrates the clear deviation between nano- and micro-hardness trends across different compositions. While nano-hardness captures

surface-level resistance and localized strengthening, micro-hardness offers a bulk-averaged metric, making both parameters essential for comprehensive mechanical characterization of glassy materials.

7.5. Quaternary V_2O_5–Na_2O–ZnO–P_2O_5 glass system

7.5.1. Analysis of DSC measurement and glass transition temperature (Tg)

The glass transition temperature (T_g) of all prepared glass samples was determined from the endothermic inflexion observed in the DSC thermograms, as illustrated in **Fig.7.11** for the x = 0.05 composition. The inset of **Fig.7.11** presents the trend of T_g as a function of V_2O_5 concentration (x). A gradual decline in T_g is observed with increasing V_2O_5 content. This decrease can be attributed to the formation and growth of nanocrystallites, as evidenced in **Fig.7.11**, which introduces a partial disruption to the glass network[26].

The simultaneous incorporation of both V_2O_5 and Na_2O plays a crucial role in modifying the phosphate glass structure. These modifiers lead to the generation of non-bridging oxygen species (NBOs), specifically P=O (PO_3^-) and P–O^- groups, which act to depolymerize the phosphate chains, effectively reducing the connectivity of the glass network. This depolymerization leads to a lower cross-linking density, which in turn decreases the thermal energy required for the transition from the glassy to rubbery state, resulting in a lower T_g.

Moreover, the cross-link density, bonding type, and chain length are known to govern the thermal behavior of phosphate-based glasses. The substitution of network formers (like P_2O_5) with network modifiers (such as V_2O_5 and Na_2O) weakens the average bond strength, further facilitating structural mobility at lower temperatures. Thus, the progressive decrease in T_g with increasing x reflects the combined influence of structural depolymerization, nanocrystallite formation, and modifier-induced disruption of the phosphate glass framework.

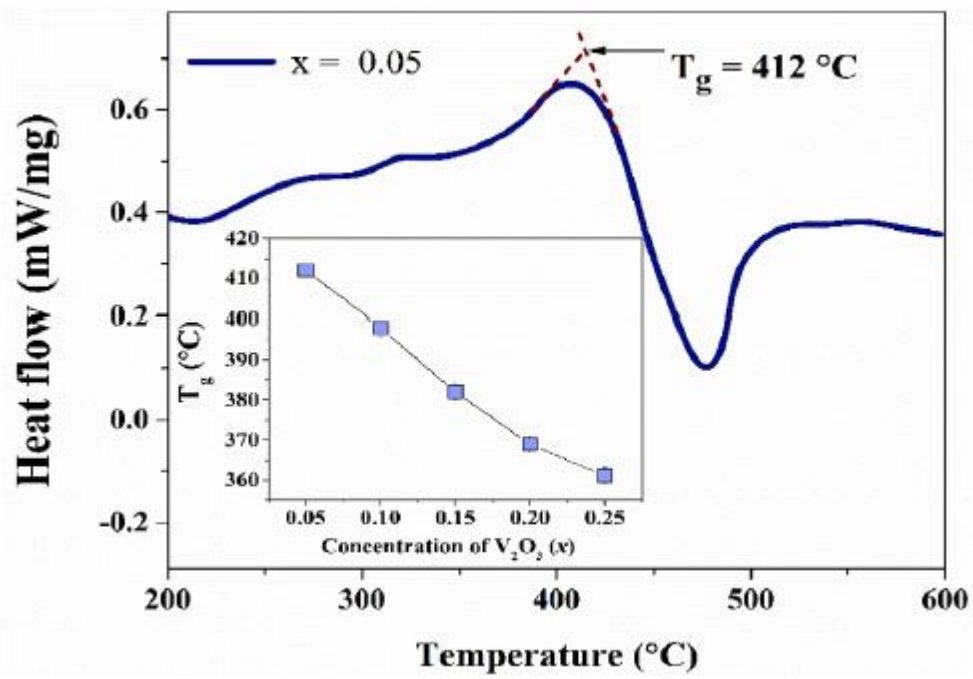

Fig.7.11 Thermal characteristics of Bi_2O_3-BaO-V_2O_5-P_2O_5 glass system

7.6. Quaternary Bi_2O_3-BaO-V_2O_5-P_2O_5 glass system

7.6.1. Thermal Analysis of BBVP Glass Ceramics

Thermal characterization, particularly through Differential Scanning Calorimetry (DSC), serves as a highly effective method for probing the crystallization behavior and phase transitions in glass systems. This technique provides crucial insights into the thermodynamic properties and structural rearrangements of glassy materials during heating. In the present study, DSC was employed to examine the thermal responses of xBi_2O_3-(0.4-x) BaO-0.3P_2O_5-0.3V_2O_5 glass systems, where x = 0.05, 0.15, 0.25, and 0.35.

For each composition, approximately 5 mg of finely powdered sample was subjected to a controlled heating program ranging from 250 °C to 700 °C at a constant heating rate of 10 °C/min. The glass transition temperature (T_g) for each sample was determined by the standard tangent method, involving the intersection of two tangents—one along the baseline and the other on the upturned slope of the DSC curve, marking the onset of structural rearrangement.

The melting temperature (T_m) was identified as the peak of the endothermic transition, while the crystallization temperature (T_c) was defined as the midpoint of the temperature range corresponding to the exothermic peak. This midpoint was determined by extrapolating the linear portions of the rising and falling edges of the crystallization peak [27,28]. Additionally, the peak crystallization temperature (T_p)—representing the maximum rate of crystallization—was marked by the inflexion point on the rising slope of the exothermic peak, signifying a steep increase in heat capacity due to the onset of crystal formation.

The derived T_g, T_c, and T_p values for all the compositions are compiled in **Table 7.6**, offering a comparative understanding of how Bi_2O_3 substitution influences thermal stability and crystallization behavior within these quaternary glass networks. These thermal parameters serve as indicators of glass stability, network rigidity, and nucleation kinetics, all of which are crucial for understanding the glass-forming tendency and potential heat-treatment applications of the synthesized glasses.

Table 7.6. Several thermal characteristics of the investigated glass specimens

x	T_g (°C) (±1°C)	T_c (°C) (±1°C)	T_p (°C) (±2°C)	$\Delta T=T_c-T_g$ (°C) (±1°C)
0.05	421	563	591	142
0.15	432	575	601	143
0.25	436	585	613	149
0.35	444	596	625	152

Table 7.6. summarizes the key thermal parameters—glass transition temperature (T_g), crystallization onset temperature (T_c), peak crystallization temperature (T_p), and the derived thermal stability ($\Delta T = T_c - T_g$)—for the glass compositions of the form xBi_2O_3-(0.4-x) BaO-$0.3P_2O_5$-$0.3V_2O_5$, where x = 0.05, 0.15, 0.25, and 0.35. These thermal characteristics provide critical insights into how varying Bi_2O_3 concentrations influence the structural rigidity and thermal resilience of the glass matrix.

From **Fig. 7.12(a)**, it is evident that each composition exhibits distinct thermal events on the DSC thermograms. The glass transition (T_g) is characterized by a subtle endothermic shift, signifying the transition of the glass from a rigid to a more thermally activated, mobile state. This transformation marks the onset of structural rearrangement without long-range atomic ordering. Following T_g, the exothermic peaks correspond to the crystallization process, with

Tc denoting the temperature at which nucleation and crystal growth begin, and T_p indicating the point of maximum crystallization rate.

Analysis of the DSC data reveals a systematic increase in T_g, T_c, and T_p with rising Bi_2O_3 content, suggesting that the incorporation of Bi_2O_3 leads to a more tightly bound and interconnected glass network. This trend reflects enhanced cross-linking density and increased network rigidity, contributing to improved thermal stability. The ΔT values further corroborate this behavior, indicating a widening gap between the onset of structural softening and the initiation of crystallization, which is desirable for materials that require high thermal durability.

Table 7.6. shows the thermal characteristics of the glass compositions xBi_2O_3-(0.4-x) BaO-$0.3P_2O_5$-$0.3V_2O_5$, where *x* is the content of Bi_2O_3 at 0.05, 0.15, 0.25 and 0.35. These parameters contain the glass transition temperature T_g, crystallisation T_c, peak crystallisation temperature T_p thermal stability $\Delta T = T_c - T_g$. Analysing the data, it is possible to observe marked dependences of the thermal properties of the glass material on the Bi_2O_3 content.

It is also clear from **Fig. 7.12(a)** that there exist various thermal events in DSC curves associated with each composition. The T_g is identified as an endothermic transition where the amorphous glass is transformed into a more mobile state. In the light of T_g, the exothermic peaks are associated with the crystallisation process, at which the start of the process is defined as the temperature at which T_c occurs, while the maximum crystallisation rate is identified as T_p. The DSC data show that as Bi_2O_3 content rises, T_g, T_c and T_p will be improved, which means that the structure becomes rigid and the thermal stability will be improved.

As depicted in **Fig. 7.12(b)** and detailed in **Table 7.6**, the glass transition temperature (T_g) and thermal stability parameter ($\Delta T = T_c - T_g$) display a consistent upward trend with increasing Bi_2O_3 concentration. Specifically, T_g increases steadily from 421 K to 444 K as x increases to 0.35, indicating that Bi_2O_3 incorporation leads to a stiffer and more rigid glass network. In parallel, the thermal stability (ΔT), which reflects the material's resistance to crystallization, improves from 142 K at x = 0.05 to 152 K at x = 0.35. This enhancement in ΔT implies greater structural stability at elevated temperatures, a desirable characteristic for high-performance glass systems.

Furthermore, the crystallization temperature (T_c) increases from 563 K to 596 K, and the peak crystallization temperature (T_p) rises from 591 K to 625 K within the same compositional range, further confirming the improved thermal resilience with higher Bi_2O_3 content.

The observed increase in T_g is primarily attributed to structural modifications induced by Bi_2O_3. Bismuth oxide is known to disrupt weaker P–O–P linkages while contributing additional non-bridging oxygens (NBOs), which can bridge charge and stabilise the network. This leads to enhanced network connectivity and cross-linking density, thereby reinforcing the glass structure. Unlike traditional borophosphate glass systems—where Bi_2O_3 typically lowers T_g—this composition reveals a dual role of Bi_2O_3, acting both as a network modifier and stabilizer, thereby significantly enhancing the glass structure and thermal stability [16,26-28].

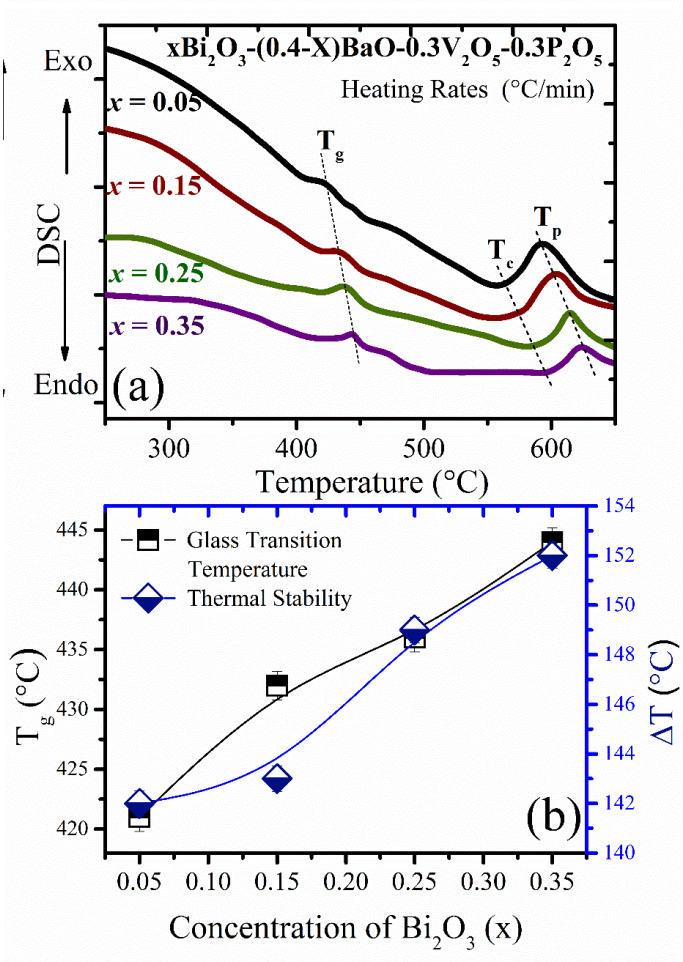

Fig. 7.12. Thermal Behavior and Stability of xBi_2O_3-(0.4-X) BaO-$0.3P_2O_5$-$0.3V_2O_5$ Glass System: **(a)** DSC curves at various Bi_2O_3 concentrations (x) and heating rates, highlighting glass transition temperature (T_g), crystallization temperature (T_c), and peak crystallization

temperature (T_p); **(b)** Correlation between Bi_2O_3 concentration (x) and glass transition temperature (T_g) along with thermal stability (ΔT).

The observed enhancement in thermal stability with increasing Bi_2O_3 content in the xBi_2O_3-(0.4-x) BaO-$0.3P_2O_5$-$0.3V_2O_5$ glass system is primarily attributed to the structural role of Bi_2O_3 as a network modifier. Incorporation of Bi_2O_3 introduces strong Bi–O bonds and P–O–Bi linkages, which contribute to an increase in the cross-link density of the phosphate glass network. This modification leads to a reduction in non-bridging oxygen (NBO) content and an increase in the rigidity of the network, thereby enhancing the resistance to thermal deformation.

The resulting structural reinforcement is directly correlated with the increases in both T_g and T_c, which is reflected in the rising values of thermal stability ($\Delta T = T_c - T_g$) with Bi_2O_3 content. Additionally, the formation of BiO_6 polyhedral clusters and partial depolymerization of the phosphate chains further contribute to improving the thermal resistance of the glass by reducing brittleness and suppressing crystallization tendencies.

Such structural transformations render the glass more stable against devitrification at elevated temperatures. These findings are consistent with previously reported trends in zinc-bismuth phosphate and lead-bismuth borophosphate glass systems, where Bi_2O_3 was shown to enhance network stability and crystallization resistance [27,28]. Differential Scanning Calorimetry (DSC) analysis confirmed that the present glass systems demonstrate good thermal stability across a wide temperature range, making them suitable candidates for high-temperature and thermally demanding applications.

7.7. Summary

In this chapter, analytical works were transparently done to check upon mechanical and thermal properties of three quaternary glass nanocomposites systems, i.e., xV_2O_5–(0.40-x)Na_2O–0.35ZnO–$0.25P_2O_5$(VNZP),xBi_2O_3-(0.4-X)BaO-$0.3P_2O_5$-$0.3V_2O_5$(BBVP), and xBi2O3-(0.40-x) Fe_2O_3-$0.35V_2O_5$-$0.25P_2O_5$(BFVP) to determine the extent to which the structural integrity, elasticity, and heat resistance varies with the composition changes. Mechanical analysis using Vickers microhardness, nano-indentation, ultrasonic velocity and elastic modulus measurements parameters gave good correlations between the network densification, cross-linking density and higher values of hardness. Specifically, the addition of Bi_2O_3 continuously increased hardness, Young's modulus and fracture toughness, demonstrating that

Bi_2O_3 equally acts as a network modifier and partial network former, strengthening the glass matrix via Bi-O-P and Bi-O-V linkages.Nano-indentation analysis showed evidence of scale dependence of hardness, whereby greater nano-hardness was observed owing to stronger localized strain gradient effects and a decreased role of microstructural heterogeneities. The mechanical performance increase that was observed as a result of increasing Bi_2O_3 and moderate V_2O_5 content was explained by a decrease in the concentration of non-bridging oxygen, better packing efficiency and prevention of microcrack propagation.

Thermal analysis was carried out using Differential Scanning Calorimetry (DSC); it was seen that incorporating Bi_2O_3 enhances thermal stability of the systems as well, which is captured by the systematically elevated values of glass transition temperature (T_g), crystallization temperature (T_c), peak crystallization temperature (T_p), and thermal stability factor (ΔT). This is regarding higher Bi-O bonds, dense cross-linking and less depolymerization of the networks, which makes the glasses less inclined to devitrification and thermal shocking. On the contrary, increased V_2O_5 loadings in VNZP glasses inclined to lower T_g on account of augmented non-bridging oxygens and partial disruption in the network.

Collectively, the results specify overall compositional tuning, especially by enriching in Bi_2O_3, measurably enhance the mechanical strength and long-term thermal stability of vanadium phosphate-based glass systems. Such improvements render the glass nanocomposites developed as prospective structural, optical and high-temperature functional applications, where mechanical strength and thermal stability of performance constitute important demands.

7.8 Reference

1. Hammad, A. H., Moustafa, E. B., Abdel-wahab, M. Sh., AbuShanab, W. S., & Wassel, A. R. (2022). Investigate the structure, mechanical, and optical properties of a novel cadmium phosphate glass containing vanadium oxide. Optik, 261, 169214. https://doi.org/10.1016/j.ijleo.2022.169214
2. Havriliak, S., & Negami, S. (1967). A complex plane representation of dielectric and mechanical relaxation processes in some polymers. Polymer, 8(2), 161–210. https://doi.org/10.1016/0032-3861(67)90021-3
3. Yamane, M., & Mackenzie, J. D. (1974). Vicker's hardness of glass. Journal of Non-Crystalline Solids, 15(2), 153–164. https://doi.org/10.1016/0022-3093(74)90044-1
4. Xu, Z., Liu, M., & Yang, F. (2024). Calculation of elastic constants of bulk metallic glasses from indentation tests. Journal of Materials Research and Technology, 28, 4382–4391. https://doi.org/10.1016/j.jmrt.2024.01.046
5. Vaidyanathan, R., Dao, M., Ravichandran, G., & Suresh, S. (2001). Study of mechanical deformation in bulk metallic glass through instrumented indentation. Acta Materialia, 49(19), 3781–3789. https://doi.org/10.1016/S1359-6454(01)00263-4
6. AlMisned, G., Baykal, D. S., Alkarrani, H., Susoy, G., & Tekin, H. O. (2024). Advancing mechanical durability and radiation shielding properties in silicon dioxide (SiO_2) glasses through various incorporations: A comparative analysis. Results in Physics, 61, 107717. https://doi.org/10.1016/j.rinp.2024.107717
7. Drozdz, D., Kulik, T., & Fecht, H. J. (2007). Nanoindentation studies of Zr-based bulk metallic glasses. Journal of Alloys and Compounds, 441(1–2), 62–65. https://doi.org/10.1016/j.jallcom.2006.09.066
8. Kim, J. J., Cho, Y., Suresh, S. A., & Argon, S. (2002). Nanocrystallization during nanoindentation of a bulk amorphous metal alloy at room temperature. Science, 295(5555), 654–657. https://doi.org/10.1126/science.1067453
9. Saddeek, Y., Yahia, I. S., Aly, K., & Dobrowolski, W. (2010). Spectroscopic, mechanical and magnetic characterization of some bismuth borate glasses containing gadolinium ions. Solid State Sciences, 12(9), 1426–1434. https://doi.org/10.1016/j.solidstatesciences.2010.05.015
10. El-Mallawany, R., Gaafar, M. S., Hesham, A., Afifi, E. A., Mwafy, A. M., & Ghonaim, A. M. (2025). RDF, IR deconvolution, bulk modulus–molar volume and shielding

parameters of some tellurite glasses. Physica B: Condensed Matter, 715, 417535. https://doi.org/10.1016/j.physb.2025.417535

11. Hisam, R., & Yahya, A. K. (2019). Elastic moduli, optical and electrical properties of mixed electronic–ionic $30Li_2O–4MoO_3–(66\text{-}x)TeO_2–xV_2O_5$ tellurite glass system. Results in Physics, 13, 102219. https://doi.org/10.1016/j.rinp.2019.102219
12. Tafida, R. A., Thakur, S., Onimisi, M. Y., Garba, S., Adamu, S. B., Shitu, I. G., & Lakin, I. I. (2024). Unveiling the elastic properties of samarium oxide zinc tellurite-based glasses: Judd–Ofelt intensity parameters through structural, experimental, and theoretical studies. Optical and Quantum Electronics, 56(6), 1–17. https://doi.org/10.1007/s11082-024-06905-7
13. El-Mallawany, R., Afifi, H. A., El-Gazery, M., & Ali, A. A. (2018). Effect of Bi_2O_3 addition on the ultrasonic properties of pentaternary borate glasses. Measurement, 116, 314–317. https://doi.org/10.1016/j.measurement.2017.11.028
14. Elkhoshkhany, N., Syala, E., & Yousef, E. S. (2020). Concentration dependence of the elastic moduli, thermal properties, and non-isothermal kinetic parameters of Yb^{3+} doped multicomponent tellurite glass system. Results in Physics, 16, 102876. https://doi.org/10.1016/j.rinp.2019.102876
15. Jang, J. S. C., Jian, S. R., Chang, C. F., Chang, L. J., Huang, Y. C., Li, T. H., Huang, J. C., & Liu, C. T. (2009). Thermal and mechanical properties of the $Zr_{53}Cu_{30}Ni_9Al_8$ based bulk metallic glass micro-alloyed with silicon. Journal of Alloys and Compounds, 478(1–2), 215–219. https://doi.org/10.1016/j.jallcom.2008.11.135
16. Mondal, R., Biswas, D., Lalwani, S. K., Chatterjee, P., Patra, A. S., & Kabi, S. (2025). Impact of Ge addition on physio-chemical, optical, and thermal properties of S–Se–Cd–Ge glasses: A study of improvement in mechanical strength. Journal of Non-Crystalline Solids, 652, 123418. https://doi.org/10.1016/j.jnoncrysol.2025.123418
17. Singh, D., Tiwari, R. S., Srivastava, O. N., Mandal, R. K., Sobti, R. C., Kaushik, A., Singh, B., & Tripathi, S. K. (2012). Synthesis and mechanical properties of $Zr_{69.5}Ga_{7.5}Cu_{12}Ni_{11}$ metallic glass and nano quasicrystal–glass composites. In Emerging paradigms in nanotechnology (p. 81). Pearson Education. ISBN: 978-81-317-8991-9
18. Oliver, W. C., & Pharr, G. M. (2004). Measurement of hardness and elastic modulus by instrumented indentation: Advances in understanding and refinements to methodology. Journal of Materials Research, 19(1), 3–20. https://doi.org/10.1557/jmr.2004.19.1.3

19. Brazil, O., & Pharr, G. (2021). Measuring Poisson's ratio during nanoindentation via lateral contact stiffness; issues of slip and plasticity. arXiv. https://doi.org/10.48550/arXiv.2103.04189
20. Fischer-Cripps, A. C. (2004). Nano-indentation. Springer-Verlag. https://doi.org/10.1007/978-0-387-22462-6
21. Wang, P., Gao, Y. & Wang, P. (2024).A comparative study of indentation size effect models for different materials. Sci Rep 14, 20010 https://doi.org/10.1038/s41598-024-71136-5
22. Anstis, G.R., Chantikul, P., Lawn, B.R. and Marshall, D.B. (1981) A Critical Evaluation of Indentation Techniques for Measuring Fracture Toughness: I, Direct Crack Measurements. Journal of the American Ceramic Society, 64, 533-538.https://doi.org/10.1111/j.1151-2916.1981.tb10320.x
23. Anderson, T.L. (2017). Fracture Mechanics: Fundamentals and Applications, Fourth Edition (4th ed.). CRC Press. https://doi.org/10.1201/9781315370293
24. Qiao, Y., Zhang, Z.-X., & Zhang, S. (2023). An Experimental Study of the Relation between Mode I Fracture Toughness, KIc, and Critical Energy Release Rate, GIc. Materials, 16(3), 1056. https://doi.org/10.3390/ma16031056
25. A. El-Adawy, Y. Moustafa, Elastic properties of bismuth borate glasses, Journal of Physics D: Applied Physics, 32 (1999) 2791.
26. Biswas, D., Rakshit, A., Hota, S. B., Kabi, S., Kuiri, B., Roy, D., & Mondal, R. (2024). Thermal, electrical, and dielectric properties of $xNa_2O–(0.4–x)B_2O_3–0.4SiO_2–0.2P_2O_5$ glassy systems for advanced material applications. Journal of Alloys and Compounds, 1010, 177878. https://doi.org/10.1016/j.jallcom.2024.177878
27. Ersundu, A. E., Sayyed, M. I., Kıbrıslı, O., Akıllı, V., & Çelikbilek Ersundu, M. (2021). A thorough investigation of the $Bi_2O_3–PbCl_2–TeO_2$ system: Glass forming region, thermal, physical, optical, structural, mechanical and radiation shielding properties. Journal of Alloys and Compounds, 857, 158279. https://doi.org/10.1016/j.jallcom.2020.158279
28. Kilic, G., Ilik, E., Mahmoud, K. A., El-Mallawany, R., El-Agawany, F. I., & Rammah, Y. S. (2020). Novel zinc vanadyl boro-phosphate glasses: $ZnO–V_2O_5–P_2O_5–B_2O_3$: Physical, thermal, and nuclear radiation shielding properties. Ceramics International, 46(15), 19318–19327. https://doi.org/10.1016/j.ceramint.2020.04.272

Chapter 8
Conclusion and Future Prospects

8.1. Introduction

The current thesis has been dedicated to a comprehensive study of quaternary vanadate phosphate glass systems with a selected set of network formers and modifiers in order to obtain a particular combination of structural, physical, optical, electrical and mechanical properties. The scientific question, which has been addressed in the work, is as follows: *How practical can compositional engineering at the atomic level be used in optimising the functional performance of glass nanocomposites for a variety of technological applications?*

The result is the design and synthesis of three individual glass systems with contrasting strategic focus, created by the melt-quenching process:

1. **V_2O_5-Na_2O-ZnO-P_2O_5(VNZP)**: Designed to cover both mixed ionic electronic conducting behaviors, but the focus of the work is on the effect of V_2O_5 concentration on the formation of nanocrystallites and the formation of conduction channels.
2. **Bi_2O_3-BaO-V_2O_5-P_2O_5(BBVP):** The goal of the compound is to maximize optical properties, refractive index, transparency and band gap tunability. through the synergistic effects of heavy metal oxides (Bi_2O_3, BaO).
3. **Bi_2O_3-Fe_2O_3-V_2O_5-P_2O_5 (BFVP)**: to obtain better mechanical strength and dielectric properties, it incorporates the capability which can be reinforced by the pyramidal-like structure of Bi_2O_3 and the valence flexibility of Fe_2O_3.

In all systems, it was systematically varied to demonstrate how it complexly affects the density of oxygen packing, molar volume, the proportion of non-bridging oxygen, structural ordering at short- and medium-range lengths and the threshold oxygen concentration at which nanocrystallite precipitate. Changes in the optical band gap, refractive index, Urbach energy, dielectric constant, AC and DC conductivity, activation energies of conduction, hardness, and elastic modulus were shown to be directly correlated with the changes resulting from these structural modifications.

The X-ray diffraction (XRD), together with Fourier-transform infrared spectroscopy (FTIR), UV-$_{Vis}$ optical spectroscopy, dielectric spectroscopy, and nanoindentation, enabled a multi-scale description to be achieved, ranging from the atomic bonding structure to the macroscopic

functional behaviour. Model-based interpretations based on the Correlated Barrier Hopping (CBH) model, Jonscher, universal power law, and Variable Range Hopping (VRH) models were further used to support the experimental observations, which were important in offering insights when it came to conduction mechanisms and dynamics of relaxation.

This chapter sums up these findings into a conclusive one, where it offers:

- ✓ System-specific summaries with the outline of property trends and structure-property correspondences of each of the three glass systems.
- ✓ The general observations of the research generalize some trends, differences, and overall knowledge between the systems.
- ✓ Future prospects, in which the future technological applications in each of the systems are determined, and research avenues to optimise further performance.

The conclusions made below provide a summary of the scientific aspect of the thesis, but also act as a reason as to why the studied glass systems may serve as potential products of the next-generation optoelectronic devices, energy storage, and dielectrics.

8.2. V_2O_5-Na_2O-ZnO-P_2O_5(VNZP) system

The VNZP system revealed that network compactness and conduction behaviour are a direct function of V_2O_5 concentration. The density rose to 3.45 g/cm³ with a correspondingly enhanced oxygen packing density, and the non-bridging oxygen (NBO) content was carefully controlled. Molar volume data (26.5-30.8 cm^3/mol) was a sign of a moderately relaxed network, which is desirable in the case of ionic transportation.

Structural compositions indicated a completely amorphous order of x = 0.05 but x = 0.10 and above showed nanocrystalline phases including, $NaV_{0.66}P_{0.34}O_3$, $Na_2V_2O_6$, $NaPO_3$, $Na_2(P_2VO_8)$, $ZnNa(PO_3)_3$, and $Na_2(VPO_6)$, overlaying the glassy medium. They showed the results of FTIR that agreed with phosphate vanadate network vibrations, and NBOs helped in the mobility of ions.

The dielectric constant ($\varepsilon^{/}$) and dielectric loss ($\varepsilon^{//}$) decreased with increasing frequency but rose with temperature. Electric modulus scaling revealed temperature-independent yet composition-dependent relaxation behaviour. Bergman's function analysis (n < 1) confirmed that dielectric relaxation was of a non-Debye type, governed by the interplay of transition metal and alkali oxide

modifications within the zinc–phosphate network. VNZP was an electrically mixed ionic-electronic conductor. Electronic conductivity was reduced, and the ionic conductivity was enhanced as there was more formation of channels rich in NBO. The AC conductivity could be described by the Correlated Barrier Hopping (CBH) model, where W_M, τ_0 and T_0 of the model increased with the concentration of V_2O_5, which increased the energy barriers and reduced the total conductivity. Scaling indicated that the process of conduction relaxation was not collapsed into a composite master curve, as it was composition-dependent.

In the VNZP glass series, indentation size effect (ISE) was observed using Vickers microhardness, where the hardness decreased with the increase in applied load, and, as a whole, Hv values decreased with high V_2O_5 contents-indicating network softening and decreased rigidity, which is advantageous in applications that require an increased formability. Nano-indentation indentation curves, as analysed by the Oliver and Pharr method, also demonstrated comparable initial elastic stiffness in the different compositions but slight differences in the plastic deformation resistance, whereby lower concentrations of V_2O_5 tended to cause a slightly greater resistance to penetration. A combination of these observations serves to emphasise the fact that limited V_2O_5 enrichment is capable of strengthening the matrix, and then over-enrichment can be used to induce a more malleable glass structure.

Having the conductivity value of the current glass compositions lies between 10^{-3} to 10^{-6} in the temperature range of 403 K to 533 K, in addition to thermal stability and tunable nanocrystallite formation, VNZP is a good possibility as a cathode material in solid-state sodium-ion batteries.

8.3. Bi_2O_3-BaO-V_2O_5-P_2O_5(BBVP) system

The densifying effect of Bi_2O_3 and BaO inclusion was emphasized in the BBVP series, which presented the densest values with the lowest molar volumes of all of the investigated systems (3.8 to 5.2 g/cm^3 and 56.21 to 61.54 cm^3 /mol, respectively). Such dense network packing found further reinforcements on the basis of optical and dielectric observations. The XRD confirmed the absence of sharp Bragg peaks, revealing the amorphous structure of all the prepared glass samples, i.e. there was no long-range crystalline order. Optically, optical band gap became higher and the Urbach energy became smaller with higher Bi_2O_3, which indicated better short-range order and

fewer defect states. The refractive index, polarizability and nonlinear refractive index all showed an increment where the photonic potential of the system is underlined.

Both $\varepsilon^{/}$ and $\varepsilon^{//}$ decreased with frequency and increased with temperature, exhibiting a scaling behaviour of the electric modulus that is independent of temperature and composition. The dielectric relaxation mechanism, as determined from Bergman's function, was also non-Debye type, influenced by structural reorganisation due to heavy-metal and alkaline-earth oxide incorporation.

Electrically, both DC and AC conductivities increased with temperature but decreased generally with a greater per cent Bi_2O_3 as more pathways based on polarons were blocked. W_M, τ_0 and T_0 were proven to be higher energy barriers at the elevated loading of bismuth as the modified CBH model fitted the AC conductivity data perfectly.

In the case of the BBVP glass system, a gradual addition of Bi_2O_3 dramatically improved both micro- and nano-hardness owing to large ionic radius, high polarizability and forceful linkages between Bi and O and P that lead to the densification of the structure, decline in molar volume, and augmentation in cross-linking density. The increased elastic modulus, fracture toughness and stored elastic energy and the decreased length of cracks brought by this compositional alteration, proved that the resistance of the crack propagation was higher and the mechanical resiliency of this material was better. The net effect of densification and increased interatomic bonding strength resulted in a stiffer, tougher and energy-absorbing structure, optimised in its application to high wear-resistant and structural stability applications.

BBVP glasses analysis in DSC revealed a consistent improvement of thermal stability with Bi_2O_3 constrained within the glasses due to increasing values of Tg, Tc, and Tp as the content of Bi_2O_3 increases. An increase in thermal stability factor ($\Delta T = T_c - T_g$) of 142 °C at x = 0.05 to 152 °C at x = 0.35 suggests better devitrification resistance and a stronger, cross-linked glass network. It is confirmed that the Bi_2O_3 concentrations indeed increase the strength of the network bonding and augment the energy required to rearrange the structure, and therefore, the system is advantageous in applications where high temperature is a demanded parameter and where crystallization behaviour must be controlled.

BBVP glasses can be used in nonlinear optical devices, optical limiters and photonic switches that are difficult to achieve because the material is optically tunable, has high density and is stable.

8.4. Bi_2O_3-Fe_2O_3-V_2O_5-P_2O_5 (BFVP) system

Strong synergetic effects between the densification effect due to Bi_2O_3 and electronic modulation due to Fe_2O_3, demonstrated in the BFVP glasses, led to remarkable mechanical and dielectric characteristics. The values of density were 3.6 to 4.9 g/cm^3 with molar volumes being 51.21 to 62.54 cm^3/mol, which supported compact structural arrangements.

Structurally, the majority of samples were amorphous, with the known crystalline phases $Fe_3(PO_4)_2$, Fe_2VO_4, $BiPO_4$, and Bi_2VO_5 receiving weak nanocrystalline peaks. This system produced the maximum values of hardness in the study-microhardness went up by 424 per cent (182-766Hv) and nanohardness by 359 per cent (191.52-828.67Hv) mechanically, whereas the elastic modulus improved by approximately 165 per cent (56.97 to 150.94 GPa), which means that this system has very strong bonding and rigidity to its network.

The dielectric constant showed enhancement at low frequencies and remained stable with temperature, reaching up to a 15 % increase at 413 K. Dielectric loss exhibited optimal dipolar relaxation at x = 0.3. For x = 0.4, the frequencies that yielded the highest values of x= 0.40 were at low-frequency implying high energy storage capabilities. With additions of Bi_2O_3, the dielectric relaxation activation energy was reduced to 0.49 eV from 0.67 eV, indicating increased ion mobility.

Mott and Greaves Variable Range Hopping (VRH) models were obeyed by the electrical conduction, and Jonscher's universal power law fitted the AC conduction. This conductivity relaxation was found to be composition-dependent, however, independent of the temperature, making it feasible to carry out the conductivity relaxation under a wide range of thermal conditions with stable performances.

The mechanical strength, dielectric properties and thermal performance of the BF-VP system together mean that it is perfectly suited to high-k capacitors, electronic packaging and energy storage.

8.5. Overall Highlights

In this thesis, integrated knowledge is provided concerning how precisely designed compositional modification of quaternary glass systems based on vanadate-phosphate glass can be used to selectively tailor structural, physical, optical, electrical, and mechanical properties needed to suit various technological applications. The highlights of the study are the following:

Controlled Structural Evolution

- All three glass systems showed a composition-dependent manner of transitioning into a completely amorphous state to a nanocomposite-dominated state with nano-sized crystalline phases embedded within the glass (matrix).
- Nanocrystallites of $NaV_{0.66}P_{0.34}O_3$, $Na_2V_2O_6$, $NaPO_3$, $Na_2(P_2VO_8)$, $ZnNa(PO_3)_3$, and $Na_2(VPO_6)$ appeared in the VNZP series at x -0.10 and altered the conductivity and density.
- The crystals of Bi-based and Fe-containing vanadate were synthesized selectively in the BBVP and BFVP series, which increased optical properties (BBVP) and mechanical properties (BFVP).

Packing efficacy and density

- With heavy metal oxides (Bi_2O_3, BaO) added to the distribution provided a 73-150 per cent increase in density over non-impregnated (VNZP) to ~5.12 g/cm^3 at maximum (BBVP) as compared to ~3.5 g/cm^3 in VNZP.
- Molar volume behavior indicated a lower free volume with Bi-rich composition, which suggested tighter atomic packing and mechanical stability.

Optical Tailoring

- VNZP: The optical band gap (E_{opt}) decreased with an increase of V_2O_5, because of the creation of non-bridging oxygen (NBO) in favour of electronic transport.
- BBVP: Bi_2O_3 addition yielded a positive effect on the E_{opt}, which decreased the Urbach energy, suggesting better short-range ordering and weaker structural disorder fits well with transparent photonic applications.

- BFVP: exhibited composition-dependent but temperature-independent AC conductivity relaxation, with high dielectric constants at low frequencies, especially for Bi-rich compositions.

Mechanical Performance

- BFVP displayed the greatest values of microhardness (766 Hv), nanohardness (828.67 Hv), as well as elastic modulus (~150.94 GPa), being better than VNZP and BBVP as a result of higher packing density and bond strength.
- These values affirm that BFVP can be used in high-load bearing dielectric and component packaging.

Cross-System Application Potential

- VNZP: Sodium-ION battery cathodes because of mixed conduction paths.
- BBVP: Transparent optical materials with a high refractive index for photonic devices.
- BFVP: Capacitors of high-k dielectric and mechanically stabilized substrates for high-temperature electronics.

Overall, the current work demonstrates that compositional design is an effective tool for developing multifunctional glass nanocomposites with specific property profiles.

8.6 Future Prospects

This study offers a clear blueprint towards achieving industry applications of vanadatephosphate glass systems using laboratory research findings. Several future research and development opportunities are suggested:

1. **Application-Specific Optimisation**
    - **VNZP System**:

        - Optimise V_2O_5 material to achieve optimum balance of ionic and electronic conductivity in solid-state sodium-ion cells.
        - Explore the parameters of controlled heat-treatment schedules to optimize nanocrystallite size and distribution in favour of improved transport properties.

- **BBVP System**:
  - Develop nonlinear optical devices, waveguides, and optical limiters where refractive index control and low optical loss are crucial.
  - Apply thin-film fabrication methods (e.g., pulsed laser deposition) to integrate these glasses into photonic circuits.
- **BFVP System**:
  - Target high-k dielectric applications in power electronics and energy storage.
  - Explore potential as mechanical support layers for microelectronics due to high hardness and modulus.

2. **Advanced Structural Characterisation**
   - Use high-resolution transmission electron microscopy (HRTEM) and synchrotron-based X-ray absorption spectroscopy to reveal atomic-level nanocrystallite-glass interface behaviour.
   - Apply pair distribution function (PDF) analysis to quantitatively map short- and medium-range structural evolution with doping.
3. **Computational Modelling and AI Prediction**
   - Implement molecular dynamics simulations and density functional theory (DFT) to predict structure–property relationships.
   - Train AI-based predictive models using current dataset trends to accelerate discovery of optimal glass compositions.
4. **Device Prototyping and Long-Term Stability Studies**
   - Fabricate prototype devices (Na-ion battery cells, optical filters, dielectric capacitors) to validate real-world performance.
   - Conduct accelerated ageing tests to evaluate stability under thermal cycling, humidity, and electrical stress.
5. **Eco-Friendly and Scalable Production**
   - Investigate low-carbon melt-quenching methods and recycling of glass cullet for sustainable manufacturing.
   - Study the substitution of costly raw materials with more abundant oxides without compromising functionality.

By following these pathways, the glass systems developed in this thesis could transition into commercially viable materials for next-generation energy storage, optoelectronics, and high-performance dielectric applications, cementing their role in the future of advanced material technology.

Sourik Brahma Hazra
21/08/2025